Quantum embedding methods in dual space for strongly interacting electronic systems

Dissertation
zur Erlangung des Doktorgrades
an der Fakultät für Mathematik, Informatik und Naturwissenschaften
des Fachbereichs Physik

der Universität Hamburg

vorgelegt von
Matteo Vandelli

Hamburg
2022

ii

Zusammenfassung

Derzeit besteht eine große methodische Lücke zwischen den numerischen Instrumenten, die in den ab-initio rechnergestützten Materialwissenschaften verwendet werden, und den Methoden, welche eingesetzt werden, um die Auswirkungen starker Korrelationen zu untersuchen.

Erstere sind in der Lage, realistische große Systeme zu behandeln, während letztere sich auf Modelle mit geringerer Anzahl an Freiheitsgraden konzentrieren, die sehr akkurat gelöst werden können. Das Ziel vorliegender Arbeit besteht darin, Instrumente zu entwickeln, die eine Brücke zwischen diesen beiden Ansätzen bilden. Um dieses Ziel zu erreichen, wurde der Pfad der dualen Theorien starker Korrelationen (Theorie dualer Fermionen und Bosonen) gewählt, welche diagrammatische Erweiterungen der dynamischen Molekularfeldtheorie sind. Die dualen Theorien beruhen auf der Aufteilung eines großen Systems in zwei Teile, d.h. in eine lokale Störstelle und einen nichtlokalen Teil. Dadurch wird das Anfangsproblem auf ein effektives Referenzproblem reduziert, welches exakt gelöst werden kann. In dieser Hinsicht gehören die dualen Theorien zur Klasse der quantenmechanischen Einbettungsmethoden.

Das erste wichtige Resultat vorliegender Arbeit ist die Erweiterung einer Approximation der Theorie dualer Bosonen, die als D-TRILEX-Theorie bezeichnet wird. Die D-TRILEX-Theorie ist aus numerischer Sicht besonders attraktiv, da sie die Komplexität der Berechnung nichtlokaler, starker Korrelationen auf die Komplexität einer *GW*-Theorie reduziert und gleichzeitig exakte lokale Vertexkorrekturen nicht-störungstheoretisch berücksichtigt. Ein weiterer Großteil vorliegender Arbeit wurde der Implementierung eines effizienten Codes gewidmet, welcher die Berechnung von Multi-Band-Systeme mit mehreren Orbitalen mittels der D-TRILEX-Theorie ermöglicht. Obwohl physikalische Argumente zugunsten der D-TRILEX-Näherung vorgebracht werden können, ist ihr Gültigkeitsbereich nicht a-priori bekannt. Folglich wird ein Benchmark benötigt, um die Genauigkeit und die Grenzen des Anwendungsbereiches bewerten zu können.

Des Weiteren stellt ein wesentlicher Bestandteil der vorliegenden Dissertation die Implementierung eines diagrammatischen Monte-Carlo-Schemas für die Theorie dualer Bosonen (DiagMC@DB) dar, die es erlaubt, alle Feynman-Diagramme der Theorie zusammenzufassen. In einer detaillierten Diskussion betrachten wir, wie die Analyse dieser Methode Ordnung-für-Ordnung es ermöglicht, Informationen über Phasenübergänge zu extrahieren. Insbesondere fassen wir die Instabilität der Ladungsdichtewellen des erweiterten Hubbard-Modells ins Auge. Später wurde DiagMC@DB verwendet, um die Genauigkeit der D-TRILEX Methode für das Hubbard-Modell mit einem Orbital (dotiert und bei halber Füllung), sowie für das erweiterte Hubbard-Modell mit nichtlokalen Wechselwirkungen zu untersuchen. Dabei wurden Bereiche ermittelt, in denen die D-TRILEX-Theorie die Ergebnisse der Theorie dualer Bosonen in guter Genauigkeit reproduziert.

Ein weiterer wichtiger Teil dieser Arbeit besteht darin, die Gültigkeit dieser Näherung an einem System mit mehreren Orbitalen zu untersuchen. Der Grund dafür ist, dass leider nur wenige exakte Lösungen für solche Systeme bestehen. Deswegen haben wir die D-TRILEX-Methode mit der exakten Diagonalisierung für ein System mit mehreren Orbitalen bestehend aus einem Dimer verglichen. Dabei haben wir sehr genaue Übereinstimmungen in den Ergebnissen festgestellt, obwohl für solch ein niederdimensionales System erwartet wird, dass DMFT kein gutes Referenzsystem ist. Außerdem haben wir sie mit der dynamischen Vertex-Approximation (DΓA) für ein Modell mit zwei Orbitalen auf einem Gitter verglichen.

Im letzten Teil diskutieren wir zwei Anwendungen der D-TRILEX-Methode. Die erste Anwendung besteht darin, Bleiadatomen auf einer Siliziumoberfläche zu untersuchen, wobei langreichweitige Wechselwirkungen und Fluktuationen entscheidend für die Beschreibung der Eigenschaften des Systems sind. Als zweite Anwendung untersuchen wir eine hoch interessante Situation, in der die Einbeziehung von nichtlokalen Fluktuationen das Bild einer rein lokalen Beschreibung der Korrelationen erheblich verändert und zu einer ausgedehnten Region mit koexistierenden metastabilen metallischen und isolierenden Phasen führt.

Abstract

There is currently a large methodological gap between the numerical tools used in *ab-initio* computational materials science and the methods used to investigate the effects of strong correlations. The former can treat realistic large-scale systems, while the latter focus on models with few degrees of freedom that can be solved very accurately. The purpose of this thesis is to develop tools that act as a bridge between these two approaches.

The route chosen in this thesis is the dual theories of strong correlations (dual fermion and dual boson theories), that are diagrammatic extensions of the dynamical mean field theory. The dual theories rely on dividing a large system into two parts, an impurity and a non-local part, reducing the initial problem into an effective reference problem that can be solved exactly. From this perspective, the dual theories effectively belong to the class of *quantum embedding methods*.

As first major result of this thesis, we extend an approximation of the dual boson theory, named D-TRILEX theory, to the multi-band framework. D-TRILEX is particularly attractive from a computational point of view, because it reduces the complexity of the calculation of non-local strong correlations to that of a *GW* calculation, while including exact local vertex corrections non-perturbatively. The development of this theory allowed us to implement an efficient code for multi-orbital and multi-site D-TRILEX calculations. Even though physical arguments can be made in favor of the D-TRILEX approximation, its regime of validity is not *a-priori* known. As a consequence, a benchmark is needed to assess its accuracy and limitations.

To this aim, an important portion of this work consisted in the implementation of a diagrammatic Monte Carlo scheme for the dual boson theory (DiagMC@DB), that allows to sum up all the Feynman diagrams of the theory in an unbiased way. I show that the order-by-order analysis of this method allows to extract information about phase transitions, in particular a charge density wave instability in the extended Hubbard model. I use the DiagMC@DB at later stages to assess the accuracy of the D-TRILEX method for the single-orbital Hubbard model at half-filling and in the doped regime, as well as for the extended Hubbard model with non-local interactions. Based on this analysis, we identify the regimes where it accurately reproduces the dual boson results.

Moreover, we investigate the validity of the approximations in a multi-orbital framework, where exact results are rare. Specifically, we compare the D-TRILEX method with exact diagonalization for a multi-orbital dimer system, finding very accurate results even for this low-dimensional system, where the impurity problem is not a good reference system. we also present an additional comparison with the dynamical vertex approximation (DΓA) for a two-orbital model on a lattice.

In the last part, we discuss two applications of the D-TRILEX method. The first consists in the study of lead adatoms (Pb) on a silicon surface, where long-range interactions and fluctuations are crucial to describe the properties of the system. As a second application, we investigate an intriguing situation where the inclusion of non-local fluctuations significantly changes the picture provided by a purely local description of the correlations and leads to an extended region of coexisting metastable metallic and insulating phases.

Contents

1 Introduction

In order to explain several emergent exotic properties of materials, it is crucial to emphasize that microscopic particles behave in an extremely different way from the picture we experience at macroscopic scales.

Specifically, our picture of a *particle* as a small sphere is insufficient as soon as quantum phenomena come into play. The microscopic world at nanoscopic or smaller scales is a quantum realm, where particles not only behave as small waves that can be more or less localized in space, but they are also indistinguishable from other particles of the same kind, in such a way that it is impossible to attach a small label to one of them and follow its motion as we can do in classical physics.

These properties are not only important for our understanding of nature, but are also crucial for the development of new technological applications. Quantum effects were seen at least as a nuisance if not as a severe limitation until few years ago, when the main goal was to push the realization of Moore's law for the density of transistors per chip to the extreme limit. Feynman and others pointed out that quantum phenomena could potentially be exploited to achieve better computational performances and to develop more sensitive sensors. Nowadays, quantum phenomena are recognized as a source of potentially unlimited ways of tuning the properties of devices, by modifying the chemical composition of the involved materials or through the creation of complex nano- and heterostructures. Quantum technologies and quantum information have become very hot topics not only in research, but also in the industry sector. However, the design of materials for new applications, capable of exploiting quantum effects, requires a deep understanding of the behavior of quantum many-body systems.

Very suitable materials for device applications are the so-called *strongly-correlated electronic systems*. In these systems, electrons do not behave as independent particles, but they strongly interact due to the Coulomb repulsion between them. The presence of strong interactions among the electrons is a necessary but not a sufficient condition to obtain a strongly correlated system. In a weakly interacting regime, also known as the Fermi liquid regime, electrons behave similarly to a gas of particles and it is the regime where the usual picture provided by the bandstructure theory of solids is applicable. This regime can be very interesting for several applications, but the electrons are nearly indenpedent and only weakly entangled. On the other hand, too strong interactions often lead to a system frozen in an insulating configuration. Typically, strong correlations between the electrons

appear in an intermediate regime between these two opposite cases of Fermi regime and the strong-coupling limit. In the intermediate regime between these two cases, we observe metal-to-insulator transitions, strong magnetic and density response functions or even superconductive fluctuations at high-temperature in some classes of materials. Since strongly correlated electrons behave as a single entangled ensemble of particles with collective behavior, a relatively weak perturbation of the system can result in very strong responses. With a proper choice of the materials, it is also possible to achieve the completely opposite situation in which the system is extremely robust against external attempts to change its state. In the most interesting cases for applications, these systems are additionally characterized by a very rich phase diagram, that offers many routes for tunability, and can host high-temperature superconductivity, heavy-fermion materials, charge density wave, complex magnetic textures or Kondo physics.

A rule-of-thumb for distinguishing materials with strong or weak correlations among the electrons is to check whether they have partially unoccupied localized orbitals, i.e. open $d-$ or $f-$shells, combined with delocalized $s-$ or $p-$orbitals, that allow the electrons to hop between the different atoms. An example of materials belonging to this class are the metal oxides that can host Mott insulating phases as well as magnetism and multi-ferroicity [1]. Interestingly, strong correlations among electrons have also been observed in completely different electronic systems, namely two-dimensional materials where the electronic orbitals are mostly only of $p-$ and $sp-$ character, as discussed in Chapter 7. As in most of the strongly correlated materials, the characterization of these systems requires a deep understanding of all the different degrees of freedom involved (electronic orbitals, localized magnetic moments, lattice vibrations...), which can become accessible only with a synergic effort of experiments, theory and computational methods.

The theoretical and computational modeling of these systems is particularly important to understand the origin of the experimental observations. However, methods for the description of strong correlations are currently often limited to aspects of the systems. The fundamental reason for this limitation is the absence of an exact method that can treat all the occurring degrees of freedom simultaneously. The exponential scaling of the many-body wave function with respect to the number of particles makes it computationally impossible to go beyond rather small clusters, while the fermionic sign problem affects many quantum Monte Carlo methods when they are applied to electrons, especially at low temperatures.

On the opposite side of the spectrum, the major tool of materials science for the description of electrons, namely the density functional theory (DFT), is very efficient in treating all the degrees of freedom of an electronic problem, but it has often proven ineffective in predicting the properties of strongly correlated electronic systems, especially the susceptibilities. Another very successful method is the dynamical mean field theory (DMFT), which is based on some assumption of locality of the self-energy of the system. This means that within DMFT the self-energy is momentum-independent and spatial

fluctuations are neglected. DMFT is able to describe strong correlations as long as they are localized on the atomic sites. This assumption of locality is well-established in some classes of compounds and can explain the interplay between itinerant electrons occupying delocalized orbitals and localized electrons in atomic-like orbitals to some extent. However, it cannot describe non-local correlations, in particular the long range correlations which are important to characterize the collective bosonic modes appearing in several correlated materials.

For these reasons, there has been an high demand for a method bridging between these different perspectives within the community of quantum many-body scientists. This high demand has prompted several attempts aimed at the development of a method to achieve that goal. The work presented in this thesis outlines a novel possible route in this direction, which is free from most of the problems occurring in the other methods described here.

The methods we propose in this thesis are based on the dual theories for treating non-local strong correlations beyond the local approximation usually provided by DMFT. Dual theories provide an exact formalism for performing a perturbative expansion around an arbitrary interacting starting point, that can be modeled as an impurity problem and solved exactly. They are based on the idea of splitting the system into two parts, couple them with an arbitrary hybridization function and then perform an Hubbard-Stratonovich transformation, which replaces the electronic variables with new dual fermionic and bosonic fields. The new system described by these new particles is in general much less correlated than the original electronic problem, since the effect of the local fluctuations is already taken into account in the impurity reference system. It is then possible to compute the observables of the original lattice system analytically. These theories have been very successful in describing several phenomena related to strong correlations and generally provide results in excellent agreement with exact calculations, in regimes where the latter are available.

Since the interacting reference point for the perturbative expansion is an impurity problem, we can look at these theories as quantum embedding methods. This correspondence can be very important since it creates a bridge between different areas of condensed matter physics and chemistry that would otherwise be separated by the respective methods and jargon. Quantum embedding methods are very important in current research on computational chemistry. They allow us to split the system of interest in different pieces. The most correlated parts are treated with very accurate methods and the rest is treated under some kind of simplified scheme, often a mean field approach. These methods are useful for two main reasons.

- They consider a much smaller subspace, limiting the number of involved degrees of freedom in the high-level part of the calculations, which is usually the most computationally expensive.

- They provide a scheme to propagate self-consistently the feedback from one part of the system into the other, by means of the hybridization between them.

- They can help the development of quantum computation, since quantum computers will probably not be able to deal with a large number of degrees of freedom in the close future. Quantum embedding could help in splitting the problem into a small system solvable with quantum computers and the rest that can be treated with hybrid methods in polynomial time.

Our expectation is that the multi-orbital and multi-site formulation of the D-TRILEX theory presented in this work can be used in combination with other methods, such as cluster Monte Carlo methods and even quantum devices, in order to extend their range of applicability to more general lattice problems and even realistic materials on the long term.

1.1   Structure of the thesis

This thesis is devoted to the development of a framework for the prediction of properties of materials with strong spatial electronic correlations. In order to achieve this goal, we briefly introduce the general framework of Green's function methods and path integral formalism in Chapter 2.

Computational challenges in the calculation of many-body electronic systems are discussed in detail in Chapter 3, where we recall the most-widely used methods to tackle the problem. Here, we also introduce the Anderson's impurity problem and we discuss quantum embedding methods such as DMFT, density matrix embedding theory (DMET), rotationally-invariant slave boson method (RISB) and self-energy embedding theory (SEET).

In Chapter 4, we introduce the dual theories of strong correlations. In particular, we derive the dual boson action in a general multi-band formalism. Here, we derive one of the main results of this work, the partially bosonized action in the multi-band framework. The latter is an optimal approximation of the dual boson theory, that allows to remove the four-point vertex functions appearing in the dual boson theory and to keep only the relatively inexpensive two- and three-point correlation functions. The additional advantage of the theory is that it can be written as an effective fermion-boson theory, similar to the electron-phonon theory in the Holstein model for polarons.

In Chapter 5, we discuss the diagrammatic Monte Carlo solution to the dual boson action (DiagMC@DB), which was developed as a part of the work for this thesis. Here, we show how the order-by-order analysis of the dual boson perturbative series can provide information about phase transitions, in particular in the case of the charge density wave (CDW) transition in the extended Hubbard model.

In Chapter 6, we present the D-TRILEX solution of the partially bosonized action discussed in Chapter 4. It consists in the first set of Feynman diagrams obtained as an expansion in terms of the fermion-boson interaction. We use this chapter to test the validity

of the theory. In order to do that, we compare D-TRILEX with DiagMC@DB and with the ladder dual fermion approximation (LDF) for the single-orbital Hubbard model on a square lattice. We additionally use the partially bosonized approximations of the four-point vertex within DiagMC@DB to analyse the role of each set of diagrams in different regimes. We also compare D-TRILEX results with the DiagMC@DB solution for the extended Hubbard model with nearest-neighbor interactions V and for the doped Hubbard model to assess the limits of validity of the approximation. Finally, we present some calculations aimed at evaluating the method in multi-orbital cases. In particular, we benchmark D-TRILEX calculations for the two-orbital Hubbard-Kanamori dimer, which can be exactly solved by exact diagonalization (ED). We conclude with a comparison with the DΓA method for the Hubbard-Kanamori model on a square lattice.

In Chapter 7, we collect results for a system of lead (Pb) adatoms on a silicon (111) surface. This system is particularly interesting, because it involves strong local as well as strong non-local interactions, that lead to a variety of phases. Additionally, spin-orbit coupling plays a major role in the geometry of magnetic excitations of this system. We disentangle the contribution coming from each channel in order to understand the origin of the CDW phase transition in this system, and at the same time we show that our method can efficiently treat this large variety of competing degrees of freedom.

In Chapter 8, we attach a pre-print based on the framework developed for this thesis, for the sake of completeness. In particular, we study a two-orbital model on a cubic lattice with crystal-field splitting and density-density on-site Coulomb interaction. Contrary to DMFT, in the vicinity of the Mott metal-to-insulator transition, we find a very broad region of the local interaction U where it is possible to obtain two different metastable solutions, corresponding to a metallic and an insulating phases. The same phase coexistence can be observed if the Hund's coupling J is included in the calculations. These findings show that non-local effects can strongly modify the picture resulting from local approximations even in three dimensions, where DMFT is widely believed to provide a very accurate description of the properties of the system.

Finally, in Chapter 9, we highlight the main conclusions and new perspectives opened by this work.

2 From quantum mechanics to Green's functions

2.1 The problem of many interacting electrons in solids

2.1.1 The Hamiltonian of an electronic system

The fundamental problem that appears in materials science and electronic structure calculations is theoretically described by the following Hamiltonian operator, that accounts for the energy of N interacting electrons

$$\hat{H} = \sum_{i=1}^{N} \left(\frac{-\hbar^2 \nabla_i^2}{2m} + U(\mathbf{r}_i, \{\mathbf{R}\}) \right) + \frac{1}{2} \sum_{i \neq j}^{N} \frac{e^2}{|\mathbf{r}_i - \mathbf{r}_j|} \tag{2.1}$$

where m is the mass of the electron, $\mathbf{r}_i$ indicates the position of the i-th electron and $U(\{\mathbf{r}, \mathbf{R}\})$ is the external potential which depends on the position of the atomic nuclei and external fields as well. This term can also contain the effect of spin-orbit coupling, hence it is not necessarily diagonal in spin space. The last term describes the Coulomb repulsion between electrons.

Even if we decide to focus only on the electronic degrees of freedom, assuming that the motion of the nuclei can be disregarded or it can be treated in the Born-Oppenheimer approximation, the Hamiltonian of Eq.(2.1) still poses a formidable challenge to computational physics, when the system is a large molecule or a solid. Following the quantum theory, the spectrum of the electronic system can be obtained by solving the stationary Schrödinger equation for a system of particles with spin 1/2 as

$$\hat{H}\psi(\mathbf{r}_1\sigma_1, ..., \mathbf{r}_N\sigma_N) = E\,\psi(\mathbf{r}_1\sigma_1, ..., \mathbf{r}_N\sigma_N). \tag{2.2}$$

If we are able to compute the energy spectrum and the eigenvectors of the Hamiltonian $\hat{H}$, all the dynamical and statistical properties of the system at equilibrium can be computed from them by using quantum mechanical expectation values, as explained in the following sections of this Chapter. Interestingly, the two equations (2.1) and (2.2) are sufficient to describe most of the physical systems occurring at energy scales small enough that

relativistic effects can be disregarded. This fact induced Dirac to make a bold statement in 1929 [2], claiming that

"the underlying physical laws necessary for the mathematical theory of ... the whole of chemistry are thus completely known, and the difficulty is only that the exact application of these laws leads to equations much too complicated to be soluble."

After years of successful applications of quantum theory to the simulation and interpretation of the experimental results, we can confirm that this statement is essentially true when applied to usual chemical processes and materials science. This quote from Dirac foresaw a very fundamental issue in the solution of the equations of quantum mechanics, in particular that the diagonalization of a problem of N quantum interacting particles (or at least of interacting fermions) is an extremely hard problem from the computational point of view [3]. As a matter of fact, it has an exponential computational cost on a classical hardware [4]. For this reason, the Hamiltonian (2.1) can be exactly diagonalized only for very small systems.

We could think of fighting the exponential scaling by using quantum computers, which work based on qubits instead of bits [5]. Quantum devices of course do not directly exhibit an exponential scaling in the number of particles that can be simulated. However, the full many-body problem is challenging also for quantum computers [6, 7], as the encoding of the very large amount of degrees of freedom that appear require very deep quantum circuits with a large amount of gates to be applied on the qubits to change their state.

The additional limitation of currently available quantum devices is that they are prone to errors induced by interaction with the environment. An error in the single operation on the qubits propagates through the computation and this results in a limitation on how deep the quantum circuits can be, before the noise makes the result unusable. This currently severely limits the number of quantum gates that can be applied, hence it reduces the complexity of the Hamiltonians that can be directly simulated on quantum hardware. Currently, no quantum advantage over classical devices has been established so far for the solution of the *ab-initio* Hamiltonian of large many-electron quantum systems in general cases of interest. This motivates the development of classical methods for the simulation of quantum systems as well as hybrid methods, that can combine the currently limited quantum devices with classical hardware.

2.1.2 Fermions, Bosons and second quantization

The Hamiltonian (2.1) is written in the space of positions of the electrons, also known as *real* space. however, in general the state of the system can be written in the complete basis corresponding to the set of eigenstates $|j\rangle$ of an arbitrary Hermitian operator $\hat{O}$,

$$\hat{O}|j\rangle = O_j|j\rangle \tag{2.3}$$

The index j characterising these states is called a *quantum number*, and it can be real space, momentum or spin of the particle and so on depending on the system. Indeed, if we consider a single-particle system, we can consider the state of the system to be represented by a generic vector $|\psi\rangle$ in a single-particle Hilbert space $\mathcal{H}^{(1)}$. The wave function of the system in the space can be recovered from the scalar product with the basis vector $|\mathbf{r}\rangle$, as $\psi(\mathbf{r}) = \langle \mathbf{r} | \psi \rangle$. Similarly, we can express the vector in the basis of the chosen operator $\hat{O}$ as

$$|\psi\rangle = \sum_j \langle j|\psi\rangle |j\rangle = \sum_j \psi_j |j\rangle. \tag{2.4}$$

In turn, the index j can be composite and corresponding to different degree of freedom. For instance, we can consider $j = \mathbf{r} = (x, y, z)$ or, in the case of solids, we can considered the combined momentum, spin and orbital index $j = (\mathbf{k}, \sigma, l)$. In an analogous way, the state of an N-particle system is described by the vector in an Hilbert space spanned by vectors the direct product of single-particle states $|j_1\rangle|j_2\rangle...|j_N\rangle \equiv |j_1\rangle \otimes |j_2\rangle \otimes ... \otimes |j_N\rangle$. However, there is a crucial fundamental symmetry in the description of quantum mechanical particles: quantum particles are inherently indistinguishable. As a consequence, the probability $p^{(2)}$ of measuring the first particle with quantum number j_1 and the other with quantum number j_2 should be the same as if we swap the numbers. This can be expressed as $p^{(2)}(j_1, j_2) = p^{(2)}(j_2, j_1)$. In practice, the state describing two particles characterised by sets of quantum numbers j_1 and j_2 should obey the relation

$$|j_1, j_2\rangle = e^{im\pi} |j_2, j_1\rangle \tag{2.5}$$

such that the probability density $p^{(2)}$ is left invariant upon an exchange of the two particles

$$p^{(2)}(j_1, j_2) = \| |j_1, j_2\rangle \|^2 = \| e^{im\pi} |j_2, j_1\rangle \|^2 = \| |j_2, j_1\rangle \|^2 = p^{(2)}(j_2, j_1). \tag{2.6}$$

It can be shown that the phase factor must be $e^{im\pi} = \pm 1$ in more than two dimensions. Elementary particles, that live in (3+1)-dimensional space, can be divided into only two categories, named bosons ($m = 0$) or fermions ($m = 1$) due to topological considerations about the exchange of different particles. Photons are an example of bosonic particles, while electrons are fermions. In dimensions equal to or less than two dimensions, this is not necessarily true [8] and the number describing the phase m can be non-integer or even a non-abelian operator [9]. The exotic particles described by these different phase factors are called anyons [10] and have been suggested as a way of realising topological quantum computing [11].

Focusing on the less exotic particles, a very important consequence of the fermionic phase $e^{i\pi} = -1$ on the behavior of fermionic particles is the *Pauli exclusion principle*. This principle states that two fermions in many-particle system cannot be in a state described by the exact same set of quantum numbers j at the same time. The most simple, yet important

example, is the well-known fact that an atomic or molecular energy level can contain only up to two electrons, one with spin up and one with spin down. This symmetry with respect to the exchange of particles dictates that the state of $\mathcal{N}$ particles is described by a suitably (anti-)symmetrized state $|j_1, j_2, ..., j_\mathcal{N}\rangle$. In the interacting case, the state cannot in general be easily decomposed in product states, but this symmetry has to hold. In the case of a system of independent fermions, the anti-symmetrized states is known as Slater determinant. The formalism described so far is known as *first quantization*.

An equivalent formalism is the *second quantization*. It can be formulated introducing a new Hilbert space, called Fock space, in which each state is indexed by the number of times each set of single-particle quantum numbers is occupied. Explicitly, we can write

$$\mathcal{F}_B = \left\{ |n_0, n_1, ...n_j...\rangle \text{ with } n_j \in \{0, 1, 2, ...\} \right\} \text{ for bosons,} \tag{2.7}$$

$$\mathcal{F}_F = \left\{ |n_0, n_1, ...n_j...\rangle \text{ with } n_j \in \{0, 1\} \right\} \text{ for fermions.} \tag{2.8}$$

For this reason, it is often referred to as occupation number basis. This allows to represent many-particle states in a more convenient way. Additionally, we can simultaneously describe systems with varying number of particles, which is very important in the case of grand-canonical ensemble, where only the average number of particles is fixed. The mathematical objects that allow to construct this mapping are the creation/annihilation operators $\hat{c}_j^\dagger / \hat{c}_j$. The basic rule common to all the kinds of particles is that $\hat{c}_j^\dagger$ *creates* a particle in the state j, which we assume to be integer without any loss of generality, so we have the immediate identification

$$|j\rangle \equiv \hat{c}_j^\dagger |0\rangle = |..., \overset{j-2}{0}, \overset{j-1}{0}, \overset{j}{1}, \overset{j+1}{0}, \overset{j+2}{0}, ...\rangle_\mathcal{F} \tag{2.9}$$

with $|0\rangle = |0, ..., 0\rangle$ denoting the empty state (or ground state). Additionally, we can remove a particle by using the annihilation operator

$$\hat{c}_j |..., \overset{j-1}{n_{j-1}}, \overset{j}{n_i}, \overset{j+1}{n_{j+1}}, ...\rangle = \begin{cases} (\xi)^{\prod_{i=1}^{j-1} n_j} |..., n_{j-1}, n_j - 1, n_{j+1}, ...\rangle & \text{if } n_j > 0 \\ 0 & \text{else} \end{cases}. \tag{2.10}$$

where $\xi = 1$ for bosons and $\xi = -1$ for fermions. Here 0 denotes the null vector in the Fock space, not to be confused with the empty state $|0\rangle$. The null vector is such that any operator applied to it yields 0 again. Now that we are perfectly able to describe single-particle states with creation operators, we need to introduce rules to create many-particle states. In order to do that, it is necessary to introduce commutation relations between the new operators. At this point, the difference between bosons and fermions becomes even more evident.

- Bosons: the particles do not acquire a phase when they are exchanged, so the operators commute.

$$\left[\hat{c}_i, \hat{c}_j\right] = 0, \quad \left[\hat{c}_i^\dagger, \hat{c}_j^\dagger\right] = 0, \quad \left[\hat{c}_i, \hat{c}_j^\dagger\right] = \delta_{ij} \tag{2.11}$$

where $[A, B] = AB - BA$ is the usual commutator operator.

- Fermions: exchanging two particles leads to a minus sign. Hence, the correct choice is

$$\left\{\hat{c}_i, \hat{c}_j\right\} = 0, \quad \left\{\hat{c}_i^\dagger, \hat{c}_j^\dagger\right\} = 0, \quad \left\{\hat{c}_i, \hat{c}_j^\dagger\right\} = \delta_{ij}, \tag{2.12}$$

where $\{A, B\} = AB + BA$ is the anticommutator of two operators. This is clear from the following example: $\left(c_i^\dagger c_j^\dagger + c_j^\dagger c_i^\dagger\right)|0\rangle = |i, j\rangle + |j, i\rangle = |i, j\rangle + (-|i, j\rangle) = 0$. When $i = j$, we get $c_i^\dagger c_i^\dagger |0\rangle = 0$, which is precisely the Pauli principle.

Another important concept that will be crucial in the rest of this work is the notion of *single-particle* and *two-particle* operators [12]. Single-particle operators are those that act only on the Hilbert space of a single-particle. In first quantization, this can be expressed as

$$\hat{A}|q_0, ..., q_N\rangle = \sum_i \left(\hat{A}|q_i\rangle\right) \otimes |q_0, ..., q_{i-1}, q_{i+1}..., q_N\rangle \tag{2.13}$$

In second quantization (assuming the action on Slater wave functions), they can be expressed as

$$\hat{A} = \sum_{ij} a_{ij} \hat{c}_i^\dagger \hat{c}_j, \tag{2.14}$$

Two-particle operators that act only on the Hilbert space of a two particles. In first quantization, two-particle operators are expressed as

$$\hat{B}|q_0, ..., q_N\rangle = \sum_{i,j} \left(\hat{B}|q_i, q_j\rangle\right) \otimes |q_0, ..., q_{i-1}, q_{i+1}..., q_{j-1}, q_{j+1}, q_N\rangle \tag{2.15}$$

In second quantization, they are written as

$$\hat{B} = \sum_{ijkl} b_{ijkl} \hat{c}_i^\dagger \hat{c}_j^\dagger \hat{c}_l \hat{c}_k. \tag{2.16}$$

The derivation of these expressions are discussed in a pedagogical way in Ref. [13]. These definitions can be generalized to *n*-particle operators, that contain *n* pairs of creation/annihilation operators.

2.1.3   Rewriting the electronic Hamiltonian in second quantized form

It is possible to rewrite the electronic Hamiltonian of Eq. (2.1) in a second-quantized form, using Eqs.(2.14) and (2.16), neglecting the degrees of freedom of the nuclei. In the basis of the position $\mathbf{r}$ and spin projection σ, the Hamiltonian for an electronic system in second-quantized form reads

$$
\begin{aligned}
\hat{H} = &\sum_{\sigma\sigma'} \int d\mathbf{r}\, \hat{\phi}_\sigma^\dagger(\mathbf{r}) \left(\frac{-\nabla^2}{2m} + U(\mathbf{r}) \right)_{\sigma\sigma'} \hat{\phi}_{\sigma'}(\mathbf{r}) \\
&+ \frac{1}{2} \sum_{\sigma\sigma'} \int d\mathbf{r} \int d\mathbf{r}' \hat{\phi}_\sigma^\dagger(\mathbf{r}) \hat{\phi}_{\sigma'}^\dagger(\mathbf{r}') V(\mathbf{r} - \mathbf{r}') \hat{\phi}_{\sigma'}(\mathbf{r}') \hat{\phi}_\sigma(\mathbf{r}),
\end{aligned}
\tag{2.17}
$$

where the $\hat{\phi}_\sigma(\mathbf{r})$ operators are the annihilation operators in real space, often called *field operators* in the literature, and we introduced the simplified notation $V(\mathbf{r})$ for the Coulomb interaction. Here, we keep the spin-dependence in the single-particle term as it can be non-diagonal in spin-space if it contains spin-orbit coupling terms, that mix the orbital angular momentum $\hat{\mathbf{L}}$ with the spin operator $\hat{\mathbf{S}} = \left(\hat{\mathbf{S}}_x, \hat{\mathbf{S}}_y, \hat{\mathbf{S}}_z \right)$ in the form $\sim \hat{\mathbf{L}} \cdot \hat{\mathbf{S}}$, or if a magnetic field acts on the system.

In the case of lattice problems or molecules, it is often more convenient to express the Hamiltonian in a more localised basis, for example the basis of functions centered on the atoms or the single-particle molecular orbitals constructed using the linear combination of atomic orbitals (LCAO). This can be done by decomposing the field operators on the chosen basis with site, spin and orbital indices $\left\{ |j\sigma l\rangle \right\}$ using

$$
\hat{\phi}_\sigma(\mathbf{r}) = \sum_{j\sigma'l} \psi_{jl}(\mathbf{r}) \delta_{\sigma\sigma'} \hat{c}_{j\sigma'l},
\tag{2.18}
$$

where we defined the wave function $\psi_{jl}(\mathbf{r}) = \langle \mathbf{r}|jl\rangle$ of the state $|jl\rangle$ and we used the trivial basis in spin-space $\{(1,0), (0,1)\}$. In this expression, we introduced an index corresponding to a basis of wave functions localised at each site j and another index l corresponding to the orbitals that appear when solving a Schrödinger equation for a localized potential.

In this localised basis of the single-particle Hilbert space, the Hamiltonian can be finally written as

$$
\hat{H} = \sum_{\substack{ij,l_1l_2,\\ \sigma\sigma'}} t_{ij,l_1l_2}^{\sigma\sigma'} \hat{c}_{i\sigma l_1}^\dagger \hat{c}_{j\sigma'l_2} + \frac{1}{2} \sum_{\substack{ijmn,\sigma\sigma'\\ l_1l_2l_3l_4}} \sum U_{ijmn}^{l_1l_2l_3l_4} \hat{c}_{i\sigma l_1}^\dagger \hat{c}_{j\sigma'l_2}^\dagger \hat{c}_{n\sigma'l_4} \hat{c}_{m\sigma l_3}.
\tag{2.19}
$$

This Hamiltonian is also known as lattice Hamiltonian, as it is expressed in a basis of localized functions. The quantities defined here are the so-called hopping term

$$t_{ij,l_1 l_2}^{\sigma\sigma'} = \int d\mathbf{r}\, \psi_{il_1}^*(\mathbf{r}) \left(\frac{-\nabla^2}{2m} + U(\mathbf{r}) \right)_{\sigma\sigma'} \psi_{jl_2}(\mathbf{r}) \tag{2.20}$$

and the interaction term (assumed to be spin-independent) reads

$$U_{ijmn}^{l_1 l_2 l_3 l_4} = \int d\mathbf{r} d\mathbf{r}'\, \psi_{il_1}^*(\mathbf{r}) \psi_{jl_2}^*(\mathbf{r}') V(\mathbf{r} - \mathbf{r}') \psi_{ml_3}(\mathbf{r}) \psi_{nl_4}(\mathbf{r}'). \tag{2.21}$$

The name *hopping terms* intuitively indicates their role in the theory: they describe an electron at site j in the orbital l_2 with spin σ' jumping to a site i. In principle, the electron can change its orbital and spin in the process, if this is not forbidden by a symmetry that enforces orbital and/or spin conservation. The steps discussed so far did not involve any relevant approximation and they are valid for the description of both molecules and materials.

Specialising it to the case of a lattice model, the Hamiltonian (2.19) can be written in the basis of Wannier's functions. These functions are localized on the lattice sites, but they exploit Bloch's theorem for periodic systems. Bloch's theorem allows to recast a problem on an infinite periodic lattice into a problem defined in a finite unit cell and a wavevector belonging to the first Brillouin Zone (BZ) of the lattice.

In a lattice problem, we can identify a unit cell with lattice vectors $\mathbf{a}_1$, $\mathbf{a}_2$ and $\mathbf{a}_3$ and containing N_{imp} atoms with N_l orbitals. The notation N_{imp} means "number of impurities" and it is chosen as the atoms are hybridized with the rest of the system. With a slight change of notation, here we move the index of the inequivalent atoms in the unit cell into the orbital index l. As a consequence, the index l runs over orbitals and atom indices such that $l \in \{0, 1, ..., N_{\text{imp}} \times N_l - 1\}$. The index j is then the position of the j-th unit cell identified by the lattice vector $\mathbf{R}_j$. With these definitions, we can apply Fourier analysis on a periodic domain to decompose the annihilation operators as

$$\hat{c}_{j\sigma l} = \sum_{\mathbf{k}} e^{i\mathbf{k}\cdot\mathbf{R}_j} \hat{c}_{\mathbf{k}\sigma l} \tag{2.22}$$

where $\sum_{\mathbf{k}}$ is the average over the Brillouin Zone. A Fourier transform of the hopping terms in the single-particle part $\hat{H}_0$ of the Hamiltonian leads to

$$\hat{H}_0 = \sum_{\mathbf{k},ll',\sigma\sigma'} \varepsilon_{\mathbf{k},ll'}^{\sigma\sigma'} \hat{c}_{\mathbf{k}\sigma l}^\dagger \hat{c}_{\mathbf{k}\sigma'l'}, \tag{2.23}$$

where $\varepsilon_{\mathbf{k},ll'}^{\sigma\sigma'} = \sum_{m,n} t_{mn,ll'}^{\sigma\sigma'} e^{-i\mathbf{k}\cdot(\mathbf{R}_m-\mathbf{R}_n)}$. Diagonalizing the matrix $\varepsilon_{\mathbf{k},ll'}^{\sigma\sigma'}$ in spin- and orbital-space gives the non-interacting electronic dispersion of the problem.

A similar transformation to the one introduced for the single-particle term can be performed also for the interaction. After few manipulations, the interacting term can be written as

$$\hat{V} = \frac{1}{2} \sum_{\mathbf{k},kv',\mathbf{q}} \sum_{\{l\},\sigma\sigma'} U_{\mathbf{q}}^{l_1 l_2 l_3 l_4} \, \hat{c}_{\mathbf{k}\sigma l_1}^{\dagger} \hat{c}_{\mathbf{q}-\mathbf{k}\sigma' l_2}^{\dagger} \hat{c}_{\mathbf{q}-\mathbf{k}'\sigma' l_4} \hat{c}_{\mathbf{k}'\sigma l_3}. \tag{2.24}$$

In momentum-space, it becomes clear that a translationally-invariant interaction depending only on the difference between the positions of the two particles $r-r'$ implies a conservation of momentum. This is a consequence of Noether's theorem, that relates symmetries of a physical system to its conserved quantities [14].

2.1.4   Statistical ensemble and the density matrix

The quantum mechanics described so far completely relies on the full knowledge of the state of the system. This immediately poses a question: what can we do in all the cases in which the state of the system is not fully accessible? The statistical nature can emerge because of uncertainty in the preparation of the state, as often occurs in quantum computing, or because we are interested in studying a system at finite temperature, hence we are interested in the thermodynamic properties of the system.

In fact, we can define the grand-canonical partition function of the system of interest with C possible configurations at inverse temperature $\beta = T^{-1}$ and chemical potential μ as

$$\mathcal{Z} = \sum_{i=1}^{C} e^{-\beta(E_i-\mu)} \tag{2.25}$$

where E_i are the energies of the allowed states. From statistical mechanics [13], it is well known that the statistical probability associated to each state in the grand-canonical ensemble is given by the Boltzmann probability distribution $p_i = e^{-\beta(E_i-\mu)}/\mathcal{Z}$. The knowledge of the partition function fully characterises the thermal properties of the system, either via logarithmic derivatives of it or via the free energy of the system defined as $\mathcal{F} = -\beta^{-1} \log \mathcal{Z}$.

In the framework of the quantum mechanics described so far, we can diagonalize the Hamiltonian, get the whole spectrum of the operator and then directly construct the partition function. This is indeed a legit method and it might be the most convenient one in the case of small systems, where the Hamiltonian can be easily diagonalized. However, in its current formulation, it does not allow for a simple way of devising systematically-improvable approximations. It turns out that there is a way of encoding statistical uncertainties on the states in an elegant way, which is called density matrix formalism.

In the density matrix formalism, we define a set of real numbers $\{\lambda_i\}_{i=1,\dots,C}$ such that $\sum_{i=1}^{C} \lambda_i = 1$ and $0 \leq \lambda_i \leq 1$. This set of numbers is the probability (density) that the state of the system is in a state $|i\rangle$. The density matrix associated to this system in the operator $\hat{\rho}$ defined as

$$\hat{\rho} = \sum_{i=1}^{C} \lambda_i |i\rangle\langle i|. \tag{2.26}$$

This formulation immediately allows to include uncertainty in the states, hence statistics, in the density matrix. Another important property of the density matrix is that the average of an operator on a system defined by the density matrix $\hat{\rho}$ is given by

$$\langle A \rangle = \mathrm{Tr}\left[\hat{A}\hat{\rho}\right] \tag{2.27}$$

The connection with statistical physics becomes much easier to draw in this case. If the numbers λ_i are chosen in such a way that

$$\lambda_i = p_i = e^{-\beta(E_i-\mu)}/\mathcal{Z}. \tag{2.28}$$

The thermal density matrix can be written as

$$\hat{\rho} = \sum_{i=1}^{C} \frac{e^{-\beta(E_i-\mu\hat{N})}}{\mathcal{Z}} |i\rangle\langle i| = \sum_{i=1}^{C} \frac{e^{-\beta(\hat{H}-\mu\hat{N})}}{\mathcal{Z}} |i\rangle\langle i| =$$
$$= \frac{e^{-\beta(\hat{H}-\mu\hat{N})}}{\mathcal{Z}} \sum_{i=1}^{C} |i\rangle\langle i| = \frac{e^{-\beta(\hat{H}-\mu\hat{N})}}{\mathcal{Z}}, \tag{2.29}$$

where we used the completeness relation for a basis $\sum_i |i\rangle\langle i| = 1$, so that the quantum thermal average of an operator in Eq. (2.27) can be expressed as

$$\langle A \rangle_{\mathrm{th}} = \frac{\mathrm{Tr}\left[e^{-\beta(\hat{H}-\mu\hat{N})}\hat{A}\right]}{\mathrm{Tr}\left[e^{-\beta(\hat{H}-\mu\hat{N})}\right]} \tag{2.30}$$

where we have used the fact that the partition function can be written in a basis-independent way as

$$\mathcal{Z} = \mathrm{Tr}\left[e^{-\beta(\hat{H}-\mu\hat{N})}\right] \tag{2.31}$$

The fact that in this expression there is no explicit reference to the eigenstates of the Hamiltonian shows that we do not need to diagonalize the Hamiltonian in the first place.

We only need the Hamiltonian operator and a suitable set of basis states. It is important to notice that there is very close connection between the thermal density matrix and the time-evolution operator $U(t - t') = \exp\{-i\left(\hat{H} - \mu\hat{N}\right)(t - t')\}$. Indeed, apart from unimportant normalization factors, the density matrix corresponds to computing the time-evolution operator at an imaginary-time $t = -i\beta$. This deep connection allows to extract a certain amount of information about the dynamics of the system from its thermodynamic observables.

We conclude this section with a comment on the different statistical distributions of fermions and bosons. In the case of fermions, the available occupation numbers for a given state are only $|0\rangle$ or $|1\rangle$, so that the probability of a state at energy E is given by the Fermi-Dirac distribution [12]

$$p(E) = n_{\mathrm{F}}(E) = \frac{1}{e^{\beta(E-\mu)} + 1}. \tag{2.32}$$

This means that the states up to μ are almost all occupied, while the states above are almost all empty. In a small window of width $\approx T$ around μ, there is a noticeable probability of finding empty states below μ and filled states above μ. The level of the last occupied state at $T = 0$ is also called the Fermi energy of the system.

The bosons on the other hand can occupy the same state without any limitation and are described by the Bose-Einstein distribution function

$$p(E) = n_{\mathrm{B}}(E) = \frac{1}{e^{\beta E} - 1}, \tag{2.33}$$

which diverges when $E \to 0$.

2.2   Path Integral formalism and Green's functions at finite temperature

2.2.1   Correlation functions, measurement and information

If the electronic properties are usually conveniently described in the Hamiltonian formalism and with methods based on the wave function, extended electronic systems are often conveniently investigated within the Green's function formulation of quantum mechanics, also known as path integral formalism.

The path integral approach provides a very "natural" description of many interacting quantum particles, as it allows for a straightforward method of performing perturbation theory at arbitrary order, at least from a formal view-point. Perturbation theory can be

then visualized in terms of Feynman diagrams, that offer an intuitive picture of the involved processes and allow to formulate physically-motivated approximations in a simpler way compared to the Hamiltonian formalism. Additionally, it directly gives access to observables, bypassing the need of computing the full wave function of the system.

In the previous paragraphs, we saw that the system is fully characterized by the knowledge of its state or density matrix. The full knowledge of these quantities in general contains a very large amount of redundancy. As a matter of fact, in a given basis, the full wave function is described by an exponential number of parameters while each observable is often just a function. Indeed, many of the coefficients of the wave function do not even contribute to the value of the observables. In the path integral formalism, the need of computing the full wave function is replaced by the computation of the Green's function, for what concerns single-particle observables, and the two-particle Green's function.

These are two examples of expectation values of creation/annihilation operators, that go under the name of *correlation function* [15] and in general it can be expressed as

$$\langle \hat{c}_i \hat{c}_j ... \hat{c}_l^\dagger \hat{c}_m^\dagger \rangle. \tag{2.34}$$

In this thesis, we only focus on systems at the thermal equilibrium in the grand-canonical ensemble, where the angular brackets indicate the thermal average defined in Eq. (2.30). This formalism is based on the density matrix $\hat{\rho}$ of Eq. (2.29) and it is also known as Matsubara formalism. It is also called imaginary-time formalism, for its connection with the time-evolution operator. A path integral formalism for systems out-of-equilibrium can be formulated in real-time in a similar fashion (see Ref. [16] for a textbook introduction).

Many experimental techniques in solid state physics involve only correlation functions with two or four fermionic operators, that correspond to measuring single-particle and two-particle observables respectively.

2.2.2 Single-particle Green's function

Working in the Matsubara formalism, we can define the Green's function of the system as the following expectation value

$$G_{ij}(\tau) = -\left\langle \mathcal{T}\hat{c}_i(\tau)\,\hat{c}_j^\dagger(0) \right\rangle = -\frac{1}{\mathcal{Z}}\operatorname{Tr}\left[e^{-(\hat{H}-\mu\hat{N})\beta}\,\hat{c}_i(\tau)\,\hat{c}_j^\dagger(0)\right] \tag{2.35}$$

where the operator evolved at the imaginary-time τ is defined as $\hat{c}_k(\tau) = e^{-(\hat{H}-\mu\hat{N})\tau}\hat{c}_k e^{(\hat{H}-\mu\hat{N})\tau}$ and $\mathcal{T}$ is the time-ordering operator defined as

$$\mathcal{T}\left[\hat{A}(\tau)\hat{B}(\tau')\right] = \theta(\tau-\tau')\hat{A}(\tau)\hat{B}(\tau') \pm \theta(\tau'-\tau)\hat{B}(\tau')\hat{A}(\tau), \tag{2.36}$$

where the plus sign refers to bosons and minus sign to fermions.

Additionally, by exploiting the properties of the trace, it can be shown that the Green's function in Eq. (2.35) in imaginary-time is a periodic function with period 2β and it is even for bosons and odd for fermions around $\tau = 0$, since $G(\tau) = \pm G(\tau - \beta)$, where the plus sign refers to bosons and minus sign to fermions [12, 15]. As a consequence, we can express it as a Fourier series. Furthermore, by Fourier analysis, it is known that the Fourier series of functions with defined parity can be expressed in terms of only even/odd coefficients, depending on whether the parity is even/odd. For this reason, the Fourier series becomes

$$G_{ij}(\tau - \tau') = \frac{1}{\beta} \sum_{n=-\infty}^{+\infty} e^{-i\nu_n(\tau-\tau')} G_{ij,\nu_n}. \tag{2.37}$$

where

$$\nu_n = \begin{cases} 2n\pi/\beta & \text{for bosons} \\ (2n+1)\pi/\beta & \text{for fermions} \end{cases} \tag{2.38}$$

are called Matsubara or imaginary frequencies. In the case of periodic systems, the creation and annihilation operators can additionally be Fourier-transformed from real-space to **k**-space within the first Brillouin zone, as $\hat{c}_i = \sum_{\mathbf{k} \in \text{BZ}} e^{i\mathbf{k} \cdot \mathbf{R}_i} \hat{c}_{\mathbf{k}l}$ where the index l indicates the orbitals/inequivalent sites in the unit cell. The Green's function for the lattice system becomes

$$G_{\mathbf{k}\nu,ll'} = - \int_0^\beta d\tau \, e^{i\nu\tau} \left\langle \hat{c}_{\mathbf{k}l}(\tau) \, \hat{c}_{\mathbf{k}l'}^\dagger(0) \right\rangle \tag{2.39}$$

This correlation function gives access to important information on the system.

Single-particle thermal averages   In particular, expectation values of any static single-particle operator on the (thermal) ground state can be computed knowing the Green's function. Recalling the expression for the thermal average of Eq. (2.30) and the second-quantized form of single-particle operator (2.14), we can write

$$\left\langle \hat{A} \right\rangle = \frac{1}{\mathcal{Z}} \text{Tr} \left[e^{-(\hat{H}-\mu\hat{N})\beta} \hat{A} \right] = \frac{1}{\mathcal{Z}} \sum_{ij} a_{ij} \, \text{Tr} \left[e^{-(\hat{H}-\mu\hat{N})\beta} \hat{c}_i^\dagger \hat{c}_j \right] =$$

$$= \frac{1}{\mathcal{Z}} \sum_{ij} a_{ij} \, \text{Tr} \left[e^{-(\hat{H}-\mu\hat{N})\beta} \left(\delta_{ij} - \hat{c}_j \hat{c}_i^\dagger \right) \right] = \sum_{ij} a_{ij} \, G_{ij}(\tau = 0^-) \tag{2.40}$$

Spectral function   The single-particle Green's function also leads to single-particle excitation energies, i.e. the energies that are available in the system if we want to remove or add a particle. Spectroscopic techniques that are sensitive to this observable are the angle-resolved photoemission spectroscopy (ARPES) [17] and inverse photoemission spectroscopy (I-ARPES). Scanning Tunnelling microscopy (STM) is also sensitive to the value of the spectral function of the highest-occupied state, also known as the Fermi energy E_F. By modelling these types of spectroscopy, as done in detail in Appendix of Ref. [18], we get that the spectral function describing these excitations is

$$A(\mathbf{k}, E) = -\frac{1}{\pi} \operatorname{Tr} \left[\operatorname{Im} G^R_{\mathbf{k}, E} \right], \tag{2.41}$$

where we have defined the retarded Green's function on the real-frequency E as

$$G^R_{\mathbf{k}, E} = (G_{\mathbf{k}, \nu})_{\nu \equiv -iE + \delta} \tag{2.42}$$

and δ is a small broadening factor. The calculation of the retarded Green's function from the Matsubara Green's function requires the computation of the Matsubara Green's function at the complex value $\nu = -iE + \delta$. This step is also known as a Wick's rotation to real frequency, which is an application of the analytical continuation of a function defined on a certain domain in the complex plane to another domain. In cases where $G_{\mathbf{k}, \nu}$ is known analytically this amounts to a simple replacement of ν. When this is not the case, numerical techniques have to be used to compute the retarded Green's function from data in the Matsubara formalism. This is general an ill-posed problem. For this reason, it is strongly affected by noise present in the data for $G_{\mathbf{k}, \nu}$ when the latter is computed using Monte Carlo methods. Bayesian techniques such as the maximum entropy method (MaxEnt) [19] or stochastic optimization methods (SOM) [20, 21] have been developed for this task. During the work for this thesis, we mostly used the MaxEnt method for this task in the implementation provided by the ana_cont software package [22].

2.2.3   Two-particle correlation functions

Two-particle correlation functions involve expectation values of two-particle operators (2.14), so in total involve four creation and annihilation operators. There are many important examples of two-particle correlation functions that will be discussed later. From the physical point of view, the most important two-particle observables are the susceptibilities. Indeed, a review of spectroscopic techniques that allow an access to two-particle observables can be found in Ref. [18]. A relevant selection for this thesis is:

- the electron energy-loss spectroscopy (EELS), whose perturbation can be expressed as $V_{\text{EELS}} = M_\mathbf{q} \hat{n}_{\mathbf{q}, ll} e^{-iEt} + \text{h. c.}$ with $E = E_{\text{out}} - E_{\text{in}}$ the energy difference and $\mathbf{q} =$

$\mathbf{k}_{\text{out}} - \mathbf{k}_{\text{in}}$ the momentum difference between incoming and outgoing electrons. Here, the electronic density operator is

$$n_{\mathbf{q},ll} = \sum_{\mathbf{k}\sigma} \hat{c}^{\dagger}_{\mathbf{k}+\mathbf{q},\sigma l} \hat{c}_{\mathbf{k},\sigma l} \tag{2.43}$$

and $M_{\mathbf{q}}$ is the matrix element of the interaction. We can apply linear response theory to obtain the response function to this external perturbation [12]. Keeping in mind that in principle we can obtain the correlation functions at the real-frequency E by analytical continuation, we get that the response function is proportional to the charge susceptibility. At the Matsubara frequency ω, this susceptibility can be written as

$$X^{\text{ch}}_{\mathbf{q}\omega} = \sum_{ll'} \int_0^{\beta} d\tau \, e^{-i\omega\tau} \left\langle \hat{n}_{\mathbf{q}ll}(\tau) \, \hat{n}_{-\mathbf{q},l'l'}(0) \right\rangle, \tag{2.44}$$

where the operators at time τ are computed using the Heisenberg equation of motion in imaginary time.

- Neutron scattering experiments work in a similar way to EELS. However, the neutrons are sensitive to the the spin operator

$$\mathbf{S}_{\mathbf{q},ll} = \sum_{\mathbf{k}\sigma\sigma'} \hat{c}^{\dagger}_{\mathbf{k}+\mathbf{q},\sigma l} \boldsymbol{\sigma}_{\sigma\sigma'} \hat{c}_{\mathbf{k},\sigma l} \tag{2.45}$$

instead, so the output signal is proportional to the spin susceptibility

$$X^{\text{sp}}_{\mathbf{q}\omega} = \sum_{ll'} \int_0^{\beta} d\tau \, e^{-i\omega\tau} \left\langle \hat{S}^{\text{sp}}_{\mathbf{q}ll}(\tau) \, \hat{S}^{\text{sp}}_{-\mathbf{q},l'l'}(0) \right\rangle \tag{2.46}$$

where the spin component is $\text{sp} = x, y, z$.

2.2.4 Path integral formalism for fermions

So far no additional practical recipe for calculating correlation function has been provided, apart from the explicit evaluation of the trace in Eq.(2.35) in a complete basis set. In the case of a small system, the basis set can be constructed using the eigenstates obtained by diagonalizing the Hamiltonian operators.

However, very powerful tools to tackle the problem of many interacting quantum particles become available if the problem is rewritten in the *path integral* formalism, in particular a consistent way of constructing perturbation theory at arbitrary order and the renormalization group method. The path integral formalism is extremely general and can be

applied in the basis of any full set of operators. In our case, we focus on the eigenstates of the creation/annihilation operators in a generic basis of states characterized by index $\{i\}$. As any operator in the formalism develop so far is expressed in terms of $\hat{c}/\hat{c}^\dagger$ operators, one quite natural possibility at this point is to choose these as operator to construct the basis set. This choice is also referred to as *coherent state path integral* approach, as the eigenstates of $\hat{c}$ are known as coherent states. The description here changes depending on the kind of particles we would like to treat. here, we focus on fermions and we highlight the difference with bosons in the end of the Chapter.

Following Ref. [13], it can be shown that the eigenvalues and eigenvectors of the creation operators for fermions are

$$\hat{c}_i \ket{\zeta} = c_i \ket{\zeta} \tag{2.47}$$

$$\bra{\zeta} \hat{c}_i^\dagger = \bra{\zeta} c_i^* \tag{2.48}$$

where c_i and c_i^* are the so-called Grassmann's numbers and any of them anticommute with the others. The eigenstates $\ket{\zeta}$ are known as the fermionic coherent states and can be explicitly constructed as

$$\ket{\zeta} = \exp\left(-\sum_i c_i \hat{c}_i^\dagger\right)\ket{0} = \left(1 - \sum_i c_i \hat{c}_i^\dagger\right)\ket{0}. \tag{2.49}$$

Here, only the zero-th and first-order terms survive, since repeated applications of the creation operator to the $\ket{0}$ return 0. It is possible to show the following closure relation for these states

$$\int d(c, c^*) \exp\left(-\sum_i c_i^* c_i\right)\ket{\zeta}\bra{\zeta} = \mathbb{1} \tag{2.50}$$

with $\int d(c, c^*) \equiv \prod_i \int dc_i \int dc_i^*$. An expression for the expectation value on any operator in second-quantized form can be obtained by including a completeness relation in terms of a generic basis $\{\ket{n}\}$ of the Fock space different from the coherent states into Eq. (2.30)

$$\langle A \rangle = \frac{1}{Z} \mathrm{Tr}\left[e^{-(\hat{H}-\mu\hat{N})\beta}\hat{A}\right] = \frac{1}{Z}\sum_n \bra{n} e^{-(\hat{H}-\mu\hat{N})\beta}\hat{A}\ket{n}. \tag{2.51}$$

This leads to the expression

$$\langle A \rangle = \frac{1}{Z} \sum_n \langle n | e^{-(\hat{H} - \mu \hat{N})\beta} \hat{A} \int d(c,\, c^*) \exp\left(-\sum_i c_i^* c_i \right) |\zeta\rangle\langle\zeta|n\rangle \tag{2.52}$$

$$= \frac{1}{Z} \int d(c,\, c^*) \exp\left(-\sum_i c_i^* c_i \right) \sum_n \langle n | e^{-(\hat{H} - \mu \hat{N})\beta} \hat{A} |\zeta\rangle\langle\zeta|n\rangle. \tag{2.53}$$

The next step would be to bring the number $\langle\zeta|n\rangle$ to the left. Since this involves commutation of Grassmann numbers, we have to recall the explicit expression for the fermionic coherent states to do that

$$|\zeta\rangle\langle\zeta|n\rangle = \left(1 - \sum_i c_i \hat{c}_i^\dagger \right) |0\rangle\langle 0| \left(1 - \sum_i c_i^* \hat{c}_i \right) |n\rangle$$

$$= \langle 0 | \left(1 - \sum_i (-1) c_i^* \hat{c}_i \right) |n\rangle \left(1 - \sum_i c_i \hat{c}_i^\dagger \right) |0\rangle = \langle -\zeta|n\rangle|\zeta\rangle \tag{2.54}$$

where the sign -1 appears when we exchange the Grassmann numbers. No commutation relation has to be used on the operators, since $\langle 0|\hat{c}_i|\zeta\rangle$ is within the expectation value. Putting this equation inside the previous one and recalling that $\sum_n |n\rangle\langle n| = \mathbb{1}$, we get

$$\langle A \rangle = \frac{1}{Z} \int d(c,\, c^*) \exp\left(-\sum_i c_i^* c_i \right) \langle -\zeta | e^{-(\hat{H} - \mu \hat{N})\beta} \hat{A} |\zeta\rangle. \tag{2.55}$$

The next step is to use the Trotter-Suzuki decomposition, that has the form

$$e^{-(\hat{H} - \mu \hat{N})\beta} = \lim_{M \to +\infty} \left[e^{-(\hat{H} - \mu \hat{N})\frac{\beta}{M}} \right]^M \tag{2.56}$$

to transform the integrals over Grassmann variables into a *path integral*. The details are discussed in books, such as Ref. [13]. The important result is that

$$\langle A \rangle = \frac{1}{Z} \int \mathcal{D}[c,\, c^*] e^{-\mathcal{S}[c,c^*]} A[c,\, c^*], \tag{2.57}$$

where we introduced the symbol for the path integral $\mathcal{D}[c,\, c^*] = \lim_{M \to +\infty} \prod_{m=0}^{M-1} \prod_i dc_{i,m}\, dc_{i,m}^*$ with m the label of the corresponding imaginary-time slice. Additionally, we have defined

the electronic action

$$
S[c, c^*] = \lim_{M \to +\infty} \frac{\beta}{M} \sum_{m=0}^{M-1} \left(c_{i,m+1}^* \left[\frac{c_{i,m+1} - c_{i,m}}{\beta/M} - \mu c_{i,m} \right] + H[c_{m+1}^*, c_m] \right) =
$$

$$
= \int_0^\beta d\tau \left(c_{i,\tau}^* (\partial_\tau - \mu) c_{i,\tau} + H[c_\tau^*, c_\tau] \right) \tag{2.58}
$$

where now the fermionic variables carry an additional time index m in the discrete form and τ in the continuous expression after we take the limit to infinity. The only caveat here is that we assumed that the operator $\hat{A}$ is written in the normal order, that means that the creation operators are located before all the annihilation operators.

Notable examples are the partition function, that can be written as

$$
\mathcal{Z} = \int \mathcal{D}[c, c^*] e^{-S[c,c^*]} \tag{2.59}
$$

and the single-particle Green's function that becomes

$$
G_{ij}(\tau) = -\frac{1}{\mathcal{Z}} \int \mathcal{D}[c, c^*] e^{-S[c,c^*]} c_{i,\tau} c_{j,0}^*. \tag{2.60}
$$

The big advantages of this formalism is that everything is written in a functional form using Grassmann variables instead of operators and that path integral expressions are already written in a time-ordered way. Of course, by following this route, we pay a price, since it is not immediately clear how to evaluate path integral expressions.

Very similar considerations hold for bosonic fields, even though the eigenstates of the bosonic annihilation operators, the bosonic coherent states, are indexed over complex numbers. As a consequence, bosonic variables commute within the path integral.

2.2.5   Key formulas for path integral evaluation

Up to this point, it is not possible to directly evaluate the path integrals discussed above. In order to to do actual calculations, we need to have a practical way of computing them. This is possible only in a limited number of cases. The most important example is a quadratic action in the Grassmann variables. Considering a quadratic action with classical fermionic sources $\eta^{(*)}$ in the form

$$
S_0[c, c^*, \eta, \eta^*] = -\sum_{ij} c_i^* \left(\mathcal{G}^{-1} \right)_{ij} c_j + \sum_i \eta_i c_i^* + \sum_i c_i \eta_i^*, \tag{2.61}
$$

where we have included the time indices inside the Latin letter for simplicity, the key observation for the evaluation of the partition function and the correlation functions in the path integral formalism is to notice that, apart from the continuous limit in the imaginary-time labels, the expression for $\mathcal{Z}_0$ with action (2.61) is nothing more than a multidimensional version of a Gaussian integration for Grassmann variables. This means that the corresponding path integral (with external sources) can be evaluated as

$$\mathcal{Z}_0[\eta, \eta^*] = \int \mathcal{D}[c, c^*]\, e^{-\mathcal{S}_0[c, c^*, \eta, \eta^*]} = \det\left(\hat{\mathcal{G}}^{-1}\right) \exp\left\{\sum_{ij} \eta_i^* \, \mathcal{G}_{ij} \, \eta_j\right\}. \tag{2.62}$$

Eq. (2.62) is particularly interesting, because it has two use cases. It can be used from left to right to solve a path integral with a quadratic action or to remove a fermionic degree of freedom if fermions with different flavors are involved, a procedure which is known as "integrating out" a fermionic field. Additionally, it can be used from right to left within a path integral $\int \mathcal{D}[\eta, \eta^*]$ over the $\eta^{(*)}$ variables to introduce a new fermionic field. This operation is effectively the inverse operation of integrating out and it is known as Hubbard-Stratonovich transformation. It allows to rewrite quartic actions in terms of a quadratic action coupled to a new field, and, despite its deceptively complicated formulation, it has a simple connection with the Gaussian integral.

Thanks to Eq. (2.62), it is possible to take successive functional derivatives of this expression to compute *n*-particle correlation functions in the form

$$\left\langle c_{i_1}...c_{i_n} c_{j_1}^*...c_{j_n}^* \right\rangle = \frac{(-1)^n}{\mathcal{Z}_0} \left. \frac{\delta^{(2n)} \mathcal{Z}_0[\eta, \eta^*]}{\delta\eta_{i_1}^*...\delta\eta_{i_n}^* \delta\eta_{j_1}...\delta\eta_{j_n}} \right|_{\eta, \eta^* \equiv 0} = \sum_{p \in \mathcal{P}} \mathrm{sgn}(p) \prod_{\alpha=1}^{n} \mathcal{G}_{i_\alpha j_{p(\alpha)}} \tag{2.63}$$

$$= \det\left(\hat{\mathcal{G}}_{i_\alpha j_\beta}\right)_{\alpha, \beta = 1, ..., n} \tag{2.64}$$

where we defined the set of permutations over the numbers $\alpha = 1, ..., n$ as $\mathcal{P}$. This expression is a very important result, as the last expression is precisely the definition of the determinant of an $n \times n$ matrix. This result is known as Wick's theorem, in its path integral formulation [23]. The case of $n = 1$ corresponds to the single-particle Green's function in the non-interacting case so that, restoring the time indices, we get

$$G_{ij}(\tau) = -\left\langle c_i(\tau) c_j^*(0) \right\rangle = \mathcal{G}_{ij}(\tau, 0) \tag{2.65}$$

In a similar way, if we consider real bosonic fields *b*, the integral (2.62) has be replaced by an integral over complex variables that lead to the very well known expression for

Gaussian integration

$$\mathcal{Z}_0^b[\eta] = \int \mathcal{D}[b] \, e^{-\sum_{ij} b_i \, A_{ij} \, b_j + \sum_i \eta_i \, b_i} = \left[\det\left(\hat{A}\right)\right]^{-\frac{1}{2}} \exp\left\{\sum_{ij} \eta_i \left(A^{-1}\right)_{ij} \eta_j\right\}. \tag{2.66}$$

Wick's theorem then states that the non-interacting correlation functions can be obtained in a very similar way as for fermions, with the difference that the determinant is replaced by the permanent, as

$$\langle b_{i_1}...b_{i_n}\rangle = \frac{1}{\mathcal{Z}_0} \left.\frac{\delta^{(n)} \mathcal{Z}_0^b[\eta]}{\delta\eta_{i_1}...\delta\eta_{i_n}}\right|_{\eta\equiv0} = \sum_{p\in\mathcal{P}} \prod_{\alpha=1}^{n} A_{i_\alpha j_{p(\alpha)}}^{-1} = \text{perm}\left(\left[\hat{A}^{-1}\right]_{i_\alpha j_\beta}\right)_{\alpha,\beta=1,...,n} \tag{2.67}$$

2.2.6 Perturbation theory

In the case of a non-quadratic action, it is in general not possible to directly compute the path integral. However, the path integral is particularly useful for developing perturbation theory, since we are working with exponential functions of Grassmann numbers instead of operators.

In particular, if we consider an action in the form

$$\mathcal{S}[c, c^*, \eta, \eta^*] = \mathcal{S}_0[c, c^*, \eta, \eta^*] + \xi\mathcal{V}[c, c^*], \tag{2.68}$$

where S_0 is the Gaussian action (2.61), $\mathcal{V}$ is a possibly non-Gaussian perturbation with strength represented by the real number ξ. The path integral can be rewritten using the Taylor expansion of the exponential as

$$\mathcal{Z}[\eta, \eta^*] = \int \mathcal{D}[c, c^*] \, e^{-\mathcal{S}_0[c,c^*,\eta,\eta^*] - \xi\mathcal{V}[c,c^*]} = \int \mathcal{D}[c, c^*] \, e^{-\mathcal{S}_0[c,c^*,\eta,\eta^*]} \sum_{n=0}^{+\infty} \frac{(-\xi\mathcal{V}[c,c^*])^n}{n!}$$

$$= \left\langle e^{-\xi\mathcal{V}[c,c^*]} \right\rangle_0, \tag{2.69}$$

provided the sum converges, a matter that will be discussed in more detail later on. Given an expression for $\mathcal{V}$, it is in principle possible to apply (2.64) for the computation of the terms in the summation.

If we consider the Hamiltonian (2.19) for electrons on a lattice, the perturbation $\mathcal{V}$ represents an interaction between two particles. This term describes two incoming particles that interact with each other with strength $U_{ijmn}^{l_1 l_2 l_3 l_4}$ and then they are scattered away. In the action formalism, we can write the action in a compact way as

$$\mathcal{S}[c, c^*] = -\sum_{ij} c_i^* \mathcal{G}_{ij}^{-1} c_j + \sum_{ijmn} U_{ijmn} c_i^* c_j^* c_n c_m, \tag{2.70}$$

where the Latin index is a short-hand notation for $i = \{\mathbf{R}_i, l_i, \sigma_i, \tau_i\}$. The perturbative expansion can be easily visualized in terms of Feynman diagrams. Indeed, if we represent the interaction U_{ijmn} as the vertex of a graph with four connections and $\mathcal{G}_{ij}$ as an oriented line that can be attached to this vertex and that represents the propagation of a free fermion, the perturbative term at order n in the series can be written as a planar graphs obtained by connecting n vertices with lines in all the possible ways. These graphs are known as *Feynman diagrams*. A diagram at order n is characterized by n closed loops. The partition function has no external indices and it can be consequently represented as a collection of "bubbles", no matter if they are all connected or not.
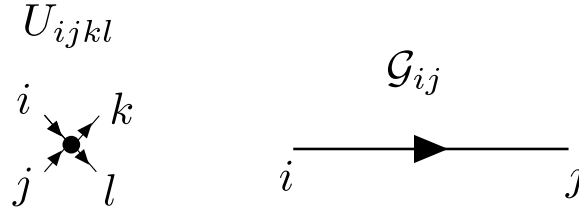
FIGURE 2.1: The diagrammatic representation of the terms with four and two Grassmann variables of the interacting quartic action $\mathcal{S}[c, c^*]$ of Eq. (2.70).

The Green's function $G_{ij}(\tau)$ can be obtained by applying two times the functional derivative to Eq. (2.69)

$$G_{ij}(\tau) = -\frac{\left\langle c_{i,\tau} c^*_{j,0} e^{-\xi \mathcal{V}[c,c^*]} \right\rangle_0}{\left\langle e^{-\xi \mathcal{V}[c,c^*]} \right\rangle_0}. \tag{2.71}$$

By expanding order-by-order in terms of the interaction, we may realise that the denominator simply cancels the disconnected terms that would appear in the series. Hence, the expansion for the Green's function, and all the expectation values of operators, consist only of fully connected Feynman diagrams. This result is known as the *linked-cluster theorem* [12, 13].
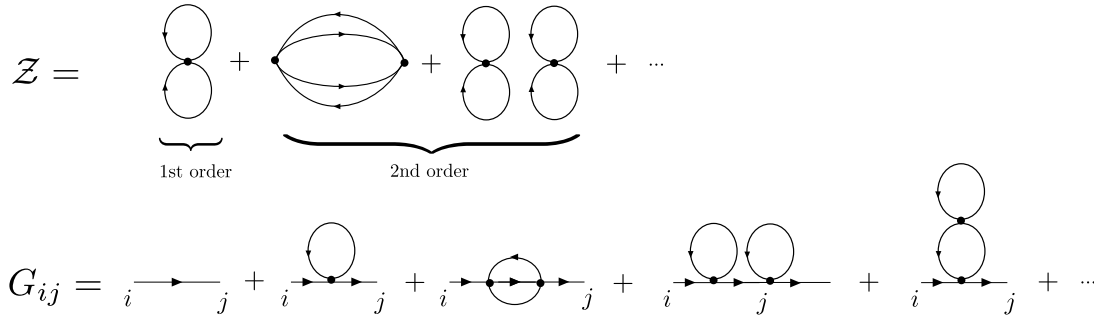
FIGURE 2.2: The diagrammatic representation of the first few terms of the expansion for the partition function $\mathcal{Z}$ and the Green's function G_{ij} of the interacting quartic action $\mathcal{S}[c, c^*]$ of Eq. (2.70).

2.2.7 Dyson's equation for the Green's function

At this point, we can derive an equation of motion for the Green's function which is also known as Dyson's equation. We start by calculating the expression

$$\sum_k \mathcal{G}_{ik}^{-1} G_{kj} = -\frac{1}{\mathcal{Z}} \int \mathcal{D}[c, c^*] \left(\sum_k \mathcal{G}_{ik}^{-1} c_k \right) c_j^* e^{-\mathcal{S}_0[c,c^*] - \xi \mathcal{V}[c,c^*]}, \tag{2.72}$$

where we recall that $\mathcal{G}_{ij}$ is the Green's function for the non-interacting reference action and G_{ij} is the Green's function of the interacting theory. We notice that, by combining Eqs. (2.62) and (2.65), we can get the quantity in brackets by differentiating $\mathcal{S}_0[c, c^*]$ with respect to c_i^*. After that, we can also anticommute the derivative and c_j^* to get

$$\sum_k \mathcal{G}_{ik}^{-1} G_{kj} = \frac{1}{\mathcal{Z}} \int \mathcal{D}[c, c^*] \, c_j^* \left(\frac{\delta}{\delta c_i^*} e^{-\mathcal{S}_0[c,c^*]} \right) e^{-\xi \mathcal{V}[c,c^*]}. \tag{2.73}$$

We then use the chain rule to obtain that

$$\frac{\delta}{\delta c_i^*} \left(e^{-\mathcal{S}_0[c,c^*] - \xi \mathcal{V}[c,c^*]} \right) = \left(\frac{\delta}{\delta c_i^*} e^{-\mathcal{S}_0[c,c^*]} \right) e^{-\xi \mathcal{V}[c,c^*]} + e^{-\mathcal{S}_0[c,c^*]} \left(\frac{\delta}{\delta c_i^*} e^{-\xi \mathcal{V}[c,c^*]} \right)$$

$$= \left(\frac{\delta}{\delta c_i^*} e^{-\mathcal{S}_0[c,c^*]} \right) e^{-\xi \mathcal{V}[c,c^*]} - \xi \left(\frac{\delta}{\delta c_i^*} \mathcal{V}[c, c^*] \right) e^{-\mathcal{S}_0[c,c^*] - \xi \mathcal{V}[c,c^*]}. \tag{2.74}$$

Plugging back in the previous equation, we get

$$\sum_k \mathcal{G}_{ik}^{-1} G_{kj} = \frac{1}{\mathcal{Z}} \int \mathcal{D}[c, c^*] \, c_j^* \left(\frac{\delta}{\delta c_i^*} + \xi \frac{\delta}{\delta c_i^*} \mathcal{V}[c, c^*] \right) e^{-\mathcal{S}_0[c,c^*] - \xi \mathcal{V}[c,c^*]}. \tag{2.75}$$
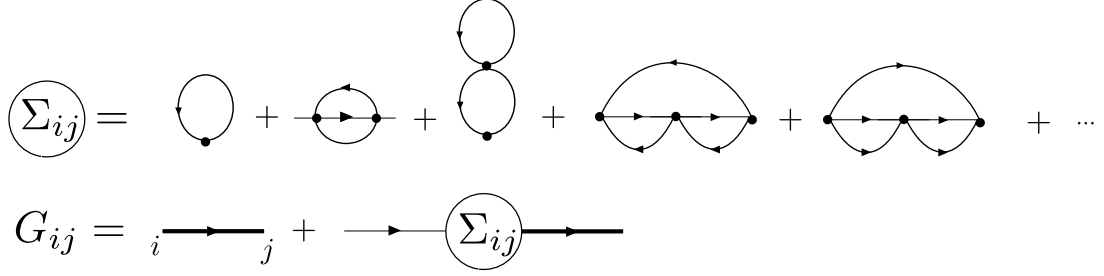
FIGURE 2.3: The diagrammatic representation of the self-energy Σ_{ij} and of the Dyson's equation (2.78), relating the Green's function G_{ij} of the interacting quartic action $\mathcal{S}[c, c^*]$ of Eq. (2.70) denoted by a thick line, Σ_{ij} and the non-interacting Green's function $\mathcal{G}_{ij}$.

We can then integrate by parts the first term, getting δ_{ij}, and we can define the self-energy Σ_{ij} through the expression

$$\xi \left\langle c_j^* \frac{\delta}{\delta c_i^*} \mathcal{V}[c, c^*] \right\rangle \equiv \sum_k \Sigma_{ik} G_{kj}. \tag{2.76}$$

This term is absent if the interaction is zero, hence it carries the contribution to the single-particle Green's function due to the fact that the propagating particle interacts with the the rest of the system. In a perturbative picture in the interaction, Σ_{ij} represents all the possible scattering mechanisms between a single-particle propagating in the interacting system at all the possible orders. In the language of Feynman diagrams, it consists in the sum of all the connected diagram with two external points that cannot be split into two valid diagrams by cutting a fermionic line. These diagrams are also known as *one-particle irreducible diagrams*. This leads to the Dyson's equation in the form

$$\sum_k \mathcal{G}_{ik}^{-1} G_{kj} = \delta_{ij} + \sum_k \Sigma_{ik} G_{kj}. \tag{2.77}$$

The terms can be reshuffled and the equation can be written in the final form as

$$G_{ij} = \mathcal{G}_{ij} + \sum_{kl} \mathcal{G}_{ik} \Sigma_{kl} G_{lj}. \tag{2.78}$$

This derivation holds for every form of the interaction $\mathcal{V}$ irrespective of the form of the non-interacting Green's function. Additionally, it is possible to derive an analogous equation for bosons, which is formally identical to (2.78). The formula (2.78) will be extensively used in the following chapters.

3 Quantum embedding for strong correlations

3.1 Strongly correlated electronic systems

3.1.1 What are strong correlations?

The simplest definition of *strong correlations* in electronic systems is a regime where the electrons cannot be described in any way as non-interacting particles. This can be reformulated by saying that in a strongly correlated regime electrons acquire some kind of collective behavior. In order to develop strong correlations, the electrons in the system need to strongly interact with each other by means of the Coulomb interaction. This is the case in Mott scenario, when some components of the interaction in Eq. (2.21) are strong enough compared to the hopping terms [24, 25]. Alternatively, the interaction strength among the electrons can be relatively weak and the electrons can still interact strongly with each other at low enough temperature. This case is known as the Slater scenario [26]. At the same time, interactions should not be too strong, otherwise the system turns into an atomic system where electrons are frozen into their positions.

A general characteristic of strong correlations is that they destroy the usual picture provided by bandstructure theory. According to bandstructure theory, electronic properties can be described by single-particle Bloch eigenstates in the form $\varepsilon_{\mathbf{k}\sigma l}$, where l indicates the band, σ the electronic spin and $\mathbf{k}$ is the quasi-momentum in the Brillouin zone of the lattice. In this case, the non-interacting Green's function can be computed exactly and reads

$$\mathcal{G}_{k\sigma l} = \frac{1}{i\nu + \mu - \varepsilon_{\mathbf{k}\sigma l}}, \tag{3.1}$$

where $k = (\mathbf{k}, \nu)$. By replacing $\nu = -iE + \delta$ with $\delta \longrightarrow 0$, this expression corresponds to a δ−function in real-frequency, meaning that there is no damping and, once an electron is excited in the system, it stays in the excited state forever. Interactions among particles modify this picture, because the particles tend to scatter with each other, leading to a renormalization of their energy spectrum and additionally introducing a finite lifetime. Indeed, when the correlations electrons in solids is weak but sizeable, a good approximation is

the Fermi liquid model [15], where the notion of electrons is abandoned in favor of the concept of *quasi-particles*. The quasi-particle states are described similarly to the bare electrons with the difference that they possess a self-energy $\Sigma_{k\sigma l}$ due to the fact that they interact with each other. As a consequence, the Green's function becomes

$$G_{k\sigma l} = \frac{1}{i\nu_n + \mu - \varepsilon_{\mathbf{k}\sigma l} - \Sigma_{k\sigma l}}. \tag{3.2}$$

In general, the quantity $\Sigma_{k\sigma l}$ is complex, hence it leads to a broadening of the δ-function of the bare electrons. According to the Fermi liquid theory, quasi-particles at the Fermi level E_{F} are not damped, meaning that in this regime they are still the most important contribution to the properties of the system. In a Fermi liquid regime, the self-energy of the quasi-electrons can be approximately written as a Taylor expansion around the first Matsubara frequency

$$\Sigma_{k\sigma l} \approx \mathrm{Re}\,(\Sigma_{k\sigma l})_{\nu=\pi/\beta} + \left(\frac{\partial \mathrm{Im}\Sigma_{k\sigma l}}{\partial \nu}\right)_{\nu=\pi/\beta} \nu. \tag{3.3}$$

The underlying assumption is that there is no constant imaginary part. The Green's function can be rewritten as

$$G_{k\sigma l} = \frac{Z_{\mathbf{k}\sigma l}}{i\nu + \mu - \tilde{\varepsilon}_{\mathbf{k}\sigma l}}, \tag{3.4}$$

such that, close to the Fermi level, the quasi-particle spectral function becomes

$$A_{\mathbf{k}\omega} \approx \sum_{\sigma l} Z_{\mathbf{k}\sigma l}\delta\,(\omega - \tilde{\varepsilon}_{\mathbf{k}\sigma l})\,. \tag{3.5}$$

The quantity $Z_{\sigma l}$ is called quasi-particle weight and $\tilde{\varepsilon}_{\mathbf{k}\sigma l} = \varepsilon_{\mathbf{k}\sigma l} + (\Sigma_{k\sigma l})_{E=E_{\mathrm{F}}}$ is the renormalized dispersion. Here, we see the effect of our assumption. When the imaginary part of the self-energy is negligible compared to the bandwidth of the system, the excitation spectrum can be well described by the renormalized dispersion $\tilde{\varepsilon}_{\mathbf{k}\sigma l}$ and we can still use these energies to define a bandstructure of the system, using the renormalized dispersion $\tilde{\varepsilon}_{\mathbf{k}\sigma l}$. The Fermi liquid theory is based on a perturbative approach in the interaction and on the fact that the ground state of the interacting system is adiabatically connected to one of the non-interacting system. As a consequence, the result is guaranteed only in the absence of gapped states appearing in the evolution from the non-interacting to the interacting system, a result which is known as the Gell-Mann and Low theorem [27].

However, in the limit of large interaction strength compared to the bandwidth, the system behaves like an atomic system, where the system is described by discrete states that have no hybridization with each other. This means that we cannot apply perturbation

theory from the non-interacting limit up to the atomic limit, since the system develops a gap in between and the Gell-Mann and Low theorem is not applicable any longer.

This is the reason why the self-energy in strongly correlated systems can be strongly affected by collective effects, leading to strong modifications of the Green's function at the Fermi surface and even opening gaps in the spectrum. As a matter of fact, strong correlations appear at the crossover between the Fermi liquid physics and the atomic physics. Depending on which kind of physics wins this competition, we can observe a metallic system, an insulating behavior or a pseudogap physics, where the opening of the gap occurs only in a part of the Brillouin zone of the system. If the single-particle gap appears in the normal phase, it is usually referred to as the Mott gap and the related transition is the Mott transition [24, 25]. On the other hand, usually the pseudogap physics is also related to strong spin, charge or particle-particle correlations [28–30]. The excitations in these channels are described by two-particle correlations, as they are associated with pairing of an electron and a hole in the case of spin and charge channels, or two electrons in the particle-particle channel. When this is the case, the term "strong fluctuations" is also often used, as usually the emergence of these correlations is accompanied by unusually large responses to external electric or magnetic fields, that are in turn linked to the susceptibility of the system in the corresponding channel.

Understanding the effect of electronic correlations in materials is currently a very active topic of research. Strong interaction between electrons is responsible for their non-trivial collective behavior and for the formation of a variety of different states of matter, as for instance Mott insulating [24, 25] and unconventional superconducting [31–33] phases. Usually, the low-energy physics of materials with strong electronic correlations is determined by a subspace of electronic bands that lie near the Fermi energy. In several situations, this correlated subspace can be effectively reduced to one band, which, for instance, is a standard approximation for cuprate superconductors [32, 34–37]. However, in most of the cases an accurate description of realistic materials with strong electronic correlations usually requires to take into account several bands that originate from different orbitals and/or atoms in the unit cell. Prominent examples of materials where the interplay of orbital degrees of freedom and strong correlations is believed to be of crucial importance are vanadates [38–41], ruthenates [42–48], nikelates [49–55], and iron-based superconductors [56–65]. Even in the case of cuprates the question whether an effective three-band model should be used instead of a single-band one is still under debate [66–75].

3.1.2 The exponential scaling of the wave function for quantum systems

The problem of many interacting electrons is a hard problem from the computational point of view. The first manifestation of this hardness appears when we consider the scaling of

the wave function in the case of N electrons. We consider a one-particle Hilbert space $\mathcal{H}^{(1)}$ with N_{imp} sites and with $N_{\text{orb}}^{(l)}$ orbitals on each site l. The dimension of this Hilbert space is $N_{\text{tot}} = 2 \sum_{l=1}^{N_{\text{imp}}} N_{\text{orb}}^{(l)}$ where the factor 2 comes from the inclusion of the possible spin projections $\sigma \in \{\uparrow, \downarrow\}$. If we consider a single-particle (or analogously N non-interacting particles), the dimension of the full Hilbert space is just the total number of degrees of freedom for the particle N_{tot}.

On the other hand, the wave function of N electrons can be conveniently decomposed in the Fock space $\mathcal{F}$ as

$$|\psi\rangle = \sum_{\{n \in [0,1]\}} a_{n_1 \ldots n_{N_{\text{tot}}}} |n_0, \, n_1 \ldots n_{N_{\text{tot}}}\rangle. \tag{3.6}$$

As each electronic state can be either empty or singly occupied ($|0\rangle$ or $|1\rangle$ respectively), there are 2 possibilities per site, orbital and spin. The total dimension of the Fock space is then

$$D = \dim(\mathcal{F}) = 2^{N_{\text{tot}}}. \tag{3.7}$$

This is the famous exponential wall that plagues the exact diagonalization method and prevents us from obtaining exact solutions for most of the quantum many-body problems of interest by using a direct approach.

The scaling with respect to the number of electrons can be improved if quantities like the total particle number $\hat{N}$ or spin $\hat{S}$ are conserved, as it is done in several implementations of the exact diagonalization method (ED) [76, 77]. In this case, the Hamiltonian is block-diagonal. If we consider for simplicity a single-orbital case per each site, each block is only characterised by total number of particles N and number of spin up electrons $N_\uparrow$ and has dimension

$$D_{\text{block}} = C_N^{N_\uparrow} C_N^{N-N_\uparrow} \tag{3.8}$$

where $C_n^k = \binom{n}{k} = \frac{n!}{k!(n-k)!}$ is the binomial coefficient [77]. Each of these sectors can be computed independently in parallel, so the bottleneck is represented by the largest block. Using that the binomial coefficient C_n^k is maximum when $k = n/2$ if n is even (or the floor/ceiling if it is odd) and the Stirling's approximation for the factorial for large n, we find that the largest block has dimension

$$\max_{N,N_\uparrow} D_{\text{block}} = \left(C_N^{N/2}\right)^2 \xrightarrow[N \gg 1]{} \frac{2^{2N}}{2\pi N}, \tag{3.9}$$

which is an improvement over the exponential scaling, but it is still much faster than polynomial in the number of electrons N.

In principle, a lattice problem contains an infinite number of sites and the situation is not significantly improved if we consider a real material with $N \sim 10^{23}$ atoms. Since a lattice has a periodic structure, we are able to formulate the problem on an infinite lattice in terms of a finite unit cell that in turn implies the presence of a finite Brillouin Zone. This is very useful in the case of a non-interacting problem, but the interacting problem is still exponential in the number of points used in the Brillouin zone, in the number of atoms and number of orbitals per atom within the unit cell. Hence, this approach is still not sufficient to solve the problem in a solid. For this reason, usually a finite plaquette is the system of choice in the context of exact diagonalization. Even though calculations on a finite plaquette can give very interesting insights on some physical processes [78], the size of the systems that can be considered are too modest to simulate realistic materials.

3.1.3 The second curse of many-fermion systems: the sign problem

A second kind of exact and unbiased numerical methods to approach many-body quantum systems are the quantum Monte Carlo methods. These methods work extremely well as long as they are applied to classical or bosonic particles, resulting in an unmatched agreement with experimental results [79] even for rather large systems. However, when they are applied to fermionic systems [80], the computational time needed to converge error bars below a chosen accuracy ϵ grows exponentially with number of particles N and inverse temperature β as $\sim e^{\beta N}$ [4]. This is the infamous fermionic sign problem [81] and appears when we try to sample numerically the Taylor expansion of the partition function $\mathcal{Z}$ of the full Hamiltonian $\hat{H} = \hat{H}_0 + \hat{H}_1$, as

$$\mathcal{Z} = \text{Tr}\left[e^{-\beta(\hat{H}_0 + \hat{H}_1)}\right] = \sum_{n=0}^{+\infty} \frac{(-1)^n}{n!} \langle (\mathcal{S}_1[c, c^*])^n \rangle_0 \tag{3.10}$$

where $\mathcal{S}_1[c, c^*]$ is the action corresponding to $\hat{H}_1$. If we consider a fermionic system described by an action with a quadratic term $\mathcal{S}_0[c, c^*]$ and a quartic interacting term $\mathcal{S}_1[c, c^*]$ of the kind of Eq. (2.70) with non-interacting Green's function $\mathcal{G}$, we can rewrite the partition function using Eq. (2.64) as

$$\mathcal{Z} = \sum_{n=0}^{+\infty} \sum_{\{i,j\}} \frac{(-1)^n}{n!} \left(\prod_{m=1}^{n} U_{i_m i_{n+m} j_m j_{m+n}} \right) \det \left(\mathcal{G}_{i_1, j_1} ... \mathcal{G}_{i_{2n}, j_{2n}} \right) \equiv \sum_{c \in C} w_c \tag{3.11}$$

where $\sum_{\{i,j\}}$ indicates summation over the range of each of the internal variables $i_1, ..., i_{2n}$ and $j_1, ..., j_{2n}$. On the other hand, the space of configurations C contains the combination of order n and the set of degrees of freedom of the vertices $\{i, j\}$. This way of writing the partition function is the basis for Determinant Diagrammatic Monte Carlo (DDMC) method [82–84]. The usual Monte Carlo sampling methods involves a stochastic sampling

from a probability distribution, that has to be positive definite (see Section 5.1.2 for more details). However, the expression (3.11) contain determinants, that can have negative sign. The way of fixing this problem is to sample the sign of the configurations $\text{sgn}(w_c)$ from the probability distribution $|w_c|$. This means that any observable O can be obtained as

$$O = \sum_{n=0}^{+\infty} \frac{(-1)^n}{n!} \left\langle (\mathcal{S}_1[c, c^*])^n \, O[c, c^*] \right\rangle_0 . \tag{3.12}$$

The expectation value of $(\mathcal{S}_1[c, c^*])^n \, O[c, c^*]$ can be rewritten in terms of determinants similarly to Eq. (3.11). In the language of Monte Carlo, the expression can be rewritten in terms of a summation over the configurations as

$$O = \frac{\sum\limits_{c \in C} O_c \, \text{sgn}(w_c) \, |w_c|}{\langle \text{sgn}(w_c) \rangle} . \tag{3.13}$$

The sign in the denominator of this equation is exactly the origin of the exponentially slow reduction of the error bars of the observables. In particular, this $\langle \text{sgn}(w_c) \rangle$ has to be computed with exponential accuracy ϵ, in order to obtain sensible results.

Several possible algorithms have been proposed to alleviate or even solve the sign problem for specific classes of problems [85–89]. However, none of them is universal. The fundamental reason behind this issue is that the problem of N interacting fermions belongs to the computational class of complexity of **NP**-hard problems [4]. Indeed, it can be shown that it is equivalent to the MAXCUT problem [90], a prototypical **NP**-complete problem. A universal "solution" of the sign problem is an algorithm that allows to compute the average sign with accuracy ϵ in polynomial time. An algorithm for the solution of the sign problem would imply an algorithm that solves an **NP**-hard problem in polynomial time, hence it would lead to the conclusion that **NP** $\equiv$ **P**, which is widely believed to be false.

Notably, some important classes of relevant systems, such as the single-orbital Hubbard model at half filling, are sign-problem free as pointed out in Ref. [83], allowing for an exact solution using quantum Monte Carlo methods, as the DDMC method quickly sketched here. Another very important example of system without sign problem is the single-orbital Anderson impurity model [91]. Other approaches to reducing this complexity are based on the stochastic sampling not from the partition function, but from the distribution of Feynman diagrams, as the diagrammatic Monte Carlo algorithm. Another possibility is to subtract the connected diagrams, which are ultimately related to the denominator in Eq. (3.13) hence to the sign problem, as it is done in the connected determinant diagrammatic Monte Carlo algorithm (CDet). These methods will be described in Sec. 5.

3.1.4 Density functional theory: mapping many-body problems into non-interacting particles

As we have seen before, the scaling of the full many-body wave function is exponential in the number of degrees of freedom of the problem. Correspondingly, the scaling of the dimension of the Hilbert space in the single-particle case is linear. For this reason, it is very tempting to try to map the problem into a single-particle case.

The most successful scheme to achieve this mapping is the density functional theory (DFT) [92]. DFT is based on the Hohenberg-Kohn theorems that establish a one-to-one correspondence between the external potential acting on an interacting electron gas and its density [93]. The external potential can be for instance the lattice potential. These theorems allow us to write the energy of the system as a functional of the electronic density alone. In practice, the problem is then solved by using the Kohn-Sham construction [94], which consists in introducing a set of non-interacting Kohn-Sham quasi-particles that have the same total energy and total energy as the original electronic problem. This allows to formally write down a set of non-linear Schrődinger-like equations for these independent particles that can be solved in polynomial time. Due to its computational efficiency, DFT is for sure the most-widely used tool for materials science calculations and allows to efficiently obtain the structure and several ground state properties of many materials and molecules. Strictly speaking, DFT is a not controllable approximation as it relies on the construction of the unknown energy functional in terms of the density. However, this functional cannot be exactly determined in a polynomial time on a classical machine [95], therefore these approximations are required in order to gain insights on the properties of the system of interest. Usually, the functional is derived based on physically-motivated Ansatz, with parameters fitted from Monte Carlo calculations.

The incredible amount of studies based on DFT and its practical predictive power in the *ab-initio* description of materials cannot be underestimated and it is based on the fact that DFT is accurate whenever the functional representing the correlations in the energy is an accurate approximation of the exact functional. However, approximations to the unknown functional are empirically not able to reproduce the features of systems where the strength of the interaction in a local basis exceeds some system-dependent threshold.

Additionally, in principle, DFT can be used to compute only observables that depend on the ground state energy or density. The application of DFT to obtain the single-particle band structure of the system is based on the assumption that the dispersion of the Kohn-Sham quasi-particles coincides with that of the electrons. This assumption is empirically valid in many cases, but it has no *a-priori* theoretical foundation. Moreover, since the density is a single-particle object, DFT should not be expected to give reliable answers when it is applied to the calculation of two-particle response functions, such as susceptibilities.

3.2   Lattice models for strongly interacting electrons

3.2.1   A general action for electrons on a lattice

All the results obtained in this thesis are valid for a general form of lattice model with several atoms in the unit cell and possibly several orbitals per atom. We additionally include non-local interactions. The model that we use is a multi-band extended Hubbard model, as described in Ref. [96]. The general action for this model has the form

$$
\mathcal{S} = - \sum_{\substack{k,\{l\}, \\ \sigma\sigma'}} c^*_{k\sigma l} \left[(i\nu + \mu)\delta_{\sigma\sigma'}\delta_{ll'} - \varepsilon^{\sigma\sigma'}_{\mathbf{k},ll'} \right] c_{k\sigma'l'} + \frac{1}{2} \sum_{\substack{q,\{l\}, \\ \{k\},\{\sigma\}}} U^{pp}_{l_1 l_2 l_3 l_4} c^*_{k\sigma l_1} c^*_{q-k,\sigma' l_2} c_{q-k',\sigma' l_4} c_{k'\sigma l_3}
$$
$$
+ \frac{1}{2} \sum_{\substack{q,\{l\}, \\ \varsigma=d,m}} V^{\varsigma}_{q,l_1 l_2,l_3 l_4} \rho^{\varsigma}_{-q,l_1 l_2} \rho^{\varsigma}_{q,l_4 l_3} + \sum_{\substack{q,\{l\}, \\ \vartheta=s,t}} V^{\vartheta}_{q,l_1 l_2,l_3 l_4} \rho^{*\vartheta}_{q,l_1 l_2} \rho^{\vartheta}_{q,l_3 l_4} \tag{3.14}
$$

In this expression, $c^{(*)}_{k\sigma l}$ is the Grassmann variable that describes the annihilation (creation) of an electron with momentum $\mathbf{k}$, fermionic Matsubara frequency ν, and spin projection $\sigma \in \{\uparrow, \downarrow\}$. The label l numerates the orbital and the site within the unit cell. To simplify notations, we use a combined index $k = (\mathbf{k}, \nu)$. Summations over momenta and frequencies are defined as:

$$
\sum_k = \frac{1}{\beta} \sum_\nu \frac{1}{N_k} \sum_{\mathbf{k}} \tag{3.15}
$$

where again $\beta = T^{-1}$ is the inverse temperature and N_k is the number of $\mathbf{k}$-points in the discretized Brillouin zone (BZ). The single-particle part of the lattice action (first term in Eq. (3.14)) contains the chemical potential μ and the single-particle Hamiltonian term $\varepsilon^{\sigma\sigma'}_{\mathbf{k},ll'}$ that has the following structure in the spin space: $\varepsilon^{\sigma\sigma'}_{\mathbf{k},ll'} = \varepsilon_{\mathbf{k},ll'}\delta_{\sigma\sigma'} + i\vec{\gamma}_{\mathbf{k},ll'} \cdot \vec{\sigma}_{\sigma\sigma'}$. The diagonal in the spin space part $\varepsilon_{\mathbf{k},ll'}$ of this matrix contains the momentum- and orbital-space representation of the hopping amplitudes between different lattice sites, and may also account for the effect of the crystal field splitting (CFS) and of the external electric field. The non-diagonal in spins contribution $\vec{\gamma}_{\mathbf{k},ll'}$ describes the spin-orbit coupling (SOC) in the Rashba form [97, 98] and the effect of the external magnetic field. $\vec{\sigma} = \{\sigma^x, \sigma^y, \sigma^z\}$ is a vector of Pauli matrices.

The on-site Coulomb potential is written in the conventional (particle-particle) form

$$
U^{pp}_{l_1 l_2 l_3 l_4} = \int dr dr' \psi^*_{l_1}(r)\psi^*_{l_2}(r')V(r - r')\psi_{l_3}(r)\psi_{l_4}(r') \tag{3.16}
$$

where $V(r - r')$ is the screened Coulomb interaction and $\psi_l(r)$ are localized on-site basis

functions. The local interaction can also be rewritten in the particle-hole representation using the following relation $U^{ph}_{l_1l_2l_3l_4} = U^{pp}_{l_1l_4l_2l_3}$. The remaining part of the interaction V^r_q in Eq. (3.14) is written in the channel representation $r \in \{\varsigma, \vartheta\}$, where $\varsigma \in \{d, m\}$ denotes charge (d) and magnetic ($m \in \{x, y, z\}$) channels, and $\vartheta \in \{s, t\}$ depicts singlet (s) and triplet (t) channels. This interaction can have an arbitrary momentum $\mathbf{q}$ and bosonic Matsubara frequency ω dependence as depicted by a combined index $q = (\mathbf{q}, \omega)$. Usually, V^r_q corresponds to the non-local interaction. However, it may also contain the frequency-dependent part of the local interaction that is not included in the $U_{l_1l_2l_3l_4}$ term.

The splitting between the local and the non-local part of the interaction is not just meant to simplify or approach. Its physical motivation is based on the fact that the non-local interaction is strongly suppressed in metals due to screening. On the other hand, usually band insulators are not strongly correlated, even in the case of strong interactions, since strong correlations typically arise in the vicinity of the Fermi surface.

Standard tools for obtaining the hopping parameters of this model from *ab-initio* calculations, in particular DFT calculations, are based on the so called Wannier projection [99, 100], implemented in many software packages, for instance [101]. The Wannier projection is based on the projection of the Bloch's states obtained from DFT onto localized functions at each site in the Brillouin zone. On the other hand, the extraction of the local $U^{pp}_{l_1l_2l_3l_4}$ and non-local $V^{\varsigma/\theta}_{q,l_1l_2l_3l_4}$ components of the Coulomb interaction can be done using constrained random phase approximation (cRPA) [102–104].

Composite fermionic variables ρ^r_{q,l_1l_2} for the considered bosonic channels describe fluctuations of corresponding densities around their average values $\rho^r_{q,l_1l_2} = n^r_{q,l_1l_2} - \left\langle n^r_{q,l_1l_2} \right\rangle$. The orbital-dependent charge and magnetic densities can be introduced as follows

$$n^d_{q,l_1l_2} = \sum_{k,\sigma} c^*_{k+q,\sigma l_1} c_{k\sigma l_2} \,, \qquad \vec{n}^m_{q,l_1l_2} = \sum_{k,\{\sigma\}} c^*_{k+q,\sigma l_1} \vec{\sigma}_{\sigma\sigma'} c_{k\sigma' l_2} \tag{3.17}$$

The corresponding densities for the particle-particle channel are the following

$$n^s_{q,l_1l_2} = \frac{1}{2} \sum_k \left(c_{q-k,\downarrow l_2} c_{k\uparrow l_1} - c_{q-k,\uparrow l_2} c_{k\downarrow l_1} \right) \,, \qquad n^{*s}_{q,l_1l_2} = \frac{1}{2} \sum_k \left(c^*_{k\uparrow l_1} c^*_{q-k,\downarrow l_2} - c^*_{k\downarrow l_1} c^*_{q-k,\uparrow l_2} \right)$$

$$n^{t0}_{q,l_1l_2} = \frac{1}{2} \sum_k \left(c_{q-k,\downarrow l_2} c_{k\uparrow l_1} + c_{q-k,\uparrow l_2} c_{k\downarrow l_1} \right) \,, \qquad n^{*t0}_{q,l_1l_2} = \frac{1}{2} \sum_k \left(c^*_{k\uparrow l_1} c^*_{q-k,\downarrow l_2} + c^*_{k\downarrow l_1} c^*_{q-k,\uparrow l_2} \right)$$

$$n^{t+}_{q,l_1l_2} = \frac{1}{\sqrt{2}} \sum_k c_{q-k,\uparrow l_2} c_{k\uparrow l_1} \,, \qquad n^{*t+}_{q,l_1l_2} = \frac{1}{\sqrt{2}} \sum_k c^*_{k\uparrow l_1} c^*_{q-k,\uparrow l_2}$$

$$n^{t-}_{q,l_1l_2} = \frac{1}{\sqrt{2}} \sum_k c_{q-k,\downarrow l_2} c_{k\downarrow l_1} \,, \qquad n^{*t-}_{q,l_1l_2} = \frac{1}{\sqrt{2}} \sum_k c^*_{k\downarrow l_1} c^*_{q-k,\downarrow l_2}. \tag{3.18}$$

They account for interactions in the singlet and triplet channels. In most physical systems, the most important channel for non-local correlations is $n^d_{q,l_1 l_2}$, that comes from the Coulomb interaction. However, the interactions in the other channels will be exploited in the derivation of the dual theories in Sec. 4.

It is important to point out that this model usually is sufficient to describe a few bands close to the Fermi surface. The embedding of these bands can have a noticeable feedback on the properties of the extended system treated at the low level approximation from which the parameters of the embedded system are extracted. For example, a discussion of the problem of charge-consistency can be found in Ref. [105]. In the rest of this thesis, we assume that the parameters of the model Hamiltonian are not significantly modified by the solution of the embedded system. The only exception is the total number of electrons, which can be adjusted by changing the chemical potential μ of the model system to match the desired total number of electrons. The validity of this approach in truly *ab-initio* calculations, where consistency is needed should be validated case by case and a self-consistency loop should be implemented in cases where the approximation is not valid.

3.2.2 A multi-orbital case: the Hubbard-Kanamori model

In the result section, we mainly focus on model systems. A particularly important case is the Hubbard-Kanamori model. In this model, the on-site Coulomb interaction term in the Hamiltonian is parametrized in the Kanamori form [106, 107] as:

$$H_U = U \sum_l n_{l\uparrow} n_{l\downarrow} + \sum_{l \neq l'} \left\{ U' n_{l\uparrow} n_{l'\downarrow} + \frac{1}{2}(U' - J) \sum_\sigma n_{l\sigma} n_{l'\sigma} - J c^\dagger_{l\uparrow} c_{l\downarrow} c^\dagger_{l'\downarrow} c_{l'\uparrow} + J c^\dagger_{l\uparrow} c^\dagger_{l\downarrow} c_{l'\downarrow} c_{l'\uparrow} \right\} \tag{3.19}$$

Here, $c^{(\dagger)}_{l\sigma}$ is the annihilation (creation) operator for an electron at the orbital l with the spin projection $\sigma \in \{\uparrow, \downarrow\}$. $n_{l\sigma} = c^\dagger_{l\sigma} c_{l\sigma}$ is the local spin-dependent density. In the notation of Eq. (3.14), the non-zero components of the Kanamori interaction are

$$
\begin{aligned}
U^{pp}_{llll} &= U & \text{intraorbital density-density} \\
U^{pp}_{ll'll'} &= U' & \text{interorbital density-density} \\
U^{pp}_{ll'l'l} &= J & \text{pair hopping} \\
U^{pp}_{lll'l'} &= J & \text{spin flip}
\end{aligned} \tag{3.20}
$$

Hamiltonian (3.19) is particularly important because it represents one of the simplest multi-orbital models that contain the features of the Hund's physics. Indeed, this interaction term represent the simplest possible model for an atom where electrons interact differently depending on the orbital they occupy (so their orbital angular momentum) and
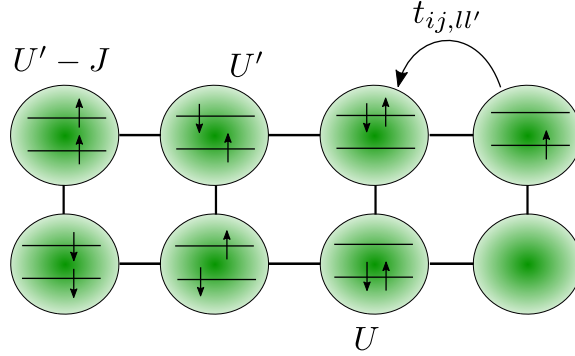
FIGURE 3.1: Simplified scheme of a lattice of sites with on-site Hubbard-Kanamori interaction. The configurations on each column of atoms is characterized by the same energy. We additionally highlight the hopping term $t_{ij,ll'}$ between different atoms i and j and bands l and l', which is the inverse Fourier transform of $\epsilon_{\mathbf{k},ll'}$.

on whether they have the same or different spin projection σ. If $J = 0$, the electrons interact with a Coulomb interaction that depends only on whether they are on the same orbital or not, no matter which spin they have. The Hund's coupling J breaks this symmetry and reduces the strength of the interaction if the electrons have parallel spin. This model captures the physics of superexchange and it is used to describe the physics of the so-called Hund's metals [107].

In our calculations, we also fix $U' = U - 2J$ to ensure rotational invariance [107]. In the single-orbital case, the on-site Coulomb interaction reduces to a Hubbard form given by the first term in Eq. (3.20).

3.2.3 A single-orbital case: the Hubbard model

When the correlated subspace consists only in a single-orbital, the local interaction Eq. (3.20) simply reduces to the first term. The corresponding lattice model is the Hubbard model [108, 109] and it is described by the full Hamiltonian

$$H = -t \sum_{\langle ij \rangle, \sigma} c_{i\sigma}^{\dagger} c_{j\sigma} + U \sum_i n_{i\uparrow} n_{i\downarrow}, \tag{3.21}$$

where t is the nearest-neighbor hopping. This model is very important in condensed matter theory, as it is the simplest non-trivial model that describes the interplay between kinetic energy (hopping term t between different sites) and potential energy (given by the local Coulomb interaction U). The former in minimized if the electrons are delocalized in the whole lattice, while the latter is minimized if no sites are doubly occupied. In momentum space, we can introduce the dispersion $\varepsilon_{\mathbf{k}}$ as the Fourier transform of t_{ij}, as done in

Eq. (2.23). If U is small compared to the bandwidth of the system, the electrons are free to move in the crystal and the model describes a metallic system. If $U \gg t$, the system describes an atomic system with two atomic orbitals with energies approximately $\pm U/2$. In this case, the system is clearly an insulator. These two phases are competing with each other, so that somewhere in between these regimes a phase transition has to occur. This interaction-driven metal-to-insulator transition is a realization of the Mott transition mentioned previously.

3.3   Quantum embedding schemes

3.3.1   Quantum embedding as dimensional reduction

As we have seen in Sec. 3.1.2 and Sec. 3.1.3, the dimensionality of the problem plays a crucial role in hindering most efforts to accurately simulate fermionic systems. The problem becomes particularly severe when we consider complex materials with several atoms in the unit cell and few orbitals each. In order to make the calculations practical, we have to reduce the complexity by reducing the size of degrees of freedom which are described accurately. In order to achieve this goal, we notice that in many situations not all the degrees of freedom are equally relevant to describe the physics of the system of interest. The two main cases where only a subset of degrees of freedom plays a crucial role are the following:

1. when we are interested in processes that involve only a specific energy scale and are weekly affected by processes on different scales, or

2. when only a subset of the system exhibits strong interactions, while the rest is effectively weakly correlated.

The first situation is very common when excitation with different energy scale appear in the system. For example, for most applications, we can neglect the bands that do not intersect the Fermi surface, as they are either completely full, if they lay below the Fermi energy E_F, or completely empty, if they lay above it. The second situation occurs when $s-$ or $p-$ delocalized orbitals coexist with $d-$ or $f-$shells that are very localized in space, as for example in transition metal oxides. The $d-$ and $f-$orbitals can be described as strongly interacting while the interactions within the others can be neglected or treated under simplifying assumptions.

In most cases, the rest of the system exerts an important feedback on the subsystem, so we cannot simply forget about it altogether. However, we can split the system into two parts, a part which contains the physics relevant to our problem and the rest. The relevant part of the system is treated with high-level methods, that ensure a very accurate
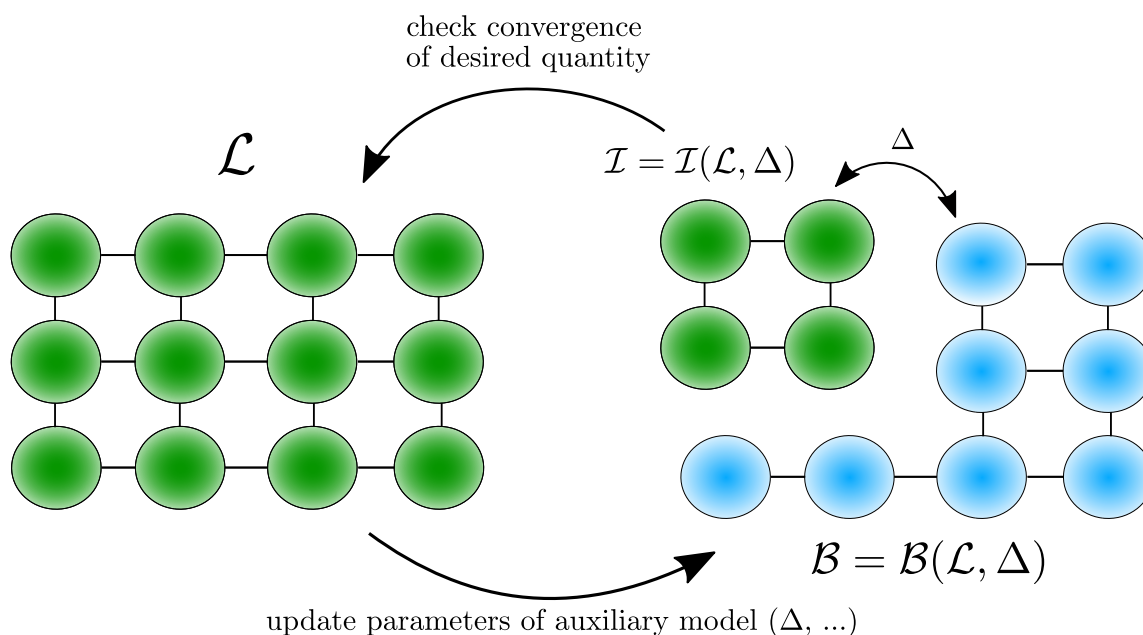
FIGURE 3.2: General scheme for quantum embedding methods. The lattice problem $\mathcal{L}$, depicted in green, is mapped into a correlated impurity problem $\mathcal{I}$ coupled to the remaining weakly (or non-)interacting sites $\mathcal{B}$ (light blue) by a hybridization function Δ. The parameters of the mapping, as the hybridization Δ, have to be computed according to some self-consistency condition, that quantifies the convergence of a property of the auxiliary model $\mathcal{I} + \mathcal{B}$ to the desired physical property of the original lattice $\mathcal{L}$.

description of the subsystem, while the rest is treated in a simplified way, that reduces the complexity of the calculation. Typically, the self-consistency between the relevant subsystem system and the rest is achieved by introducing an hybridization function Δ between the two systems as an unknown parameter that has to be optimized by assuming some general property of the combined system. This class of methods is referred to as *quantum embedding methods* [110] and has been extensively applied in the context of quantum chemistry [111]. The smaller relevant subsystem is often referred to as impurity. Indeed, the quantum embedding scheme can be applied to study the properties of point defects in solids [112], where the full system is treated within DFT and the degrees of freedom of the point defect are solved using exact diagonalization. All the embedding methods require the careful determination of the values of the Coulomb interaction within the subspace, in order to avoid issues with double counting of the contributions accounted for in the extended system.

   The embedding model that we use is based on the mapping of the original lattice into an impurity model, as described in Fig. 3.2. In particular, we have a lattice problem $\mathcal{L}$, which is too large to be solved directly, because it contains too many degrees of freedom.

To make the problem tractable, we introduce an impurity problem consisting of a smaller system $\mathcal{I}$ with few atomic sites, coupled to a non-interacting bath $\mathcal{B}$. The parameters of the $\mathcal{I} + \mathcal{B}$ system are then optimized, often self-consistently, in order to reproduce a target property of the lattice.

The embedding can be performed based on different choices of this property. As we are interested in a statistic ensemble at finite temperature, one possibility is to use the density-matrix $\hat{\rho}$ as a central quantity to achieve the embedding. This is the case for the density-matrix embedding theory (DMET) [113, 114]. The same quantity is central within the rotationally-invariant slave-boson approach (RISB) [115, 116]. In particular, the DMET method was later recognized as a limiting case of the RISB method [117]. Other important embedding schemes aim at reproducing spectroscopic experiments. These schemes often involve dynamical quantities in the embedding. This is the case for the self-energy in the dynamical mean field theory (DMFT) [118]. DMFT is a method that allows to map an extended problem into an Anderson impurity problem (see Eq. (3.22)) and self-consistently obtain an approximation to the Green's function.

The use of the self-energy as basis for the embedding is used also in the case of the self-energy embedding theory (SEET) [119–121]. The SEET method describes a general way of embedding the self-energy of a smaller strongly interacting cluster within a larger, possibly weakly interacting, system. For this reason, SEET is not directly comparable with DMET, RISB or even DMFT. As a matter of fact, some diagrammatic extensions of DMFT can be seen as applications of the SEET formalism [120], even though their derivation follows completely different routes.

3.3.2   The Anderson's impurity model

Most of the quantum embedding methods are based on the assumption that the lattice problem can be efficiently mapped into a smaller system consisting of a single or a few correlated sites coupled to an environment made of non-interacting bath sites. This problem is known as an impurity model. This model was initially proposed to explain the Kondo effect, that appears when the nearly-free conduction electrons in a material interact with the spin of magnetic point defects, inducing a minimum of the resistivity at a characteristic temperature T_K [122]. The impurity model is also extremely important in the description of quantum dots and molecular junctions [123].

In this section, we describe a general multi-orbital and multi-site impurity problem, so that we do not introduce any distinction between a multi-orbital impurity and a cluster impurity containing different sites. The larger system is described as a collection of non-interacting degrees of freedom of the bath indicated with $b \in \mathcal{B}$. The atomic system $\mathcal{I}$ is modeled as a discrete set of orbitals $\{l\}$ populated by interacting electrons. The coupling between the bath sites and the atomic system is described in terms of hopping processes
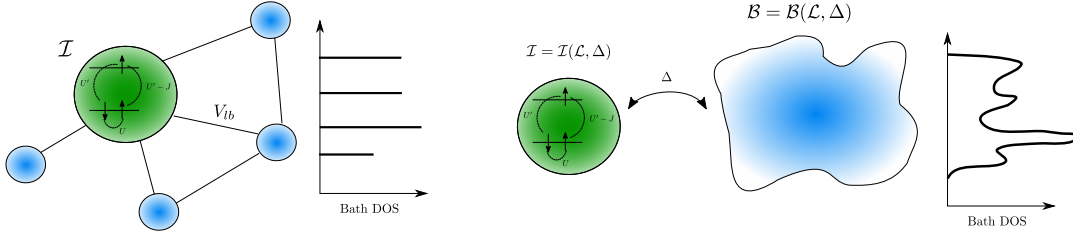
FIGURE 3.3: Pictorial representation of an impurity model coupled to several non-interacting bath sites (left) and to an infinite number of bath sites (right). The latter mimics the coupling to an infinite lattice with a continuous density of states (DOS). In limit of an infinite lattice, we integrate out the bath sites and we obtain the frequency-dependent hybridization function Δ, written in Eq. (3.26).

V_{lb}^{σ}: an electron can be destroyed on the impurity and created on a bath site and vice versa. We assume without loss of generality that this process conserves spin.

An impurity model is described by the following Hamiltonian

$$\hat{H}_{\text{imp}} = \underbrace{\sum_{\sigma} \varepsilon_{ll'}^{\sigma\sigma'} \hat{c}_{\sigma l}^{\dagger} \hat{c}_{\sigma' l'} + H_{\text{int}}[\hat{c}^{\dagger}, \hat{c}]}_{\hat{H}_{\text{atom}}} + \underbrace{\sum_{b\sigma} \varepsilon_{b} f_{\sigma b}^{\dagger} f_{\sigma b}}_{\hat{H}_{\text{bath}}} + \underbrace{\sum_{bl\sigma} V_{lb}^{\sigma} \hat{c}_{\sigma l}^{\dagger} f_{\sigma b} + V_{lb}^{*,\sigma} f_{\sigma b}^{\dagger} \hat{c}_{\sigma l}}_{\hat{H}_{\text{hyb}}}. \quad (3.22)$$

where the electronic interaction on the atom is written in general form as

$$H_{\text{int}}[\hat{c}^{\dagger}, \hat{c}] = \frac{1}{2} \sum_{\{l\},\{\sigma\}} U_{l_1 l_2 l_3 l_4}^{pp} \hat{c}_{\sigma l_1}^{\dagger} \hat{c}_{\sigma' l_2}^{\dagger} \hat{c}_{\sigma' l_4} \hat{c}_{\sigma l_3} \quad (3.23)$$

The impurity problem in the Hamiltonian form can be solved by diagonalizing the Hamiltonian (exact diagonalization or ED) when the number of sites is small. Current computational tools allow to diagonalize systems up to few dozens of atoms before hitting the exponential wall. The problem can be also conveniently formulated in the action formalism. The reason for choosing this route is that the resulting impurity action can be formulated in terms of the impurity electrons only, and the bath sites can be integrated out.

By using the path integral formulation of Section 2.2.4, the problem (3.22) can be converted to the action formalism as

$$\mathcal{Z}_{\text{imp}} = \int \mathcal{D}[c^*, c] \int \mathcal{D}[f^*, f] \exp\left\{ -\sum_{\nu\sigma ll'} c_{\nu\sigma l}^{*} \left[(i\nu + \mu)\delta_{\sigma\sigma'}\delta_{ll'} - \varepsilon_{ll'}^{\sigma\sigma'} \right] c_{\nu\sigma l'} + H_{\text{int}}[c^*, c] \right\}$$

$$\times \exp\left\{ -\sum_{\nu b\sigma} f_{\nu\sigma b}^{*} (i\nu + \mu - \varepsilon_b) f_{\nu\sigma b} + \sum_{\nu bl\sigma} \left(V_{lb}^{\sigma} c_{\nu\sigma l}^{*} f_{\nu b\sigma} + V_{lb}^{*,\sigma} f_{\nu\sigma b}^{*} c_{\nu\sigma l} \right) \right\} \quad (3.24)$$

The bath degrees of freedom in the equation above can be integrated out by means of Gaussian integration, since they appear only up to second-order in the bath $f^{(*)}$ operators. The integration leads to

$$\mathcal{Z}_{\text{imp}} = \int \mathcal{D}[c^*, c] \exp\left\{ -\sum_{\nu\sigma ll'} c^*_{\nu\sigma l} \left[(i\nu + \mu)\delta_{\sigma\sigma'}\delta_{ll'} - \varepsilon^{\sigma\sigma'}_{ll'} - \Delta^{\sigma\sigma'}_{\nu,ll'} \right] c_{\nu\sigma l'} + H_{\text{int}}[c^*, c] \right\}$$

(3.25)

where we have defined the hybridization function as

$$\Delta^{\sigma\sigma'}_{\nu,ll'} = \sum_b \frac{V^\sigma_{lb} V^{*,\sigma}_{l'b\sigma'}}{i\nu - \varepsilon_b}$$

(3.26)

In the case of a collection of a finite number of bath sites, the density of states (DOS) of the impurity problem consists in several discrete levels available. If we want to correctly capture the physics of a lattice problem, it is desirable to have a continuous DOS, as shown in Fig. 3.22. In order to achieve this goal, we have to take the limit of an infinite number of bath sites. The Anderson impurity model (AIM) is the limit of an infinite number of bath sites for this model [124], so the case when $b = 1, ..., +\infty$. In this case, the bath index b is often replaced by a sum over the momenta $\mathbf{k}$ within the Brillouin zone of a lattice in the continuous limit. In this case, the hybridization function Δ_ν is the central quantity when describing the impurity problem. Most of the solvers based on Monte Carlo schemes work in the action formalism and make use of the hybridization function.

3.3.3 Difference between density matrix embeddings and DMFT

The impurity model described above is a suitable candidate for the embedding, as it can describe conduction electrons thanks to the bath sites, strongly interacting localized electrons on the atomic sites by means of the local parameters $\epsilon^{\sigma\sigma'}_{ll'}$ and $U^{pp}_{l_1 l_2 l_3 l_4}$, and the hopping between them through the hopping terms V^σ_{lb} in the Hamiltonian formalism or the hybridization function $\Delta^{\sigma\sigma'}_{\nu,ll'}$ in the action formalism.

The next step is the choice of the target quantity of the lattice that we want to reproduce with the embedding strategy. The difference between the embedding methods described previously regards precisely the observables which are extracted from the impurity problem. DMET and RISB aim at extracting information about static observables, while DMFT aims at the Green's function (or alternatively the self-energy). This turns out to be the main reason why the computational complexity of the DMET and RISB methods in substantially lower than that of DMFT, but also the reason why DMFT results in a better approximation of the lattice problem for a given impurity model. However, the possibility

of using cluster impurity problems at a lower computational cost can favor RISB in some cases.

In the DMET/RISB methods, the quantity to be computed is the single-particle density matrix of the embedded problem, that can be then written as

$$\hat{\rho}_{1P} = \begin{pmatrix} \rho_{\text{imp}} & \rho_{\text{hyb}} \\ \rho_{\text{hyb}}^{\dagger} & \rho_{\text{bath}} \end{pmatrix} \quad \text{with}$$

$$\left(\rho_{\text{imp}}\right)_{ll'}^{\sigma\sigma'} = \langle \hat{c}_{l\sigma}^{\dagger} \hat{c}_{l'\sigma'} \rangle_{\text{imp}}$$
$$\left(\rho_{\text{hyb}}\right)_{ll'}^{\sigma\sigma'} = \langle \hat{f}_{l\sigma}^{\dagger} \hat{c}_{l'\sigma'} \rangle_{\text{imp}}. \tag{3.27}$$

where the $c^{(\dagger)}$ and $f^{(\dagger)}$ are the impurity and bath creation (annihilation) operators respectively.

Despite the very different theoretical foundation of the two methods, the only practical difference appears in the number of free parameters to be optimized in the two methods. Both methods require only a finite number of bath levels that are related to the number of sites not included in the impurity problem $N - N_{\text{imp}}$ and work using the Hamiltonian representation of the impurity model (3.22). Specifically, in the DMET formalism the only free parameters of the auxiliary impurity model to be optimized are the local energies $\epsilon_{ll'}^{\sigma\sigma'}$. In the RISB method, on the other hand, an additional matrix R that describes the quasiparticle weight of each band is optimized as well [125]. This parameter is computed as

$$R_{ll'}^{\sigma\sigma'} = \sum_{\sigma''l''} \left\{ \left(\hat{\rho}_{\text{imp}}\right)_{ll''}^{\sigma\sigma''} \left[\hat{\rho}_{\text{hyb}} \left(1 - \hat{\rho}_{\text{hyb}}\right)\right]^{-1/2} \right\}_{l''l'}^{\sigma''\sigma'}. \tag{3.28}$$

DMFT differs from these two embedding methods as it is based on the self-consistent optimization of the impurity Green's function, which can be obtained from the path integral (3.25) as

$$g_{\nu,ll'}^{\sigma\sigma'} = -\langle c_{\nu\sigma l} c_{\nu\sigma l'}^{*} \rangle_{\text{imp}} \tag{3.29}$$

and it is a function of the non-hermitian hybridization function $\Delta_{\nu,ll'}^{\sigma\sigma'}$.

The impurity Green's function contains information both about the atomic physics related to the subsystem and about the physics of the delocalized electrons that can hop onto the atomic subsystem.

Since the Green's function is a function of the Matsubara frequency ν (or alternatively of the imaginary time τ), an infinite number of equations should in principle be available in order to compute it for each Matsubara frequency ν_n with indices $n = 0, ..., +\infty$. The

impurity problem contains a sufficient number of degrees of freedom to determine independently g_ν for each Matsubara frequency if the number of bath sites is infinite. The determination of the Green's function in DMFT will be discussed in the next section.

The embedding between all these methods were shown to be connected to each other by Ayral *et al.* in Ref. [125]. In their analysis, it turns out that DMFT can be regarded as the limit of RISB when the number of bath sites goes to infinity. From the impurity Green's function, we can define the self-energy of the impurity $\left(\Sigma_\nu^{\text{imp}}\right)_{ll'}^{\sigma\sigma'}$ using the Dyson equation

$$\left(g_\nu^{-1}\right)_{ll'}^{\sigma\sigma'} = (i\nu + \mu)\delta_{ll'}\delta_{\sigma\sigma'} - \Delta_{\nu,ll'}^{\sigma\sigma'} - \left(\Sigma_\nu^{\text{imp}}\right)_{ll'}^{\sigma\sigma'}. \tag{3.30}$$

In the DMFT approach, the self-energy at each frequency is determined numerically in an independent fashion for each frequency ν, so that no explicit functional form is assumed for $\left(\Sigma_\nu^{\text{imp}}\right)_{ll'}^{\sigma\sigma'}$. DMFT assumed that the non-local self-energy of the lattice is $\Sigma_{k,ll'}^{\sigma\sigma'} \approx \left(\Sigma_\nu^{\text{imp}}\right)_{ll'}^{\sigma\sigma'}$. On the other hand, it is possible to compute the self-energy in DMET and RISB. Both methods assume a precise form of the self-energy. Explicitly, they read

$$\Sigma_{k,ll'}^{\sigma\sigma'} \approx -\varepsilon_{ll'}^{\sigma\sigma'} \quad \text{for DMET}, \tag{3.31}$$

$$\Sigma_{k,ll'}^{\sigma\sigma'} \approx \left\{ i\nu \left[\mathbb{1} - (R^\dagger \cdot R)^{-1} \right] - \varepsilon + R \cdot \varepsilon \cdot (R^\dagger)^{-1} \right\}_{ll'}^{\sigma\sigma'} \quad \text{for RISB}. \tag{3.32}$$

The DMET self-energy is fully local and it is not dynamical at all, while the RISB self-energy is linear in frequency and contains information about the quasi-particle weights R, which appear in the coefficients of the linear term of the self-energy in terms of ν. Since the self-energy in both methods contain a constant term, both methods contain the necessary information to describe the Mott transition. Indeed, both DMET and RISB have been applied to the one- and two-dimensional Hubbard model [117, 126], leading to accurate spectra in regimes where the computational cost of DMFT is prohibitive.

3.3.4 DMFT: self-consistency equations and methods for its solution

In this section, we will dive into the DMFT method, which is currently the most-widely used method for describing strong correlations in solids [127, 128], also due to its feasibility in combination with DFT [129, 130]. The reason behind its success is that DMFT approximates very well the local physics of realistic materials and it is able to capture the Mott transition [107]. Indeed, DMFT assumes neither weak interactions among electrons nor a narrow bandwidth, so in this sense it is *non-perturbative* in both the interaction strength and the bandwidth. DMFT consists in assuming a mapping between the original
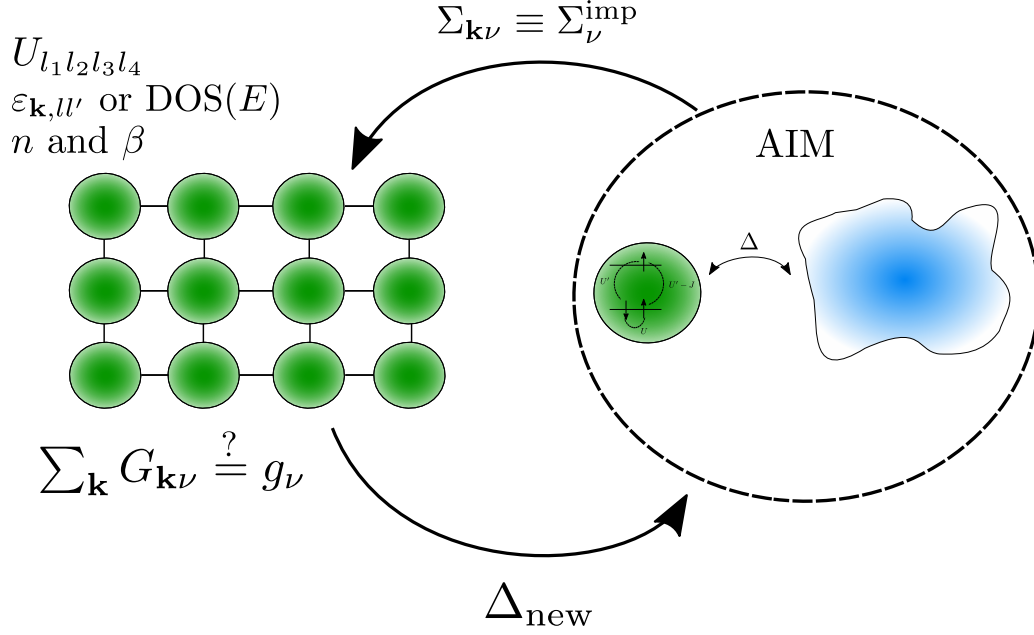
FIGURE 3.4: DMFT self-consistency cycle for the determination of the lattice Green's function.

lattice problem of Eq. (3.14) with only local interaction $U_{l_1 l_2 l_3 l_4}^{pp}$

$$
S = -\sum_{\substack{k,\{l\}, \\ \sigma\sigma'}} c_{k\sigma l}^* \left[(i\nu + \mu)\delta_{\sigma\sigma'}\delta_{ll'} - \varepsilon_{\mathbf{k},ll'}^{\sigma\sigma'} \right] c_{k\sigma'l'} + \frac{1}{2} \sum_{\substack{q,\{l\}, \\ \{k\},\{\sigma\}}} U_{l_1 l_2 l_3 l_4}^{pp} c_{k\sigma l_1}^* c_{q-k,\sigma' l_2}^* c_{q-k',\sigma' l_4} c_{k'\sigma l_3}
$$

(3.33)

and Anderson impurity model, described by the action in the path integral Eq. (3.25), namely

$$
S_{\text{imp}} = -\sum_{\nu\sigma} c_{\nu\sigma}^* \left[(i\nu + \mu)\delta_{\sigma\sigma'}\delta_{ll'} - \Delta_{\nu,ll'}^{\sigma\sigma'} \right] c_{\nu\sigma} + \frac{1}{2} \sum_{\substack{\omega,\{l\}, \\ \{\nu\},\{\sigma\}}} U_{l_1 l_2 l_3 l_4}^{pp} c_{\nu\sigma l_1}^* c_{\omega-\nu,\sigma' l_2}^* c_{\omega-\nu',\sigma' l_4} c_{\nu'\sigma l_3}
$$

(3.34)

Historically, this mapping was derived as an exact result in the limit of infinite connectivity z of the lattice, where z is the number of nearest-neighbor sites [118, 131]. For this reason, DMFT provides the exact solution of the Hubbard model on the Bethe lattice. The application to finite connectivity is motivated by scaling reasons, as the DMFT solution is the leading term when z is sufficiently large.

The main assumption behind the DMFT mapping is that the self-energy is local, i.e. it does not depend on momentum. This approximation can be summarized as

$$\Sigma_{k,ll'}^{\sigma\sigma'} \approx \left(\Sigma_\nu^{\text{imp}}\right)_{ll'}^{\sigma\sigma'} = (i\nu + \mu)\delta_{ll'}\delta_{\sigma\sigma'} - \Delta_{\nu,ll'}^{\sigma\sigma'} - \left(g_\nu^{-1}\right)_{ll'}^{\sigma\sigma'} \tag{3.35}$$

where the g_ν and Δ_ν are the Green's function and hybridization function of the impurity model. The only parameter that must be adapted in order to fully characterise the optimal model is the impurity hybridization function Δ_ν. Here comes the second important piece of the DMFT workflow: the self-consistency condition to determine Δ_ν. The condition of choice is that the Green's function of the impurity problem has to be equal to the local Green's function of the lattice $G_\nu^{\text{loc}} = \sum\limits_{\mathbf{k}\in\text{BZ}} G_{\mathbf{k}\nu}^{\text{latt}}$. This condition can be explicitly written as

$$\left(G_\nu^{\text{loc}}\right)_{ll'}^{\sigma\sigma'} \equiv g_{\nu,ll'}^{\sigma\sigma'}, \tag{3.36}$$

which is a set of equations in $\nu, \sigma^{(')}$ and $l^{(')}$. This equation implicitly determines a self-consistency condition on the hybridization function, where the form of the local Green's function explicitly reads

$$\left(G_\nu^{\text{loc}}\right)_{ll'}^{\sigma\sigma'} = \sum_{\mathbf{k}\in\text{BZ}} \left(\frac{1}{i\nu + \mu - \varepsilon_{\mathbf{k}} - \Sigma_{\mathbf{k}\nu}^{\text{latt}}}\right)_{ll'}^{\sigma\sigma'} = \sum_{\mathbf{k}\in\text{BZ}} \left(\frac{1}{g_\nu^{-1} + (\Delta_\nu - \varepsilon_{\mathbf{k}})}\right)_{ll'}^{\sigma\sigma'}. \tag{3.37}$$

Since at fixed Δ_ν the quantities g_ν and Σ_ν^{imp} are uniquely defined and can be obtained by solving the corresponding Anderson impurity problem, we can write the implicit equation for Δ_ν as

$$\sum_{\mathbf{k}\in\text{BZ}} \left(\frac{1}{g_\nu^{-1} + (\Delta_\nu - \varepsilon_{\mathbf{k}})}\right)_{ll'}^{\sigma\sigma'} = g_{\nu,ll'}^{\sigma\sigma'}. \tag{3.38}$$

The DMFT self-consistency scheme is depicted in Fig. 3.4.

3.3.5   Solving the Anderson impurity model

The solution of the AIM to extract the g_ν is far from trivial, as the computation of g_ν from Eq. (3.29) based on the action (3.34) cannot be done directly, as the action is non-quadratic.

Without aiming at a thorough review of the methods, we summarise the main routes for the exact solution of the impurity model that have been pursued recently. One possibility is to use exact diagonalization, where a finite number of bath sites is considered such that the Hamiltonian (3.22) can be used instead of the action (3.34) [132]. Convergence as a function of the number of bath sites has to be checked, keeping in mind the exponential scaling

of the wave function as a function of the number of bath sites considered. This approach has seen a recent revival thanks to the use of efficient algorithms for the calculation of the first few eigenvectors of sparse Hamiltonians based on the Lanczos method [133]. Recently, an efficient implementation of ED for solving the impurity problem on a quantum hardware has been suggested in Ref. [134].

A second main route consists in using quantum Monte Carlo methods (QMC). The first method deployed for the study of impurity problems is the Hirsch-Fye QMC method [135], which is based on the discrete Trotter factorization of the imaginary time. The most used class of stochastic algorithms for quantum impurity problems is the continuous-time QMC, in its various flavors based on the strong-coupling expansion (CT-INT) [136], the introduction of auxiliary fields (CT-AUX) [137–139] or on the hybridization expansion (CT-HYB) [140–142]. The detailed discussion of these methods is beyond the scope of this thesis and can be found in Ref. [143].

In addition to these widely used methods, it is worth mentioning that the diagrammatic Monte Carlo based on connected determinants [144] as well as the inchworm QMC algorithm [145] were recently proposed as methods to overcome the sign problem in multi-orbital quantum impurity models. Other techniques have been efficiently applied to the solution of the Anderson impurity model such as numerical renormalization group approach [146] and density-matrix renormalization group approach (DMRG) [147] have been employed for the solution of the Anderson impurity problem. The DMRG can be efficiently combined with matrix product states (MPS) [148, 149].

3.4 Methods for the study of non-local correlations

3.4.1 Considerations about single-site DMFT

The main strength of DMFT compared to most of the other methods is that it is a non-perturbative method. In this sense, there is no assumption that the interaction is much smaller or much larger than the bandwidth. However, it assumes that the connectivity of the lattice is large (or alternatively that the number of dimensions of the lattice is large). In low dimensions, this is not *a-priori* a justified assumption as $d \leq 3 \ll +\infty$, so a the use of DMFT is based on the assumption that correlations among electrons act mostly at the local level. When this is not the case, the DMFT approximation is not valid. One evident failure of DMFT in low dimensions is probably the prediction of spurious phase transitions that would be allowed in larger dimensions but not in one- or two-dimensional cases, as discussed in more detail in Chapter 5.

Currently, the main parameters that one can use to determine the choice of the method are how weak the local interaction is with respect to the bandwidth of the system. When

the local interaction is strong compared to the bandwidth, for example, we expect weak-coupling approaches to give a poor description of the system, as they assume an underlying Fermi liquid structure, while the actual physics moves in the direction of a Mott insulating phase. Single-site DMFT is able to capture the Mott transition and also the coexistence of metallic and insulating phases that accompanies this first order transition in both single-band [150–156] and multi-orbital [157–161] systems.

Despite its numerous successes, single-site DMFT is insufficient in some cases, because this theory accounts only for local correlation effects. Even if the interaction is purely local, it can give rise to important non-local correlation effects that extend over several lattice sites. Another obvious limitation is that DMFT does not account for non-local Coulomb interactions at all in its single-site version. This problem can be partially cured by using the extended DMFT (EDMFT), which introduces a bosonic hybridization function Y_ω in addition to the electronic hybridization function described so far [162–165]. Despite accounting for non-local interactions, EDMFT is still based on the assumption of locality of the correlations.

3.4.2   Cluster methods

A route to go beyond the local picture provided by DMFT, while still taking advantage of the non-perturbative description of local electronic correlations, consists in considering a finite cluster of lattice sites instead of a single-site impurity problem. The cluster problem allows to take into account spatial correlation effects within the cluster [29, 127, 166–170]. As a matter of fact, considering even only short-range correlations beyond single-site DMFT significantly modifies the shape of the coexistence region for the Mott transition and drastically reduces the critical value of the interaction. This modification can be observed when a 2×2 cluster is considered in DMFT, instead of a single-site [155].

However, cluster extensions of DMFT can treat only correlations (or interactions) within the cluster size. Considering a finite-size cluster also limits the kind of orderings of the system that can be observed. Indeed, a finite-size cluster corresponds to considering only certain points the the Brillouin zone, usually restricted to the some high-symmetry points. Considering a 2×2- or 4×4-cluster is sufficient to describe short-range anti-ferromagnetism or charge ordering between nearest-neighbors, but cannot describe the effects of long range fluctuations, that can have even more dramatic consequences [171]. Long-range collective modes, such has plasmons and magnons described by the density and magnetic susceptibilities, with incommensurate structure, such as spin spirals, are described by a wavevector **q** which does not lie at high-symmetry points of the Brillouin zone of the lattice, hence information about these modes would be lost. The effect of considering a small cluster in the presence of incommensurate orders and the corresponding loss of resolution on the orderings present in the system has been studied in Ref. [172].

Additionally, these methods are usually based on quantum Monte Carlo solvers that often suffer from a fermionic sign problem in multi-orbital calculations [173]. This issue can be cured only in very specific cases by a proper design of the Monte Carlo updates [174–177]. Other solvers for cluster problems rely on the exact diagonalization (ED) method [32, 178], the complexity of which scales exponentially with the number of orbitals and the total number of impurity sites plus bath sites.

Attempts to go beyond these assumptions of locality using unbiased quantum Monte Carlo (QMC) methods are so far limited to specific parameter regimes or symmetries due to the fermionic sign problem [177, 179–184].

3.4.3 Diagrammatic techniques

The other main route to study non-local correlations in condensed matter physics is represented by diagrammatic methods, based on considering only certain classes of Feynman diagrams. Unfortunately, most of the available theoretical methods for multi-orbital systems are limited to a weakly correlated regime, such as the *GW* [92, 185–187] or the fluctuation-exchange approximation (FLEX) [188–192]. The *GW* method is able to describe non-local charge fluctuations and, as such, it can be combined with DMFT in order to efficiently account for non-local density-density interactions [40, 193–207]. An issue common to all the approaches based on the *GW* formalism is that only charge fluctuations are taken into account, but spatial magnetic fluctuations are neglected. In most of the realistic materials, the Coulomb interaction is the main source of correlations, especially in three-dimensional systems. In these cases, spin fluctuations are strongly screened by charge fluctuations, hence the effect of the local interaction is well described by DMFT. However, in cases where spin fluctuations cannot be neglected altogether, the idea of combining diagrammatic approaches with DMFT is still a particularly promising route towards an accurate description of the non-local correlation effects [208]. In all these cases, the key idea of these approaches is to use the DMFT impurity problem as a reference system for a diagrammatic expansion in order to describe the non-local electronic correlations in the form of the most relevant Feynman diagrams. Since all these methods combine the local self-energy Σ_ν^{imp} of the strongly interacting impurity problem with additional non-local self-energy contributions Σ_k^{rest} coming from the non-local, presumably more weakly interacting extended system, they can be considered as applications of the ideas behind the SEET formalism. Examples of such theories are the the dynamical vertex approximation (DΓA) [209–214], the triply irreducible local expansion (TRILEX) [215–217], the dual fermion (DF) [218–223], the dual boson (DB) [224–230], and the dual TRILEX (D-TRILEX) [48, 231–235] methods.

Among them, DF, DB, and DΓA have the most sophisticated diagrammatic structures that allow for a very accurate description of both local and non-local correlation effects [236]. At the same time, these methods generally suffer from high computational

costs that limit the application of these approaches in multi-band setups. For instance, the diagrammatic expansion in DF, DB, and DΓA involves the exact local four-point vertex function of the reference system. Evaluating this frequency-dependent object in a multi-band case is very expensive numerically, because it contains four external points that have independent frequency and band indices. Additionally, using the four-point vertex in a diagrammatic expansion is frequently hindered by the need of inverting the Bethe-Salpeter equation (BSE), which requires large computational resources both in terms of time for the calculation and of memory consumption for storing the full momentum and frequency dependent vertices. For this reason, among the three methods only the DΓA [211–213] and the second-order DF [237] approaches have been extended to the multi-band case so far.
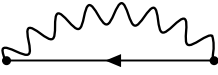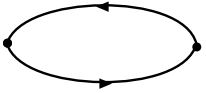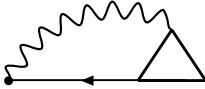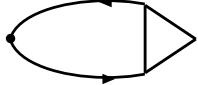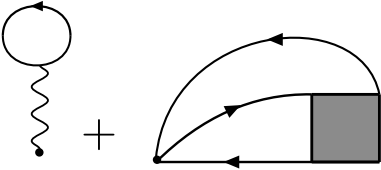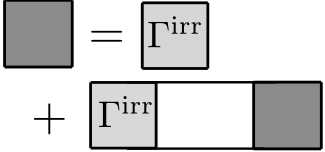
Method	Approximation for Σ_k	$F_{kk'q}$ / Π_q
GW + EDMFT		
TRILEX		
DΓA		

FIGURE 3.5: Sketch of the main diagrams included in the diagrammatic methods beyond DMFT. Dual theories (DF, DB and D-TRILEX) are discussed separately. Straight lines describe the DMFT Green's function. Wiggly lines represent the renormalized interaction in the theory (or the bare interaction in DΓA).

On the contrary, *GW*+DMFT and TRILEX methods have a much simpler diagrammatic structure compared to DF, DB, and DΓA, which makes the former very attractive for multi-band calculations. Indeed, as we have already mentioned, *GW*+DMFT has been intensively used many realistic calculations. This simplicity is shown in Fig. 3.5. On the contrary to the other diagrammatic extensions of DMFT, the *GW*+DMFT does not require the evaluation of three- or four-point correlation functions of the impurity. This is a major advantage from the computational point of view, since the evaluation of these correlation functions using Monte Carlo methods is computationally expensive and efficient ways based on the Lanczos algorithm to extract correlation functions from exact

diagonalization are limited to the single-particle Green's function and the susceptibility (two-point correlation functions) [238]. However, the *GW*+DMFT sacrifices vertex corrections that can be crucial for an accurate description of magnetic, optical and transport properties [48, 204, 239–246]. The TRILEX method partially cures these drawbacks by considering both the charge and magnetic fluctuations, and also by introducing vertex corrections in the form of the local Hedin's vertex [247] of the DMFT impurity problem. The diagrammatic expansion based on the three-point vertices is still relatively simple, because it does not require to invert the BSE in momentum and frequency space. This is a clear computational advantage over DF, DB, and DΓA. However, TRILEX is affected by a double-counting problem known as Fierz ambiguity [248–250] when the charge and magnetic fluctuations are taken into account simultaneously [217]. Additionally, vertex corrections in the original formulation of TRILEX are included in diagrams in an asymmetric way. This diagrammatic structure leads to inconsistent results in a strong-coupling limit [251] and does not have a correct symmetry in the orbital [48] space. Overall better performances of the TRILEX method were shown in the weak coupling limit when a symmetric version of the theory was used [236]. This symmetric version, however, does not solve the Fierz ambiguity and partially sacrifices the consistency of the theory. In order to resolve the aforementioned issues of *GW*+DMFT and TRILEX, the D-TRILEX approach was recently developed [231].

4 Dual theories of strong correlations

4.1 A dual space with weakly correlated particles

4.1.1 The idea behind the dual theories

In this Chapter, we introduce a class of diagrammatic extensions of DMFT, known as dual theories, that are able to deal with systems with non-local strong correlations. Here, we follow very closely the derivation presented by the author of this thesis and collaborators in Ref. [96].

Dual theories consist in a formally exact way of performing a perturbative expansion around a generic interacting starting point [222, 223]. As a consequence, they are in principle exact. Approximations have to be introduced at later stages in order to make the calculations tractable. The arbitrary interacting reference point is often chosen to be an impurity problem, consisting of one or more atoms coupled to the external environment by means of an hybridization function. The reason for this choice is that the impurity problems mimics the separation that physically occurs in a lattice between itinerant electrons, nearly free to hop from one atomic site to another, and localized electrons on $d-$ or $f-$orbitals.

The introduction of the impurity reference problem starts with the arbitrary separation between the "local" degrees of freedom of an impurity problem and the "non-local" lattice degrees of freedom. These are then coupled with each other by introducing the up-to-now arbitrary hybridization function that can be fixed with a proper choice of the self-consistency procedure. From this perspective, it is clear that dual theories consist in a formally exact way of performing a quantum embedding by separating a strongly interacting subspace and a weakly interacting one. This correspondence is strengthened further by solving the impurity problem exactly and then applying approximations to the non-local part, in a very similar way to what is done in lattice quantum embedding methods, where approximations are imposed on the interacting part of the weakly interacting subsystem.

The two main representatives of these theories are the dual fermion theory (DF), originally proposed in Ref. [218], and the dual boson theory (DB) [224]. The DF is formulated with an action without non-local interactions and as such in requires only the additions of dual fermionic variables f and f^*. The DB additionally allows us to treat non-local interactions $V_{\mathbf{q}}$ and achieves this goal by decoupling the non-local interactions by introducing
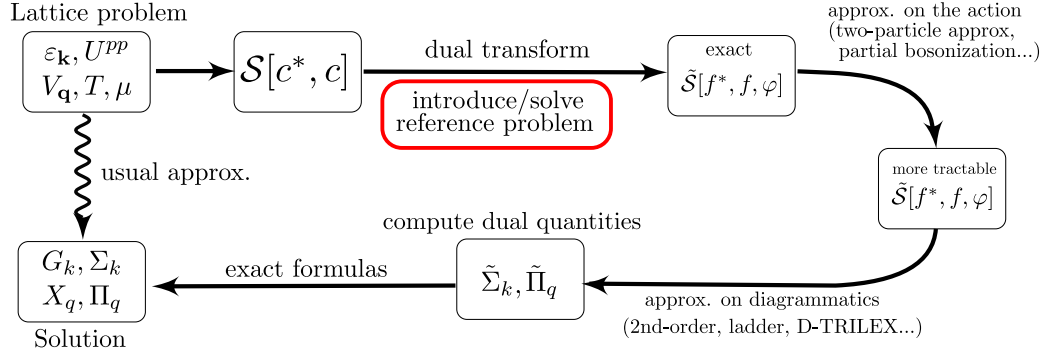
FIGURE 4.1: Scheme to obtain observables from the dual theories.

bosonic fields φ. Since the DF technique can be regarded as a particular application of the DB technique to cases where non-local interactions are absent, we will focus on the latter. We will then refer to the theory as DF if the interactions are only local and DB otherwise.

The last part of the Chapter is devoted to the derivation of an approximation to the DB theory, the partially bosonized action in dual space, originally introduced in Refs. [231] and extended to the multi-band case in Ref. [96]. This approximation allows us to derive a particularly efficient numerical method, the D-TRILEX method, described in Chapter 6.

From the conceptual point of view, all the theories belonging to this class follow the same scheme, sketched in Fig. 4.1:

1. The original electronic action of Eq. (3.14) is divided into a local part $\mathcal{S}_{\mathrm{imp}}$ and a non-local part $\mathcal{S}_{\mathrm{rem}}$, such that $\mathcal{S}_{\mathrm{latt}} = \mathcal{S}_{\mathrm{imp}} + \mathcal{S}_{\mathrm{rem}}$.

2. An arbitrary hybridization function is added to $\mathcal{S}_{\mathrm{imp}}$ and subtracted from $\mathcal{S}_{\mathrm{rem}}$.

3. One or several path integral transformations known as the Hubbard-Stratonovich transformation are exploited to introduce new fields in the theory. These can be fermions f and f^* or bosons φ.

4. The original fermions now appear only in the impurity problem and their coupling to the dual fields is at most quadratic. They are integrated out using exact path integral relations. This leads to an action defined only in terms of the dual particles $\tilde{\mathcal{S}}$.

5. Apply the required approximations to simplify the action $\tilde{\mathcal{S}}$ and/or to restrict the set of diagrams considered in the diagrammatic expansion.

6. Use exact relations between the dual and the lattice observables to compute the observables of the original lattice problem.

4.1.2   Some relevant results of the dual theories

The dual theories have been so far mainly applied to single-orbital lattice models. In the early stages of the theory, it was shown that the DF was able to capture antiferomagnetic fluctuations as well as the formation of Fermi arcs in a two-dimensional Hubbard model on a square lattice [219].

Another important phenomenon well-captured by the dual theories is the Mott metal-to-insulator transition. Even though the DMFT approach captures this transition for the Hubbard model, DMFT predict a too large value for the Hubbard interaction U, because it lacks non-local correlations that generally give a more insulating character to the system. However, even the simple second-order dual fermion describes the transition to a much higher level of accuracy, in rather good agreement with cluster DMFT calculations [252].

From a computational point of view, the development of the ladder dual fermion (LDF) set the current standard for dual calculations. This approximation is based on considering only a subclass of diagrams, as shown later in Chapter 5. This approximation is able to predict long range charge [253] as well as magnetic fluctuations [254]. In the same work, it was also argued that the LDF method fulfills the Mermin-Wagner theorem, that forbids the spontaneous breaking of continuous symmetries in dimensions lower than three [255], provided that the size of the lattice (or the corresponding number of k-points in momentum space) and the number of Matsubara frequencies is large enough. Furthermore, a LDF study of the cubic Hubbard model showed a phase boundary for the antiferromagnetic state appearing in the model in close agreement with exact quantum Monte Carlo calculations [256].

The same considerations hold true for its extension to the extended Hubbard model, the ladder dual boson methods, that were shown to predict a phase boundary for the CDW in very good agreement with cluster calculations [225–227]. The presence of a resonant antiferromagnetic mode in a model for cuprates was discussed in Ref [228].

Calculations beyond the ladder approximation with a larger subset of diagrams, known as parquet approximation, was applied to the low-energy description of magnetic and superconductive excitations in the Hubbard model, showing a phase diagram for parameters [257]. These results predict a superconductive ground state for the doped Hubbard model with next- and next-to-next-nearest-neighbor hopping t' and t'' with all the parameters set to those predicted for the BSSCO high-temperature superconductor. These results have been obtained under the approximation that a single Matsubara frequency is the only relevant contribution. Other attempts towards a parquet dual fermion methods were based on some assumption to simplify the form of the vertex functions [258, 259].

Going beyond the single-site impurity starting point is a challenging task, because these theories require the computation of the four-point vertex functions of the impurity problem and computationally expensive inversions of Bethe-Salpeter equations in frequency and orbital indices. some applications of dual theories beyond the single-orbital

and single-site Hubbard model were attempted. As an example, an early attempt in the direction of extending the DF method to multi-site systems was discussed in Ref. [260], when the LDF method was applied to the problem of quantum criticality in an honeycomb lattice. The second-order DF method was recently extended to the multi-band case, based on the well-established machinery of the TRIQS software library [261] in Ref. [237], where calculations based on a dimer reference system are reported. The viability of the DF method based on a cluster reference system was investigated in Refs. [262, 263]. Recently, this concept was used in Ref. [78] to show that superconductivity can be efficiently described at the level of an Hubbard plaquette.

We conclude by mentioning that, based on dual techniques, it was possible to derive effective Heisenberg model for spin densities and Ising models for charge densities, that not only allow one to calculate all possible exchange interactions, but also provide the full description of the dynamics of the system [264–266].

4.2 Multi-orbital dual boson action

4.2.1 Introducing the dual variables

We start with isolating the reference (impurity) problem from the initial lattice action (3.14). Here, we consider a very general impurity model with possibly many orbitals and many sites. Additionally, we consider also a bosonic hybridization function in addition to the fermionic hybridization discussed in the context of DMFT. The addition of the bosonic hybridization is necessary to treat non-local correlations, but can also be used to describe physical bosonic excitations of the system, such as phonons. The action for this general reference system

$$
\mathcal{S}_{\text{imp}} = -\sum_{\substack{\nu,\{l\}, \\ \sigma\sigma'}} c^*_{\nu\sigma l} \left[(i\nu + \mu)\delta_{\sigma\sigma'}\delta_{ll'} - \Delta^{\sigma\sigma'}_{\nu,ll'} \right] c_{\nu\sigma'l'} + \frac{1}{2}\sum_{\substack{q,\{k\}, \\ \{l\},\{\sigma\}}} U^{pp}_{l_1l_2l_3l_4} c^*_{k,\sigma,l_1} c^*_{q-k,\sigma',l_2} c_{q-k',\sigma',l_4} c_{k',\sigma,l_3}
$$
$$
+ \frac{1}{2}\sum_{\omega,\{l\},\varsigma} Y^{\varsigma}_{\omega,l_1l_2,l_3l_4} \rho^{\varsigma}_{-\omega,l_1l_2} \rho^{\varsigma}_{\omega,l_4l_3} + \sum_{\omega,\{l\},\vartheta} Y^{\vartheta}_{\omega,l_1l_2,l_3l_4} \rho^{*\vartheta}_{\omega,l_1l_2} \rho^{\vartheta}_{\omega,l_3l_4} \tag{4.1}
$$

contains momentum-independent parts of the lattice action (3.14). The fermionic $\Delta^{\sigma\sigma'}_{\nu,ll'}$ and bosonic $Y^r_{\omega,l_1l_2,l_3l_4}$ hybridization function enter the impurity problem of the (extended) DMFT [118, 162–165, 267]. In Eq. (4.1) these quantities are written in a general frequency ν (ω), band l, spin σ, and channel $r \in \{\varsigma, \vartheta\}$ dependent form. The explicit definition of these channels can be found in the discussion of Eq. (3.14). These hybridization functions are usually determined according to some self-consistency condition and their form depends on the choice of the reference system and on the initial problem. The composite

variables ρ^r_{ω,l_1l_2} coupled to the bosonic hybridization functions are defined in Eqs. (3.17)-(3.18), with the obvious difference that being local they do not carry a spatial momentum.

The remaining part of the lattice action reads

$$
\mathcal{S}_{\text{rem}} = \sum_{k,\{l\}} \sum_{\sigma\sigma'} c^*_{k\sigma l} \tilde{\varepsilon}^{\sigma\sigma'}_{k,ll'} c_{k\sigma'l'} + \frac{1}{2} \sum_{q,\{l\},\varsigma} \tilde{V}^{\varsigma}_{q,l_1l_2,l_3l_4} \rho^{\varsigma}_{-q,l_1l_2} \rho^{\varsigma}_{q,l_4l_3} + \sum_{q,\{l\},\vartheta} \tilde{V}^{\vartheta}_{q,l_1l_2,l_3l_4} \rho^{*\vartheta}_{q,l_1l_2} \rho^{\vartheta}_{q,l_3l_4}.
$$
(4.2)

Here, we defined the quantities $\tilde{\varepsilon}^{\sigma\sigma'}_{k,ll'} = \varepsilon^{\sigma\sigma'}_{\mathbf{k},ll'} - \Delta^{\sigma\sigma'}_{\nu,ll'}$ and $\tilde{V}^r_{q,l_1l_2,l_3l_4} = V^r_{q,l_1l_2,l_3l_4} - Y^r_{\omega,l_1l_2,l_3l_4}$, so that the relation

$$
\mathcal{S}_{\text{latt}} = \mathcal{S}_{\text{imp}} + \mathcal{S}_{\text{rem}}
$$
(4.3)

still holds true. At this point, we want to decouple the non-local terms in Eq. (4.2) and, in order to achieve this goal, we need to introduce new fermionic fields f, f^* and new bosonic fields φ^r. This is the first step of the famous dual boson transformation. The reason for decoupling the ρ^r_{q,l_1l_2} terms is to remove the quartic operators associate with these terms. The reason for decoupling the fermionic fields will become clear after few more steps. In order to achieve this goal, we perform the following exact path integral transformation, know as Hubbard-Stratonovich transformations, to the partition function of $\mathcal{S}_{\text{rem}}$

$$
\exp\left\{ -\sum_{k,\{l\}} \sum_{\sigma\sigma'} c^*_{k\sigma l} \tilde{\varepsilon}^{\sigma\sigma'}_{k,ll'} c_{k\sigma'l'} \right\} =
$$

$$
\mathcal{D}_f \int D[f^*, f] \exp\left\{ \sum_{k,\{l\}} \sum_{\sigma\sigma'} \left(f^*_{k\sigma l} \left[\tilde{\varepsilon}^{-1}_k \right]^{\sigma\sigma'}_{ll'} f_{k\sigma'l'} - f^*_{k\sigma l} c_{k\sigma l} - c^*_{k\sigma l} f_{k\sigma l} \right) \right\}
$$
(4.4)

$$
\exp\left\{ -\frac{1}{2} \sum_{q,\{l\},\varsigma} \rho^{\varsigma}_{-q,l_1l_2} \tilde{V}^{\varsigma}_{q,l_1l_2,l_3l_4} \rho^{\varsigma}_{q,l_4l_3} \right\} =
$$

$$
\mathcal{D}_\varphi \int D[\varphi^{\varsigma}] \exp\left\{ \sum_{q,\{l\},\varsigma} \left(\frac{1}{2} \varphi^{\varsigma}_{-q,l_1l_2} \left[(\tilde{V}^{\varsigma}_q)^{-1} \right]_{l_1l_2,l_3l_4} \varphi^{\varsigma}_{q,l_4l_3} - \varphi^{\varsigma}_{-q,l_1l_2} \rho^{\varsigma}_{q,l_2l_1} \right) \right\}
$$
(4.5)

$$
\exp\left\{ -\sum_{q,\{l\},\vartheta} \rho^{*\vartheta}_{q,l_1l_2} \tilde{V}^{\vartheta}_{q,l_1l_2,l_3l_4} \rho^{\vartheta}_{q,l_3l_4} \right\} =
$$

$$
\mathcal{D}_\varphi \int D[\varphi^{*\vartheta}, \varphi^{\vartheta}] \exp\left\{ \sum_{q,\{l\},\vartheta} \left(\varphi^{*\vartheta}_{q,l_1l_2} \left[(\tilde{V}^{\vartheta}_q)^{-1} \right]_{l_1l_2,l_3l_4} \varphi^{\vartheta}_{q,l_3l_4} - \varphi^{*\vartheta}_{q,l_1l_2} \rho^{\vartheta}_{q,l_1l_2} - \rho^{*\vartheta}_{q,l_1l_2} \varphi^{\vartheta}_{q,l_1l_2} \right) \right\}
$$
(4.6)

The terms $\mathcal{D}_f = -\det[\tilde{\varepsilon}_k]$ and $\mathcal{D}_\varphi^{-1} = -\sqrt{\det\left[\tilde{V}_q\right]}$ can be neglected, because they do not affect the calculation of expectation values. After these transformations the lattice action takes the following form

$$
\begin{aligned}
\mathcal{S}' = & -\sum_{k,\{l\}}\sum_{\sigma\sigma'} f^*_{k\sigma l}\left[\tilde{\varepsilon}_k^{-1}\right]_{ll'}^{\sigma\sigma'} f_{k\sigma'l'} + \sum_{k,\sigma,l}\left\{(f^*_{k\sigma l} + \eta^*_{k\sigma l})\,c_{k\sigma l} + c^*_{k\sigma l}\,(f_{k\sigma l} + \eta_{k\sigma l})\right\} + \mathcal{S}_{\text{imp}} \\
& -\sum_{q,\{l\},\vartheta}\left\{\varphi^{*\,\vartheta}_{q,l_1l_2}\left[(\tilde{V}_q^\vartheta)^{-1}\right]_{l_1l_2,l_3l_4}\varphi^\vartheta_{q,l_3l_4} - \left(\varphi^{*\,\vartheta}_{q,l_1l_2} + j^{*\,\vartheta}_{q,l_1l_2}\right)\rho^\vartheta_{q,l_1l_2} - \rho^{*\,\vartheta}_{q,l_1l_2}\left(\varphi^\vartheta_{q,l_1l_2} + j^\vartheta_{q,l_1l_2}\right)\right\} \\
& -\sum_{q,\{l\},\varsigma}\left\{\frac{1}{2}\varphi^\varsigma_{-q,l_1l_2}\left[(\tilde{V}_q^\varsigma)^{-1}\right]_{l_1l_2,l_3l_4}\varphi^{\varsigma'}_{q,l_4l_3} - \left(\varphi^\varsigma_{-q,l_1l_2} + j^\varsigma_{-q,l_1l_2}\right)\rho^\varsigma_{q,l_2l_1}\right\}
\end{aligned}
\tag{4.7}
$$

where we additionally introduced source fields $\eta^{(*)}$ and $j^{(*)}$ for fermionic $c^{(*)}$ and composite $\rho^{(*)}$ variables, respectively. These fields will be used to derive the connection between the dual and lattice quantities.

4.2.2 Integrating out the lattice operators

Now, we shift fermionic $f^{(*)} \to \hat{f}^{(*)} = f^{(*)} - \eta^{(*)}$ and bosonic $\varphi^{(*)} \to \hat{\varphi}^{(*)} = \varphi^{(*)} - j^{(*)}$ variables to decouple the source fields from original Grassmann variables $c^{(*)}$. After that the lattice action becomes

$$
\begin{aligned}
\mathcal{S}' = & -\sum_{k,\{l\}}\sum_{\sigma\sigma'} \hat{f}^*_{k\sigma l}\left[\tilde{\varepsilon}_k^{-1}\right]_{ll'}^{\sigma\sigma'} \hat{f}_{k\sigma'l'} + \sum_{k,\sigma,l}(f^*_{k\sigma l}c_{k\sigma l} + c^*_{k\sigma l}f_{k\sigma l}) \\
& + \sum_{q,\{l\},r}\left(\varphi^\varsigma_{-q,l_1l_2}\rho^\varsigma_{q,l_2l_1} + \varphi^{*\,\vartheta}_{q,l_1l_2}\rho^\vartheta_{q,l_1l_2} + \rho^{*\,\vartheta}_{q,l_1l_2}\varphi^\vartheta_{q,l_1l_2}\right) + \mathcal{S}_{\text{imp}} \\
& -\frac{1}{2}\sum_{q,\{l\},\varsigma}\hat{\varphi}^\varsigma_{-q,l_1l_2}\left[(\tilde{V}_q^\varsigma)^{-1}\right]_{l_1l_2,l_3l_4}\hat{\varphi}^\varsigma_{q,l_4l_3} - \sum_{q,\{l\},\vartheta}\hat{\varphi}^{*\,\vartheta}_{q,l_1l_2}\left[(\tilde{V}_q^\vartheta)^{-1}\right]_{l_1l_2,l_3l_4}\hat{\varphi}^\vartheta_{q,l_3l_4}
\end{aligned}
\tag{4.8}
$$

At this step, we notice that all the operators corresponding to lattice fermions are coupled only locally and they are connected non-locally only through the dual variables. For this reason, we can integrate out the reference problem $\mathcal{S}_{\text{imp}}$ by explicitly taking the path integral over fermionic $c^{(*)}$ variables. For a matter of convenience, we additionally rescale the fermionic $f^{(*)}$ and bosonic $\varphi^{(*)}$ fields by the arbitrary parameters B_ν^{-1} and α_ω^{-1}, respectively. These parameters could have been introduced in Eqs. (4.4)- (4.5) and (4.6) directly in the definition of the HS transformation but were omitted to keep a light-weight notation. They

can be fixed depending on convenience and are useful in practical implementations.

$$\int D[c^*, c] \exp\left\{ -S_{\text{imp}} - \sum_{k,ll',\sigma\sigma'} \left(f^*_{k\sigma l} \left[B^{-1}_\nu \right]^{\sigma\sigma'}_{ll'} c_{k\sigma'l'} + c^*_{k\sigma l} \left[B^{-1}_\nu \right]^{\sigma\sigma'}_{ll'} f_{k\sigma'l'} \right) \right.$$

$$\left. - \sum_{q,\{l\},\{r\}} \left(\varphi^{\varsigma}_{-q,l_1 l_2} [\alpha^{-1}_\omega]^{\varsigma\varsigma'}_{l_1 l_2, l_3 l_4} \rho^{\varsigma'}_{q,l_4 l_3} + \varphi^{*\vartheta}_{q,l_1 l_2} [\alpha^{-1}_\omega]^{\vartheta\vartheta'}_{l_1 l_2, l_3 l_4} \rho^{\vartheta'}_{q,l_3 l_4} + \rho^{*\vartheta}_{q,l_1 l_2} [\alpha^{-1}_\omega]^{\vartheta\vartheta'}_{l_1 l_2, l_3 l_4} \varphi^{\vartheta'}_{q,l_3 l_4} \right) \right\} =$$

$$Z_{\text{imp}} \exp\left\{ - \sum_{k,\{l\},\{\sigma\}} f^*_{k\sigma_1 l_1} \left[B^{-1}_\nu \right]^{\sigma_1\sigma_2}_{l_1 l_2} g^{\sigma_2\sigma_3}_{\nu,l_2 l_3} \left[B^{-1}_\nu \right]^{\sigma_3\sigma_4}_{l_3 l_4} f_{k\sigma_4 l_4} \right.$$

$$- \frac{1}{2} \sum_{q,\{l\},\{\varsigma\}} \varphi^{\varsigma_1}_{-q,l_1 l_2} [\alpha^{-1}_\omega]^{\varsigma_1\varsigma_2}_{l_1 l_2, l'_1 l'_2} \chi^{\varsigma_2\varsigma_3}_{\omega,l'_1 l'_2, l'_3 l'_4} [\alpha^{-1}_\omega]^{\varsigma_3\varsigma_4}_{l'_3 l'_4, l_3 l_4} \varphi^{\varsigma_4}_{l_4 l_3}$$

$$\left. - \sum_{q,\{l\},\{\vartheta\}} \varphi^{*\vartheta_1}_{q,l_1 l_2} [\alpha^{-1}_\omega]^{\vartheta_1\vartheta_2}_{l_1 l_2, l'_1 l'_2} \chi^{\vartheta_2\vartheta_3}_{\omega,l'_1 l'_2, l'_3 l'_4} [\alpha^{-1}_\omega]^{\vartheta_3\vartheta_4}_{l'_3 l'_4, l_3 l_4} \varphi^{\vartheta_4}_{q,l_3 l_4} - \tilde{\mathcal{F}}[f,\varphi] \right\} \tag{4.9}$$

Z_{imp}, $g^{\sigma\sigma'}_{\nu,ll'}$ and $\chi^{rr'}_{\omega,l_1 l_2, l_3 l_4}$ are respectively the partition function, the Green's function, and the susceptibility of the reference (impurity) problem. Following the rescaling, the fields $\hat{\varphi}^{(*)}$ are redefined as $\hat{\varphi}^{(*)} = \varphi^{(*)}\alpha^{-1} - j^{(*)}$.

4.2.3   The dual boson action

After integrating out the reference system S_{imp}, the action contains only the dual degrees of freedom and takes the form of the dual boson problem

$$\tilde{S} = - \sum_{\{l'\},\{\sigma'\}} \hat{f}^*_{k\sigma_1 l_1} B^{\sigma_1\sigma'_1}_{\nu,l_1 l'_1} \left[\left((\varepsilon_{\mathbf{k}} - \Delta_\nu)^{-1} - g_\nu \right)^{-1} \right]^{\sigma'_1\sigma'_2}_{l'_1 l'_2} B^{\sigma'_2\sigma_2}_{\nu,l'_2 l_2} \hat{f}_{k\sigma_2 l_2} + \tilde{\mathcal{F}}[f,\varphi]$$

$$- \frac{1}{2} \sum_{q,\{l\},\{\varsigma\}} \left\{ \hat{\varphi}^{\varsigma}_{-q,l_1 l_2} \left[\left(\tilde{V}^{\varsigma}_q \right)^{-1} \right]_{l_1 l_2, l_3 l_4} \hat{\varphi}^{\varsigma}_{q,l_4 l_3} - \varphi^{\varsigma_1}_{-q,l_1 l_2} [\alpha^{-1}_\omega]^{\varsigma_1\varsigma_2}_{l_1 l_2, l'_1 l'_2} \chi^{\varsigma_2\varsigma_3}_{q,l'_1 l'_2, l'_3 l'_4} [\alpha^{-1}_\omega]^{\varsigma_3\varsigma_4}_{l'_3 l'_4, l_3 l_4} \varphi^{\varsigma_4}_{q,l_4 l_3} \right\}$$

$$- \sum_{q,\{l\},\{\vartheta\}} \left\{ \hat{\varphi}^{*\vartheta}_{q,l_1 l_2} \left[\left(\tilde{V}^{\vartheta}_q \right)^{-1} \right]_{l_1 l_2, l_3 l_4} \hat{\varphi}^{\vartheta}_{q,l_3 l_4} - \varphi^{*\vartheta_1}_{q,l_1 l_2} [\alpha^{-1}_\omega]^{\vartheta_1\vartheta_2}_{l_1 l_2, l'_1 l'_2} \chi^{\vartheta_2\vartheta_3}_{\omega,l'_1 l'_2, l'_3 l'_4} [\alpha^{-1}_\omega]^{\vartheta_3\vartheta_4}_{l'_3 l'_4, l_3 l_4} \varphi^{\vartheta_4}_{q,l_3 l_4} \right\}. \tag{4.10}$$

where the dual interaction $\tilde{\mathcal{F}}$ collects all the non-quadratic terms in the dual fields. The quadratic terms describe the bare propagators of the dual particles. In particular, the dual

Dual fermionic Green's function   Dual bosonic propagator
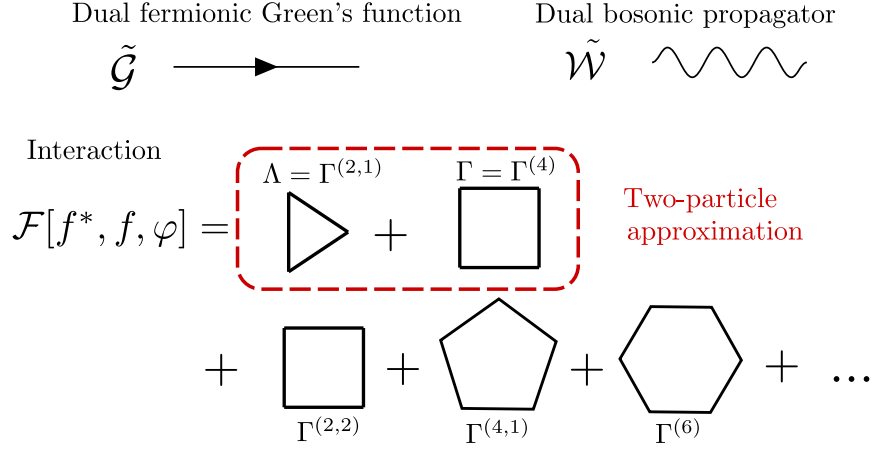

FIGURE 4.2: Diagrammatic representation of the terms in the dual boson action (4.10). In particular, the fermionic Green's function of Eq. (4.11) is indicated by a straight line, while the bosonic propagator in Eq. (4.12) is represented by a wiggly line. The first few terms contributing to $\mathcal{F}[f, f^*, \varphi]$ are also shown.

fermions $f^{(*)}$ are described by the bare dual fermionic Green's function that has the following form

$$\tilde{\mathcal{G}}^{\sigma_1\sigma_2}_{k,\,l_1l_2} = \sum_{\{l'\},\{\sigma'\}} B^{\sigma_1\sigma'_1}_{\nu,\,l_1l'_1} \left[\left((\varepsilon_{\mathbf{k}} - \Delta_\nu)^{-1} - g_\nu \right)^{-1} \right]^{\sigma'_1\sigma'_2}_{l'_1l'_2} B^{\sigma'_2\sigma_2}_{\nu,\,l'_2l_2}. \tag{4.11}$$

On the other hand, the propagation of the dual bosons $\phi^{(*)}$, described by the dual bosonic propagator

$$\bar{W}^{r_1r_2}_{q,\,l_1l_2,\,l_3l_4} = \sum_{\{r'\},\{l'\}} \alpha^{r_1r'_1}_{\omega,\,l_1l_2,\,l'_1l'_2} \left[\left(\tilde{V}^{-1}_q - \chi_\omega \right)^{-1} \right]^{r'_1r'_2}_{l'_1l'_2,\,l'_3l'_4} \alpha^{r'_2r_2}_{\omega,\,l'_3l'_4,\,l_3l_4}. \tag{4.12}$$

Since the impurity problem is not Gaussian, the dual interaction $\tilde{\mathcal{F}}$ contains an infinite series of terms, that can be written as

$$\tilde{\mathcal{F}}[f,\varphi] = \sum_{\{k\},\{l\},\{\sigma\}} \sum_{n=2}^{+\infty} \frac{(-1)^n}{n!} \left[\Gamma^{(2n)}_{\nu_1...\nu_{2n}} \right]^{\sigma_1\sigma'_1...\sigma_n\sigma'_n}_{l_1l'_1...l_nl'_n} f^*_{k_1\sigma_1l_1} f_{k'_1\sigma'_1l'_1} \cdots f^*_{k_1\sigma_1l_1} f_{k'_n\sigma'_nl'_n}$$

$$+ \sum_{\substack{\{k\},\{l\},\{\sigma\} \\ \{q\},\{L\},\{\varsigma\}}} \sum_{n,m=1}^{+\infty} \frac{(-1)^n}{n!m!} \left[\Gamma^{(2n,m)}_{\nu_1...\nu_{2n};\omega_1...\omega_m} \right]^{\sigma_1\sigma'_1...\sigma_n\sigma'_n;\varsigma_1...\varsigma_m}_{l_1l'_1...l_nl'_n;L_1L'_1...L_mL'_m} f^*_{k_1\sigma_1l_1} f_{k'_1\sigma'_1l'_1} \cdots f^*_{k_1\sigma_1l_1} f_{k'_n\sigma'_nl'_n} \varphi^{\varsigma_1}_{q_1,L_1L'_1} \cdots \varphi^{\varsigma_m}_{q_m,L_mL'_m}$$

$$\tag{4.13}$$

where $\Gamma^{(2n)}$ is the connected $2n$-point (or $n-$particle) impurity vertex, while $\Gamma^{(2n,m)}$ is the $(2n+m)$-point (or $n-$fermion-$m-$boson) impurity vertex. The expression for these vertices are connected to the correlation functions of the impurity problem as

$$
\left[\Gamma^{(2n,m)}_{\nu_1...\nu_{2n};\omega_1...\omega_m}\right]^{\sigma_1...\sigma_{2n};\varsigma_1...\varsigma_{2m}}_{l_1...l_{2n};L_1...L_{2m}} =
$$

$$
\sum_{\{\overline{\sigma}\},\{\overline{l}\},\{\overline{\varsigma}\}} \left\langle c_{\nu_1\overline{\sigma}_1\overline{l}_1}c^*_{\nu_2,\overline{\sigma}_2\overline{l}_2}...c_{\nu_{2n-1}\overline{\sigma}_{2n-1}\overline{l}_{2n-1}}c^*_{\nu_{2n},\overline{\sigma}_{2n}\overline{l}_{2n}}\rho^{\overline{\varsigma}_1}_{\omega_1,\overline{L_1L_2}}...\rho^{\overline{\varsigma}_m}_{\omega_m,\overline{L_{2m-1}L_{2m}}}\right\rangle_{\mathrm{connected}}
$$

$$
\times \left[B^{-1}_{\nu_1}\right]^{\overline{\sigma}_1\sigma_1}_{\overline{l}_1 l_1}...\left[B^{-1}_{\nu_{2n}}\right]^{\overline{\sigma}_{2n}\sigma_{2n}}_{\overline{l}_{2n}l_{2n}}\left[\alpha^{-1}_{\omega_1}\right]^{\overline{\varsigma}_1\varsigma_1}_{\overline{L_1L_1'}L_1L_2}...\left[\alpha^{-1}_{\omega_m}\right]^{\overline{\varsigma}_{2m-1}\varsigma_{2m}}_{\overline{L_{2m}L_{2m-1}}L_{2m-1}L_{2m}}. \tag{4.14}
$$

The expressions for the vertices with only external fermionic lines are given by the same formula with $\Gamma^{(2n)} = \Gamma^{(2n,m=0)}$. Indeed, the only reason to separate them is to distinguish between purely fermionic interactions and interaction terms involving external bosons. The latter are absent in the dual fermion theory. Due to energy conservation, the sum of the frequencies of the vertex has to be 0, reducing the number of free external frequencies by one. In principle, all these correlation functions can be computed using suitable impurity solvers. However, due to the increasing number of external legs, the number of external parameters to be sampled increases fast with the number of legs, making the sample of high-order correlations functions unpractical. Additionally, the diagrammatic structure of the theory becomes more complicated, when higher-order diagrams are included.

4.2.4 The dual boson action in the two-particle approximation

The calculation of the impurity correlation functions beyond the first few vertices with $n > 2$ and $m > 1$ is numerically challenging and was rarely attempted [222, 268]. For this reason, the standard approximation considers only the four-point fermionic vertex and three-point vertex coupling two fermions with one boson [269]. The validity of this approximation for many models and in several ranges of parameters is confirmed by benchmarks with methods that do not rely on the dual transformation [220, 221, 263]. Following this standard approximation used in most of the works based on dual theories, the interaction part of the action $\widetilde{\mathcal{F}}[f,\varphi]$ is truncated at the level of the two-particle correlations
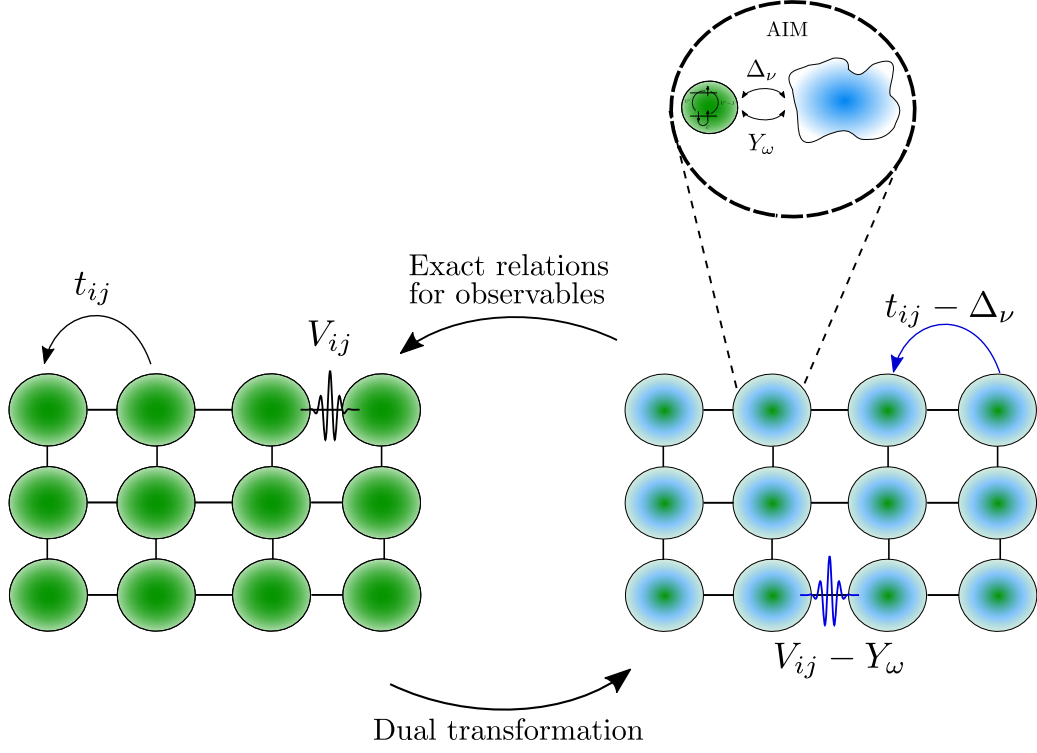
FIGURE 4.3: Representation of the effect of the dual transformation on the lattice. The original lattice problem is transformed into a lattice of impurities, solved exactly. The original hopping t_{ij} and non-local interaction V_{ij} between sites on the original lattice is replace by hopping of dual fermions and bosons between impurities with renormalized hopping terms, as highlighted in the figure. In turn, the particles can interact with each other through the various interaction terms contained in $\tilde{\mathcal{F}}[f, \varphi]$.

functions and reads

$$\tilde{\mathcal{F}}[f, \varphi] \simeq \sum_{q, \{k\}} \sum_{\{\nu\}, \{l\}} \sum_{\{\sigma\}, \varsigma/\vartheta} \times$$

$$\times \left\{ \frac{1}{4} \left[\Gamma_{\nu\nu'\omega} \right]^{\sigma_1\sigma_2\sigma_3\sigma_4}_{l_1 l_2 l_3 l_4} f^*_{k\sigma_1 l_1} f_{k+q, \sigma_2 l_2} f^*_{k'+q, \sigma_4 l_4} f_{k'\sigma_3 l_3} + \Lambda^{\sigma\sigma'\varsigma}_{\nu\omega, l_1, l_2, l_3 l_4} f^*_{k\sigma l_1} f_{k+q, \sigma', l_2} \varphi^\varsigma_{q, l_4 l_3} \right.$$

$$\left. + \frac{1}{2} \left(\Lambda^{\sigma\sigma'\vartheta}_{\nu\omega, l_1, l_2, l_3 l_4} f^*_{k\sigma l_1} f^*_{q-k, \sigma', l_2} \varphi^\vartheta_{q, l_3 l_4} + \Lambda^{*\sigma\sigma'\vartheta}_{\nu\omega, l_1, l_2, l_3 l_4} \varphi^{*\vartheta}_{q, l_3 l_4} f_{q-k, \sigma', l_2} f_{k\sigma l_1} \right) \right\} \qquad (4.15)$$

Here, $\Gamma = \Gamma^{(4)}$ is the four-point (fermion-fermion) vertex function, which is related to the exact correlation function of the reference problem. Using

$$[\Gamma_{\nu\nu'\omega}]^{\sigma_1\sigma_2\sigma_3\sigma_4}_{l_1l_2l_3l_4} = \sum_{\{l'\},\{\sigma'\}} \left\langle c_{\nu\sigma'_1l'_1} c^*_{\nu+\omega,\sigma'_2l'_2} c^*_{\nu'\sigma'_3l'_3} c_{\nu'+\omega,\sigma'_4l'_4} \right\rangle_{\text{connected}} \times$$

$$\times \left[B^{-1}_\nu\right]^{\sigma'_1\sigma_1}_{l'_1l_1} \left[B^{-1}_{\nu+\omega}\right]^{\sigma'_2\sigma_2}_{l'_2l_2} \left[B^{-1}_{\nu'}\right]^{\sigma'_3\sigma_3}_{l'_3l_3} \left[B^{-1}_{\nu'+\omega}\right]^{\sigma'_4\sigma_4}_{l'_4l_4} . \qquad (4.16)$$

The three-point (fermion-boson) vertex functions $\Lambda = \Gamma^{(2,1)}$ have the following form

$$\Lambda^{\sigma_1\sigma_2\varsigma}_{\nu\omega,l_1,l_2,l_3l_4} = \sum_{\{\sigma'\},\{l'\},\varsigma'} \left\langle c_{\nu\sigma'_1l'_1} c^*_{\nu+\omega,\sigma'_2l'_2} \rho^{\varsigma'}_{-\omega,l'_3l'_4} \right\rangle \left[B^{-1}_\nu\right]^{\sigma'_1\sigma_1}_{l'_1l_1} \left[B^{-1}_{\nu+\omega}\right]^{\sigma'_2\sigma_2}_{l'_2l_2} \left[\alpha^{-1}_\omega\right]^{\varsigma'\varsigma}_{l'_3l'_4l_3l_4} \qquad (4.17)$$

$$\Lambda^{\sigma_1\sigma_2\vartheta}_{\nu\omega,l_1,l_2,l_3l_4} = \sum_{\{\sigma'\},\{l'\},\vartheta'} \left\langle c_{\nu\sigma'_1l'_1} c_{\omega-\nu,\sigma'_2l'_2} \rho^{*\vartheta'}_{\omega,l'_3l'_4} \right\rangle \left[B^{-1}_\nu\right]^{\sigma'_1\sigma_1}_{l'_1l_1} \left[B^{-1}_{\omega-\nu}\right]^{\sigma'_2\sigma_2}_{l'_2l_2} \left[\alpha^{-1}_\omega\right]^{\vartheta'\vartheta}_{l'_3l'_4l_3l_4} \qquad (4.18)$$

$$\Lambda^{*\sigma_1\sigma_2\vartheta}_{\nu\omega,l_1,l_2,l_3l_4} = \sum_{\{\sigma'\},\{l'\},\vartheta'} \left\langle \rho^{\vartheta'}_{\omega,l'_3l'_4} c^*_{\omega-\nu,\sigma'_2l'_2} c^*_{\nu\sigma'_1l'_1} \right\rangle \left[B^{-1}_\nu\right]^{\sigma'_1\sigma_1}_{l'_1l_1} \left[B^{-1}_{\omega-\nu}\right]^{\sigma'_2\sigma_2}_{l'_2l_2} \left[\alpha^{-1}_\omega\right]^{\vartheta'\vartheta}_{l'_3l'_4l_3l_4} \qquad (4.19)$$

If the scaling parameters are chosen as $B^{\sigma\sigma'}_{\nu,ll'} = g^{\sigma\sigma'}_{\nu,ll'}$ and

$$\alpha^{rr'}_{\omega,l_1l_2,l'_1l'_2} = \delta_{l_1,l'_1}\delta_{l_2,l'_2}\delta_{rr'} + \sum_{l_3,l_4} \tilde{U}^r_{\omega,l_1l_2,l_3l_4} \chi^{rr'}_{\omega,l_3l_4,l'_1l'_2} \qquad (4.20)$$

where $\tilde{U}^r_{\omega,l_1l_2,l_3l_4} = U^r_{l_1l_2,l_3l_4} + Y^r_{\omega,l_1l_2,l_3l_4}$ is the bare interaction of the reference system and U^r is defined in Eqs. (4.53)–(4.56), then $\Lambda^{\sigma\sigma'r}_{\nu\omega}$ takes the usual form of the three-point vertex of the reference system [18, 227, 230–232, 269]. This rescaling is used in Chapter 5. However, in this case the vertex functions contain the inverse of the impurity Green's function $g^{\sigma\sigma'}_{\nu,ll'}$, that has to be determined numerically, usually by means of CT-QMC methods. If this is the case, then a big numerical noise can appear at large frequencies at large frequencies. At the same time, inverting $\alpha^{rr'}_\omega$ does not lead to the numerical noise due to the presence of a delta-function term in Eq. (4.20). For this reason in the implementation of the D-TRILEX method, we keep $\alpha^{rr'}_\omega$ in the form of Eq. (4.20) and set $B^{\sigma\sigma'}_{\nu,ll'} = \delta_{\sigma\sigma'}\delta_{ll'}$ to avoid divisions by noisy impurity quantities. The calculation of the vertex functions from common impurity solvers is discussed in Sec. 4.6.

4.3 Partially bosonized theory in the multi-orbital framework

4.3.1 The partially bosonized approximation for the four-fermion vertex

In this section, we aim at deriving a simplified version of the dual boson action of Eq. (4.10) with interaction truncated at the two-particle level (4.15), by removing the four-point vertex from the theory. This has important computational consequences, because vertex (4.16) is rather numerically expensive to compute, especially in a multi-orbital case. Additionally, this is the first step to derive the D-TRILEX theory discussed in later chapters. The reader not interested in the details of this derivation can directly skip the next subsections and go to Sec. 4.3.5.

This approximation allows us to eliminate the four-point vertex from the theory by introducing arbitrary counter terms $\bar{w}$ in the lattice action according to Eq. (4.40) that should approximately cancel the four-point vertex. First, we rewrite the interaction of the reference system (4.1) in the particle-hole representation

$$
\frac{1}{2} \sum_{\omega,\{\nu\}} \sum_{\{l\},\{\sigma\}} U^{pp}_{l_1 l_2 l_3 l_4} c^*_{\nu\sigma l_1} c^*_{\omega-\nu,\sigma' l_2} c_{\omega-\nu',\sigma' l_4} c_{\nu'\sigma l_3} =
$$

$$
\frac{1}{2} \sum_{\omega,\{\nu\}} \sum_{\{l\},\{\sigma\}} U^{pp}_{l_1 l_2 l_3 l_4} c^*_{\nu\sigma l_1} c_{\nu'\sigma l_3} c^*_{\omega-\nu,\sigma' l_2} c_{\omega-\nu',\sigma' l_4} - \frac{1}{2} \sum_{\nu,\{l\},\sigma} U^{pp}_{l_1 l_2 l_3 l_4} c^*_{\nu\sigma l_1} c_{\nu\sigma l_4} \delta_{l_2 l_3} =
$$

$$
\frac{1}{2} \sum_{\omega,\{\nu\}} \sum_{\{l\},\{\sigma\}} U^{ph}_{l_1 l_2 l_3 l_4} c^*_{\nu\sigma l_1} c_{\nu+\omega,\sigma l_2} c^*_{\nu'+\omega,\sigma' l_4} c_{\nu'\sigma' l_3} - \frac{1}{2} \sum_{\nu,\{l\},\sigma} U^{pp}_{l_1 l_2 l_3 l_4} c^*_{\nu\sigma l_1} c_{\nu\sigma l_4} \delta_{l_2 l_3} \quad (4.21)
$$

which results in the following relation $U^{ph}_{l_1 l_2 l_3 l_4} = U^{pp}_{l_1 l_4 l_2 l_3}$. Now, let us antisymmetrize the interaction as (quadratic terms in Grassmann $c^{(*)}$ variables are neglected for simplicity)

$$
\frac{1}{2} \sum_{\omega,\{\nu\}} \sum_{\{l\},\{\sigma\}} U^{ph}_{l_1 l_2 l_3 l_4} c^*_{\nu\sigma l_1} c_{\nu+\omega,\sigma l_2} c^*_{\nu'+\omega,\sigma' l_4} c_{\nu'\sigma' l_3} =
$$

$$
\frac{1}{8} \sum_{\omega,\{\nu\}} \sum_{\{l\},\{\sigma\}} \Gamma^{0\,d}_{l_1 l_2 l_3 l_4} \left(c^*_{\nu\sigma l_1} c_{\nu+\omega,\sigma l_2} \right) \left(c^*_{\nu'+\omega,\sigma',l_4} c_{\nu',\sigma',l_3} \right) +
$$

$$
\frac{1}{8} \sum_{\omega,\{\nu\}} \sum_{\{l\},\{\sigma\}} \Gamma^{0\,m}_{l_1 l_2 l_3 l_4} \left(c^*_{\nu\sigma_1 l_1} \vec{\sigma}_{\sigma_1\sigma_2} c_{\nu+\omega,\sigma_2 l_2} \right) \left(c^*_{\nu'+\omega,\sigma_4 l_4} \vec{\sigma}_{\sigma_4\sigma_3} c_{\nu'\sigma_3 l_3} \right) \quad (4.22)
$$

in order to obtain the expressions for the bare four-point vertex functions of the reference system in the particle-hole channel

$$\Gamma^{0\,d}_{l_1l_2l_3l_4} = 2U^{ph}_{l_1l_2l_3l_4} - U^{ph}_{l_1l_3l_2l_4} = 2U^{pp}_{l_1l_4l_3l_2} - U^{pp}_{l_1l_3l_2l_4}\,, \qquad \Gamma^{0\,m}_{l_1l_2l_3l_4} = -U^{ph}_{l_1l_3l_2l_4} = -U^{pp}_{l_1l_4l_3l_2} \quad (4.23)$$

Alternatively, the interaction can also be antisymmetrized in the particle-particle channel

$$\frac{1}{2}\sum_{\omega,\{v\}}\sum_{\{l\},\{\sigma\}} U^{ph}_{l_1l_2l_3l_4} c^*_{v\sigma l_1} c_{v+\omega,\sigma l_2} c^*_{v'+\omega,\sigma'l_4} c_{v'\sigma'l_3} =$$

$$\frac{1}{4}\sum_{\omega,\{v\},\{l\}} \Gamma^{0\,s}_{l_1l_2l_3l_4} \left(c^*_{v\uparrow l_1} c^*_{\omega-v\downarrow l_2} - c^*_{v\downarrow l_1} c^*_{\omega-v,\uparrow l_2}\right)\left(c_{\omega-v',\downarrow l_4} c_{v'\uparrow l_3} - c_{\omega-v',\uparrow l_4} c_{v'\downarrow l_3}\right) +$$

$$\frac{1}{4}\sum_{\omega,\{v\},\{l\}} \Gamma^{0\,t}_{l_1l_2l_3l_4} \left(c^*_{v\uparrow l_1} c^*_{\omega-v,\downarrow l_2} + c^*_{v\downarrow l_1} c^*_{\omega-v,\uparrow l_2}\right)\left(c_{\omega-v',\downarrow l_4} c_{v'\uparrow l_3} + c_{\omega-v',\uparrow l_4} c_{v'\downarrow l_3}\right) +$$

$$\frac{1}{2}\sum_{\omega,\{v\},\{l\}} \Gamma^{0\,t}_{l_1l_2l_3l_4} \left\{\left(c^*_{v\uparrow l_1} c^*_{\omega-v,\uparrow l_2}\right)\left(c_{\omega-v',\uparrow l_4} c_{v'\uparrow l_3}\right) + \left(c^*_{v\downarrow l_1} c^*_{\omega-v,\downarrow l_2}\right)\left(c_{\omega-v',\downarrow l_4} c_{v'\downarrow l_3}\right)\right\} \qquad (4.24)$$

which gives the corresponding bare vertex functions

$$\Gamma^{0\,s}_{l_1l_2l_3l_4} = \frac{1}{2}\left(U^{ph}_{l_1l_3l_4l_2} + U^{ph}_{l_1l_4l_3l_2}\right) = \frac{1}{2}\left(U^{pp}_{l_1l_2l_3l_4} + U^{pp}_{l_1l_2l_4l_3}\right) \qquad (4.25)$$

$$\Gamma^{0\,t}_{l_1l_3l_4l_2} = \frac{1}{2}\left(U^{ph}_{l_1l_3l_4l_2} - U^{ph}_{l_1l_4l_3l_2}\right) = \frac{1}{2}\left(U^{pp}_{l_1l_2l_3l_4} - U^{pp}_{l_1l_2l_4l_3}\right) \qquad (4.26)$$

Note that the obtained expressions (4.23), (4.25) and (4.26) coincide with the standard definition for the vertex functions in FLEX approach (see e.g. Ref. [130]).

One can also formally rewrite the interaction of the reference system (4.1) in the channel representation as

$$\frac{1}{2}\sum_{\omega,\{v\}}\sum_{\{l\},\{\sigma\}} U^{ph}_{l_1l_2l_3l_4} c^*_{v\sigma l_1} c_{v+\omega,\sigma l_2} c^*_{v'+\omega,\sigma'l_4} c_{v'\sigma'l_3} +$$

$$\frac{1}{2}\sum_{\omega,\{l\},\varsigma} Y^{\varsigma}_{\omega,\,l_1l_2,\,l_3l_4}\, \rho^{\varsigma}_{-\omega,\,l_1l_2}\, \rho^{\varsigma}_{\omega,\,l_4l_3} + \sum_{\omega,\{l\},\vartheta} Y^{\vartheta}_{\omega,\,l_1l_2,\,l_3l_4}\, \rho^{*\,\vartheta}_{\omega,\,l_1l_2}\, \rho^{\vartheta}_{\omega,\,l_3l_4} =$$

$$\frac{1}{2}\sum_{\omega,\{l\},\varsigma} \tilde{U}^{\varsigma}_{\omega,\,l_1l_2,\,l_3l_4}\rho^{\varsigma}_{-\omega,\,l_1l_2}\, \rho^{\varsigma}_{\omega,\,l_4l_3} + \sum_{q,\{l\},\vartheta} \tilde{U}^{\vartheta}_{\omega,\,l_1l_2,\,l_3l_4}\rho^{*\,\vartheta}_{q,\,l_1l_2}\, \rho^{\vartheta}_{q,\,l_3l_4} \qquad (4.27)$$

In order to determine the bare interaction $\tilde{U}^r_{\omega,\,l_1l_2,\,l_3l_4} = U^r_{l_1l_2,\,l_3l_4} + Y^r_{\omega,\,l_1l_2,\,l_3l_4}$ of the reference system for every r channel, we antisymmetrize the expression (4.27). Following
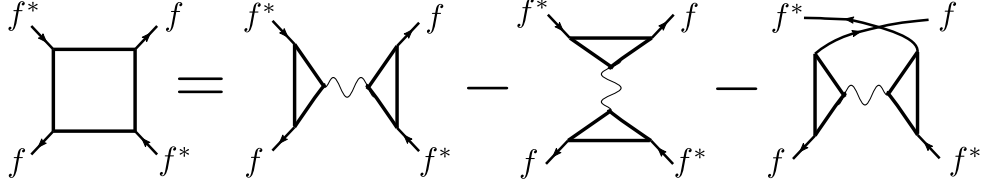
FIGURE 4.4: Diagrammatic representation of the partially bosonized approximation of the four-fermion vertex corresponding to Eq. (4.34). Coefficients and channel indices are omitted for clarity. The pictorial representation explains the distinction between the horizontal contributions $\left[M_{\nu\nu'\omega}^{\varsigma\varsigma'}\right]_{l_1l_2l_3l_4}^{\sigma_1\sigma_2\sigma_3\sigma_4}$, the vertical contributions $\left[M_{\nu,\nu+\omega,\nu'-\nu}^{\varsigma\varsigma'}\right]_{l_1l_3l_2l_4}^{\sigma_1\sigma_3\sigma_2\sigma_4}$ and the particle-particle contributions $\left[M_{\nu,\nu',\omega+\nu+\nu'}^{\vartheta\vartheta'}\right]_{l_1l_4l_3l_2}^{\sigma_1\sigma_4\sigma_3\sigma_2}$. Fermionic legs are attached to the vertices for clarity.

the works [231, 232], the bare four-point vertex functions (4.23) take the following form

$$\left[\Gamma_{\nu\nu'\omega}^{0\,d}\right]_{l_1l_2l_3l_4} = 2\tilde{U}_{\omega,l_1l_2,l_3l_4}^{d} - \tilde{U}_{\nu'-\nu,l_1l_3,l_2l_4}^{d} - 3\tilde{U}_{\nu'-\nu,l_1l_3,l_2l_4}^{m} + \tilde{U}_{\omega+\nu+\nu',l_1l_4,l_3l_2}^{s} - 3\tilde{U}_{\omega+\nu+\nu',l_1l_4,l_3l_2}^{t}$$
$$= 2U_{l_1l_2l_3l_4}^{ph} - U_{l_1l_3l_2l_4}^{ph} + o\,(Y) \tag{4.28}$$

$$\left[\Gamma_{\nu\nu'\omega}^{0\,m}\right]_{l_1l_2l_3l_4} = 2\tilde{U}_{\omega,l_1l_2,l_3l_4}^{m} + \tilde{U}_{\nu'-\nu,l_1l_3,l_2l_4}^{m} - \tilde{U}_{\nu'-\nu,l_1l_3,l_2l_4}^{d} - \tilde{U}_{\omega+\nu+\nu',l_1l_4,l_3l_2}^{s} - \tilde{U}_{\omega+\nu+\nu',l_1l_4,l_3l_2}^{t}$$
$$= -U_{l_1l_3l_2l_4}^{ph} + o\,(Y) \tag{4.29}$$

Using the idea of Ref. [231] we associate the static parts U^{ph} of the vertex functions (4.28) and (4.29) with the longitudinal contributions $\tilde{U}_\omega^\varsigma$. After doing that, we immediately get

$$U_{l_1l_2,l_3l_4}^{d} = \frac{1}{2}\left(2U_{l_1l_2l_3l_4}^{ph} - U_{l_1l_3l_2l_4}^{ph}\right) = \frac{1}{2}\left(2U_{l_1l_4l_2l_3}^{pp} - U_{l_1l_4l_3l_2}^{pp}\right) \tag{4.30}$$

$$U_{l_1l_2,l_3l_4}^{m} = -\frac{1}{2}U_{l_1l_3l_2l_4}^{ph} = -\frac{1}{2}U_{l_1l_4l_3l_2}^{pp} \tag{4.31}$$

The same procedure can be performed for the particle-particle channel. Since the variables $\rho_\omega^{(*)\,\vartheta}$ are already defined in the antisymmetrized form (3.18), the bare interaction in the particle-particle channel simply coincides with the bare vertex defined in Eqs. (4.25) and (4.25)

$$U_{l_1l_2,l_3l_4}^{s} = \frac{1}{2}\left(U_{l_1l_3l_4l_2}^{ph} + U_{l_1l_4l_3l_2}^{ph}\right) = \frac{1}{2}\left(U_{l_1l_2l_3l_4}^{pp} + U_{l_1l_2l_4l_3}^{pp}\right) \tag{4.32}$$

$$U_{l_1l_2,l_3l_4}^{t} = \frac{1}{2}\left(U_{l_1l_3l_4l_2}^{ph} - U_{l_1l_4l_3l_2}^{ph}\right) = \frac{1}{2}\left(U_{l_1l_2l_3l_4}^{pp} - U_{l_1l_2l_4l_3}^{pp}\right) \tag{4.33}$$

As in previous works on D-TRILEX method [231, 232], The conventional definition for the four-point vertex corresponds to the choice $B_{\nu,ll'}^{\sigma\sigma'} = g_{\nu,ll'}^{\sigma\sigma'}$.

Following the derivation presented in Refs. [231, 232] and inspired by Refs. [264,

265], in the multi-band case the partially approximation for the fermion-fermion vertex function reads

$$\left[\bar{\Gamma}_{\nu\nu'\omega}\right]_{l_1l_2l_3l_4}^{\sigma_1\sigma_2\sigma_3\sigma_4} = \sum_{\{r\}} \left\{ \left[M_{\nu\nu'\omega}^{\varsigma\varsigma'}\right]_{l_1l_2l_3l_4}^{\sigma_1\sigma_2\sigma_3\sigma_4} - \left[M_{\nu,\nu+\omega,\nu'-\nu}^{\varsigma\varsigma'}\right]_{l_1l_3l_2l_4}^{\sigma_1\sigma_3\sigma_2\sigma_4} - \left[M_{\nu,\nu',\omega+\nu+\nu'}^{\vartheta\vartheta'}\right]_{l_1l_4l_3l_2}^{\sigma_1\sigma_4\sigma_3\sigma_2} \right\}$$

(4.34)

where the partially bosonized collective electronic fluctuations in different channels are

$$\left[M_{\nu\nu'\omega}^{\varsigma\varsigma'}\right]_{l_1l_2l_3l_4}^{\sigma_1\sigma_2\sigma_3\sigma_4} = \sum_{\{l'\}} \Lambda_{\nu\omega,l_1,l_2,l'_1l'_2}^{\sigma_1\sigma_2\varsigma} \bar{w}_{\omega,l'_1l'_2,l'_3l'_4}^{\varsigma\varsigma'} \Lambda_{\nu'+\omega,-\omega,l_4,l_3,l'_4l'_3}^{\sigma_4\sigma_3\varsigma'} \qquad (4.35)$$

$$\left[M_{\nu\nu'\omega}^{\vartheta\vartheta'}\right]_{l_1l_2l_3l_4}^{\sigma_1\sigma_2\sigma_3\sigma_4} = \sum_{\{l'\}} \Lambda_{\nu\omega,l_1,l_2,l'_1l'_2}^{\sigma_1\sigma_2\vartheta} \bar{w}_{\omega,l'_1l'_2,l'_3l'_4}^{\vartheta\vartheta'} \Lambda_{\nu'\omega,l_3,l_4,l'_3l'_4}^{*\sigma_3\sigma_4\vartheta'} \qquad (4.36)$$

The bosonic fluctuation that connects the three-point vertices in Eqs. (4.35) and (4.36) is

$$\bar{w}_{\omega,l_1l_2,l_3l_4}^{rr'} = w_{\omega,l_1l_2,l_3l_4}^{rr'} - \bar{u}_{l_1l_2l_3l_4}^{r}\delta_{rr'} \qquad (4.37)$$

It corresponds to the renormalized interaction $w^{rr'}$ of the reference system that can be obtained from the corresponding susceptibility as

$$w_{\omega,l_1l_2,l_3l_4}^{rr'} = \tilde{U}_{l_1l_2,l_3l_4}^{r}\delta_{rr'} + \sum_{\{l'\}} \tilde{U}_{l_1l_2,l'_1l'_2}^{r} \chi_{\omega,l'_1l'_2,l'_3l'_4}^{rr'} \tilde{U}_{l'_3l'_4,l_3l_4}^{r'} \qquad (4.38)$$

As has been discussed in Refs. [231, 232], the choice (4.53)–(4.56) for the bare interaction U^r in different r channels provides the best possible partially bosonized approximation for the four-point vertex function (4.34). However, this choice leads to the double-counting of the bare interaction of the reference problem. This double-counting is removed by the $\bar{u}^r$ term that enters Eq. (4.37). The expression for this term can be obtained in the same way as in Refs. [231, 232], and for the multi-band case explicitly reads

$$\bar{u}_{l_1l_2,l_3l_4}^{\varsigma} = \frac{1}{2}U_{l_1l_2,l_3l_4}^{\varsigma}, \qquad \bar{u}_{l_1l_2,l_3l_4}^{\vartheta} = U_{l_1l_2,l_3l_4}^{\vartheta} \qquad (4.39)$$

4.3.2 Effect of the approximation on the vertex

We may wonder what is the effect of the approximation (4.34) on the fermion-fermion vertex. Of course, if the approximation leads to unreasonable values of the fermion-fermion vertex, there would be no point in developing a theory based on it, no matter how attractive the theory would be in terms of simplicity of its solution. To check whether the approximation reproduces well the exact fermion-fermion vertex, we look at the exact vertex in the $\Gamma_{\nu\nu',\omega=0}$ and compare it with its approximated version $\bar{\Gamma}_{\nu\nu',\omega=0}$. In particular,

we studied the case of an impurity obtained by converging a DMFT calculation based on the half-filled Hubbard model on a square lattice in a broad region of the local interaction U and we found very comparable results for the exact fermion-fermion interaction Γ and its approximated form that only contains contributions that are reducible in terms of bosonic interaction lines. This can be seen by looking at figures 4.5-4.8, where we show four different values of the interaction U, starting at small coupling $U = 2$ up to strong coupling $U = 12$. In all the figures, in the upper panels we show the vertex in the density channel for the exact calculation Γ^d (left) and in the partially bosonized approximation $\overline{\Gamma}^d$. In the middle panels, the results for Γ^m and $\overline{\Gamma}^m$ are displayed for the magnetic channel m. Finally, the bottom row shows the density (left) and magnetic (right) vertices in the exact case (crosses with dashed lines) and partially bosonized case (dots with full lines) along some symmetry path in the (ν, ν')-plane. The hopping for the corresponding square lattice Hubbard model is set to $t = 1$.

In all the figures, there is a very evident noise at large frequencies in the exact vertex function. This is related to the fact that we compute the impurity single-particle Green's function and impurity four-point correlation function using continuous-time QMC. In particular, to obtain these plots, we used the CT-HYB method in its implementation provided in the ALPS software package [142, 270]. In order to obtain the vertex from the four-point correlation function, we have to use Eq. (4.16) and we have to fix the arbitrary functions B_ν. In these calculations, we stick to the conventional choice of the vertex function, putting $B_\nu = g_\nu$, hence the noisy data at large frequency. However, dual calculations based on this vertex functions are still accurate, since the dual Green's function is $\tilde{G}_{\mathbf{k}\nu} = G_{\mathbf{k}\nu}^{\mathrm{DMFT}} - g_\nu$, so that it decays as $\sim \nu^{-2}$ as a function of the Matsubara frequency. The results obtained with the approximated $\overline{\Gamma}$ at the two lower values of the interaction $U = 2$ and $U = 4$ are rather similar to the exact result Γ both in the density (d) and in the magnetic (m) channels. On the other hand, the structure at $U = 8$ is well reproduced but the values differ significantly if $\nu = -\nu'$ at low frequency. Finally, in the case $U = 12$, the partially bosonized approximation reproduces very well the main peaks appearing at $\nu_n = \nu'_n$ for the $n = \pm1$. Based on these observations, we expect that replacing the exact vertex with its partially bosonized approximation could have a noticeable impact on the calculation of the observables in the regime of interaction strength close to the bandwidth of the system, i.e. $U \approx 8$.
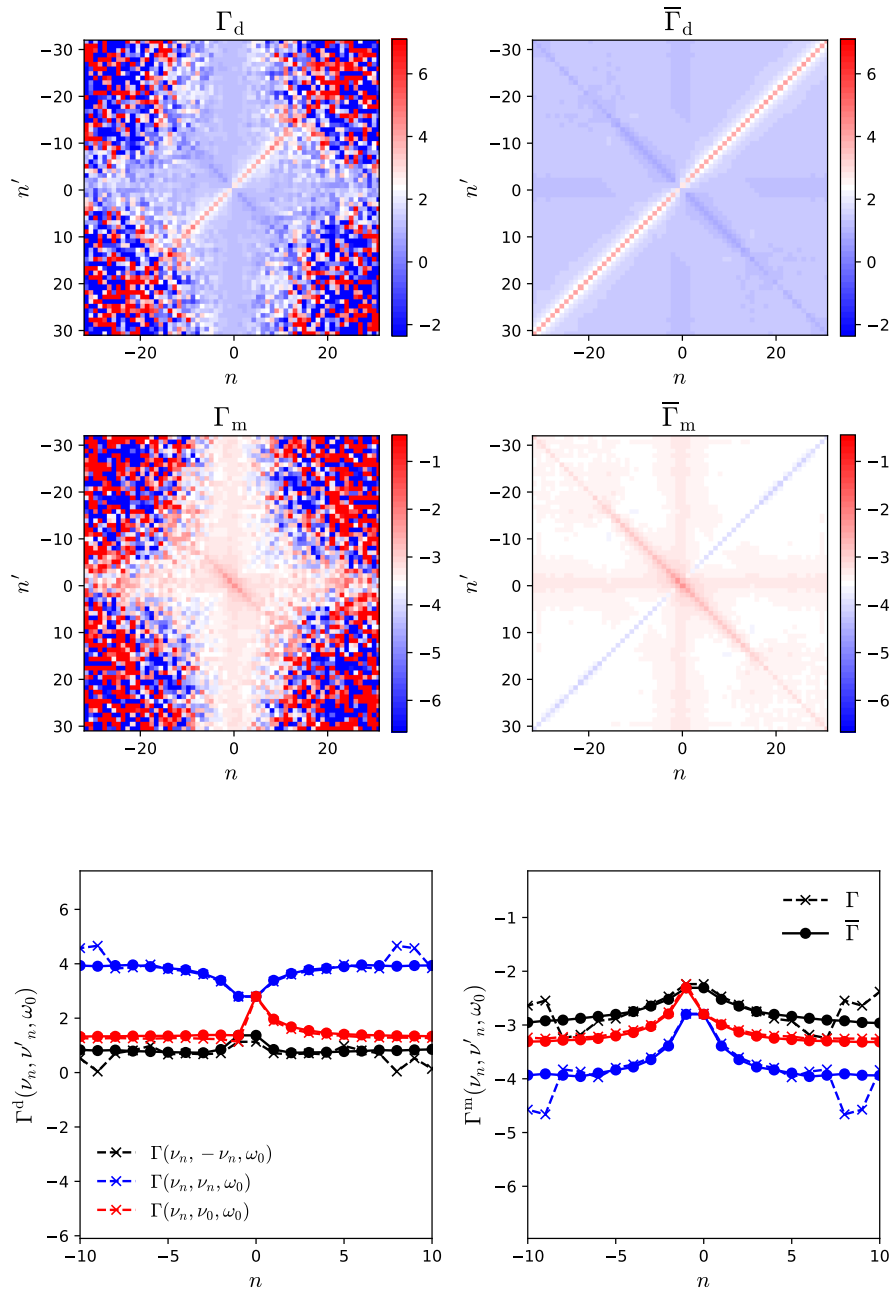
FIGURE 4.5: Comparison between the exact vertex $\Gamma_{\nu\nu'\omega}$ and its partially bosonized approximation $\overline{\Gamma}_{\nu\nu'\omega}$ for the impurity obtained solving self-consistently the DMFT problem for the Hubbard model on the square lattice at half-filling. The parameters are $U = 2$ and $\beta = 4$, which means weakly interacting regime. The bosonic frequency is $\omega = 0$.
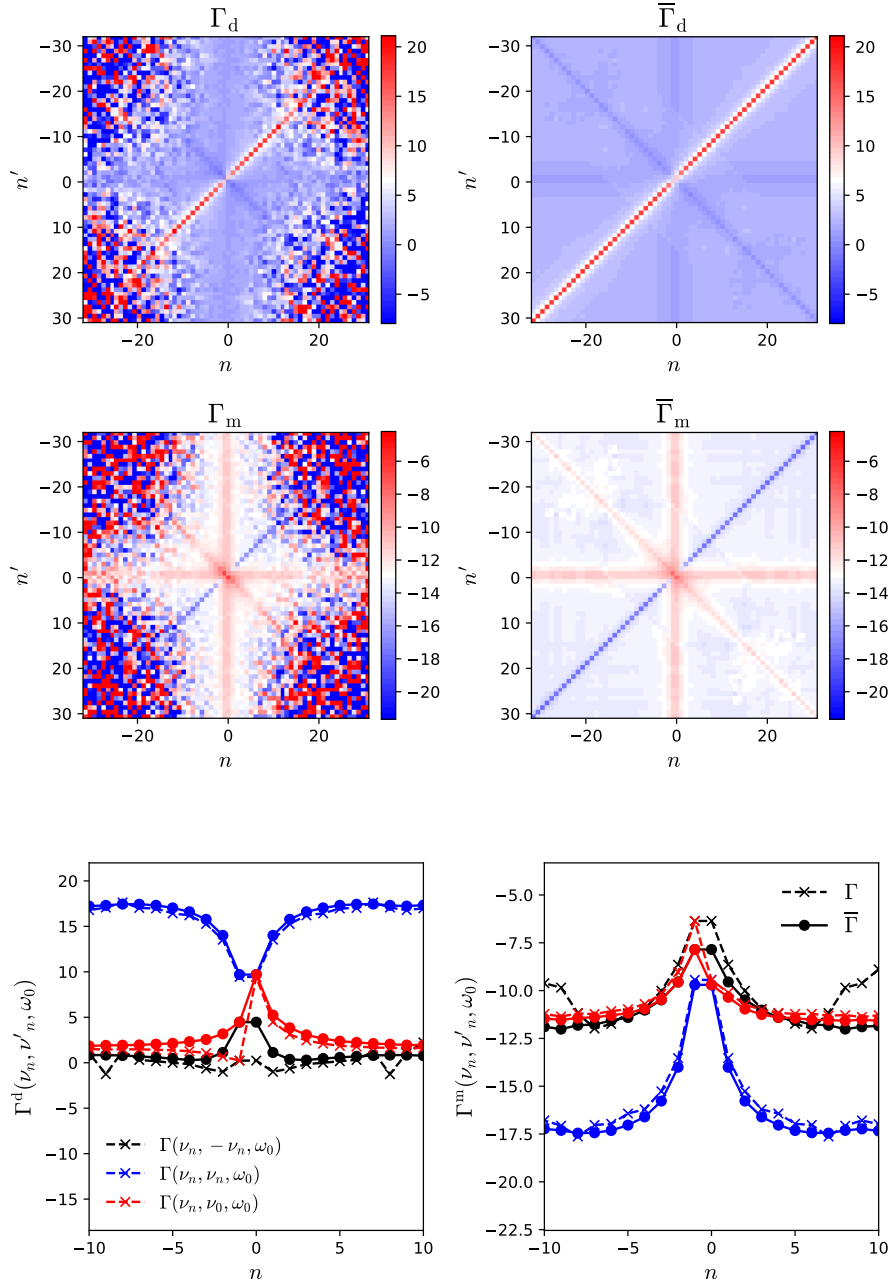
FIGURE 4.6: Comparison between the exact vertex $\Gamma_{\nu\nu'\omega}$ and its partially bosonized approximation $\overline{\Gamma}_{\nu\nu'\omega}$ for the impurity obtained solving self-consistently the DMFT problem for the Hubbard model on the square lattice at half-filling. In this plot, we consider the intermediate coupling regime with parameters $U = 4$ and $\beta = 4$.
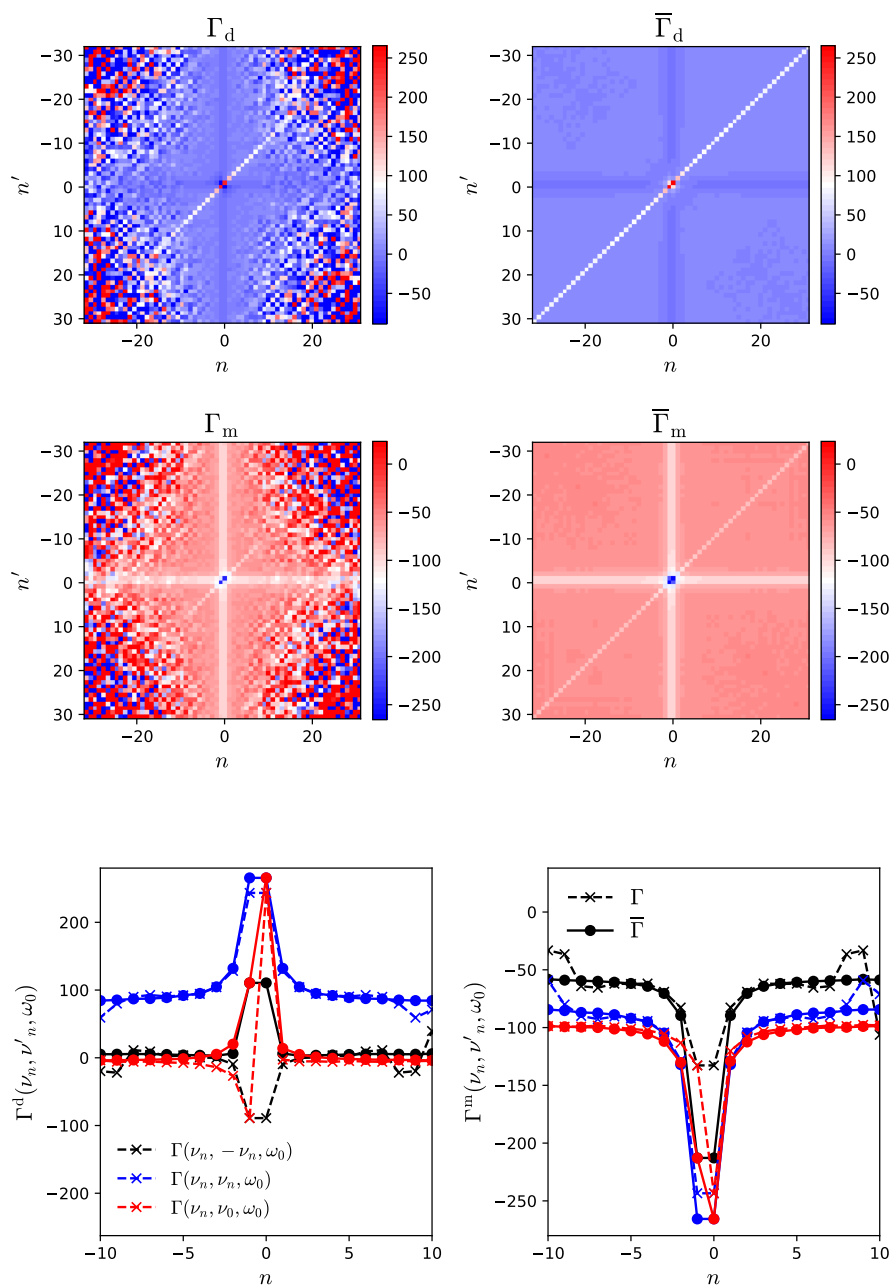
FIGURE 4.7: Same vertices as in Fig 4.5 for a stronger coupling regime with parameters $U = 8$ and $\beta = 2$. Here, the interaction strength equals the bandwidth of the lattice system of the converged DMFT.
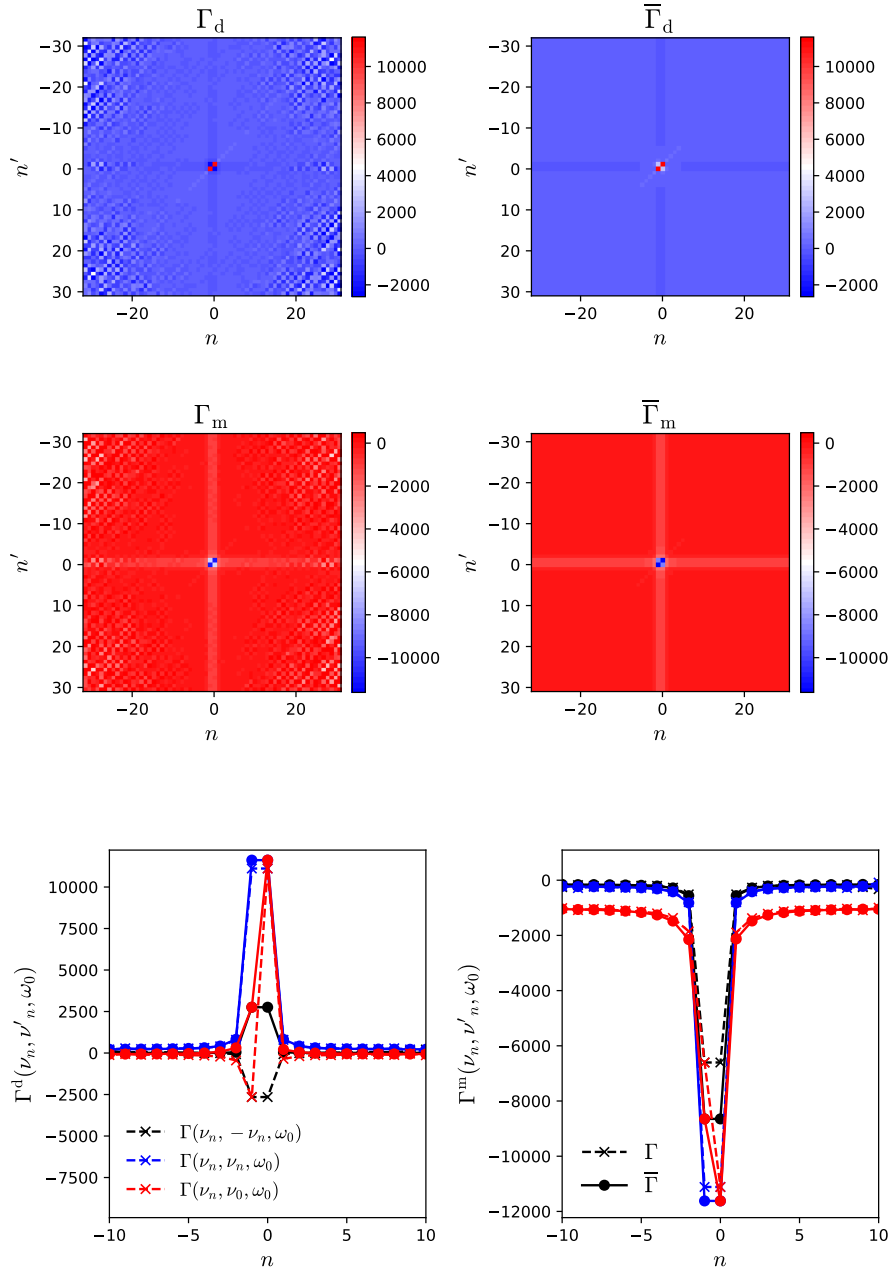
FIGURE 4.8: Same vertices as in Fig 4.5 for the strong coupling regime with parameters $U = 12$ and $\beta = 2$. The interaction strength is considerably larger than the bandwidth of the lattice system of the converged DMFT.

4.3.3 An additional bosonic Hubbard-Stratonovich transformation

In order to eliminate the four-point vertex function Γ^{ph} from the theory, we add and subtract the following terms

$$\frac{1}{2}\sum_{q,\{l\}}\sum_{\varsigma\varsigma'}\varphi^{\varsigma}_{-q,l_1l_2}\left[\bar{w}^{-1}_{\omega}\right]^{\varsigma\varsigma'}_{l_1l_2,l_3l_4}\varphi^{\varsigma'}_{q,l_4l_3}+\sum_{q,\{l\}}\sum_{\vartheta\vartheta'}\varphi^{*\,\vartheta}_{q,l_1l_2}\left[\bar{w}^{-1}_{\omega}\right]^{\vartheta\vartheta'}_{l_1l_2,l_3l_4}\varphi^{\vartheta'}_{q,l_3l_4} \tag{4.40}$$

from the dual action (4.10). At this step, $\bar{w}_{\omega}$ are introduced as arbitrary quantities. Further, they will be adjusted to obtain the partially bosonized approximation for the four-point vertex function (see Appendix 4.3.1). After restoring the explicit form of the bosonic source fields, the dual boson action becomes

$$\tilde{\mathcal{S}}=-\mathrm{Tr}_{\sigma,l}\sum_{k}\left\{\hat{f}^{*}_{k}\tilde{\varepsilon}^{-1}_{k}\hat{f}_{k}-f^{*}_{k}g_{v}f_{k}\right\}+\tilde{\mathcal{F}}[f,\varphi]+\frac{1}{2}\mathrm{Tr}_{\varsigma,l}\sum_{q}\varphi_{-q}\bar{w}^{-1}_{\omega}\varphi_{q}+\mathrm{Tr}_{\vartheta,l}\sum_{q}\varphi^{*}_{q}\bar{w}^{-1}_{\omega}\varphi_{q}$$

$$-\mathrm{Tr}_{\vartheta,l}\sum_{q}\left\{\varphi^{*}_{q}\alpha^{-1}_{\omega}\left(\tilde{V}^{-1}_{q}-\chi_{\omega}+\alpha_{\omega}\bar{w}^{-1}_{\omega}\alpha_{\omega}\right)\alpha^{-1}_{\omega}\varphi_{q}+j^{*}_{q}\tilde{V}^{-1}_{q}j_{q}-\varphi^{*}_{q}\alpha^{-1}_{\omega}\tilde{V}^{-1}_{q}j_{q}-j^{*}_{q}\tilde{V}^{-1}_{q}\alpha^{-1}_{\omega}\varphi_{q}\right\}$$

$$-\mathrm{Tr}_{\varsigma,l}\sum_{q}\left\{\frac{1}{2}\varphi_{-q}\alpha^{-1}_{\omega}\left(\tilde{V}^{-1}_{q}-\chi_{\omega}+\alpha_{\omega}\bar{w}^{-1}_{\omega}\alpha_{\omega}\right)\alpha^{-1}_{\omega}\varphi_{q}+\frac{1}{2}j_{-q}\tilde{V}^{-1}_{q}j_{q}-\varphi_{-q}\alpha^{-1}_{\omega}\tilde{V}^{-1}_{q}j_{q}\right\} \tag{4.41}$$

where we explicitly isolated the terms that contain the bosonic source fields $j^{(*)}$. To shorten the expression, we omitted band, spin, and channel indices that can be easily restored using the fact that all multiplications in Eq. (4.41) are performed in the matrix form. Now, we perform the following Hubbard-Stratonovich transformations

$$\exp\left\{\frac{1}{2}\mathrm{Tr}_{\varsigma,l}\sum_{q}\varphi_{-q}\alpha^{-1}_{\omega}\left[\tilde{V}^{-1}_{q}-\chi_{\omega}+\alpha_{\omega}\bar{w}^{-1}_{\omega}\alpha_{\omega}\right]\alpha^{-1}_{\omega}\varphi_{q}\right\}=\mathcal{D}_{b}\int D[b^{\varsigma}]\times$$

$$\times\exp\left\{-\mathrm{Tr}_{\varsigma,l}\sum_{q}\left(\frac{1}{2}b_{-q}\bar{w}^{-1}_{\omega}\alpha_{\omega}\left[\tilde{V}^{-1}_{q}-\chi_{\omega}+\alpha_{\omega}\bar{w}^{-1}_{\omega}\alpha_{\omega}\right]^{-1}\alpha_{\omega}\bar{w}^{-1}_{\omega}b_{q}-\varphi_{-q}\bar{w}^{-1}_{\omega}b_{q}\right)\right\} \tag{4.42}$$

$$\exp\left\{\mathrm{Tr}_{\vartheta,l}\sum_{q}\varphi^{*}_{q}\alpha^{-1}_{\omega}\left[\tilde{V}^{-1}_{q}-\chi_{\omega}+\alpha_{\omega}\bar{w}^{-1}_{\omega}\alpha_{\omega}\right]\alpha^{-1}_{\omega}\varphi_{q}\right\}=\mathcal{D}_{b}\int D[b^{\vartheta}]\times$$

$$\times\exp\left\{-\mathrm{Tr}_{\vartheta,l}\sum_{q}\left(b^{*}_{q}\bar{w}^{-1}_{\omega}\alpha_{\omega}\left[\tilde{V}^{-1}_{q}-\chi_{\omega}+\alpha_{\omega}\bar{w}^{-1}_{\omega}\alpha_{\omega}\right]^{-1}\alpha_{\omega}\bar{w}^{-1}_{\omega}b_{q}-\varphi^{*}_{q}\bar{w}^{-1}_{\omega}b_{q}-b^{*}_{q}\bar{w}^{-1}_{\omega}\varphi_{q}\right)\right\}$$

$$\tag{4.43}$$

where the terms $\mathcal{D}_b^{-1} = \sqrt{\det\left[\bar{w}\alpha^{-1}\left[\tilde{V}^{-1} - \chi + \alpha\bar{w}^{-1}\alpha\right]\alpha^{-1}\bar{w}\right]}$ can again be neglected, because they also do not affect the calculation of correlation functions. The dual action becomes

$$\tilde{S}' = -\operatorname{Tr}_{\sigma,l} \sum_k \left\{\hat{f}_k^* \tilde{\varepsilon}_k^{-1} \hat{f}_k - f_k^* g_\nu f_k\right\} + \tilde{\mathcal{F}}[f, \varphi]$$

$$+ \operatorname{Tr}_{\vartheta,l} \sum_q b_q^* \bar{w}_\omega^{-1} \alpha_\omega \left[\tilde{V}_q^{-1} - \chi_\omega + \alpha_\omega \bar{w}_\omega^{-1} \alpha_\omega\right]^{-1} \alpha_\omega \bar{w}_\omega^{-1} b_q - \operatorname{Tr}_{\vartheta,l} \sum_q j_q^* \tilde{V}_q^{-1} j_q$$

$$+ \frac{1}{2} \operatorname{Tr}_{\varsigma,l} \sum_q b_{-q} \bar{w}_\omega^{-1} \alpha_\omega \left[\tilde{V}_q^{-1} - \chi_\omega + \alpha_\omega \bar{w}_\omega^{-1} \alpha_\omega\right]^{-1} \alpha_\omega \bar{w}_\omega^{-1} b_q - \frac{1}{2} \operatorname{Tr}_{\varsigma,l} \sum_q j_{-q} \tilde{V}_q^{-1} j_q$$

$$+ \operatorname{Tr}_{\vartheta,l} \sum_q \varphi_q^* \bar{w}_\omega^{-1} \varphi_q - \operatorname{Tr}_{\vartheta,l} \sum_q \left\{\varphi_q^* \bar{w}_\omega^{-1} \left(b_q - \bar{w}_\omega \alpha_\omega^{-1} \tilde{V}_q^{-1} j_q\right) + \left(b_q^* - j_q^* \tilde{V}_q^{-1} \alpha_\omega^{-1} \bar{w}_\omega\right) \bar{w}_\omega^{-1} \varphi_q\right\}$$

$$+ \frac{1}{2} \operatorname{Tr}_{\varsigma,l} \sum_q \varphi_{-q} \bar{w}_\omega^{-1} \varphi_q - \operatorname{Tr}_{\varsigma,l} \sum_q \varphi_{-q} \bar{w}_\omega^{-1} \left(b_q - \bar{w}_\omega \alpha_\omega^{-1} \tilde{V}_q^{-1} j_q\right) \tag{4.44}$$

4.3.4 Integrating out the old bosonic fields

We shift bosonic variables as $b^{(*)} \to \hat{b}^{(*)} = b^{(*)} + \bar{w}\alpha^{-1}\tilde{V}^{-1} j^{(*)}$ to decouple the sources $j^{(*)}$ from the dual bosonic fields $\varphi^{(*)}$. After that the fields $\varphi^{(*)}$ can be integrated out as

$$\int D[\varphi^\varsigma] \exp\left\{-\frac{1}{2} \operatorname{Tr}_{\varsigma,l} \sum_q \varphi_{-q} \bar{w}_\omega^{-1} \varphi_q + \operatorname{Tr}_{\varsigma,l} \sum_q \left(b_{-q} \bar{w}_\omega^{-1} - \sum_{k,\sigma\sigma'} f_{k\sigma}^* f_{k+q,\sigma'} \Lambda_{\nu\omega}^{\sigma\sigma'}\right) \varphi_q\right\} =$$

$$\mathcal{Z}_\varphi \exp\left\{\frac{1}{2} \operatorname{Tr}_{\varsigma,l} \sum_q b_{-q} \bar{w}_\omega^{-1} b_q - \operatorname{Tr}_{\varsigma,l} \sum_{q,k} \sum_{\sigma\sigma'} \Lambda_{\nu\omega}^{\sigma\sigma'} f_{k\sigma}^* f_{k+q,\sigma'} b_q\right.$$

$$\left. + \frac{1}{2} \operatorname{Tr}_{\varsigma,l} \sum_{q,\{\sigma\}} \sum_{k,k'} \Lambda_{\nu\omega}^{\sigma_1\sigma_2} \bar{w}_\omega \Lambda_{\nu'+\omega,-\omega}^{\sigma_4\sigma_3} f_{k\sigma_1}^* f_{k+q,\sigma_2} f_{k'+q,\sigma_4}^* f_{k'\sigma_3}\right\} \tag{4.45}$$

$$\int D[\varphi^{*\vartheta}, \varphi^{\vartheta}] \exp \left\{ - \text{Tr}_{\vartheta,l} \sum_q \varphi_q^* \bar{w}_\omega^{-1} \varphi_q + \text{Tr}_{\vartheta,l} \sum_q \left(b_q^* \bar{w}_\omega^{-1} \varphi_q + \varphi_q^* \bar{w}_\omega^{-1} b_q \right) \right.$$

$$\left. - \frac{1}{2} \text{Tr}_{\vartheta,l} \sum_{q,k} \sum_{\sigma\sigma'} \left(f_{k\sigma}^* f_{q-k,\sigma'}^* \Lambda_{\nu\omega}^{\sigma\sigma'} \varphi_q + \varphi_q^* \Lambda_{\nu\omega}^{*\sigma\sigma'} f_{q-k,\sigma'} f_{k\sigma} \right) \right\} =$$

$$\mathcal{Z}_\varphi \exp \left\{ \text{Tr}_{\vartheta,l} \sum_q b_q^* \bar{w}_\omega^{-1} b_q - \frac{1}{2} \text{Tr}_{\vartheta,l} \sum_{q,k} \sum_{\sigma\sigma'} \left(f_{k\sigma}^* f_{q-k,\sigma'}^* \Lambda_{\nu\omega}^{\sigma\sigma'} b_q + b_q^* \Lambda_{\nu\omega}^{*\sigma\sigma'} f_{q-k,\sigma'} f_{k\sigma} \right) \right.$$

$$\left. + \frac{1}{4} \text{Tr}_{\vartheta,l} \sum_{q,\{\sigma\}} \sum_{k,k'} \Lambda_{\nu\omega}^{\sigma_1\sigma_2} \bar{w}_\omega \Lambda_{\nu'\omega}^{\sigma_3\sigma_4} f_{k\sigma_1}^* f_{q-k,\sigma_2}^* f_{q-k',\sigma_4} f_{k'\sigma_3} \right\} \tag{4.46}$$

where $\mathcal{Z}_\varphi$ is a partition function of the Gaussian part of the bosonic action. As discussed in Appendix 4.3.1 and Refs. [231, 232], quartic terms that appear at the last lines of Eqs. (4.45) and (4.46) approximately cancel the fermion-fermion (Γ) part of the interaction (4.15) if the $\bar{w}_\omega^{rr'}$ quantities are taken in the form of Eq. (4.37).

As the result, the problem reduces to a partially bosonized dual action

$$\tilde{\mathcal{S}}_{fb} = - \text{Tr}_{\sigma,l} \sum_k \left\{ \hat{f}_k^* \tilde{\varepsilon}_k^{-1} \hat{f}_k - f_k^* g_\nu f_k \right\}$$

$$+ \frac{1}{2} \text{Tr}_{\varsigma,l} \sum_q \hat{b}_{-q} \bar{w}_\omega^{-1} \alpha_\omega \left[\tilde{V}_q^{-1} - \chi_\omega + \alpha_\omega \bar{w}_\omega^{-1} \alpha_\omega \right]^{-1} \alpha_\omega \bar{w}_\omega^{-1} \hat{b}_q - \frac{1}{2} \text{Tr}_{\varsigma,l} \sum_q j_{-q} \tilde{V}_q^{-1} j_q$$

$$- \frac{1}{2} \text{Tr}_{\varsigma,l} \sum_q b_{-q} \bar{w}_\omega^{-1} b_q + \text{Tr}_{\varsigma,l} \sum_{q,k} \sum_{\sigma\sigma'} \Lambda_{\nu\omega}^{\sigma\sigma'} f_{k\sigma}^* f_{k+q,\sigma'} b_q$$

$$+ \text{Tr}_{\vartheta,l} \sum_q \hat{b}_q^* \bar{w}_\omega^{-1} \alpha_\omega \left[\tilde{V}_q^{-1} - \chi_\omega + \alpha_\omega \bar{w}_\omega^{-1} \alpha_\omega \right]^{-1} \alpha_\omega \bar{w}_\omega^{-1} \hat{b}_q - \text{Tr}_{\vartheta,l} \sum_q j_q^* \tilde{V}_q^{-1} j_q$$

$$- \text{Tr}_{\vartheta,l} \sum_q b_q^* \bar{w}_\omega^{-1} b_q + \frac{1}{2} \text{Tr}_{\vartheta,l} \sum_{q,k} \sum_{\sigma\sigma'} \left(f_{k\sigma}^* f_{q-k,\sigma'}^* \Lambda_{\nu\omega}^{\sigma\sigma'} b_q + b_q^* \Lambda_{\nu\omega}^{*\sigma\sigma'} f_{q-k,\sigma'} f_{k\sigma} \right) \tag{4.47}$$

that upon neglecting fermionic $\eta^{(*)}$ and bosonic $j^{(*)}$ source takes the simple form shown in Eq. (4.49) of the main text. The new bare fermionic Green's function for this action is defined in Eq. (4.50). The bare dual bosonic propagator reads

$$\tilde{\mathcal{W}}_{q,l_1l_2,l_3l_4}^{r_1r_2} = \sum_{\{r'\},\{l'\}} \alpha_{\omega,l_1l_2,l_1'l_2'}^{r_1r_1'} \left[\left(\tilde{V}_q^{-1} - \chi_\omega \right)^{-1} \right]_{l_1'l_2',l_3'l_4'}^{r_1'r_2'} \alpha_{\omega,l_3'l_4',l_3l_4}^{r_2'r_2} + \bar{w}_{\omega,l_1l_2,l_3l_4}^{r_1r_2} \tag{4.48}$$

Substituting the explicit expression (4.37) for the $\bar{w}_\omega^{rr'}$ quantities leads for the final form for the bare bosonic propagator shown in Eq. (4.51).

4.3.5   The partially bosonized action

The steps developed so far allow us to extend the formalism of the partially bosonized action presented in Refs. [231, 232] to multi-band systems. Collecting the terms and removing the sources in Eq. (4.47), we obtain an expression for the effective partially bosonized dual action written in terms of fermion f and boson b variables that explicitly reads

$$
\mathcal{S}_{fb} = -\sum_{k,\{l\}} \sum_{\sigma\sigma'} f^*_{k\sigma l} \left[\tilde{\mathcal{G}}_k^{-1}\right]^{\sigma\sigma'}_{ll'} f_{k\sigma'l'} - \frac{1}{2} \sum_{q,\{l\}} \sum_{\varsigma\varsigma'} b^\varsigma_{-q,l_1l_2} \left[\tilde{W}_q^{-1}\right]^{\varsigma\varsigma'}_{l_1l_2,l_3l_4} b^{\varsigma'}_{q,l_4l_3}
$$

$$
- \sum_{q,\{l\}} \sum_{\vartheta\vartheta'} b^{*\,\vartheta}_{q,l_1l_2} \left[\tilde{W}_q^{-1}\right]^{\vartheta\vartheta'}_{l_1l_2,l_3l_4} b^{\vartheta'}_{q,l_3l_4} + \mathcal{F}\left[f,b\right] \tag{4.49}
$$

It is important to emphasize that this action describes only those correlation effects that are not taken into account by the reference problem, hence there are no double counting issue between the impurity problem and the dual action. This means that double counting issues have to be taken care of when constructing the initial lattice model of (3.14), but they are absent in our theory.

As mentioned before, in the multi-orbital D-TRILEX implementation we exclude these scaling factors by setting $B^{\sigma\sigma'}_{\nu,ll'} = \delta_{ll'}\delta_{\sigma\sigma'}$. This simplifies the expression (4.11) for the bare dual fermionic Green's function to

$$
\tilde{\mathcal{G}}^{\sigma\sigma'}_{k,ll'} = \left[\left((\varepsilon_\mathbf{k} - \Delta_\nu)^{-1} - g_\nu\right)^{-1}\right]^{\sigma\sigma'}_{ll'} \tag{4.50}
$$

where $\Delta^{\sigma\sigma'}_{\nu,ll'}$ and $g^{\sigma\sigma'}_{\nu,ll'} = -\langle c_{\nu\sigma l} c^*_{\nu\sigma'l'}\rangle$ are respectively the fermionic hybridization and the Green's function of the reference system. Note that within the convention chosen here, the dimension of the dual Green's function (4.50) does not correspond to [1/Energy] dimension of a physical Green's function.

The bosonic propagator (renormalized interaction) of the partially bosonized dual action (4.49) is the following (see Appendix 4.2.1)

$$
\tilde{W}^{rr'}_{q,l_1l_2,l_3l_4} = \mathcal{W}^{rr'}_{q,l_1l_2,l_3l_4} - \bar{u}^r_{l_1l_2,l_3l_4}\delta_{rr'} \tag{4.51}
$$

Here, $\bar{u}^\varsigma_{l_1l_2,l_3l_4} = \frac{1}{2}U^\varsigma_{l_1l_2,l_3l_4}$ and $\bar{u}^\vartheta_{l_1l_2,l_3l_4} = U^\vartheta_{l_1l_2,l_3l_4}$ are the corrections that prevent the double counting of the interaction between different channels (see Appendix 4.3.1). The renormalized interaction $\mathcal{W}^{rr'}_q$ of extended DMFT [162–165, 267] can be obtained from the

corresponding Dyson equation

$$\left[\mathcal{W}_q^{-1}\right]_{l_1l_2,\,l_3l_4}^{rr'} = \left[\left(U^r + V_q^r\right)^{-1}\right]_{l_1l_2,\,l_3l_4} \delta_{rr'} - \Pi_{\omega,\,l_1l_2,\,l_3l_4}^{\mathrm{imp}\,rr'} \tag{4.52}$$

that involves the polarization operator $\Pi_{\omega,\,l_1l_2,\,l_3l_4}^{\mathrm{imp}\,rr'}$ of the reference (impurity) problem and the bare interaction in the channel representation (see Appendix 4.3.1)

$$U_{l_1l_2l_3l_4}^d = \frac{1}{2}\left(2U_{l_1l_2l_3l_4}^{ph} - U_{l_1l_3l_2l_4}^{ph}\right) = \frac{1}{2}\left(2U_{l_1l_4l_2l_3}^{pp} - U_{l_1l_4l_3l_2}^{pp}\right) \tag{4.53}$$

$$U_{l_1l_2l_3l_4}^m = -\frac{1}{2}U_{l_1l_3l_2l_4}^{ph} = -\frac{1}{2}U_{l_1l_4l_3l_2}^{pp} \tag{4.54}$$

$$U_{l_1l_2l_3l_4}^s = \frac{1}{2}\left(U_{l_1l_3l_4l_2}^{ph} + U_{l_1l_4l_3l_2}^{ph}\right) = \frac{1}{2}\left(U_{l_1l_2l_3l_4}^{pp} + U_{l_1l_2l_4l_3}^{pp}\right) \tag{4.55}$$

$$U_{l_1l_2l_3l_4}^t = \frac{1}{2}\left(U_{l_1l_3l_4l_2}^{ph} - U_{l_1l_4l_3l_2}^{ph}\right) = \frac{1}{2}\left(U_{l_1l_2l_3l_4}^{pp} - U_{l_1l_2l_4l_3}^{pp}\right) \tag{4.56}$$

The interacting term of the effective action (4.49) (see Appendix 4.2.1)

$$\mathcal{F}[f,b] = \sum_{q,\{k\}} \sum_{\{\nu\},\{\sigma\}} \sum_{\{l\},\varsigma/\vartheta} \left\{ \Lambda_{\nu\omega,\,l_1,\,l_2,\,l_3l_4}^{\sigma\sigma'\varsigma} f_{k\sigma l_1}^* f_{k+q,\sigma',l_2} b_{q,l_4l_3}^\varsigma \right.$$
$$\left. + \frac{1}{2}\left(\Lambda_{\nu\omega,\,l_1,\,l_2,\,l_3l_4}^{\sigma\sigma'\vartheta} f_{k\sigma l_1}^* f_{q-k,\sigma',l_2}^* b_{q,l_3l_4}^\vartheta + \Lambda_{\nu\omega,\,l_1,\,l_2,\,l_3l_4}^{*\,\sigma\sigma'\vartheta} b_{q,l_3l_4}^{*\,\vartheta} f_{q-k,\sigma',l_2} f_{k\sigma l_1}\right) \right\} \tag{4.57}$$

contains only the momentum-independent three-point interaction vertex function $\Lambda_{\nu\omega}^{(*)}$ of the reference system. The explicit expression of $\Lambda_{\nu\omega}^{(*)}$ can be found in Eqs. (4.17)–(4.19). The four-point (fermion-fermion) vertex function (4.16) is eliminated from the theory by using a partially bosonized approximation for the interaction [231, 232, 264–266].

4.4 Physical quantities from the dual space

4.4.1 Dressed dual Green's functions

The dual theories work in the virtual space of dual variables (4.49) that describes electronic correlations beyond the ones of the reference system. This formulation of the theory allows one to avoid double-counting of correlation effect that are already taken into account by the reference problem. We specialize our treatment to the partially bosonized action of Eq. (4.49), even though most of the equations hold also for the dual boson action with very small variations. In particular, the treatment of the dual fermionic variables as well as their connection with the Green's function of the lattice is identical for the two actions,

since the transformation introduced in the partially bosonized action does not affect the fermionic degrees of freedom. In order to discuss the relation between dual and lattice quantities, we first have to extract information about the interacting dual problem. This can be done through the dressed (or interacting) dual Green's functions

$$\tilde{G}_{k,ll'}^{\sigma\sigma'} = -\langle f_{k\sigma l} f_{k\sigma'l'}^* \rangle \tag{4.58}$$

$$W_{q,l_1l_2,l_3l_4}^{\varsigma\varsigma'} = -\langle b_{q,l_2l_1}^{\varsigma} b_{-q,l_3l_4}^{\varsigma'} \rangle \tag{4.59}$$

$$W_{q,l_1l_2,l_3l_4}^{\vartheta\vartheta'} = -\langle b_{q,l_1l_2}^{\vartheta} b_{q,l_3l_4}^{*\vartheta'} \rangle. \tag{4.60}$$

The first step is to introduce the Dyson equations for the dual Green's functions. These are the equations that allow us to compute the interacting fermionic and bosonic Green's functions of the dual problem and they valid for both the dual boson theory and the partially bosonized action.

The dressed Green's function $\tilde{G}_k$ and the renormalized interaction $\tilde{W}_q^{\varsigma}$ of the effective partially bosonized dual problem (4.49) are related to the non-interacting Green's functions via Dyson equations

$$\left[\tilde{G}_k^{-1}\right]_{ll'}^{\sigma\sigma'} = \left[\tilde{\mathcal{G}}_k^{-1}\right]_{ll'}^{\sigma\sigma'} - \tilde{\Sigma}_{k,ll'}^{\sigma\sigma'} \tag{4.61}$$

$$\left[\tilde{W}_q^{-1}\right]_{l_1l_2,l_3l_4}^{\varsigma\varsigma'} = \left[\tilde{\mathcal{W}}_q^{-1}\right]_{l_1l_2,l_3l_4}^{\varsigma\varsigma'} - \tilde{\Pi}_{q,l_1l_2,l_3l_4}^{\varsigma\varsigma'}$$

$$\left[\tilde{W}_q^{-1}\right]_{l_1l_2,l_3l_4}^{\vartheta\vartheta'} = \left[\tilde{\mathcal{W}}_q^{-1}\right]_{l_1l_2,l_3l_4}^{\vartheta\vartheta'} - \tilde{\Pi}_{q,l_1l_2,l_3l_4}^{\vartheta\vartheta'} \tag{4.62}$$

where we introduced the dual self-energy $\tilde{\Sigma}_{k,ll'}$ and the dual polarization $\tilde{\Pi}_{q,l_1l_2,l_3l_4}^{\varsigma}$, which are the dual counterparts of the self-energy and polarization of the lattice. Indeed, it can be shown that there is an exact connection between the corresponding quantities in the dual space and in the original lattice space.

In a similar way to what has been discussed for the lattice space, the dual quantities $\tilde{\Sigma}_{k,ll'}$ and $\tilde{\Pi}_{q,l_1l_2,l_3l_4}^{\varsigma}$ can be written in terms of Feynman diagrams as the sum of all the diagrams which are irreducible with respect to the cut a fermionic or a bosonic line respectively.

4.4.2   Connecting the dual quantities and lattice quantities

The source fields introduced in Eq. (4.7) allows one to derive expressions for the correlation functions of the initial lattice problem (3.14) even though the original Grassman variables $c^{(*)}$ have been already integrated out. This can be done by taking functional derivatives of the action (4.47) with respect to the fields with the sources $\eta^{(*)}$ and $j^{(*)}$, which amounts to derive with respect to $\hat{f}^{(*)}$ and $\varphi^{(*)}$ and remove the hat. By definition,

the fermionic Green's function can be found as

$$
G_{k,ll'}^{\sigma\sigma'} = -\langle c_{k\sigma l} c_{k\sigma'l'}^* \rangle = -\frac{1}{\mathcal{Z}} \frac{\partial^2 \mathcal{Z}}{\partial \eta_{k\sigma l}^* \partial \eta_{k\sigma'l'}} \tag{4.63}
$$

where $\mathcal{Z}$ is the partition function of the problem. Taking into account that the source fields enter only the partially bosonized dual action (4.47), the lattice Green's function becomes

$$
\begin{aligned}
G_{k,ll'}^{\sigma\sigma'} &= -\left[\tilde{\varepsilon}_k^{-1}\right]_{ll'}^{\sigma\sigma'} - \sum_{l_1 l_2} \sum_{\sigma_1 \sigma_2} \left[\tilde{\varepsilon}_k^{-1}\right]_{ll_1}^{\sigma\sigma_1} \langle f_{k\sigma_1 l_1} f_{k\sigma_2 l_2}^* \rangle_{\tilde{S}_{fb}} \left[\tilde{\varepsilon}_k^{-1}\right]_{l_2 l'}^{\sigma_2\sigma'} \\
&= -\left[\tilde{\varepsilon}_k^{-1}\right]_{ll'}^{\sigma\sigma'} + \sum_{l_1 l_2} \sum_{\sigma_1 \sigma_2} \left[\tilde{\varepsilon}_k^{-1}\right]_{ll_1}^{\sigma\sigma_1} \tilde{G}_{kl_1 l_2}^{\sigma_1\sigma_2} \left[\tilde{\varepsilon}_k^{-1}\right]_{l_2 l'}^{\sigma_2\sigma'}
\end{aligned} \tag{4.64}
$$

Using the Dyson equation for the dressed dual fermionic Green's function (4.61) and substituting the explicit form for the bare dual fermionic Green's function (4.50) allows us to obtain the following relation for the lattice Green's function

$$
\left[G_k^{-1}\right]_{ll'}^{\sigma\sigma'} = \left[\left(g_\nu + \tilde{\Sigma}_k\right)^{-1}\right]_{ll'}^{\sigma\sigma'} + \Delta_{\nu,ll'}^{\sigma\sigma'} - \varepsilon_{\mathbf{k},ll'}^{\sigma\sigma'}. \tag{4.65}
$$

The expression (4.67) for the lattice self-energy can then be obtained straightforwardly using the standard Dyson equation for the lattice Green's function

$$
\left[G_k^{-1}\right]_{ll'}^{\sigma\sigma'} = \left[\mathcal{G}_k^{-1}\right]_{ll'}^{\sigma\sigma'} - \Sigma_{k,ll'}^{\sigma\sigma'} = (i\nu + \mu)\delta_{ll'}\delta_{\sigma\sigma'} - \varepsilon_{\mathbf{k},ll'}^{\sigma\sigma'} - \Sigma_{k,ll'}^{\sigma\sigma'}. \tag{4.66}
$$

Alternatively, one can compute directly the lattice self-energy. Indeed, comparing Eqs. (4.65) and (4.66) and after a few manipulations, we get to the expression

$$
\Sigma_{k,ll'}^{\sigma\sigma'} = \Sigma_{\nu,ll'}^{\mathrm{imp},\sigma\sigma'} + \sum_{l_1 \sigma_1} \tilde{\Sigma}_{k,ll_1}^{\sigma\sigma'} \left[\left(\mathbb{1} + g_\nu \cdot \tilde{\Sigma}_k\right)^{-1}\right]_{l_1 l'}^{\sigma\sigma'}. \tag{4.67}
$$

The lattice susceptibilities can be obtained in a similar way as

$$
X_{q,l_1 l_2, l_3 l_4}^{ss'} = -\langle \rho_{q,l_2 l_1}^s \rho_{-q,l_3 l_4}^{s'} \rangle = -\frac{1}{\mathcal{Z}} \frac{\partial^2 \mathcal{Z}}{\partial j_{-q,l_1 l_2}^s \partial j_{q,l_4 l_3}^{s'}} \tag{4.68}
$$

$$
X_{q,l_1 l_2, l_3 l_4}^{\vartheta\vartheta'} = -\langle \rho_{q,l_1 l_2}^\vartheta \rho_{q,l_3 l_4}^{*\vartheta'} \rangle = -\frac{1}{\mathcal{Z}} \frac{\partial^2 \mathcal{Z}}{\partial j_{q,l_1 l_2}^{*\vartheta} \partial j_{q,l_3 l_4}^{\vartheta'}} \tag{4.69}
$$

The part of the action that depends on the bosonic sources is in the following form

$$
\begin{aligned}
\tilde{S}_j = \frac{1}{2} \mathrm{Tr}_{\varsigma,l} \sum_q j_{-q} \, C_q \, j_q + \mathrm{Tr}_{\varsigma,l} \sum_q j_{-q} \, R_q \, b_q \\
+ \mathrm{Tr}_{\vartheta,l} \sum_q j_q^* \, C_q \, j_q + \mathrm{Tr}_{\vartheta,l} \sum_q \left(j_q^* \, R_q \, b_q + j_q^* \, R_q \, b_q \right)
\end{aligned}
\tag{4.70}
$$

where the terms C_q and R_q explicitly read

$$
C_q = \tilde{V}_q^{-1} \left[\tilde{V}_q^{-1} - \chi_\omega + \alpha_\omega \bar{w}_\omega^{-1} \alpha_\omega \right]^{-1} \tilde{V}_q^{-1} - \tilde{V}_q^{-1}
$$
$$
R_q = \tilde{V}_q^{-1} \left[\tilde{V}_q^{-1} - \chi_\omega + \alpha_\omega \bar{w}_\omega^{-1} \alpha_\omega \right]^{-1} \alpha_\omega \bar{w}_\omega^{-1}
\tag{4.71}
$$

Therefore, the susceptibility takes the form

$$
X_{q,\,l_1 l_2,\,l_3 l_4}^{r_1 r_2} = C_{q,\,l_1 l_2,\,l_3 l_4}^{r_1 s_2} + \sum_{\{l'\},\{r'\}} R_{q,\,l_1 l_2,\,l_1' l_2'}^{r_1 r_1'} \tilde{W}_{q,\,l_1' l_2',\,l_3' l_4'}^{r_1' r_2'} R_{q,\,l_3' l_4',\,l_3 l_4}^{r_2' r_2}
\tag{4.72}
$$

Importantly, the terms C_q and R_q are not divergent. For this reason, the divergence of the susceptibility X_q and of the renormalized dual interaction $\tilde{W}_q$ occurs at the same time. After some algebra, the expression (4.72) can be drastically simplified, and the inverse susceptibility takes the form of a standard Dyson equation

$$
\left[X_q^{-1} \right]_{l_1 l_2,\,l_3 l_4}^{rr'} = \left[\Pi_q^{-1} \right]_{l_1 l_2,\,l_3 l_4}^{rr'} - \left(U_{l_1 l_2,\,l_3 l_4}^r + V_{q,\,l_1 l_2,\,l_3 l_4}^r \right) \delta_{rr'}
\tag{4.73}
$$

with the following polarization operator of the lattice problem

$$
\Pi_{q,\,l_1 l_2,\,l_3 l_4}^{rr'} = \Pi_{\omega,\,l_1 l_2,\,l_3 l_4}^{\mathrm{imp}\,rr'} + \sum_{l' l'',\,r_1} \tilde{\Pi}_{q,\,l_1 l_2,\,l' l''}^{rr_1} \left[\left(\mathbb{1} + \bar{u} \cdot \tilde{\Pi}_q \right)^{-1} \right]_{l' l'',\,l_3 l_4}^{r_1 r'}
\tag{4.74}
$$

The $\bar{u}_{l_1 l_2,\,l_3 l_4}^r$ term is defined in Sec. 4.3.1. It is important to emphasize that the derived relations for the Green's function (4.65) and the susceptibility (4.73) do not depend on the particular approximation used to obtain the dual self-energy $\tilde{\Sigma}$ and the dual polarization operator $\tilde{\Pi}$.

4.5   Quantum embedding in dual space

The dual boson action (4.10) is a general method to develop a perturbation theory with respect to an interacting reference system. The reference system is introduced to account for some (usually local or short-range) part of electronic correlations numerically exactly,
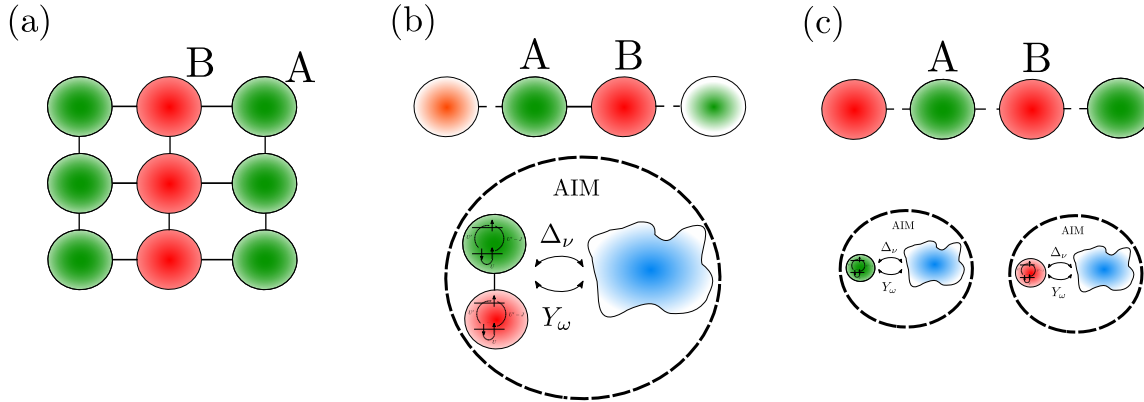
FIGURE 4.9: Distinction between different choices of the splitting of the lattice (a) with different types of atoms, A and B. In (b), we show the choice of a cluster reference system, which is a problem that involves $N_{imp} \times N_l$ orbitals in the impurity problem. It includes short-range hopping terms and interactions within the cluster in the reference AIM, but it breaks translational symmetry, as highlighted by the cut dashed bonds. In (c), we show a multi-impurity reference system. It does not include even short-range hopping terms and interactions, that have to be included diagrammatically, but neither it breaks the symmetry of the lattice (all the bonds are "cut").

and its particular form depends on the considered lattice problem [223]. This system can be a general impurity problem in the form of Eq. (4.1). For instance, in DMFT-based calculations the reference system corresponds to a single-impurity [118], several isolated impurities [260, 271], or a finite cluster [29, 127, 166–170] problems. The choice of the reference system is not restricted to a converged DMFT calculation. Another possibility is to reduce the DMFT local impurity problem to an atomic problem in the spirit of the Hubbard-I approximation [108, 109, 130]. It is also possible to build the diagrammatic expansions on the basis of the impurity problem of the extended dynamical mean field theory (EDMFT) [162–165, 267] by introducing a bosonic hybridization function (see Section 4.2.1). The latter accounts for the effect of the non-local interaction on the local electronic correlations and could play an important role when the non-local interactions are strong. Alternatively, in the spirit of the cluster perturbation theory, one can consider a finite plaquette as a reference system [78, 223]. The limit of an infinite plaquette as a reference system corresponds to the exact solution of the problem. For this reason, we expect the accuracy of the dual theories to improve with enlarging the cluster size similarly to what has been shown for the TRILEX approach [217]. Indeed, as the spatial size of the reference problem is increased, the range of electronic correlations that are treated within the exactly-solved cluster reference problem is also increased. Additionally, using a cluster reference system allows for the study of broken symmetry phases. In this regard, instead of viewing the cluster methods and the multi-band dual theories as competing approaches,

one could consider the dual theories as a method to improve the cluster solution of a problem by diagrammatically adding long-range correlations that are not captured by a finite cluster, in situations where the computational costs prevent a further increase of the cluster's size. As mentioned before, this can be particularly appealing for quantum computation as the number of available qubits is usually not large enough to encode the whole system and it is preferable to use them to represent only the strongly correlated part.

As such, the dual boson method can be already viewed as a quantum embedding theory with the advantage that it is formulated in an exact way. This allows for any kind of systematic improvements and choices of the most suitable approximations in a given context. The improvement with respect to DMFT, DMET and RISB is that non-local effects are added using diagrammatic expansions around the impurity problem, instead of approximating the solution of the problem directly with the impurity density matrix in the case of DMET/RISB or the impurity self-energy in the case of DMFT, that is local by definition. As a matter of fact, the impurity self-energy corresponds to the zeroth-order approximation to the dual boson diagrammatics.

Unfortunately, the exact action (4.10) is not practical to be solved directly and approximations have to be introduced. This can be done at the dual boson level by truncating the form of the interaction and, at a later stage, by putting limitations on the considered diagrams, either by considering a limited number of allowed topologies (dressed second-order dual boson or ladder diagrams) or in the order to be reached (DiagMC@DF or DiagMC@DB, discussed in Chapter 5). Similar considerations hold for the partially bosonized action, even though this theory already involves an additional approximation at the action level.

In this theses, we are mainly concerned in assessing the accuracy of the dual theories and benchmarking the methods. For this reason, we perform all the calculations based on the single-impurity DMFT reference problem for a matter of consistency. Further studies on the performances of other choices of the reference problem are important and they will be carried out in future works. In particular, we speculate that a cluster starting point could resolve the issues that the method faces when a single-impurity reference problem is used in broken symmetry phases. In those cases, even simpler reference systems, such as the DMET impurity with several sites, could be a better starting point when the size of the cluster reference problem is increased. Indeed, DMET for a 2-by-2 cluster was shown to be almost as accurate as cluster DMFT and is characterised by a considerably lower computational cost. Unfortunately, even for this simplified impurity problem, vertex functions should be computed using ED with a certain number of auxiliary bath sites, QMC methods or approximate schemes. The solution of the impurity based on wave function methods, such as matrix-product states or neural network quantum states [272], would grant access to all the correlation functions of the impurity without hitting the exponential wall of the regular ED techniques, at the cost of exactness in the solution of the reference problem.

4.6 Numerical calculation of vertex functions

It is important to mention that in the most available impurity solvers based on continuous-time QMC method [83, 140, 143, 273], the two-particle quantities of the reference system are defined in imaginary time τ with a different order of the operators compared to our case.

For instance, in w2dynamics package [274] the time-ordered two-particle correlation functions are computed as $G_{abcd} = \langle \mathcal{T}_\tau c_a c_b^\dagger c_c c_d^\dagger \rangle$ [275]. Here, T_τ is the imaginary-time ordering operator and the Latin indices $a = \{l_a, \sigma_a, \tau_a\}$ describe the orbital, spin, and imaginary-time dependence. Often, the correlation functions are directly measured in the Matsubara space as a function of ω (or ν and ω), by performing a Fourier transform on the fly. In order to exploit these correlation functions in D-TRILEX, they have to be recast in the form used in Eqs. (4.17)–(4.19) for the vertex functions and in the form of the susceptibility $\chi^{ss'}_{\omega, l_1 l_2, l_3 l_4} = -\langle \rho^s_{\omega, l_2 l_1} \rho^{s'}_{-\omega, l_3 l_4} \rangle$. Taking into account that $\rho^r_{\omega, l_1 l_2} = n^r_{\omega, l_1 l_2} - \langle n^r_{\omega, l_1 l_2} \rangle$, where the densities n^r_ω are defined in Eqs. (3.17) and (3.18), the quantities required for constructing D-TRILEX diagrammatic expansion can be obtained by subtracting the disconnected parts from the corresponding correlation functions of the reference system. Note also that the fermionic operators in G_{abcd} have to be placed in a desired order by applying commutation relations, which may also lead to additional contributions to the disconnected terms. Below we report how to retrieve the susceptibility and the three-point vertex from correlation functions usually computed in CT-QMC methods. Similar procedures can be used to compute the four-point and higher-order vertices.

4.6.1 Calculation of the impurity susceptibility

In this subsection, we derive the explicit connections with the vertex functions used in D-TRILEX and those computed in w2dynamics. We report them, as different choices of the order of the operators in the definition of the correlation functions used in other software packages require similar manipulations. In the following, we omit time-ordering operators in the correlation functions and we define the combined indices $a = \{l_a, \sigma_a, \tau_a\}$ to simplify the notation. Here, we assume the paramagnetic case. Similar considerations hold for the polarized case, but the derivation needs some small modifications, as we cannot simply average over spin.

In w2dynamics, the impurity two-particle Green's function with one bosonic frequency is computed as the integral

$$G^{\text{w2dyn}}_{abcd,\omega} = \int_0^\beta d\tau e^{i\omega\tau} \langle T_\tau d_a(\tau) d_b^\dagger(\tau) d_c d_d^\dagger \rangle. \tag{4.75}$$

In D-TRILEX, the impurity susceptibility is defined as

$$\chi^{ph}_{abcd} = -\langle \rho^{ph}_{ba} \rho^{ph}_{cd} \rangle. \tag{4.76}$$

Inserting $\rho = n - \langle n \rangle$, we arrive at

$$\chi^{ph}_{abcd} = -\langle n^{ph}_{ba} n^{ph}_{cd} \rangle + \langle n^{ph}_{ba} \rangle \langle n^{ph}_{cd} \rangle. \tag{4.77}$$

If we explicitly insert the density channel, we have

$$\chi^{d}_{abcd} = -\langle n^{d}_{ba} n^{d}_{cd} \rangle + n_{ba} n_{cd}, \tag{4.78}$$

where the disconnected term is written in a way that includes the possibility for off-diagonal contributions to the density.

Here, we make the dependence on spin explicit, so that the Latin indices do not carry spin σ_a anymore for the rest of the derivation. Additionally, we define the impurity density matrix as

$$n_{ab} \equiv \langle n^{d}_{ab} \rangle = n_{ab,\uparrow} + n_{ab,\downarrow}. \tag{4.79}$$

In usual cases, where the dispersion is constant and so is the hybridization function of the impurity problem, we can replace the local density matrix with the occupation of the orbital as $n_{ab} = n_a \delta_{ab}$.

The very same steps can be repeated in the magnetic channel, where we have

$$\chi^{m}_{abcd} = -\langle n^{m}_{ba} n^{m}_{cd} \rangle = -\langle m_{ba} m_{cd} \rangle + m_{ba} m_{cd}. \tag{4.80}$$

Here the disconnected term $m_{ba} m_{cd}$ vanishes, since the expectation value of the magnetization is zero in the paramagnetic regime.

Unfortunately w2dynamics measures not $\langle d^\dagger d d^\dagger d \rangle$, but $\langle d d^\dagger d d^\dagger \rangle$. That means that we have to transform the expectation value $\langle nn \rangle$ to this operator ordering. This has to be done outside the path integral formalism. This is a tricky point. In the path integral formalism, we are allowed to swap operators appearing in the action or due to expansions of the the exponent, but we are not allowed to swap the operators appearing in the expectation value, since a time-ordering is implied. The commutation of these operators has to be performed

in the operatorial formalism.

$$
\begin{aligned}
\langle n_{ba}^{d/m} n_{cd}^{d/m} \rangle &= \langle (d_{b\uparrow}^\dagger d_{a\uparrow} \pm d_{b\downarrow}^\dagger d_{a\downarrow})(d_{c\uparrow}^\dagger d_{d\uparrow} \pm d_{c\downarrow}^\dagger d_{d\downarrow}) \rangle \\
&= \langle d_{b\uparrow}^\dagger d_{a\uparrow} d_{c\uparrow}^\dagger d_{d\uparrow} \pm d_{b\uparrow}^\dagger d_{a\uparrow} d_{c\downarrow}^\dagger d_{d\downarrow} \pm d_{b\downarrow}^\dagger d_{a\downarrow} d_{c\uparrow}^\dagger d_{d\uparrow} + d_{b\downarrow}^\dagger d_{a\downarrow} d_{c\downarrow}^\dagger d_{d\downarrow} \rangle \\
&= \langle ((\delta_{ab} - d_{a\uparrow} d_{b\uparrow}^\dagger)(\delta_{cd} - d_{d\uparrow} d_{c\uparrow}^\dagger) \pm (\delta_{ab} - d_{a\uparrow} d_{b\uparrow}^\dagger)(\delta_{cd} - d_{d\downarrow} d_{c\downarrow}^\dagger) \\
&\quad \pm (\delta_{ab} - d_{a\downarrow} d_{b\downarrow}^\dagger)(\delta_{cd} - d_{d\uparrow} d_{c\uparrow}^\dagger) + (\delta_{ab} - d_{a\downarrow} d_{b\downarrow}^\dagger)(\delta_{cd} - d_{d\downarrow} d_{c\downarrow}^\dagger)) \rangle \\
&= \langle 2\delta_{ab}\delta_{cd}(1 \pm 1) \\
&\quad - \delta_{ab}(d_{d\uparrow} d_{c\uparrow}^\dagger + d_{d\downarrow} d_{c\downarrow}^\dagger \pm d_{d\downarrow} d_{c\downarrow}^\dagger \pm d_{d\uparrow} d_{c\uparrow}^\dagger) \\
&\quad - \delta_{cd}(d_{a\uparrow} d_{b\uparrow}^\dagger + d_{a\downarrow} d_{b\downarrow}^\dagger \pm d_{a\uparrow} d_{b\uparrow}^\dagger \pm d_{a\downarrow} d_{b\downarrow}^\dagger) \\
&\quad + d_{a\uparrow} d_{b\uparrow}^\dagger d_{d\uparrow} d_{c\uparrow}^\dagger \pm d_{a\uparrow} d_{b\uparrow}^\dagger d_{d\downarrow} d_{c\downarrow}^\dagger \pm d_{a\downarrow} d_{b\downarrow}^\dagger d_{d\uparrow} d_{c\uparrow}^\dagger + d_{a\downarrow} d_{b\downarrow}^\dagger d_{d\downarrow} d_{c\downarrow}^\dagger \rangle \\
&= 2\delta_{ab}\delta_{cd}(1 \pm 1) \\
&\quad - \delta_{ab}(1 \pm 1)(\langle d_{d\uparrow} d_{c\uparrow}^\dagger \rangle + \langle d_{d\downarrow} d_{c\downarrow}^\dagger \rangle) - \delta_{cd}(1 \pm 1)(\langle d_{a\uparrow} d_{b\uparrow}^\dagger \rangle + \langle d_{a\downarrow} d_{b\downarrow}^\dagger \rangle) \\
&\quad + \langle d_{a\uparrow} d_{b\uparrow}^\dagger d_{d\uparrow} d_{c\uparrow}^\dagger \pm d_{a\uparrow} d_{b\uparrow}^\dagger d_{d\downarrow} d_{c\downarrow}^\dagger \pm d_{a\downarrow} d_{b\downarrow}^\dagger d_{d\uparrow} d_{c\uparrow}^\dagger + d_{a\downarrow} d_{b\downarrow}^\dagger d_{d\downarrow} d_{c\downarrow}^\dagger \rangle
\end{aligned} \tag{4.81}
$$

Now, we can add and subtract the densities

$$
\begin{aligned}
\langle n_{ba}^{d/m} n_{cd}^{d/m} \rangle &= 2\delta_{ab}\delta_{cd}(1 \pm 1) - \delta_{ab}(1 \pm 1)\, n_{cd} - \delta_{cd}(1 \pm 1)\, n_{ba} \\
&\quad + \langle d_{a\uparrow} d_{b\uparrow}^\dagger d_{d\uparrow} d_{c\uparrow}^\dagger \pm d_{a\uparrow} d_{b\uparrow}^\dagger d_{d\downarrow} d_{c\downarrow}^\dagger \pm d_{a\downarrow} d_{b\downarrow}^\dagger d_{d\uparrow} d_{c\uparrow}^\dagger + d_{a\downarrow} d_{b\downarrow}^\dagger d_{d\downarrow} d_{c\downarrow}^\dagger \rangle
\end{aligned} \tag{4.82}
$$

where again we have used the spin-summed occupation $n_{ba} = \langle n_{ba\uparrow} + n_{ba\downarrow} \rangle$. Altogether the density susceptibility is

$$
\chi_{abcd}^d = n_{ba} n_{cd} - 2\delta_{ab}(\delta_{cd} - n_{cd}) - 2\delta_{cd}(\delta_{ab} - n_{ba}) - \sum_{\sigma\sigma'} \langle d_{a\sigma} d_{b\sigma}^\dagger d_{d\sigma'} d_{c\sigma'}^\dagger \rangle \tag{4.83}
$$

and the magnetic susceptibility is

$$
\chi_{abcd}^m = - \sum_{\sigma\sigma'} (-1)^{\sigma+\sigma'} \langle d_{a\sigma} d_{b\sigma}^\dagger d_{d\sigma'} d_{c\sigma'}^\dagger \rangle. \tag{4.84}
$$

The symbol $(-1)^{\sigma+\sigma'}$ gives $+1$ if both spins are equal, and (-1) if they are opposite.

4.6.2   Calculation of the impurity three-point correlation function

In w2dynamics, the impurity two-particle Green's function with one fermionic and one bosonic frequency is defined as

$$G^{\nu\omega}_{abcd} = \frac{1}{\beta} \int_0^\beta d\tau_1 d\tau_2 d\tau_3 e^{i\nu\tau_1 - i(\nu-\omega)\tau_2 - i\omega\tau_3} \langle T_\tau d_a(\tau_1) d_b^\dagger(\tau_2) d_c(\tau_3) d_d^\dagger(\tau_3)\rangle \qquad (4.85)$$

In order to compute the impurity three-point vertex defined in Eq. (4.17)-(4.19), we additionally need the impurity three-point correlation function $L^{d/m}_{abcd}$, defined as

$$L^{d/m}_{abcd} = \langle d_{a\uparrow} d_{b\uparrow}^\dagger \rho^{d/m}_{cd}\rangle. \qquad (4.86)$$

Again, the time/frequency dependence is omitted for a clearer notation. In the following, keep in mind, that the second operator pair is at equal time. We have to bring this to a form that depends only on correlation functions that we directly obtain in quantum Monte Carlo. This requires a modification of the ordering of the operators, as follows

$$
\begin{aligned}
L^{d/m}_{abcd} &= \langle d_{a\uparrow} d_{b\uparrow}^\dagger \rho^{d/m}_{cd}\rangle \\
&= \langle d_{a\uparrow} d_{b\uparrow}^\dagger n^{d/m}_{cd}\rangle - \langle d_{a\uparrow} d_{b\uparrow}^\dagger\rangle\langle n^{d/m}_{cd}\rangle \\
&= \langle d_{a\uparrow} d_{b\uparrow}^\dagger [d_{c\uparrow}^\dagger d_{d\uparrow} \pm d_{c\downarrow}^\dagger d_{d\downarrow}]\rangle - \langle d_{a\uparrow} d_{b\uparrow}^\dagger\rangle\langle n^{d/m}_{cd}\rangle \\
&= \langle d_{a\uparrow} d_{b\uparrow}^\dagger [\delta_{cd} - d_{d\uparrow} d_{c\uparrow}^\dagger \pm (\delta_{cd} - d_{d\downarrow} d_{c\downarrow}^\dagger)]\rangle - \langle d_{a\uparrow} d_{b\uparrow}^\dagger\rangle\langle n^{d/m}_{cd}\rangle \\
&= \delta_{cd}(1 \pm 1)\langle d_{a\uparrow} d_{b\uparrow}^\dagger\rangle - [\langle d_{a\uparrow} d_{b\uparrow}^\dagger d_{d\uparrow} d_{c\uparrow}^\dagger\rangle \pm \langle d_{a\uparrow} d_{b\uparrow}^\dagger d_{d\downarrow} d_{c\downarrow}^\dagger\rangle] - \langle d_{a\uparrow} d_{b\uparrow}^\dagger\rangle\langle n^{d/m}_{cd}\rangle \\
&= \delta_{ab}\delta_{cd}\langle d_{a\uparrow} d_{b\uparrow}^\dagger\rangle[(1 \pm 1) - \langle n^{d/m}_{cd}\rangle] - [\langle d_{a\uparrow} d_{b\uparrow}^\dagger d_{d\uparrow} d_{c\uparrow}^\dagger\rangle \pm \langle d_{a\uparrow} d_{b\uparrow}^\dagger d_{d\downarrow} d_{c\downarrow}^\dagger\rangle] \qquad (4.87)
\end{aligned}
$$

In the density channel this amounts to

$$L^d_{abcd} = -G_{ab}(2\delta_{cd} - n_{cd}) - [\langle d_{a\uparrow} d_{b\uparrow}^\dagger d_{d\uparrow} d_{c\uparrow}^\dagger\rangle + \langle d_{a\uparrow} d_{b\uparrow}^\dagger d_{d\downarrow} d_{c\downarrow}^\dagger\rangle] \qquad (4.88)$$

and in the magnetic channel

$$L^m_{abcd} = -[\langle d_{a\uparrow} d_{b\uparrow}^\dagger d_{d\uparrow} d_{c\uparrow}^\dagger\rangle - \langle d_{a\uparrow} d_{b\uparrow}^\dagger d_{d\downarrow} d_{c\downarrow}^\dagger\rangle] \qquad (4.89)$$

We can now exploit spin-symmetry/paramagnetism to average over components:

$$L^d_{abcd} = -G_{ab}(2\delta_{cd} - n_{cd}) - \frac{1}{2}\sum_{\sigma\sigma'}\langle d_{a\sigma} d_{b\sigma}^\dagger d_{d\sigma'} d_{c\sigma'}^\dagger\rangle \qquad (4.90)$$

and

$$L^m_{abcd} = -\frac{1}{2}\sum_{\sigma\sigma'}(-1)^{\sigma+\sigma'}\langle d_{a\sigma}d^\dagger_{b\sigma}d_{d\sigma'}d^\dagger_{c\sigma'}\rangle \tag{4.91}$$

A multiplicative factor β has to be introduced, because the definition of the correlation function in w2dynamics is divided by that factor.

5 Diagrammatic Monte Carlo for dual theories

5.1   The DiagMC algorithm

5.1.1   A scheme for summing up all the Feynman diagrams

In this section, we summarize a technique originally introduced by N. Prokof'ev and B. Svistunov [276] to numerically evaluate a perturbation expansion up to an arbitrary order, dubbed diagrammatic Monte Carlo method (DiagMC). The difference between DiagMC and other QMC algorithms is that QMC algorithms usually explore the configurations based on the probability distribution of the diagrams of the partition function, while DiagMC draws samples from the probability distribution of the diagrams of the observable of interest. This is a crucial difference, because the former is an extensive quantity that depends on the size of the system, while the observables do not depend on the size. As a consequence, DiagMC can be applied directly in the thermodynamic limit.

In this thesis, this idea is applied to the calculation of the dual self-energy of dual theories. As the perturbative series is a Taylor expansion of an analytical function, it can be shown that the result of summing up the series coincides with the value of the function at the point where the series is computed, as long as the point lies within its convergence radius. If this condition is met, the result of diagrammatic Monte Carlo is exact and unbiased. Additionally, it is possible to give an upper bound to the error by analysing the convergence order-by-order, as opposed to the usual techniques such as second-order perturbation theory or theories based on certain subsets of diagrams, like the ladder approximation. The main idea behind the DiagMC method is to rephrase perturbation theory in terms of Feynman diagrams. As discussed in previous sections, Feynman diagrams at arbitrary order can be constructed by following simple graphical rules. In the specific case of a quartic interaction term, as for instance both the extended Hubbard model and the DF

action with only four-point vertices, the diagrammatic elements in the simplest scheme are a line corresponding to bare fermionic propagator and a vertex with four legs corresponding to the interaction. This method is of particular interest, because it is exact, it works in the thermodynamic limit and it is not plagued by the infamous sign problem to the same extent as most of the other Monte Carlo methods when applied to many-particle fermionic systems [4, 81, 277, 278].

The application of this technique to the dual boson action requires a truncation of the infinite series of interaction terms. Here, we truncate the expansion at the two-particle level, so we stick to Eq. (4.15) of Sect. 4.2.1. By doing that, we sacrifice the "exactness" of the method to some extent, as we do not get an exact solution of the original lattice problem. However, we do still obtain an exact solution of the dual action at the two-particle level and we can estimate the impact of considering only certain classes of dual diagrams on the solution of that action, as discussed in Refs. [221, 230, 232]. Additionally, here we consider only the original bare and "semi-bold" DiagMC scheme of Ref. [279] for reasons that will be clarified later. In this section, we follow very closely the work presented by the author of this thesis and collaborators in Ref. [230].

5.1.2 The Metropolis-Hastings algorithm in a nutshell

When dealing with summations of Feynman diagrams, it is necessary to compute high-dimensional summations/integrals and also it is necessary to explore a large space of different diagram topologies. This becomes quickly unfeasible by using direct summation and deterministic quadrature schemes. However, there is a useful tool that can deal with summations over very large configuration spaces, namely the class of Markov chain Monte Carlo methods (MCMC), which is one of the most successful and widely used schemes in computational sciences. A detailed description of the method at the textbook level can be found in Ref. [280].

The MCMC allows to evaluate summations over multi-dimensional configuration spaces of both discrete and continuous variables in the form

$$\mathcal{I}_p = \sum_C f_C \, p_C. \tag{5.1}$$

As highlighted, it is necessary to split the integral into an integrand function f and a probability (distribution) p, which is characterised by the property of being real, positive and bounded. The idea of MCMC is to generate a random sequence of configurations $c_i = \{C\}$ for $i = 0, ..., M$ steps according to some rules and to sample from this sequence, in such a way that the expectation value $\langle f \rangle_{\text{MC}}$ over the sequence converges to the value of

the integral as the number of Monte Carlo steps M is increased

$$\lim_{M \to +\infty} \langle f \rangle_{\text{MC}} \equiv \mathcal{I}_p. \tag{5.2}$$

As the name of the method suggests, this sequence is chosen to be a Markov chain, which is a discrete stochastic process in which the conditional probability of generating any element c_{i+1} at the $(i + 1)$-th step depends only on the element c_i at the previous step.

In order to correctly reproduce the quantity $\mathcal{I}_p$, the generated Markov chain must reproduce the distribution p_C as $M \to +\infty$. In order for that to be true, we need to enforce two conditions:

1. the Markov chain $\{c_i\}$ is ergodic, meaning that system is able to explore all the available configurations and it does not get stuck in any specific of them. In other words, the Markov chain is non-periodic.

2. the detailed balance condition is satisfied, namely $P(c_{i+1} = C|c_i = \overline{C})\, p_{\overline{C}} = P(c_{i+1} = \overline{C}|c_i = C)\, p_C$.

The first condition is necessary in order to explore the role of all the configurations. Instead, the second condition is sufficient [281] and there are schemes that are based on weaker conditions (see for instance [282]).

In particular, we stick to the original choice of the Metropolis-Hastings technique [283, 284] to perform a high-dimensional summation [285]. Other possibilities to sum over the diagrams using quasi-Monte Carlo techniques based on low-discrepancy sequences have been recently suggested [286].

The Metropolis-Hastings (MH) algorithm provides an explicit rule for constructing a Markov chain, that respects the detailed balance condition (see Ref. [284]) and has the correct probability distribution, given that the updates are designed in such a way that all the configurations are accessible. Explicitly, the Markov chain is constructed as follows:

1. At the i-th step, the configuration is $c_i = C$.

2. A new configuration $c_p = \overline{C}$ is randomly proposed.

3. the probability of accepting a move $R_{C \to \overline{C}}$ from the current configuration c_i to the proposed configuration c_p is computed, according to the formula

$$R_{C \to \overline{C}} = \min \left\{ 1, \frac{\mathcal{P}(C|\overline{C})}{\mathcal{P}(\overline{C}|C)} \cdot \frac{p_{\overline{C}}}{p_C} \right\}, \tag{5.3}$$

where p_C and $p_{\overline{C}}$ are the probabilities of the initial and proposed configuration respectively.

4. After the acceptance probability is computed, the proposed configuration $\overline{C}$ is chosen as a new configuration with probability $R_{C \rightarrow \overline{C}}$. This means that a random number u is generated from the uniform distribution in the interval $[0, 1]$. If $u \leq R_{C \rightarrow \overline{C}}$, the move is accepted and the configuration $c_{i+1} = \overline{C}$ becomes the next configuration. Otherwise, the next configuration is chosen to be equal to the old one $c_{i+1} = C$.

5. After the update, the measurements are performed on the new configuration c_{i+1}.

The Metropolis-Hastings algorithm has become one of the most successful algorithms for estimating high-dimensional sums and integrals due to its simplicity, the various techniques to estimate the error and the generality of the scheme.

5.1.3   DiagMC for fermions with quartic interaction

Here we present the DiagMC algorithm for fermions with a general quartic interaction, as introduced originally in Refs. [287, 288]. Any action defined on lattice in the form

$$\mathcal{S}_\xi[c, c^*] = - \sum_{ij} c_i^\dagger \, G_{ij}^{-1} \, c_j + \frac{\xi}{2} \sum_{ijkl} \Gamma_{ijkl} c_i^\dagger c_j^\dagger c_l c_k \qquad (5.4)$$

where G_{ij} is the single particle Green's function, Γ_{ijkl} is the interaction vertex and ξ is a complex parameter that controls the convergence. The case $\xi = 1$ corresponds to the physical action. Any correlation function can be expressed as a perturbative series in terms of the parameter ξ within the convergence radius of the series $|\xi| < R$ for some $R \geq 0$. The case we are interested in is when $R > 0$, meaning that the perturbative series in convergent in some region around $\xi = 0$. The convergence radius of diagrammatic series can in principle present a null convergence radius, as pointed out originally by Dyson in his paper about the convergence of the diagrammatic series in Quantum Electrodynamics (QED) [289]. Contrary to QED, lattice problems have a bounded spectrum so there are no issues with ultraviolet divergencies. Additionally, it was later proven mathematically that the convergence radius of the diagrammatic series on a discrete lattice at large enough temperature compared to the interaction strength is always larger than 0 [290].

The first step of the method is to define the partial summation of Feynman diagrams $O_{N_{max}}$ corresponding to the quantity O, with increasing number of vertices N_{max}, as

$$O_{N_{max}}(y) = \sum_{n=0}^{N_{max}} \sum_{\{x_i\}, C_n} \mathcal{D}_{C_n}(\{x_i\}, y) \, \xi^n. \qquad (5.5)$$

In this expression, the term $\mathcal{D}_{C_n}$ is the value of the diagram corresponding to a given topology C_n, while y is a combined index that collects all the dependence on the external legs, n indicates the number of vertices that appear in the diagram and $\mathcal{D}_{C_n}$ is the value

of a specific diagram. Additionally x_i is shorthand notation for the internal degrees of freedom, that can be for example $(i, \tau, \sigma)_i$ corresponding to band-site index, time and spin that originate from the presence of loops of Green's functions. If the indices vary over a continuous range, as in the case of time or momentum components, the corresponding summation has to be converted into an integral.

Since the reference action $\mathcal{S}_0[c, c^*] = -\sum_{ij} c_i^\dagger G_{ij}^{-1} c_j$ is quadratic, we can apply Wick's theorem to compute the numerical value of each diagram as products of bare Green's functions G_{ij} and vertices Γ_{ijkl} only. This means that the diagrammatic expansion of this action is characterised by lines that connect vertices with 4 corners. Each line is directed and each vertex has two slots for the incoming (outgoing) lines corresponding to the destruction (creation) operators.

In the limit of infinite $N_{max} \to +\infty$, the series of Eq. (5.5) converges to the exact value of the observable O

$$O(y) = \lim_{N_{max} \to +\infty} O_{N_{max}}(y), \tag{5.6}$$

provided that the limit in Eq. (5.5) is well defined and convergent for the chosen parameters as $N_{max} \to +\infty$. Divergencies of the diagrammatic series are often related to physical instabilities or to some unphysical behavior of the starting point, for example the antiferromagnetic phase transition of DMFT [221].

In the DiagMC method, we aim at summing up the series in Eq. (5.5) numerically. However, the direct computation of the series by numerical quadrature and summations is impossible. The reasons are that at any order of the perturbation expansion, the number of diagram topologies in general increases as $(2n)!$, which are the permutations of $2n$ directed connections between n vertices with 2 incoming and 2 outgoing slots. In the case of the Hubbard model, thanks to the simple form of the interaction, the scaling is significantly reduced to $(n!)^2$ as explained in Ref. [291], but it remains still factorial in the number of diagrams. More details about the counting of Feynman diagrams can be found in Ref. [292]. This is a manifestation of the fermionic sign problem and makes the sampling time needed for an accurate estimation of the series longer and longer as the order increases. Even without this fundamental issue, that intrinsically limits the maximum order N_{max} that can be reasonably reached with this method, the number of internal degrees of freedom involved in Eq. (5.5) makes any deterministic evaluation of the first few diagrams of the series impractical already at relatively low orders. If we consider a single diagram with two external legs, quartic interactions and n vertices, the number of loops L is equal to the number of vertices $L = n$. Each loop introduces a free summation over sites (or momentum) and over time (or frequency), introducing at least a total number of $n \times (D + 1)$ degrees of freedom to sum over.

The idea of DiagMC is to alleviate this "curse of dimensionality" in the evaluation of the terms by using the Metropolis-Hastings algorithm to construct all the Feynman

diagrams up to any finite order. However, the terms $\mathcal{D}_{C_n}$ are not necessarily real in general and for sure not positive for fermions. For this reason, the value of a diagram needs to be split into its absolute value and a complex phase factor, which in this context is called the complex sign, as follows

$$\mathcal{D}_{C_n}(\{x_i\}, y) = \text{sgn}\left(\mathcal{D}_{C_n}(\{x_i\}, y)\right) \cdot \left|\mathcal{D}_{C_n}(\{x_i\}, y)\right|. \tag{5.7}$$

By performing this splitting, the quantity $\left|\mathcal{D}_{C_n}(\{x_i\}, y)\right|$ has the correct properties to be identified as a probability distribution, hence we can apply the method.

The summation over the perturbation order n, topologies and internal degrees of freedom is performed using a Metropolis-Hastings scheme [285], where the function to be sampled is the $\text{sgn}\left(\mathcal{D}_{C_n}(\{x_i\}, y)\right)$, and the probability distribution is given by the amplitude $\left|\mathcal{D}_{C_n}(\{x_i\}, y)\right|$ in order to respect the requirement of positive weight function.

Following the original implementation by Gukelberger (see Ref. [293]), each configuration C corresponds to a directed graph, which is identified by an ordered set of vertices $V_1, V_2, ..., V_n$, with n the order of the diagram. In order to uniquely represent the graph, we also have to attach information about the connection of each vertex with the others. Each of four slots of a vertex is connected to another slot of a vertex, that can be the same or a different one. The four possible slot positions of a vertex are $p \in \{\text{NE}, \text{SE}, \text{NW}, \text{SW}\}$ corresponding to the cardinal positions. The information about the connections of a vertex is stored by attaching the id number of the neighboring vertex and its slot id to each slot of each vertex $V_m = \left(s_{\text{NE}}^{(m)}, s_{\text{SE}}^{(m)}, s_{\text{NW}}^{(m)}, s_{\text{SW}}^{(m)}\right)$, where each slot carries the index and the neighbor identification number $s_p^{(m)} = (i, V_i, p_i)$. This is enough to fully characterize a diagram since the value of a vertex is simply $\Gamma_{ijkl} = \Gamma(V_m)$ and the bare Green's functions can be computed by retrieving the incoming/outgoing indices of the vertices $G_{ij} = G(V_{\text{out}}, V_{\text{in}})$.

This representation gives an intuitive and efficient picture that allows us to design the updates so that all the contributions to the expansion (5.5) can be generated by changing how the vertices are connected to each other by means of the bare Green's functions. One efficient way of updating the configuration in the bare diagrammatic Monte Carlo algorithm is the worm algorithm used in Ref. [221], as described later in the Section. This algorithm is based on the evaluation of topologies one by one, by means of local updates. The advantage is that only a small subset of elements of the diagram have to be recomputed and updated. The drawback is that the sampling has to explore the full space with a factorially growing number of topologies. The grouping of different topologies of diagrams into a single class of diagrams that could be sampled at once (like the Hugenholz diagrams) could improve the algorithm. Indeed, efficient algorithms that express all connected diagrams of the perturbative expansion with different topologies up to a given order have been developed by using determinants [294] for various observables and correlation functions [295–298]. The use of connected determinants significantly reduces the computational cost of the calculation and increases substantially the maximum order that can be

reached [299]. A detailed description of the CDet method and of DiagMC schemes based on bold series can be found in ref. [291].

5.1.4 Worm algorithm and updates in DiagMC

In our implementation, we work in momentum and frequency-space. The worm algorithm is needed in our implementation as it allows to enforce momentum conservation, which is a non-local property of the diagram, by means of updates that act locally on few elements of a diagram [221]. As a consequence, the number of floating point operations at each step of the MH algorithm is dramatically reduced. The Worm algorithm introduces a set of unphysical updates that allow the transition between all the different possible topologies contributing to a given observable. In particular, these updates introduce a fictitious propagator, the "worm", which carries a frequency-momentum $\delta = (\nu_\delta, \mathbf{k}_\delta)$. The introduction of the worm itself violates Matsubara frequency and momentum conservation. However, it allows to switch between configurations where the frequency and momentum are conserved. In our implementation, there are two different sectors of the configuration space: the physical one with no worm where the measurements can occur, and the worm space, which is used to explore the configurations and topologies.

Since the DiagMC explicitly handles a single diagram at a time, it is possible to explicitly reduce the number of topologies considered by introducing appropriate checks. This allows for example to compute the self-energy, which is the sum of all the one-particle irreducible diagrams with two external legs, and two-particle irreducible quantities directly [293]. This means that we sample all the diagrams with one incoming and one outgoing line that are also irreducible with respect to a cut of a fermionic line. This can be practically implemented by imposing the condition that no internal line can carry the same momentum and frequency dependence of the external lines. Of course, this excludes some valid diagrams that by accident carry the same momentum and frequency, but the set of these contributions has zero measure in momentum space, hence it does not change the value of the integral.

We provide a quick overview of the updates used to switch between different configurations. The set of updates that we use is the same proposed in Ref. [221], so we follow closely what was presented there. A diagrammatic sketch of the main updates is provided in Fig. 5.1. Here, we already denote the propagator lines with the symbol for the dual Green's function $\tilde{G}$ and the vertices are indicated as Γ, but this set of updates is valid also for other actions in momentum space, such as the Hubbard model.

Create/Delete Worms (CWO/DWO)   This update is needed to switch between the space of the physical diagrams and the unphysical worm sector. If the diagram already has a worm, the CWO update is directly rejected. Otherwise, a random corner of a random vertex is chosen with both ends attached there. The momentum and the frequency of the
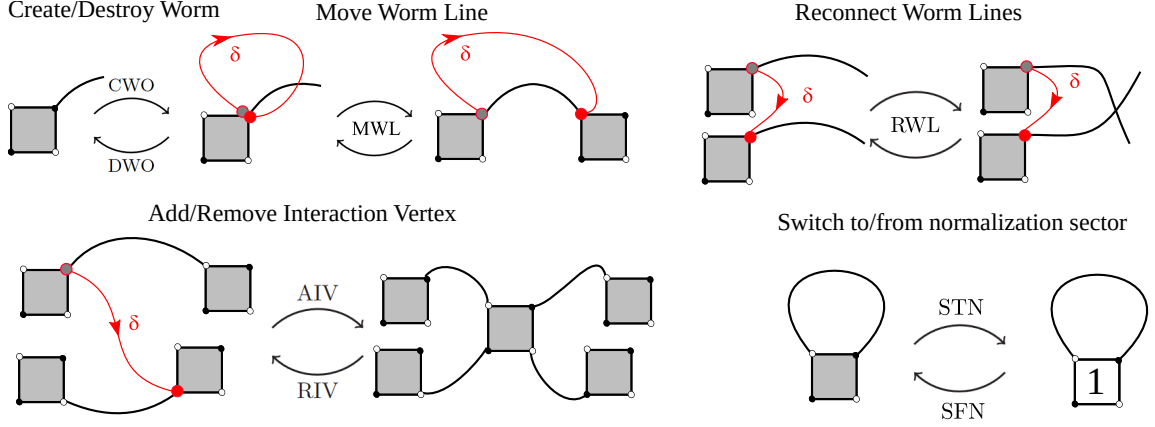
FIGURE 5.1: Summary of the main updates in our implementation of DiagMC based on the worm algorithm. The worm is described by a direct red line that carries an unphysical frequency-momentum δ. Grey boxes indicate fermion-fermion vertices, while the white box indicates a vertex that evaluates to 1 whenever frequency-momentum conservation is respected.

worm are drawn from a uniform distribution over the BZ P_δ and from a discrete set of bosonic frequencies $-\omega_{N_\Delta}, \ldots, \omega_{N_\Delta}$ with $P_\Delta = 1/(2N_\Delta + 1)$. The proposal probability for a specific CWO move is hence $\mathcal{P}_{\text{CWO}} = P_\delta P_\Delta/4n$, where n denotes the number of vertices in the current diagram. The converse DWO update is accepted with $\mathcal{P}_{\text{DWO}} = 1$ if the two ends of the worm are on the same corner of the same vertex, and rejected otherwise. Since the worm sector is unphysical, we can add an arbitrary weight factor $C_W(n, \delta)$.

Now, we can construct the acceptance ratio by imposing the detailed balance between these updates

$$R_{\text{CWO}} \equiv \frac{\mathcal{A}_{\text{CWO}}}{\mathcal{A}_{\text{DWO}}} = \frac{1}{R_{\text{DWO}}} = \frac{\mathcal{P}_{\text{DWO}}}{\mathcal{P}_{\text{CWO}}} C_W(n, \delta) = \frac{4n C_W(n, \delta)}{P_{\vec{\delta}} P_\Delta}. \tag{5.8}$$

With the choice $C_W(n, \delta) = P_\delta P_\Delta/4n$ all the allowed updates are accepted, maximizing the sampling efficiency.

Move Worm along Line/Vertically/Horizontally (MWL/MWV/MWH)   Once a worm is created, one of its ends can be randomly chosen with probability 1/2 and it can be moved to a neighboring corner of the same vertex or along the propagator line to the corner of the neighbor vertex, keeping in mind that the worm behaves as a propagator. The convention is that any excess frequency enters the diagram between the end of the propagator and the (amputated) leg of the vertex.

The resulting acceptance ratios are then

$$R_{\text{MWL}} = \tilde{G}'/\tilde{G}, \qquad\qquad R_{\text{MWV}} = \Gamma'/\Gamma = R_{\text{MWH}}, \qquad\qquad (5.9)$$

where $\tilde{G} = \tilde{G}_{\mathbf{k}\nu\sigma}$ and $\tilde{G}' = \tilde{G}_{\mathbf{k}\pm\delta,\nu\pm\Delta,\sigma}$ denote the propagators with old and new 4-momentum indices, respectively, and correspondingly for the vertex.

Reconnect Worm Lines (RWL)   This update allows to change the topology of the diagrams and is possible only if both ends of the worm are at the beginning of a propagator line. The two ends of the propagators located at the position of the two worm ends are swapped and the frequency-momentum of the worm is modified by the difference $k - k'$ between the two lines. Additionally, the number of fermionic loops always changes by ± 1, so a -1 sign has to be included. Again, this update is its own inverse update and reads

$$R_{\text{RWL}} = -C_W(n, \delta')/C_W(n, \delta). \qquad\qquad (5.10)$$

With the above choice for C_W, $|R_{\text{RWL}}| = 1$ unless the new excess frequency would be too large and $P_{\Delta'} = C_W(n, \delta') = 0$.

Add/Remove Interaction Vertex (AIV/RIV)   The AIV and the RIV updates allow to increase or decrease the diagram order n by one respectively. Without focusing on the details, the AIV removes a worm and adds a four-fermion vertex Γ instead, while the RIV removes a vertex and replaces it with a worm carrying the bosonic frequency and the exchanged momentum of the removed vertex Γ.

Taking into account that adding/removing a vertex changes the number of loops, hence it increases/decreases the number of summations over momentum and frequency, we have to multiply/divide by a factor $-T/V_{\text{BZ}}$ where V_{BZ} is the volume of the Brillouin zone.

The final expression for the acceptance ratio reads

$$R_{\text{AIV}} = \frac{1/4n}{1/(2-\delta_{\sigma\sigma'})} \cdot \frac{-s_F T\Gamma'\left(\prod_{i=1}^{4}\tilde{G}'_i\right)/V_{\text{BZ}}}{\left(\prod_{i=1}^{2}\tilde{G}_i\right)C_W(n,\delta)} = -\frac{s_F(2-\delta_{\sigma\sigma'})T\Gamma'\left(\prod_{i=1}^{4}\tilde{G}'_i\right)}{4V_{\text{BZ}}n\left(\prod_{i=1}^{2}\tilde{G}_i\right)C_W(n,\delta)}, \qquad (5.11)$$

where $s_F = -1$ if the updates change the number of fermion loops and $+1$ otherwise, n is the diagram order before the AIV update, the primed quantities denote the vertex and propagators inserted by AIV, and the non-primed $\tilde{G}_i$ the replaced propagators.

Switch To/From Normalization sector (STN/SFN)   Since the Metropolis algorithm samples the integral up to an unknown constant, this update designed to keep track of

this constant. A possible strategy to achieve this goal is to select a specific configuration that can be computed directly and sample it.

In our case, we introduce an unphysical diagram, that can be easily computed explicitly outside Monte Carlo, and we store its value in a suitable accumulator N_{norm}. The chosen diagram is simply a single vertex with unitary value with the upper corners connected by a single bare dual Green's function. Its value is given by

$$\mathcal{N} = \sum_{\mathbf{k}\nu} \left| \tilde{\mathcal{G}}_{\mathbf{k}\nu} \right|, \tag{5.12}$$

which is computed directly from the analytical expression for the bare dual propagator $\tilde{\mathcal{G}}$. The normalized dual self-energy $\tilde{\Sigma}_{\mathbf{k}\nu}$ is then straightforwardly computed from the normalization accumulator N_{norm} using the following equation

$$\tilde{\Sigma}_{\mathbf{k}\nu} = \frac{\mathcal{N}}{N_{\text{norm}}} \left\langle \tilde{\Sigma}_{\mathbf{k}\nu} \right\rangle_{\text{MC}}. \tag{5.13}$$

Given this choice of the normalization diagram, this move to the unphysical normalization space can occur only if the diagram order is $n = 1$. In the STN, a Γ vertex is replaced by an identity vertex $\mathbb{1}$. The converse update replaces a $\mathbb{1}$ vertex by a Γ vertex and spin is randomly chosen to improve ergodicity. We therefore have proposal probabilities $\mathcal{P}_{\text{STN}} = 1/2$ and $\mathcal{P}_{\text{SFN}} = 1/4$. Finally, the acceptance ratio reads

$$R_{\text{STN}} = \frac{\tilde{G}'}{2\Gamma\tilde{G}}. \tag{5.14}$$

In the paramagnetic phase, $\tilde{G}' = \tilde{G}$ and $R_{\text{STN}} = 1/(2\Gamma)$.

Swap Measuring Propagator (SMP)   A new propagator is chosen as the measuring propagator. This update simply improves the efficiency of the sampling. The acceptance ratio is given by

$$R_{\text{SMP}} = \frac{\tilde{G}'}{\tilde{G}} \tag{5.15}$$

where $\tilde{G}'$ is the value of the old measuring propagator, which was assigned the value of 1, and $\tilde{G}$ is the value of new measuring propagator, before it is assigned the value of 1.

5.2 DiagMC in dual space

5.2.1 Dual fermion DiagMC

Approaches based on a small-coupling expansion work very well in the regime of small to moderate couplings, but start to fail when U is of the order of half of the bandwidth [277, 300], no matter how efficiently the different topologies are sampled. These failures are related to the finite convergence radius of the diagrammatic series and can be improved using resummation techniques [295] or by using different reference points for the diagrammatic expansion [301]. However, no general recipe has so far been found to interpolate between the small and the large coupling regimes in all cases.

The DF technique, described in the Chapter 4, is a very promising tool to perform this interpolation between the weak and the strong coupling regimes. Indeed, diagrammatic Monte Carlo was applied to the dual fermion technique in Refs. [220, 221]. Additionally, it was used as a benchmark method in Ref. [232]. In analogy to the case of the dual boson action, the dual fermion action has an infinite series of interaction terms. These terms correspond to any even-legged fermionic correlation functions. In the following we restrict ourselves to the action truncated at the two-particle level. In this case, the action has the same shape as Eq. (5.4). The bare Green's function is the bare dual Green's function $\tilde{\mathcal{G}}$ while the vertex function is the 4-point vertex obtained from the impurity problem.

It is important to point out that in principle the DiagMC scheme is not limited to the case of a quartic interaction, but could be applied to the full series of interaction terms. Currently, the main limitation lies in the capability of accurately computing correlation functions with six or more external points using continuous-time quantum Monte Carlo codes, as discussed in the previous chapter.

Since our implementation is based on that of Ref. [221], it makes sense to quickly review the results obtained in that work, which enables us to describe the DiagMC for dual fermions (DiagMC@DF). The DiagMC@DF was compared with the Determinantal Diagrammatic Monte Carlo technique (DDMC) and with the ladder approximation to the dual fermion expansion. Following the notations introduced in Ref. [230], the quantity computed within DiagMC@DF is the dual self-energy, so the coefficients $a_n(\mathbf{k}, \nu)$ in the expansion of the dual self-energy

$$\tilde{\Sigma}_{\mathbf{k}\nu}(\xi) = \sum_{n=1}^{N_{max}} a_n(\mathbf{k}, \nu)\, \xi^n. \tag{5.16}$$

Even though the dual self-energy is not a correlation function of the dual theory, it is connected to the bare dual Green's function by a Dyson equation, hence it has an expansion in terms of Feynman diagrams in terms of one-particle irreducible diagrams, in the same way as its lattice counterpart.

The self-energy can be the computed using Eq. (4.65) together with the Dyson equation $G_{\mathbf{k}\nu}^{-1} = i\nu + \mu - h_{\mathbf{k}} - \Sigma_{\mathbf{k}\nu}$. In the simplest case of the single-band Hubbard model, this becomes simply

$$\Sigma_{\mathbf{k}\nu} = \Sigma_\nu^{\text{imp}} + \frac{\tilde{\Sigma}_{\mathbf{k}\nu}}{1 + g_\nu \tilde{\Sigma}_{\mathbf{k}\nu}}. \tag{5.17}$$

An important consideration that allows to reduce the number of the topologies that need to be sampled is that the bare dual Green's function based on a converged EDMFT impurity problem is completely non-local as a consequence of the EDMFT self-consistency conditions. Explicitly, this means that

$$\sum_{\mathbf{k}} \tilde{\mathcal{G}}_{\mathbf{k}\nu} = \left(\sum_{\mathbf{k}} G_{\mathbf{k}\nu}^{\text{EDMFT}} \right) - g_\nu = 0. \tag{5.18}$$

This allows to remove all the diagrams where a Green's function line has the two ends connected to the same local fermion-fermion vertex, the so-called tadpole diagrams, indicated as Σ^{td} in the following, since they involve expressions of the kind

$$\sum_{\mathbf{k}} \sum_{\nu} \Gamma_{\nu\nu'\omega}^{\sigma\sigma'\sigma''\sigma'''} \tilde{\mathcal{G}}_{\mathbf{k}\nu} = 0, \tag{5.19}$$

no matter how they are connected to the rest of the diagram. The property (5.19) does not hold if the reference impurity problem is chosen to be different from the (E)DMFT one.

Tadpole diagrams are important to ensure ergodicity and are useful to switch between physical and normalization sectors, due to their simple structure. However, simply avoiding measurements of the tadpole diagrams allows for a significant reduction of the number of measurements needed to reduce the error bars below a certain threshold. During our simulations, this reduction was up to an order or magnitude.

Results in Ref. [221] are shown at half-filling for the single-band Hubbard model on a square lattice. At the inverse temperature $\beta = 2$, the agreement with DDMC is within the error bars for all the value of the Hubbard interaction U. At lower temperature, however, a slower convergence or even divergence of the series (5.16) was observed. The divergence was related to the fact that the DMFT starting point exhibits an unphysical Neél temperature also in two-dimensions. Indeed, the lattice system has to obey the Mermin-Wagner theorem that forbids the breaking of continuous symmetries in one- and two-dimensional systems [255]. However, DMFT is exact in infinite dimensions and carries information about the antiferromagnetic broken-symmetry phase, that occurs in dimensions equal or larger than three [302]. Comparisons with the results for the DMFT Neél temperature shown in Ref. [303] seem to confirm this statement. This shows that one has to be careful in the choice of the starting point in the case of dual theories, in cases where the reference

problem breaks some fundamental symmetry of the system.

Calculations in the case of the doped Hubbard model are also reported in Ref. [221]. They demonstrate the validity of the method also away from half-filling. In that case, the DDMC method suffers from a severe sign problem that prevents its application. The DiagMC@DF results are benchmarked against bare DiagMC results, based on a weak coupling expansion [287, 288].

The measurement is performed in the space of Matsubara frequencies and irreducible representations of the momentum [293]. The different irreducible representations of momentum on the square lattice are $\Gamma = \{A1g, A2g, B1g, B2g, Eu_x, Eu_y\}$. the basis functions are given by $\psi_{l,m}^{(\gamma)}(\mathbf{k})$ with $\gamma \in \Gamma$ and l, m integers. These functions are simply symmetrized and real combinations of the functions e^{ilk_x} and e^{imk_y}, which respect the symmetries of the lattice. The projection of a function $f(\mathbf{k})$ on this complete and orthonormal basis set can be obtained as

$$f_{(l,m)}^{(\gamma)} = \sum_{\mathbf{k}} \psi_{l,m}^{(\gamma)}(\mathbf{k}) f(\mathbf{k}). \tag{5.20}$$

Analogously, the original function can be retrieved by its coefficients as

$$f(\mathbf{k}) = \sum_{\gamma \in \Gamma} \sum_{l,m} \psi_{l,m}^{(\gamma)}(\mathbf{k}) f_{(l,m)}^{(\gamma)}. \tag{5.21}$$

Conveniently, the (dual) self-energy is a function of the electronic dispersion. From group-theoretical arguments follows that the only non-zero contribution comes from basis functions corresponding to the $\gamma = A1g$ representation, also called s-wave symmetry. Instead of using two indices (l, m), we can also recall that the condition on the construction of these functions is $0 \le m \le l$, hence we can enumerate them with a single index i which follows $l + m$ and choosing the smaller l if the sum is the same for different cases. For example, we have that $i = 0 \rightarrow (0, 0)$, $i = 1 \rightarrow (1, 0)$, $i = 2 \rightarrow (1, 1)$, $i = 2 \rightarrow (2, 0)$ and so on. We can then measure the dual self-energy projected onto the i-th basis function $\psi_i^{(s)}(\mathbf{k})$ with $s-$symmetry by sampling the new coefficients within Monte Carlo

$$\tilde{\Sigma}_{N_{max}}(i, \nu; \xi) = \sum_{n=1}^{N_{max}} \left[\sum_{\mathbf{k}} a_n(\mathbf{k}, \nu)\psi_i^{(s)}(\mathbf{k}) \right] \xi^n = \sum_{n=1}^{N_{max}} a_n(i, \nu) \xi^n. \tag{5.22}$$

where we simply have applied Eq. (5.20) and have exploited the linearity of the projection. The self-energy of Eq.(5.16) in momentum space can be then obtained from Eq. (5.22) for any $\mathbf{k}$-point by applying Eq. (5.21). This allows to reduce the basis for measurements of several orders of magnitude by exploiting the symmetries of the lattice. Additionally, since the basis of irreducible representations is discrete, there is no need for an explicit binning of momentum space.

In practical calculations, a finite maximum number of basis functions has to be introduced. The number $i_{\max}$ of basis functions considered effectively acts as a cut-off in real-space and convergence as a function of the number of the number of basis functions has to be checked. This check was performed in the case of the dual fermion technique [221], where it was shown that 10 basis functions are sufficient to describe the behavior of the dual self-energy in all the cases considered there.

5.2.2 Introducing the dual bosons in the DiagMC scheme

FIGURE 5.2: $\tilde{\Sigma}_k^{\mathrm{ladd}}$ represents the topology of higher-order diagrams included in the ladder approximation of the dual boson theory, while $\tilde{\Sigma}_k^{\mathrm{corr}}$ represents topologies that appear in the full diagrammatic expansion, but are not included in the ladder.

The goal of this Chapter is to introduce the non-local interactions in the theory, so that we can treat the extended Hubbard model. In order to achieve this goal, we have to solve the dual boson action instead of the dual fermion action. The reason is that the only way to decouple the non-local interaction V_q in the action of the extended Hubbard model is by introducing additional bosonic degrees of freedom through an additional Hubbard-Stratonovich transformation. However, even if we truncate the expansion in terms of the vertices at the two-particle level, we have an action that contains both fermions and bosons that interact with each other. Indeed, the dual boson action (4.10) at the two-particle approximation (4.15) for the single-orbital case leads to

$$\tilde{S} = -\sum_{\mathbf{k},\nu,\sigma} f^*_{\mathbf{k}\nu\sigma} \tilde{\mathcal{G}}^{-1}_{\mathbf{k}\nu\sigma} f_{\mathbf{k}\nu\sigma} - \frac{1}{2}\sum_{\mathbf{q},\omega,\varsigma} \phi^\varsigma_{-\mathbf{q},-\omega} \tilde{\mathcal{W}}^{\varsigma\,-1}_{\mathbf{q}\omega} \phi^\varsigma_{\mathbf{q}\omega} + \tilde{\mathcal{F}}[f,\phi]. \tag{5.23}$$

where the bare dual propagators have been defined as

$$\tilde{\mathcal{G}}_{\mathbf{k}\nu\sigma} = \left[g_\nu^{-1} + \Delta_\nu - \epsilon_\mathbf{k}\right]^{-1} - g_\nu = G^{\mathrm{EDMFT}}_{\mathbf{k}\nu\sigma} - g_{\nu\sigma}, \tag{5.24}$$

$$\tilde{\mathcal{W}}^\varsigma_{\mathbf{q}\omega} = \alpha^\varsigma_\omega \left[V^{\varsigma\,-1}_{\mathbf{q}} - \chi^\varsigma_\omega\right]^{-1} \alpha^\varsigma_\omega = W^{\varsigma\,\mathrm{EDMFT}}_{\mathbf{q}\omega} - w^\varsigma_\omega, \tag{5.25}$$

where g_ν and w_ω^ς are the Green's function and renormalized interaction of the auxiliary impurity problem, respectively, and the impurity susceptibility is $\chi_\omega^\varsigma = -\langle \rho_{-\omega}^\varsigma \rho_\omega^\varsigma \rangle_{\text{imp}}$. Additionally, $\alpha_\omega^\varsigma = 1 + U^\varsigma \chi_\omega^\varsigma$ with $U^{\text{ch/sp}} = \pm U/2$. In the single-orbital case, the interaction term truncated at the two-particle level (4.15) is given by the fermion-boson part with a charge and spin components and the local fermion-fermion part

$$\tilde{\mathcal{F}}[f, \phi] = \sum_{\substack{\mathbf{q},\mathbf{k},\omega,\nu \\ \varsigma,\sigma,\sigma'}} \Lambda_{\nu\omega}^\varsigma f_{\mathbf{k}\nu\sigma}^* \sigma_{\sigma\sigma'}^\varsigma f_{\mathbf{k}+\mathbf{q},\nu+\omega,\sigma'} \phi_{\mathbf{q}\omega}^\varsigma$$

$$+ \frac{1}{4} \sum_{\substack{\mathbf{q},\omega \\ \{\mathbf{k},\nu,\sigma\}}} \Gamma_{\nu\nu'\omega}^{\sigma\sigma'\sigma''\sigma'''} f_{\mathbf{k}\nu\sigma}^* f_{\mathbf{k}+\mathbf{q},\nu+\omega,\sigma'} f_{\mathbf{k}'+\mathbf{q},\nu'+\omega,\sigma'''}^* f_{\mathbf{k}'\nu'\sigma''}. \tag{5.26}$$

This action is clearly not suitable to apply the DiagMC algorithm for a quartic interaction described before. We might apply a different version of DiagMC that was designed to tackle the polaron problem [276, 285, 304]. However, by inspection of the action (5.23), it turns out that there is no need to stir away from the algorithm for fermions with quartic interaction. The reason is that the action (5.23) is at most quadratic in the bosonic fields $\phi_{\mathbf{q}\omega}^\varsigma$, hence the bosons can be integrated out exactly. The procedure is analogous to Eq. (4.45), if we set the fields $b_\omega^\varsigma = 0$.

The result of this procedure is a modified dual fermion action

$$\tilde{S} = -\sum_{\mathbf{k},\nu,\sigma} f_{\mathbf{k}\nu\sigma}^* \tilde{\mathcal{G}}_{\mathbf{k}\nu\sigma}^{-1} f_{\mathbf{k}\nu\sigma}$$

$$+ \frac{\xi}{8} \sum_{\substack{\mathbf{q},\omega,\varsigma \\ \{\mathbf{k},\nu,\sigma\}}} \overline{\Gamma}_{\nu\nu'\omega}^{\varsigma,\mathbf{k}\mathbf{k}'\mathbf{q}} f_{\mathbf{k}\nu\sigma}^* \sigma_{\sigma\sigma'}^\varsigma f_{\mathbf{k}+\mathbf{q},\nu+\omega,\sigma'} f_{\mathbf{k}'+\mathbf{q},\nu'+\omega,\sigma'''}^* \sigma_{\sigma'''\sigma''}^\varsigma f_{\mathbf{k}'\nu'\sigma''}, \tag{5.27}$$

where we introduced a new momentum dependent fermion-fermion vertex that combines the vertex function of the local impurity problem and the non-local interaction contained in the bare $\tilde{W}_{\mathbf{q}}$ between fermions mediated by dual bosonic fields

$$\overline{\Gamma}_{\nu\nu'\omega}^{\text{ch},\mathbf{k}\mathbf{k}'\mathbf{q}} = \Gamma_{\nu\nu'\omega}^{\text{ch}} + 2\tilde{M}_{\nu,\nu',\omega}^{\text{ch},\mathbf{q}} - \tilde{M}_{\nu,\nu+\omega,\nu'-\nu}^{\text{ch},\mathbf{k}'-\mathbf{k}} - 3\tilde{M}_{\nu,\nu+\omega,\nu'-\nu}^{\text{sp},\mathbf{k}'-\mathbf{k}},$$

$$\overline{\Gamma}_{\nu\nu'\omega}^{\text{sp},\mathbf{k}\mathbf{k}'\mathbf{q}} = \Gamma_{\nu\nu'\omega}^{\text{sp}} + 2\tilde{M}_{\nu,\nu',\omega}^{\text{sp},\mathbf{q}} + \tilde{M}_{\nu,\nu+\omega,\nu'-\nu}^{\text{sp},\mathbf{k}'-\mathbf{k}} - \tilde{M}_{\nu,\nu+\omega,\nu'-\nu}^{\text{ch},\mathbf{k}'-\mathbf{k}}. \tag{5.28}$$

Here, we introduce the momentum-dependent contributions to the vertex obtained by integrating out the bosonic degrees of freedom as $\tilde{M}_{\nu,\nu',\omega}^{\varsigma,\mathbf{q}} = \Lambda_{\nu,\omega}^\varsigma \tilde{W}_{\mathbf{q}\omega}^\varsigma \Lambda_{\nu'+\omega,-\omega}^\varsigma$.

Each contribution to the series expansion (5.5) can be written as a combination of the two kinds of diagrammatic elements introduced in the DiagMC@DF scheme: fermionic lines that represent dual Green's functions $\tilde{\mathcal{G}}$ (called also propagator lines) and vertices $\overline{\Gamma}$, which are now described in Eq. (5.28). Thanks to this transformation, we do not need to
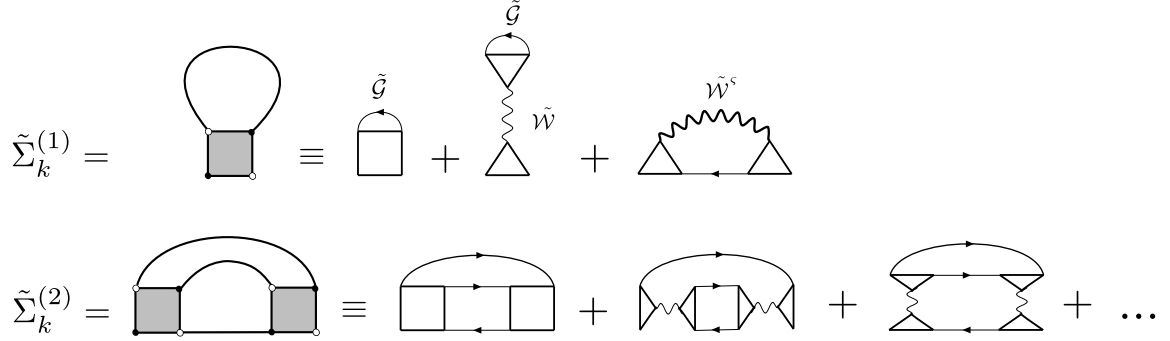
FIGURE 5.3: First diagram topologies in the representation used in the DiagMC@DB representation compared with those of the original dual boson theory.

introduce any substantial changes from DiagMC@DF in the acceptance-rejection scheme. The only difference is the fact that in our case the bare fermion-fermion vertex function (5.28) contains a momentum-dependent part, hence it is not local in space anymore. The simultaneous sampling of contributions coming from the fermion-fermion scattering and boson exchange processes efficiently reduces the number of topologies, compared to a sampling where treat local and non-local vertices as separate diagrammatic objects. However, it has a consequence on the sampling, since the property expressed in Eq. (5.19) does not hold anymore if the vertex is momentum-dependent, even in the case of EDMFT starting point. For this reason it is necessary to sample the tadpole diagrams, that contain the insertion of second-order DB diagram for the self-energy.

5.2.3   Using the semi-bold scheme to reduce the number of topologies

Even though we cannot neglect the tadpole diagrams completely, there is a way of consistently removing diagrammatic contributions by using the semi-bold DiagMC scheme of Ref. [279]. Within this scheme, we can identify the contribution to self-energy of the topologies that we want to exclude and write it as a functional of the Green's function $\tilde{\Sigma}^{\text{sb}} = \tilde{\Sigma}^{\text{sb}}[\tilde{\mathcal{G}}]$. In the semi-bold scheme, we replace the bare Green's function of the DiagMC scheme in all diagrams with a new Green's function $\tilde{\mathcal{G}}_{\text{sb}}$ that is dressed by the self-energy $\tilde{\Sigma}^{\text{sb}}$ found as the self-consistent solution of the Dyson equation

$$\tilde{\mathcal{G}}_{\text{sb}}^{-1} = \tilde{\mathcal{G}}^{-1} - \Sigma^{\text{sb}}[\tilde{\mathcal{G}}_{\text{sb}}]. \tag{5.29}$$

This formal transformation of the series is exact in the sense that they are guaranteed to converge to the same physical answer within the convergence radius of both series, so when the convergence parameter $|\xi| < R_{\text{bare}} \wedge |\xi| < R_{\text{sb}}$, as discussed in Ref. [279], with the only caveat that the subset of diagrams excluded with the semi-bold procedure is finite.
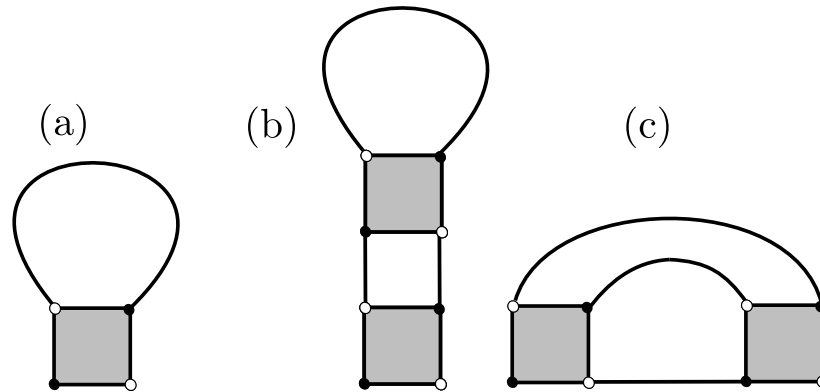
FIGURE 5.4: Diagram topologies for the self-energy up to the second order. Topology (a) represents the tadpole diagram, (b) is the second-order diagram with a tadpole insertion, while (c) is the topology with two vertices connected by three propagator lines.

However, the convergence properties of the semi-bold series are generally different from the bare series [305].

In principle, any kind of topology can be excluded by this procedure, but there is a balance between the computational time saved by avoiding the sampling of the additional diagrams corresponding to the topology and the computational overhead introduced to self-consistently solve Eq. (5.29) and to perform the necessary tests to identify the current topology during the DiagMC run. As an example, in the work on DiagMC@DB of Ref. [230], we chose to exclude only the tadpole diagrams $\tilde{\Sigma}^{\mathrm{sb}}[\tilde{\mathcal{G}}] = \tilde{\Sigma}^{(1)}[\tilde{\mathcal{G}}_{\mathrm{sb}}]$, so that effectively we reduced the number of diagrammatic topologies needed for a DiagMC@DB calculation to those of DiagMC@DF based on EDMFT. However, by using the semi-bold scheme, we do not need to start from a EDMFT impurity problem at all, but we can exclude the diagrams independently on the starting point. The exclusion of the tadpole diagrams is quite simple. It suffices to check that no propagator line has both ends connected to the same vertex. However, we can choose to exclude even more complicated sets of diagrammatic contributions. As a matter of fact, in the work presented in Ref. [232], we opted for the exclusion of both the tadpole and the second-order diagrams. In that case, we computed $\tilde{\Sigma}^{\mathrm{sb}} = \tilde{\Sigma}^{(1)}[\tilde{\mathcal{G}}] + \tilde{\Sigma}^{(2)}[\tilde{\mathcal{G}}]$ self-consistently using DiagMC@DB with maximum order $N_{max} = 2$ and we used the resulting $\tilde{\mathcal{G}}_{\mathrm{sb}}$ as a bare propagator for DiagMC. Excluding the topologies up to second-order is again rather simple, as the two diagrammatic topologies at second order correspond to a diagram that features a tadpole insertion (excluded by the exclusion of the tadpoles) and a diagram where two vertices are connected to each other by three propagators. The overhead introduced to perform the checks for the exclusion of these diagrams does not seem to hinder the efficiency of the procedure, based on our tests.

In our tests, we did not observe any noticeable extension of the convergence radius R_{sb}

compared to the bare convergence radius R_{bare}. The improvement of using the semi-bold scheme in the range of parameters we considered is purely in terms of reduced error bars, hence a sharp reduction in the computational time needed to reach a target accuracy.

5.3   Results obtained using DiagMC@DB

The problem that we addressed using DiagMC@DB is the extended Hubbard model on a square lattice with nearest-neighbor tight-binding hopping t, local Hubbard interaction U and nearest-neighbor interaction. The Hamiltonian of this system reads

$$\hat{H} = -t \sum_{\langle i,j \rangle, \sigma} c_{i\sigma}^{\dagger} c_{j\sigma} + U \sum_i n_{i\uparrow} n_{i\downarrow} + V \sum_{\langle i,j \rangle} n_i n_j. \tag{5.30}$$

The filling was chosen to be half filling, hence the chemical potential $\mu = U/2$. As previously discussed, the DiagMC@DB calculations are performed in momentum space, which is a continuous space. In momentum space, the dispersion reads

$$\epsilon_{\mathbf{k}} = -2t \left(\cos k_x + \cos k_y \right) \tag{5.31}$$

and the non-local interaction term of the Hamiltonian can be rewritten as

$$V_{\mathbf{q}} = 2V(\cos q_x + \cos q_y). \tag{5.32}$$

5.3.1   Output of a DiagMC@DB calculation

In order to efficiently store the results, we sample the series in the space of irreducible representations according to Eq. (5.22). Additionally, if we want to study the convergence to the exact self-energy at infinite order, we should consider the cumulative sum of coefficients rather than the coefficients themselves. With the expression the "dual self-energy at order n", we indicate the cumulative sum over the coefficients

$$\tilde{\Sigma}_n(\mathbf{k}, \nu) = \sum_{m=1}^{n} a_m(\mathbf{k}, \nu) \tag{5.33}$$

as a function of the order $n = 1, ..., N_{max}$, and we set $\xi = 1$ to obtain the physical result. The dual self-energy $\tilde{\Sigma}_n(\mathbf{k}, \nu)$ can be obtained from the measured coefficients as

$$\tilde{\Sigma}_n(\mathbf{k}, \nu) = \sum_{i=0}^{i_{\text{max}}} \tilde{\Sigma}_n(i, \nu) \, \psi_i^{(s)}(\mathbf{k}) = \sum_{m=1}^{n} \sum_{i=0}^{i_{\text{max}}} a_m(i, \nu) \, \psi_i^{(s)}(\mathbf{k}), \tag{5.34}$$
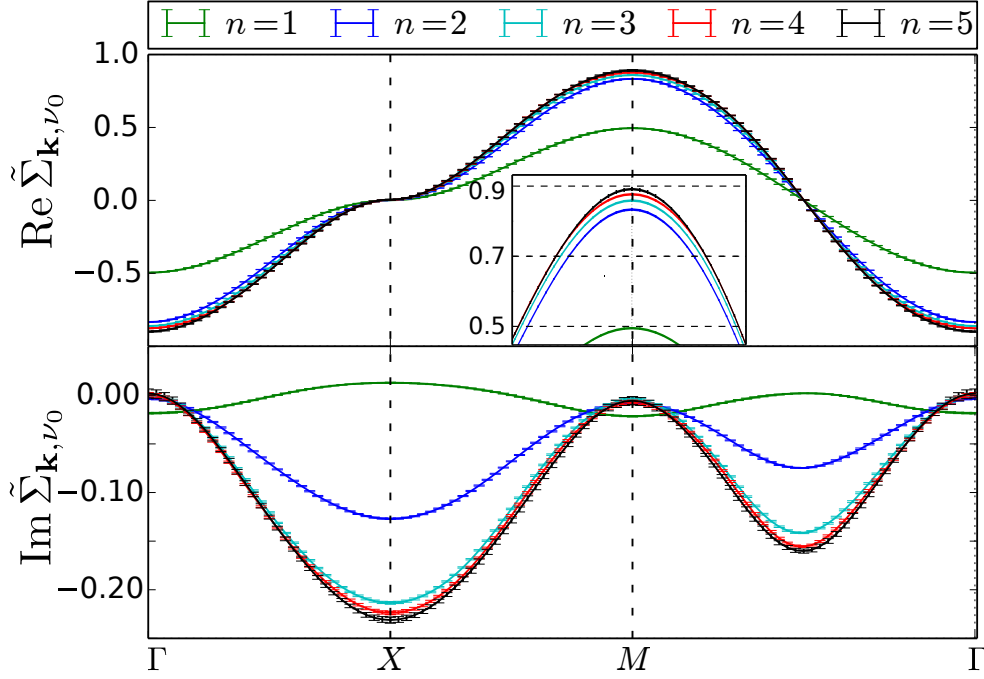
FIGURE 5.5: Convergence of the real (top panel) and imaginary (bottom panel) parts of the dual self-energy $\tilde{\Sigma}_n(\mathbf{k}, \nu)$ obtained for the zeroth Matsubara frequency ν_0. The result is plotted along the high-symmetry path in momentum space $\mathbf{k}$ as a function of the expansion order n. The parameters are $U = 5$, $V = 1.25$, and $\beta = 2$ in the units of the hopping amplitude. The inset shows the convergence of the real part around the $M = \{\pi, \pi\}$ point. This figure is reproduced from Ref. [230].

where the basis functions $\psi_i^{(s)}(\mathbf{k})$ are defined in Eq. (5.21). The physical partial sums are given by setting $\tilde{\Sigma}_n(i, \nu) = \tilde{\Sigma}_n(i, \nu; \xi = 1)$ in Eq. (5.22). The cut-off index $i_{\max}$ of the basis functions is chosen to guarantee appropriate convergence. An example of the results that can be obtained from a DiagMC@DB calculation is shown in Fig. 5.5. This calculations shows the dual self-energy at the first Matsubara frequency along the high-symmetry path in the Brillouin zone and it is performed at $U = 5$, $V = 1.25$ and $\beta = 2$. The series considered is the bare series without the exclusion of any topology. As a consequence, the last order that was possible to converge within reasonable error bars is the fifth-order.

The order-by-order analysis of the dual self-energy is a very useful tool to determine which diagrammatic contributions are important in dual theories. As a matter of fact,

we can directly judge if second-order approximations are accurate in this context. As it can clearly be seen, the first-order term, which contains the diagrams in the first line of Fig. 5.3, contributes significantly to the real part of the dual self-energy, making up to approximately 50% of the value along the whole path in the Brillouin zone. This is not surprising as the value of the non-local interaction V is quite large and we expect the diagram with a dual boson insertion to be roughly proportional to the non-local interaction V. The second-order contribution contains the second-order dual fermion diagram, so two fermion-fermion vertices connected to each other. It is not surprising then that this contribution almost fully contains the remaining contribution to the real part of the dual self-energy. Based on this analysis, we expect second-order DF and second-order DB methods to accurately describe the real part of the dual self-energy. However, by looking at the imaginary part we notice that the second order still misses around 50% of the momentum dependence at the nodal point $N = \left(\frac{\pi}{2}, \frac{\pi}{2}\right)$ anti-nodal point $X = (\pi, 0)$. In order to capture this contribution, it is necessary to include diagrams at the third order (which still miss around 5% of the contributions) or higher orders. The error bars are obtained by applying the standard Jackknife resampling analysis to a sufficiently large number of Monte Carlo runs.

5.3.2   Charge density wave in the extended Hubbard model on a square lattice

The extended Hubbard model of Eq. (5.30) exhibits a competition between the local interaction U and the non-local interaction V. This competition leads to a phase transition between the regime where the local physics dominates and the regime where the non-local physics wins.

The reason is that putting two electrons on the same site costs an energy U, hence the local U favors a configuration with one electron per site. On the other hand, putting two electrons on neighbouring sites becomes unfavourable if V is large, hence the non-local interaction favors a charge density wave (CDW) with a checkerboard configuration, in which doubly occupied sites alternate with empty sites. On a mean field level and at $T = 0$, in both configurations the electrons are frozen to their sites, so they have zero kinetic energy. In this situation, the CDW phase transition to this state occurs when V is large enough to overcome the effect of the on-site Coulomb repulsion. The transition from the Mott state with mainly singly-occupied states to the CDW state occurs when $V = U/z$, where z is the number of neighbours. Based on this consideration, on a square lattice the CDW transition occurs around $V^{\mathrm{MF}} = V/4$.

Of course, both the presence of temperature and of quantum tunnelling effects quantitatively affects this picture. As a consequence, a perturbative expansion at small values of U,

where the assumption of perfect electronic localization is surely not valid, predicts the onset of the CDW phase at $V \simeq U/8+$const [306]. In the intermediate regime, more advanced mean-field estimates can be obtained based on RPA or *GW* theories and give the transition point at $V \simeq U/4$ [205], in agreement with the simplest classical mean field argument. This behavior is reproduced at moderate interaction strength by DCA calculations [307, 308]. Finally, as we shall see below, for large values of *U* and large temperatures the position of the onset of the CDW phase appears shifts towards the value $V \simeq U$ which can be found using the Peierls-Feynman-Bogoliubov variational principle [309]. Dual boson calculations are in good agreement with the DCA results and interpolate between all these different trends in the weak-, moderate- and strong-coupling regimes [225, 227].

Depending on the method used, the transition to a symmetry broken phase can be identified in different ways. The first possibility is to use a large enough cluster to reproduce the larger unit induced by the breaking of the symmetry. The system can be pushed towards the broken-symmetry phase by applying small symmetry-breaking fields in the Hamiltonian, that bias the system towards the lower symmetry state. We can then extrapolate the broken-symmetry state in the limit of vanishing external fields. This technique is exploited in cluster calculations, for instance in DCA calculations [307, 308].

Usually, the appearance of a broken-symmetry phase is signalled already in the normal phase by a divergence of the corresponding component of the susceptibility. In the case of the CDW [225, 227, 229], this susceptibility is the charge susceptibility, related to our conventions as

$$X_{\mathbf{q}\omega}^{\text{ch}} = -X_{\mathbf{q}\omega}^{d} = \left\langle n_{\mathbf{q}\omega}^{d} n_{-\mathbf{q},-\omega}^{d} \right\rangle. \tag{5.35}$$

This approach is used in most diagrammatic techniques. Among those, the ladder dual boson approach will be used as a comparison with DiagMC@DB.

5.3.3 CDW from single-particle observables

As we discussed before, two-particle quantities inherently convey information about second-order phase transitions and symmetry-breaking. However, we can extract information about a phase transition also from single-particle observables. In particular, we know that a physical phase transition is associated with a non-analyticity of the series corresponding to the observables of interest. This does not necessarily mean that we observe a divergence of the self-energy, for example. Indeed, in a self-consistent method, extracting information about a phase transition from the single-particle observables, such as the self-energy, requires a careful analysis that goes under the name of *fluctuation diagnostics* [30, 259, 310]. On the other hand, within DiagMC, we can exploit an additional possibility to investigate the transition. We recall that we construct the series order-by-order starting from the a non-interacting case which is our case is the non-interacting dual fermion action.

Since the dual action (5.27) is explicitly constructed for the translationally-symmetric phase, we expect to have a non-analytical point, also called singularity in this context, on the real axis corresponding to $0 < \text{Re}\,\xi \leq 1$ and $\text{Im}\,\xi = 0$. This results in a divergence of the infinite diagrammatic expansion in terms of bare quantities of the theory at the value corresponding to the phase transition [221, 225, 227, 229, 265]. When this happens, it is sufficient to analyse some specific components of the self-energy in order to find the parameters at which the transition takes place. In this case, the critical value V_{CDW} for the CDW phase transition can be found in a controlled way from the analytic structure of the dual self-energy $\tilde{\Sigma}$ as a function of the complex expansion parameter ξ. The critical point $V = V_{\text{CDW}}$ is marked by the singularity appearing in the function $\tilde{\Sigma}(\xi)$ at $\xi = 1$. When V is increased beyond V_{CDW} in the symmetry-broken phase, the singularity moves closer to the origin of the complex plane $\xi = 0$, so that the physical $\tilde{\Sigma}(\xi = 1)$ remains inaccessible by its power-series expansion (5.16). A different power series expansion based on the ground state with broken symmetry should be used there.

There are several ways of extracting the critical value V_{CDW} at which the transition occurs. A simple method is to look at some component of the self-energy $a_n(\mathbf{k}, \nu_n)$ as a function of n and to apply the Cauchy-D'Alemebert ratio test for the convergence of the series. This test states that, if we consider the quantity,

$$L = \lim_{n \to +\infty} \left| \frac{a_{n+1}}{a_n} \right|, \tag{5.36}$$

the series is convergent if $L < 1$ and divergent if $L > 1$. Unfortunately, this method often requires the calculation of many series coefficients to extract a reliable estimation of the limit $n \to +\infty$. A more sophisticated method that allows for a less crude estimation of the transition point was introduced in Ref. [311] and has been routinely applied in the context of DiagMC [295]. This method allows to accurately evaluate the specific location of the singularity ξ_s, when several expansion orders for the series are available. In particular, this method assumes a generic power-law behavior near the singularity

$$\tilde{\Sigma}(\xi) \propto (\xi_s - \xi)^{\eta} \tag{5.37}$$

for $|\xi - \xi_s| \ll 1$ with some real number η. Assuming this kind of behavior is typical for a continuous phase transition. The method allows to extract the ξ_s from the behavior of the series coefficients a_n in Eq. (5.16). The position of the singularity ξ_s crosses $\xi = 1$ at the critical value V_{CDW}. As shown in Refs. [230, 295], ξ_s can be found from a finite number of coefficients $\{a_n\}$ with a reliable error bar that includes both the systematic and statistical Monte Carlo error.
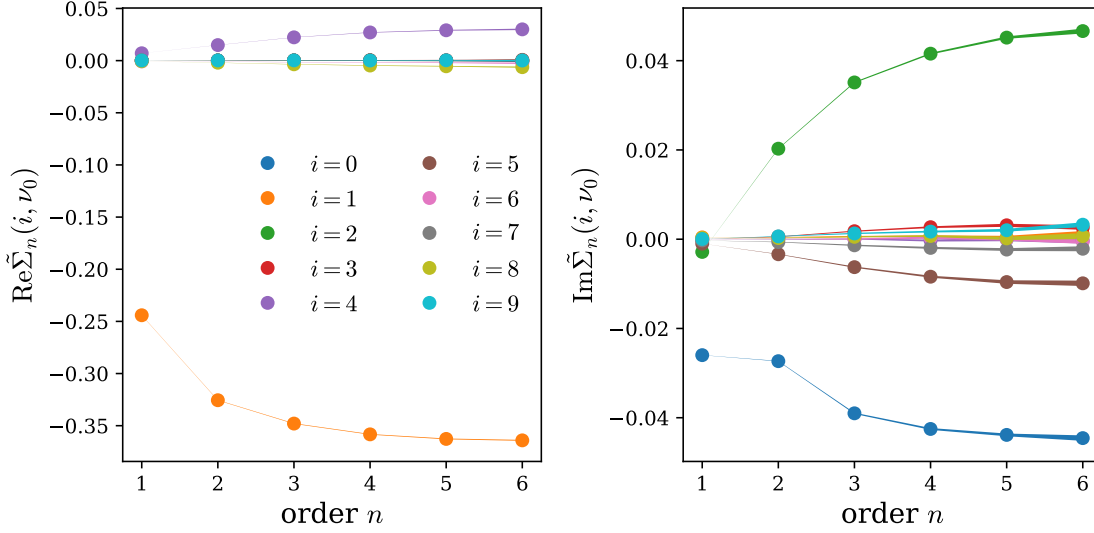
FIGURE 5.6: Convergence properties of the cumulative dual self-energy $\tilde{\Sigma}$ as a function of the expansion order for the first few basis functions characterized by index i. Parameters are chosen to be $U = 3.5$, $V = 1.08$ and $\beta = 4$ and exhibit a clear convergence for all the basis functions.

5.3.4 Order-by-order analysis of the dual self-energy

It is important to choose the coefficient of the series that exhibits a clear divergence as the order n increases. In principle all the components that are non-zero by symmetry are a suitable choice for the analysis, however we found that the best choices are the physical motivated ones. The choice of the Matsubara frequency is clear, since in most of our calculations the components with $\nu = \nu_0 = \pi/\beta$ are the largest ones. The only possible exception at large U, where the system is Mott insulating and the self-energy at the lowest Matsubara component is not necessarily the largest component. For what concerns the momentum space, we explored the choice of a specific point in momentum space $a_n(\mathbf{k} = M, \nu_0)$. However, we noticed that the choice of a specific point in momentum space was extremely sensitive to noise. Additionally, the divergence may not occur simultaneously at each point in momentum space, as it is clear from the original paper about DiagMC@DF.

The choice of Ref. [230] was to consider the coefficient $\{\mathrm{Re}\, a_n(\mathbf{k}, \nu_0)\}$, for $n = 1, \dots, N_{max}$ projected on the first A_{1g}-symmetric harmonic $\psi_1^{(s)}(\mathbf{k}) = \cos(k_x) + \cos(k_y)$ to produce a numerical series from the functional one. In practice, there is no need to perform this projection, as in our implementation the measurement is already directly performed in the basis of irreducible representations of the square lattice symmetry group.

The choice of this basis function can be understood by looking at Fig. 5.6 and Fig. 5.7,
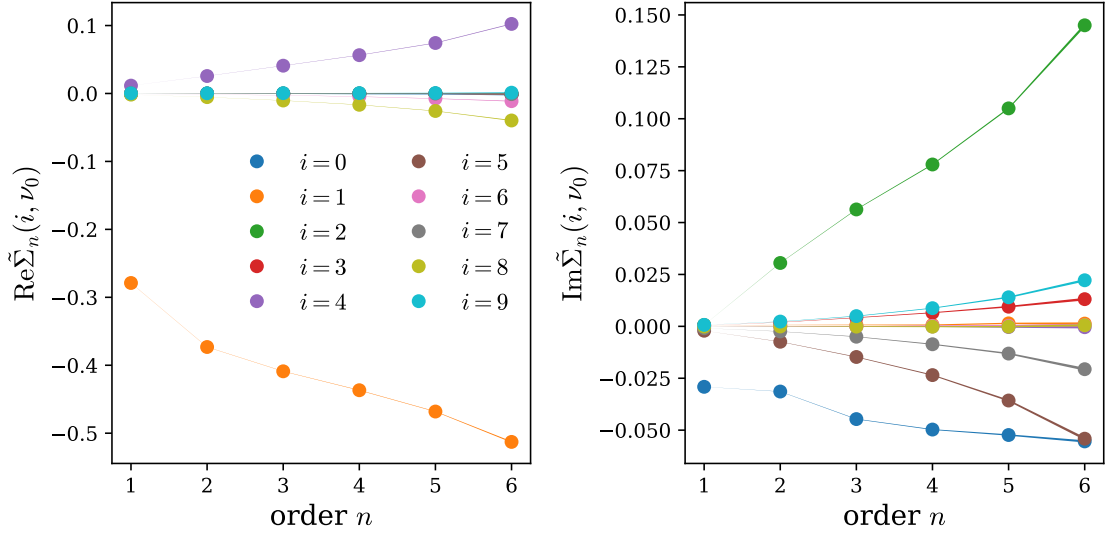
FIGURE 5.7: Convergence properties of the cumulative dual self-energy $\tilde{\Sigma}$ as a function of the expansion order for the first few basis functions characterized by index i. Parameters are chosen to be $U = 3.5$, $V = 1.18$ and $\beta = 4$. Data for some choice of the basis function exhibit a clear divergence, for instance $i = 1$ for the real part and $i = 2$ for the imaginary part.

that show the behavior of the partial sums $\tilde{\Sigma}_n(i, \nu_0) = \sum_{m=0}^n a_m(i, \nu_0)$ for the different indices i corresponding to s-symmetry of the basis. In the semi-bold case, we added the contributions $m = 0$ that correspond to the semi-bold dual self-energy $\tilde{\Sigma}_{\mathrm{sb}}$ projected on the basis of symmetrized functions. Fig. 5.6 shows the convergent case at $U = 3.5$ and $V = 1.08$, while Fig. 5.7 shows results for the divergent case $U = 3.5$ and $V = 1.18$. The projection on the first function $\psi_0^{(s)}(\mathbf{k}) = 1$, which is constant, does not seem a good option, because it does not exhibit any clear divergent behavior as n is increased. On the other hand, projection on the $s-$symmetric function with index 1 is the largest contribution to the real part of $\tilde{\Sigma}$ and clearly displays a change of behavior from the convergent to the divergent case. Another possible choice is the coefficient of the $\psi_2^{(s)}(\mathbf{k}) = \cos k_x \cos k_y$ basis function that represents the main contribution to the imaginary part and corresponds to the index 2 in the plots. The figures also show the convergence of the coefficients as a function of the number of basis functions in the momentum basis. Coefficients higher than $i > 5$ can be safely neglected in most cases. In Figs. 5.8 and 5.9, we show the cumulative coefficients $\tilde{\Sigma}_n(i = 1, \nu_0)$ for different values of V up to order 6 for $U = 2.5$ and $U = 3.5$ respectively. The upper panel displays data for the bare series, while the lower panel displays results for the semi-bold series. The width of the line collecting the points represents the stochastic Monte Carlo error. Clearly, results obtained with the semi-bold series have much smaller error bars than for the bare series for both the values of U considered and across all the
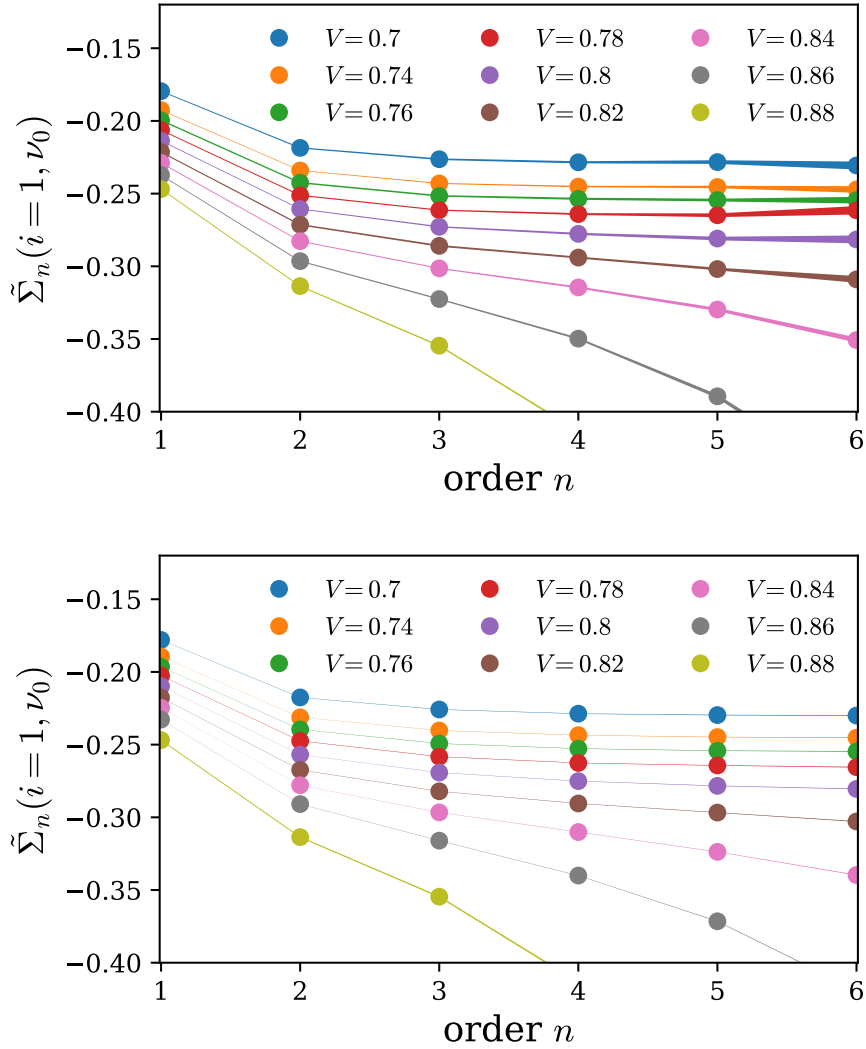
FIGURE 5.8: Convergence properties of the cumulative dual self-energy as a function of the expansion order for different values of the non-local interaction V. Upper panel shows the bare expansion and lower panel the semi-bold one. The parameters are chosen to be $U = 2.5$ and $\beta = 4$. The data is shown for a particular component of the irreducible representation of momentum, the $A1g$, and at Matsubara frequency ν_0. The semi-bold series clearly shows smaller error bars compared to the bare series at a fixed number of measurements.

values of V considered in both cases, allowing for a much better infinite-order limit extrapolation. It is already possible to see from inspection of Fig. 5.8, that the partial sums for $U = 2.5$ exhibit a change of behavior around the value of non-local interaction $V = 0.78$.

This change of behavior involves the transition between a clear convergence to a divergent behavior and it occurs both in the bare and in the semi-bold series. This is visible also for $U = 3.5$ around $V = 1.14$ in Fig. 5.9. In the same way, we can identify the same kind of behavior in the large-U behavior in Fig. 5.10.
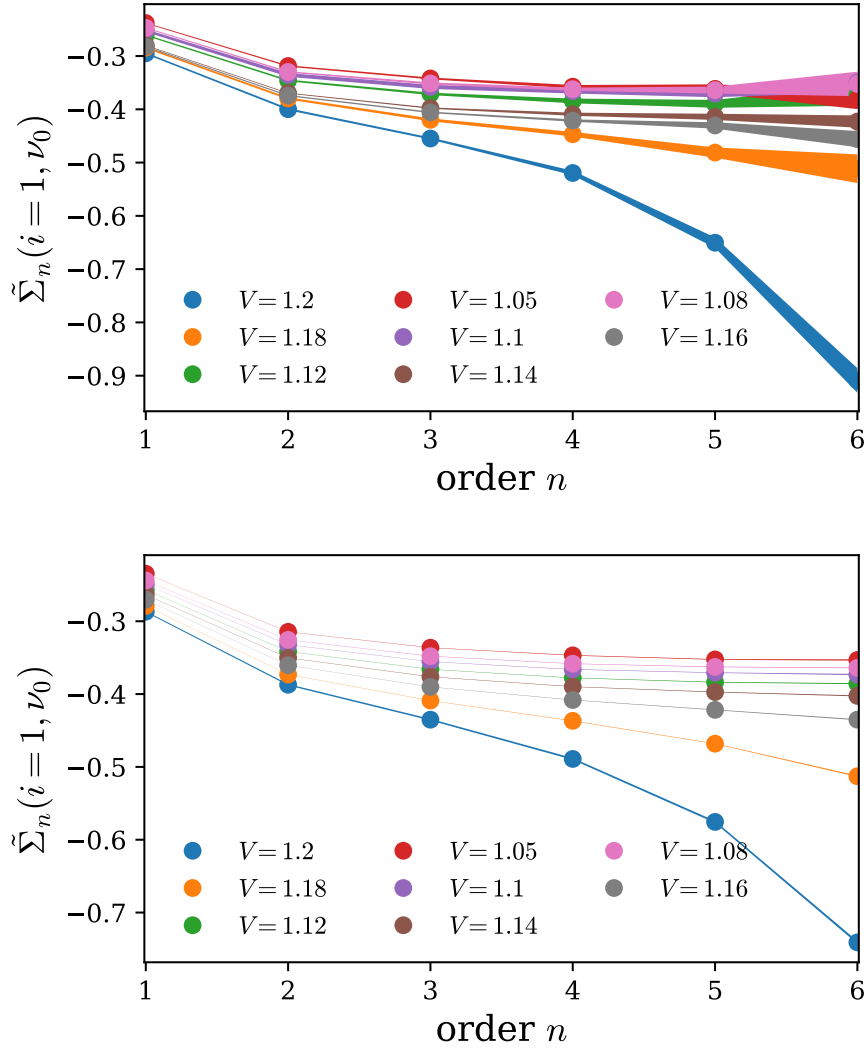
FIGURE 5.9: Convergence properties of the cumulative dual self-energy as a function of the expansion order for different values of the non-local interaction V. Upper panel shows the bare expansion and lower panel the semi-bold one. The parameters are chosen to be $U = 3.5$ and $\beta = 4$. The data is shown for a particular component of the irreducible representation of momentum, the $A1g$, and at Matsubara frequency ν_0. As before, the semi-bold series clearly shows smaller error bars compared to the bare series at a fixed number of measurements.
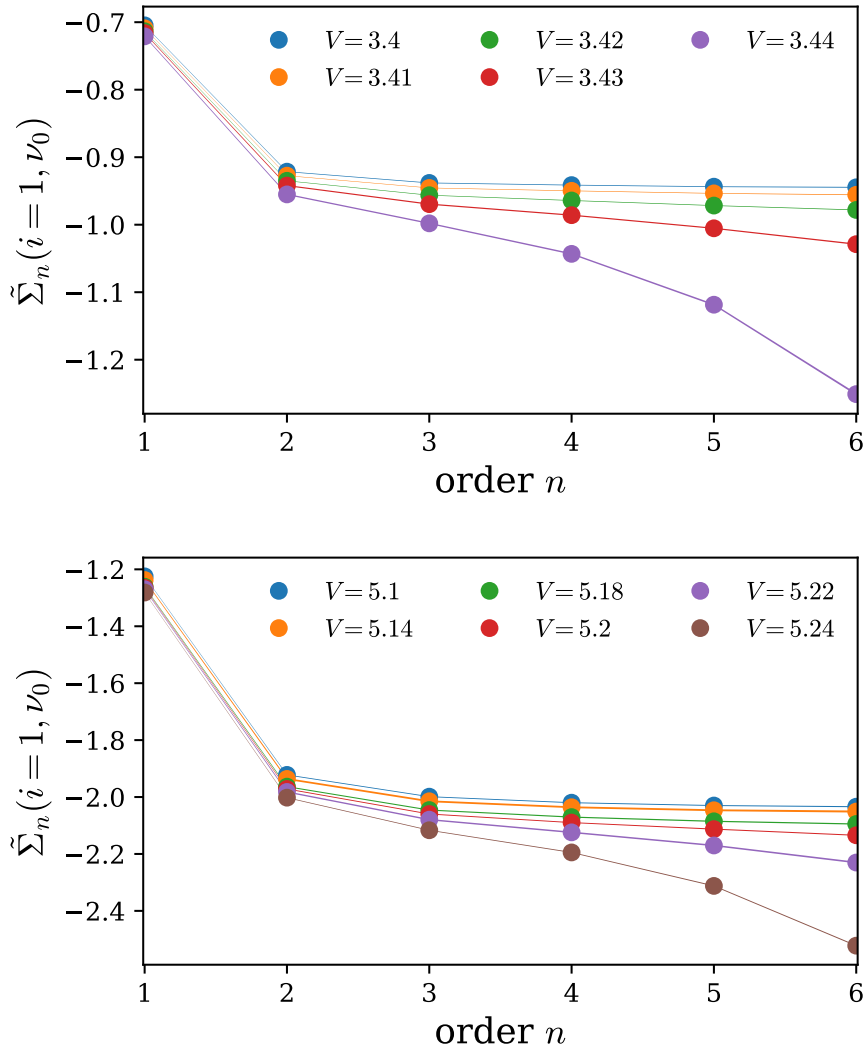
FIGURE 5.10: Convergence properties of the cumulative dual self-energy as a function of the expansion order obtained with the semi-bold expansion at large value of U. The parameters are chosen to be $U = 6.5$ (upper panel) and $U = 7.5$ (lower panel). The inverse temperature is $\beta = 2$. Different colors represent different values of the non-local interaction V. The data is shown for a particular component of the irreducible representation of momentum, the $A1g$, and at Matsubara frequency ν_0.
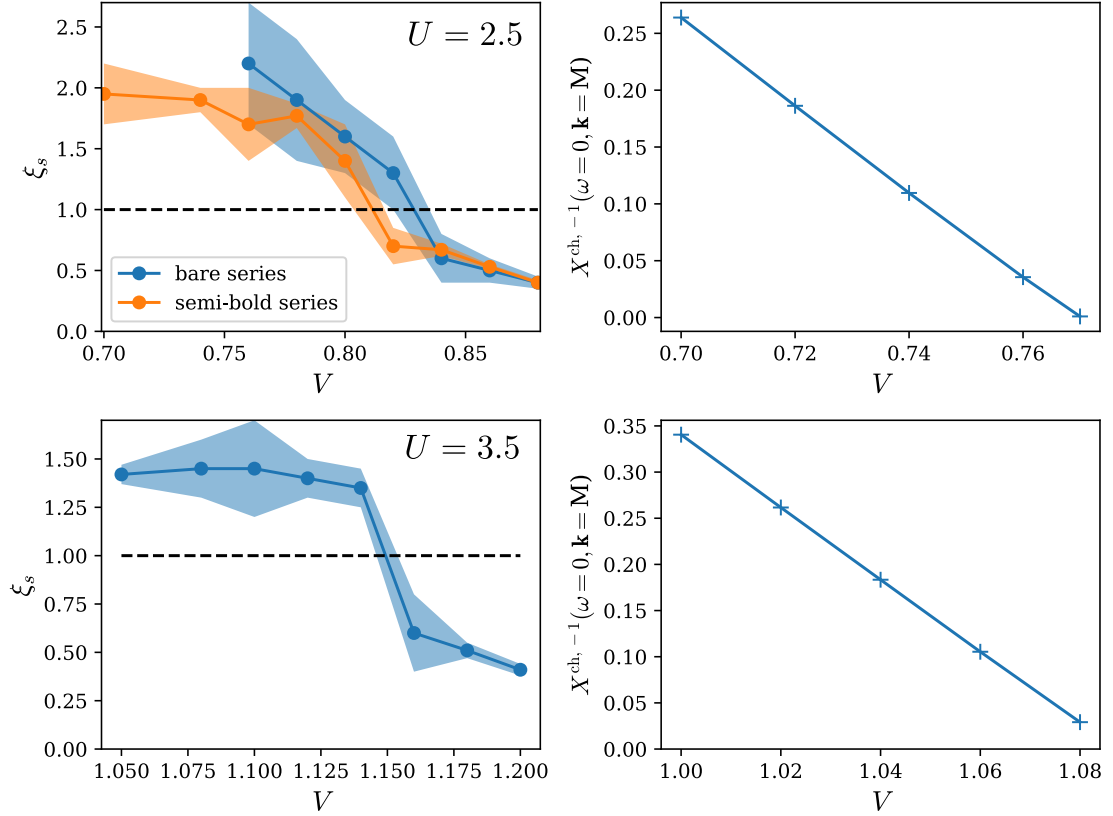
FIGURE 5.11: Convergence radius of the series at small U. Upper panel shows $U = 2.5$ and the lower panel shows $U = 3.5$. Results are obtained at $\beta = 4$. The right panels show the corresponding static charge susceptibility at the k-point M$= (\pi, \pi)$.

5.3.5   Extrapolation of the convergence radius of the series in CDW regime

From this data, we can extract the position of the critical V at which the phase transition occurs by using the expression of Eq. (5.37). In particular, we can compute the V^{CDW} at which the singularity reaches $\xi_s = 1$, meaning that the convergence radius of the series must be smaller that $\xi = 1$. We also validated this result by computing the charge susceptibility (5.35) in the ladder DB approximation and we showed that its inverse $1/X^{\text{ch}}(\omega = 0, \mathbf{k} = \text{M})$ diverges roughly at the same position where ξ_s of series crosses 1 in all the considered cases. Figures 5.11 and 5.12 show the results for the convergence radius ξ_s (left panels) and the charge susceptibility (right panels) precisely show this agreement. The shaded area in the plots for the convergence radius shows the error bar that contains
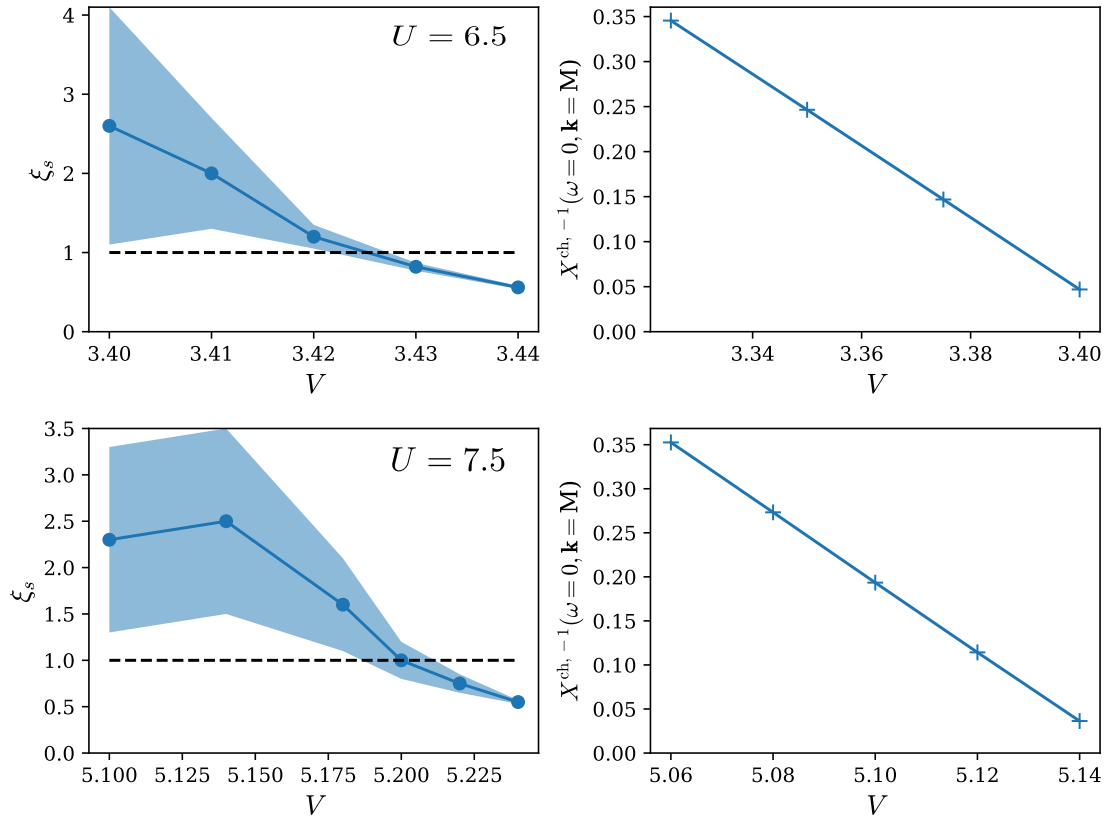
FIGURE 5.12: Convergence radius of the series at large U. Upper panel shows $U = 6.5$ and the lower panel shows $U = 7.5$. Results are obtained at $\beta = 2$. The right panels show the corresponding static charge susceptibility at the k-point M= (π, π).

both the stochastic and the fitting error. These error bars are estimated in the most conservative way and probably overestimate the actual uncertainty in the convergence radius. That said, the error becomes smaller as ξ_s is closer to 1 and, despite the large error bars given by the method, it is possible to unambiguously determine the critical value of V where ξ_s crosses the line $\xi_s(V) = 1$ in all the considered cases.

The specific values of V_{CDW} are:

U	V^{CDW} (DiagMC@DB)	V^{CDW} (ladder DB)
2.5	0.81(1)	0.77
3.5	1.15(1)	1.09
6.5	3.42(1)	3.41
7.5	5.20(2)	5.15
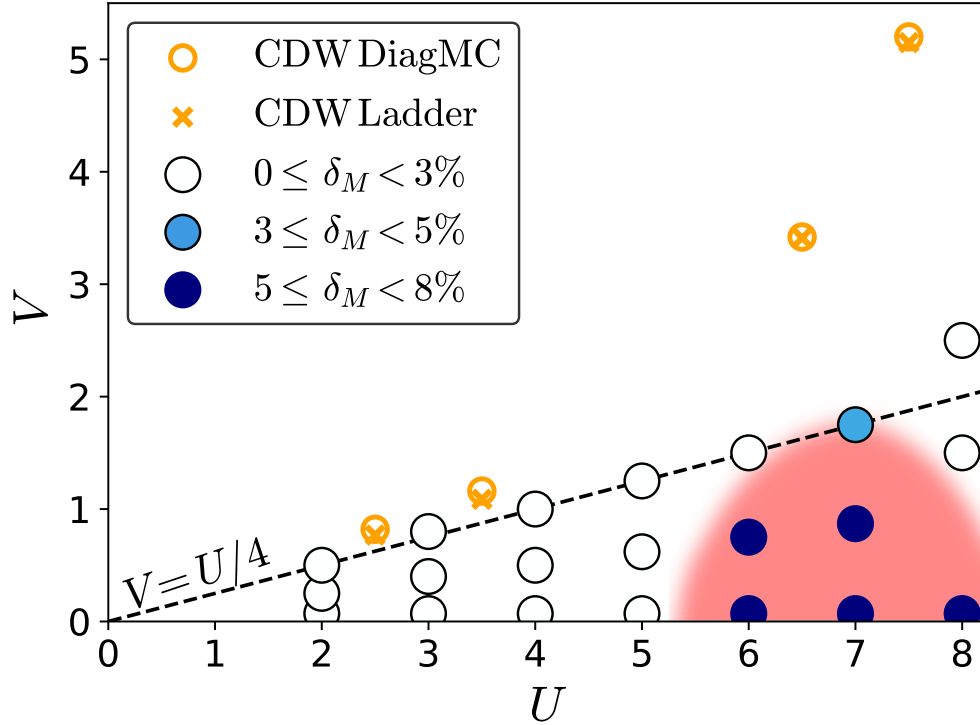
FIGURE 5.13: Phase diagram of the dual boson action obtained using DiagMC@DB. Originally, published in Ref. [230].

The four points exhibit a clear non-linear behavior, with some change of the slope of the phase boundary somewhere between $U = 3.5$ and $U = 6.5$. We find a quantitative good agreement with previous dual boson, which also predict a change in the slope around the onset of the Mott transition [225, 227, 265], and DCA calculations [307, 312]. Our results for $U = 2.5$ show also a very good agreement with the value obtained with GW+DMFT in Ref. [205].

We find that ladder DB underestimates the critical V of the CDW phase. This behavior is reasonable, since the DiagMC@DB method contains additional diagrammatic contributions that contribute to the screening of the longitudinal fluctuations. The difference with respect to the DiagMC@DB method, however, is always less than 5%. This is a result that has fundamental implications on the ladder DB method. Indeed, it shows that the longitudinal contributions contained in the ladder DB method are the largest contributions and are sufficient to accurately characterize the phase transition.

5.3.6   Comparison with ladder DB

In addition to the study of the CDW phase transition within DiagMC@DB, we also compared the results with the ladder DB method for different values of U and V parameters. In order to quantify the difference between the two methods, we investigated the quantity

$$
\delta_M = \mathrm{Re}\left[\frac{\overline{\Sigma}_{M,\nu_0}^{\mathrm{DiagMC}} - \overline{\Sigma}_{M,\nu_0}^{\mathrm{ladd.}}}{\overline{\Sigma}_{M,\nu_0}^{\mathrm{DiagMC.}}} \right], \tag{5.38}
$$

where $\overline{\Sigma}_{M,\nu_0}$ is the difference between the self-energy in the specified method and the DMFT self-energy $\Sigma_{\nu_0}^{\mathrm{imp}}$, and ν_0 is the lowest positive Matsubara frequency. The self-energy is computed from the dual self-energy using Eq. (5.17) and we considered the result at $N_{\mathrm{max}} = 5$ to be converged to a sufficient accuracy, so that we can simply apply the formula without considering the effects of errors. The choice of the M-point in the formula is based on the fact that the largest difference in the Brillouin Zone is always located at the point in our calculations for this model and at half filling.

By considering the quantity δ_M, we could get a picture of the regions in the $U - V$ plane where the ladder approximation is a good approximation and where it is not, as it is shown in Fig. 5.13. In general, we find a rather good agreement in the whole plane, as the difference between the two methods never exceeds 8%. However, it is also clear that the region of largest difference between the two methods is located around $U \approx 7$ and at lower values of V. As a matter of fact, the region of largest mismatch between the methods coincides with the region where calculations using cluster DMFT and dual theories locate the Mott transition of the square lattice Hubbard model. Indeed, in this regime, transverse fluctuations in the spin channel can significantly screen the ladder hence affecting the self-energy. These non-linear and incoherent processes related to the onset of the transition cannot be captured within the ladder approximation.

On the other hand, when V is large enough, the physics of the CDW dominates over all the other processes in the spin channel, no matter if they are longitudinal or transverse. This physics manifests itself in the longitudinal charge channel, included both in DiagMC@DB and in the ladder approximation.

Indeed, from our studies we observe that the absolute difference between the DiagMC@DB and ladder DB is not strongly modified upon the increase of V. However, the self-energy is strongly increased so that the relative difference δ_M is reduced.

5.4   Summary of the Chapter

In this Chapter, we introduced the DiagMC@DB and we showed how this method can be used to compute observables of the dual action truncated at the two-particle level in

an exact and unbiased way. In order to reduce the computational time to achieve reasonable error bars, we introduced a semi-bold scheme that allows for the exclusion of simple diagrammatic topologies that can be computed in advance.

We then discussed how to obtain the critical parameters of phase transitions by analysing the series order-by-order and we applied this method to estimation of the CDW phase transition in the extended Hubbard model on a square lattice.

Finally, we compared the ladder DB method with DiagMC@DB in order to estimate when the method is accurate. We found that ladder DB is a rather good approximation in the whole $U - V$ plane, but shows the largest discrepancy with respect to DiagMC@DB in the region of values of U around the Mott transition and small values of the non-local interaction V.

6 The D-TRILEX approach to strong correlations

6.1 D-TRILEX solution for the partially bosonized action

6.1.1 Advantages of the D-TRILEX method

D-TRILEX has a very similar diagrammatic structure to TRILEX. However, it was derived following a rather different route, namely as an approximation of the DB theory. For this reason, D-TRILEX has the same degree of internal consistency as the DB approach. In particular, it treats both charge and magnetic fluctuations without facing the Fierz ambiguity issue, and also possesses a desired symmetry for the vertex corrections. Originally, the D-TRILEX method was formulated and implemented in the single-orbital form [231]. In this context, it retains a high degree of accuracy compared with its parental DB theory [232]. Specifically, this approach captures both the reduction of the critical value of the critical interaction for the Mott transition with respect to the DMFT prediction [231] and the pseudogap formation in the Slater regime of a single-orbital Hubbard model [232]. Additionally, D-TRILEX correctly reproduces the momentum differentiation in the electronic self-energy predicted by an exact benchmark in a model relevant for cuprates [232]. These successes of the method achieved in a single-orbital context made it desirable to extend the D-TRILEX approach to a multi-band framework. An early attempt in this direction was the application of a simplified version of the method to the study of magnetic fluctuations in a three-orbital model for perovskites [48]. The promising results obtained in that case motivated us to derive a general formulation of the multi-band D-TRILEX theory and to develop a numerical implementation that does not rely on a specific model.

6.1.2 General form for D-TRILEX diagrams

In this Chapter, we present the derivation of the multi-band D-TRILEX approach and we discuss some benchmark calculations. In this theses, we strictly follow the derivation presented in Ref. [96], which was coauthored by the author of this thesis. The D-TRILEX method is derived as the simplest set of diagrams that can be constructed from the partially bosonized action, in a very similar fashion to the *GW* formalism.

In order to extend this formalism to the multi-band framework, we follow the derivation presented in Refs. [231, 232]. We recall from Sec. 4.3.5 the form of the effective partially bosonized dual action of Eq. (4.49) written in terms of fermion f and boson b variables

$$
\mathcal{S}_{fb} = -\sum_{k,\{l\}} \sum_{\sigma\sigma'} f^*_{k\sigma l} \left[\tilde{\mathcal{G}}_k^{-1} \right]_{ll'}^{\sigma\sigma'} f_{k\sigma' l'} - \frac{1}{2} \sum_{q,\{l\}} \sum_{\varsigma\varsigma'} b^{\varsigma}_{-q,l_1 l_2} \left[\tilde{W}_q^{-1} \right]_{l_1 l_2, l_3 l_4}^{\varsigma\varsigma'} b^{\varsigma'}_{q,l_4 l_3}
$$

$$
- \sum_{q,\{l\}} \sum_{\vartheta\vartheta'} b^{*\,\vartheta}_{q,l_1 l_2} \left[\tilde{W}_q^{-1} \right]_{l_1 l_2, l_3 l_4}^{\vartheta\vartheta'} b^{\vartheta'}_{q,l_3 l_4} + \mathcal{F}[f,b] \tag{6.1}
$$

with the interaction term $\mathcal{F}[f,b]$ defined in Eq. (4.57). In order to obtain the leading diagrams of the theory, we can expand the action up to the second order within the path integral. This procedure corresponds to calculating the Luttinger-Ward functional of the dual theory to the second order. In the D-TRILEX approach the self-energy $\tilde{\Sigma}$ and the polarization operator $\tilde{\Pi}$ are obtained self-consistently from an analog of the Almbladh functional [313] that corresponds to the partially bosonized dual action (4.49). The Almbladh functional is a generalization of the Luttinger-Ward functional [314–316] that includes also the possibility for a screened interaction. Keeping only the first diagrammatic terms, we derive the explicit expressions for the functional as

$$
\Phi[\tilde{G}, \tilde{W}, \Lambda] = -\frac{1}{2} \sum_{q,k} \sum_{\{l\},\{\sigma\}} \sum_{\varsigma\varsigma'} \Lambda^{\sigma_1\sigma_2\varsigma}_{\nu\omega, l_1, l_2, l_3 l_4} \tilde{G}^{\sigma_2\sigma_8}_{k+q,l_2 l_8} \tilde{G}^{\sigma_7\sigma_1}_{k,l_7 l_1} \tilde{W}^{\varsigma\varsigma'}_{q, l_3 l_4, l_5 l_6} \Lambda^{\sigma_8\sigma_7\varsigma'}_{\nu+\omega,-\omega, l_8, l_7, l_6 l_5}
$$

$$
+ \frac{1}{2} \sum_{k,k'} \sum_{\{l\},\{\sigma\}} \sum_{\varsigma\varsigma'} \Lambda^{\sigma_1\sigma_2\varsigma}_{\nu,\omega=0, l_1, l_2, l_3 l_4} \tilde{G}^{\sigma_2\sigma_1}_{k,l_2 l_1} \tilde{G}^{\sigma_7\sigma_8}_{k',l_7 l_8} \tilde{W}^{\varsigma\varsigma'}_{q=0, l_3 l_4, l_5 l_6} \Lambda^{\sigma_8\sigma_7\varsigma'}_{\nu',\omega=0, l_8, l_7, l_6 l_5}.
$$
$$\tag{6.2}$$

Note that the contribution of the particle-particle ϑ channel to the introduced functional is neglected, because the renormalization of the bare interaction in the particle-particle channel is believed to be negligibly small at standard fillings in the case of repulsive interactions at general fillings [232, 317]. The dual self-energy and the dual polarization operator can be found by taking the functional derivative of the functional (6.2)

$$
\tilde{\Sigma}^{\sigma\sigma'}_{k,ll'} = \frac{\partial \Phi[\tilde{G}, \tilde{W}, \Lambda]}{\partial \tilde{G}^{\sigma'\sigma}_{k,l'l}} \bigg|_{\tilde{W},\Lambda}, \qquad \tilde{\Pi}^{\varsigma\varsigma'}_{q,l_1 l_2, l_3 l_4} = -2 \frac{\partial \Phi[\tilde{G}, \tilde{W}, \Lambda]}{\partial \tilde{W}^{\varsigma'\varsigma}_{q,, l_3 l_4, l_1 l_2}} \bigg|_{\tilde{G},\Lambda} \tag{6.3}
$$
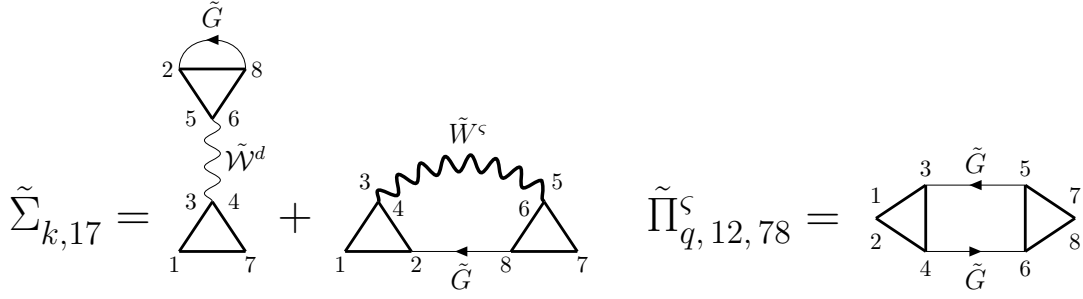
FIGURE 6.1: Diagrammatic representation for the dual self-energy $\tilde{\Sigma}$ (left) and the dual polarization operator $\tilde{\Pi}$ (right). The two processes contributing to $\tilde{\Sigma}$ are expressed mathematically in Eqs. (6.4). The expression for $\tilde{\Pi}$ is explicitly written in Eq. (6.5). Wavy lines represent dual bosonic propagators and straight lines depict dual Green's function, as explicitly indicated in the Figure. Triangles represent three-point vertex functions $\Lambda_{\nu\omega}^{\varsigma}$. Numbers correspond to band indices. The bosonic end of the triangle can be identified by the fact that it carries two band indices. Reproduced from Ref. [96].

This results in the following equations for the dual self-energy and polarization

$$
\begin{aligned}
\tilde{\Sigma}_{k,l_1l_7}^{\sigma_1\sigma_7} &= \left(\tilde{\Sigma}^{\text{TP}}\right)_{k,l_1l_7}^{\sigma_1\sigma_7} + \left(\tilde{\Sigma}^{GW}\right)_{k,l_1l_7}^{\sigma_1\sigma_7} \\
&= -\sum_{q,\varsigma\varsigma'}\sum_{\{l\},\{\sigma\}} \Lambda_{\nu\omega,l_1,l_2,l_3l_4}^{\sigma_1\sigma_2\varsigma} \tilde{G}_{k+q,l_2l_8}^{\sigma_2\sigma_8} \tilde{W}_{q,l_3l_4,l_5l_6}^{\varsigma\varsigma'} \Lambda_{\nu+\omega,-\omega,l_8,l_7,l_6l_5}^{\sigma_8\sigma_7\varsigma'} \\
&\quad + \sum_{k',\varsigma\varsigma'}\sum_{\{l\},\{\sigma\}} \Lambda_{\nu,\omega=0,l_1,l_7,l_3l_4}^{\sigma_1\sigma_7\varsigma} \tilde{W}_{q=0,l_3l_4,l_5l_6}^{\varsigma\varsigma'} \Lambda_{\nu',\omega=0,l_8,l_2,l_6l_5}^{\sigma_8\sigma_2\varsigma'} \tilde{G}_{k',l_2l_8}^{\sigma_2\sigma_8} \qquad (6.4)
\end{aligned}
$$

$$
\tilde{\Pi}_{q,l_1l_2,l_7l_8}^{\varsigma\varsigma'} = \sum_{k}\sum_{\{l\},\{\sigma\}} \Lambda_{\nu+\omega,-\omega,l_4,l_3,l_2l_1}^{\sigma_4\sigma_3\varsigma} \tilde{G}_{k,l_3l_5}^{\sigma_3\sigma_5} \tilde{G}_{k+q,l_6l_4}^{\sigma_6\sigma_4} \Lambda_{\nu\omega,l_5,l_6,l_7l_8}^{\sigma_5\sigma_6\varsigma'} \qquad (6.5)
$$

Here, $\tilde{G}_k^{\sigma\sigma'}$ and $W_q^{\varsigma\varsigma'}$ are the dressed fermionic and bosonic propagators of the partially bosonized dual problem (4.49) that can be found using Dyson equations (4.61) and (4.62), respectively. The diagrammatic representation of these equations is shown in Fig. 6.1. In the expression for the dual self-energy, we highlighted the two contributions $\tilde{\Sigma}^{\text{TP}}$ and $\tilde{\Sigma}^{GW}$, that have the same diagrammatic structure as the Hartree term and the GW self-energy respectively up to local vertex corrections.

These two equations in combination with the corresponding fermionic and bosonic Dyson's equations of Eqs. (4.61)-(4.62) consist in a system of equations that have to be solved self-consistently. This kind of non-linear fixed point equations does not have a unique solution and one has to adopt strategies to achieve convergence in difficult regimes as discussed in Ref. [318]. In most cases, regimes of difficult convergence or divergence of the self-consistent cycle correspond to physical instabilities.

Note that the D-TRILEX diagrams (6.4)-(6.5) represent the leading contribution to the self-energy and the polarisation operator of the partially bosonized dual action (4.49) in both the weak and the strong coupling limits independently from the dimensionality of the problem. Indeed, at weak coupling the D-TRILEX diagrammatic expansion is a perturbative expansion in terms of the renormalised interaction (4.51). On the other hand, in the strong coupling limit the bare dual Greens function, which is purely non-local, is small, because electrons in the system are strongly localized (4.50).

6.1.3   Lattice quantities from a D-TRILEX calculation

Here, we quickly smmarize all the steps of a D-TRILEX calculation. For simplicity, in this summary we neglect the particle-particle channels and we assume a paramagnetic calculation. In paramagnetic regime, all the fermionic quantities do not depend on spin. As a consequence, we can write the Green's function and all the single-particle fermionic quantities in a spin-independent fashion as

$$G_{k,ll'}^{\sigma\sigma'} = G_{k,ll'}\delta_{\sigma\sigma'}. \tag{6.6}$$

Similarly, the matrix structure of the susceptibility and all the other bosonic quantities reduces to

$$\left(X_q\right)_{l_1l_2,\,l_3l_4}^{\varsigma\varsigma'} = \left(X_q\right)_{l_1l_2,\,l_3l_4}^{\varsigma} \delta_{\varsigma\varsigma'} \tag{6.7}$$

for $\varsigma = d, m$ with $m = s_x = s_y = s_z$, hence we can do calculations only for a single spin projection and the others will be identical.

The single- and two-particle quantities for the initial lattice problem (3.14) can be obtained from the dual quantities using the following exact relations (see Section 4.4). The most convenient relation for the practical calculation of the lattice Green's function $G_{k,ll'}$ involves the dual self-energy $\tilde{\Sigma}$

$$\left[G_k^{-1}\right]_{ll'} = \left[\left(g_\nu + \tilde{\Sigma}_k\right)^{-1}\right]_{ll'} + \Delta_{\nu,ll'} - \varepsilon_{\mathbf{k},ll'} \tag{6.8}$$

Calculating $G_{k,ll'}$ be means of Eq. (6.8) has an advantage, because this expression does not involve the self-energy of the reference problem $\Sigma_{\nu,ll'}^{\text{imp}}$. The latter is not a correlation function and is usually calculated by inverting the corresponding Dyson equation for the Green's function $g_{\nu,ll'}$ of the reference problem

$$\Sigma_{\nu,ll'}^{\text{imp}} = (i\nu + \mu)\delta_{ll'} - \Delta_{\nu,ll'} - \left[g_\nu^{-1}\right]_{ll'} \tag{6.9}$$

Consequently, $\Sigma_{\nu,ll'}^{\text{imp}}$ obtained in this way contains big numerical noise at large frequencies ν. This problem can be cured by employing improved estimator methods that consist in computing higher-order correlation functions [319–321]. However, in multi-band calculations this procedure is numerically expensive. For this reason, it is preferable to compute the lattice Green's function using Eq. (6.8), and the lattice self-energy (4.67) separately.

Contrary to the self-energy, the polarization operator of the reference system $\Pi_{\omega}^{\text{imp}\,\varsigma}$ is not very noisy, because it has the same dimension as the susceptibility of the reference system $\chi_{\omega,l_1l_2,l_3l_4}^{\varsigma} = -\langle \rho_{\omega,l_2l_1}^{\varsigma} \rho_{-\omega,l_3l_4}^{\varsigma} \rangle$. Indeed, the polarization operator is defined through the corresponding Dyson equation as

$$\left[\left(\Pi_{\omega}^{\text{imp}\,\varsigma} \right)^{-1} \right]_{l_1l_2,l_3l_4} = \left[\left(\chi_{\omega}^{\varsigma} \right)^{-1} \right]_{l_1l_2,l_3l_4} + U_{l_1l_2,l_3l_4}^{\varsigma} \tag{6.10}$$

For this reason, the lattice susceptibility X_q^{ς} is convenient to obtain directly from the Dyson equation (see Section 4.4)

$$\left[\left(X_q^{\varsigma} \right)^{-1} \right]_{l_1l_2,l_3l_4} = \left[\left(\Pi_q^{\varsigma} \right)^{-1} \right]_{l_1l_2,l_3l_4} - \left[U^{\varsigma} + V_q^{\varsigma} \right]_{l_1l_2,l_3l_4} \tag{6.11}$$

that involves the polarization operator of the lattice problem

$$\Pi_{q,l_1l_2,l_3l_4}^{\varsigma} = \Pi_{\omega,l_1l_2,l_3l_4}^{\text{imp}\,\varsigma} + \sum_{l',l''} \tilde{\Pi}_{q,l_1l_2,l'l''}^{\varsigma} \left[\left(\mathbb{1} + \bar{u}^{\varsigma} \cdot \tilde{\Pi}_q^{\varsigma} \right)^{-1} \right]_{l'l'',l_3l_4} \tag{6.12}$$

Importantly, as shown in Section 4.4, the divergence in the lattice susceptibility X_q^{ς} occurs at the same time as in the renormalized interaction $\tilde{W}_q^{\varsigma}$ that enters the term $\tilde{\Sigma}^{GW}$ in the self-energy (6.4). This allows the D-TRILEX approach to capture the formation of the pseudogap in the electronic spectral function in the paramagnetic regime in the vicinity of a symmetry broken phase in the system [233, 235].

Finally, the polarization operator in the D-TRILEX approach (6.5) has the same structure as the exchange interaction $\mathcal{J}^{\varsigma}$ between charge and/or magnetic densities derived in Refs. [264–266] in the many-body framework. This fact allows for a direct calculation of the exchange interaction within the D-TRILEX scheme using the following relation

$$\mathcal{J}_{q,l_1l_2,l_3l_4}^{\varsigma} = \sum_{\{l'\}} \left[\left(\Pi_{\omega}^{\text{imp}\,\varsigma} \right)^{-1} \right]_{l_1l_2,l_1'l_2'} \left[\tilde{\Pi}_q^{\varsigma} \right]_{l_1'l_2',l_3'l_4'} \left[\left(\Pi_{\omega}^{\text{imp}\,\varsigma} \right)^{-1} \right]_{l_3'l_4',l_3l_4} \tag{6.13}$$

This quantity is computed at the first iteration of the D-TRILEX self-consistent cycle, because instead of the dressed dual Green's functions $\tilde{G}$ the dual polarization operator (6.5) in the expression for the exchange interaction contains the bare dual Green's functions $\tilde{\mathcal{G}}$ (see Ref. [266]). Note that in Eq. (6.13) the inverse of the polarization operator of the reference problem appears to the left and right of the dual polarization operator due to

a different definition of the vertex function used in Refs. [264–266]. We stress that the obtained relations between the dual and the lattice quantities are valid for any form of the self-energy and the polarisation operator of the partially bosonized dual action (4.49). Focusing on the D-TRILEX approach, it accounts for the leading diagrammatic contributions in both the weak and the strong coupling limits, as previously mentioned. Specifically, the D-TRILEX polarisation operator (6.5) becomes the leading contribution (the second-order in terms of the dual Green's functions) to the susceptibility (apart from the impurity polarisation operator) in the strong coupling limit. More elaborate contributions have at least four dual Green's functions in their structure, so they can be disregarded and D-TRILEX becomes accurate in the regime close to the atomic limit also at the two-particle level. As an additional confirmation of this fact, the expression in Eq. (6.13) gives the correct result for the exchange interaction $\sim t^2/U$ in the atomic limit [264]. For the sake of completeness, we note that the D-TRILEX solution based on the DMFT reference problem is exact for arbitrary interaction strength in the limit of infinite dimensions at the single-particle level, but not at the two particle level, because it uses the partially bosonized approximation (see Section 4.3.1) instead of the exact four-point vertex function. However, based on the results presented in the current and previous works [232], we stress that there is no correlation between the exactness of the theory in the limit of infinite dimensions and the accuracy of the theory in finite dimensions.

In addition to dynamical quantities it is possible to compute the density and the energy in a D-TRILEX calculation. The density for each site-orbital index l can be calculated using the regular formula, based on the Green's function

$$\langle n_{l\sigma}\rangle = \frac{1}{2} + \sum_k \mathrm{Re}\,(G_k)_{ll}^{\sigma\sigma} = \frac{1}{2} + \frac{1}{\beta}\sum_\nu \mathrm{Re}\left(G_\nu^{\mathrm{loc}}\right)_{ll}^{\sigma\sigma} \tag{6.14}$$

and the total density is simply $\langle n\rangle = \sum_{l\sigma}\langle n_{l\sigma}\rangle$. In our calculations, we employed a fitting of the first few even orders in $1/\nu$ of the tail of the local Green's function G_ν^{loc} to get an accurate result.

Another important single-particle observable of the system is the average energy of the system. It can be obtained as the expectation value of the Hamiltonian H corresponding to action (3.14) of the system, $\langle E\rangle_{\mathrm{tot}} = \langle H\rangle$. The total energy $\langle E\rangle_{\mathrm{tot}} = \langle E\rangle_{\mathrm{kin}} + \langle E\rangle_{\mathrm{pot}}$ can be split into a single-particle kinetic contribution $\langle E\rangle_{\mathrm{kin}}$ and a potential energy $\langle E\rangle_{\mathrm{pot}}$ coming from the interaction. The kinetic part corresponds to

$$\langle E\rangle_{\mathrm{kin}} = \sum_{\substack{k,\{l\},\\ \sigma\sigma'}} \left[\varepsilon_{\mathbf{k},ll'}^{\sigma\sigma'} - \mu\delta_{ll'}\delta_{\sigma\sigma'}\right]\langle c_{k\sigma l}^* c_{k\sigma'l'}\rangle = \sum_{\substack{k,\{l\},\\ \sigma\sigma'}} \left(\varepsilon_{\mathbf{k},ll'}^{\sigma\sigma'} - \mu\delta_{ll'}\delta_{\sigma\sigma'}\right)G_{k,ll'}^{\sigma\sigma'} \tag{6.15}$$

The potential contribution is the expectation value of the interacting terms

$$\langle E \rangle_{\text{pot}} = \frac{1}{2} \sum_{q,\{k\}} \sum_{\{l\},\{\sigma\}} U^{pp}_{l_1 l_2 l_3 l_4} \left\langle c^*_{k \sigma l_1} c^*_{q-k,\sigma' l_2} c_{q-k',\sigma' l_4} c_{k' \sigma l_3} \right\rangle + \frac{1}{2} \sum_{q,\{l\},\varsigma} V^{\varsigma}_{q, l_1 l_2, l_3 l_4} \left\langle \rho^{\varsigma}_{-q, l_1 l_2} \rho^{\varsigma}_{q, l_4 l_3} \right\rangle$$

(6.16)

where we neglected particle-particle contributions. After recasting the interaction in the particle-hole representation (4.21), we can use the relation (4.68) and the definition of $\rho^{\varsigma}_{q, ll'}$ to replace the expectation values of four operators with the quantities computed in D-TRILEX

$$\langle n^{\varsigma}_{q, l_2 l_1} n^{\varsigma}_{-q, l_3 l_4} \rangle = -X^{\varsigma}_{q, l_1 l_2, l_3 l_4} + \langle n^{\varsigma}_{q, l_2 l_1} \rangle \langle n^{\varsigma}_{-q, l_3 l_4} \rangle$$

(6.17)

Following these replacements and excluding unphysical term due to Pauli principle, the final expression for the potential energy in the Kanamori approximation for the interaction reads

$$\langle E \rangle_{\text{pot}} = -\frac{1}{2} \sum_{q,\{l\}} U^{ph}_{l_3 l_4 l_1 l_2} \left[X^d_q \right]_{l_1 l_2 l_3 l_4} + \frac{1}{2} \sum_{\{l\}} U^{ph}_{l_3 l_4 l_1 l_2} \langle n^d_{l_2 l_1} \rangle \langle n^d_{l_3 l_4} \rangle$$

$$+ \frac{1}{4} \sum_{q,l} U^{ph}_{llll} \left[X^d_q \right]_{llll} + \frac{1}{4} \sum_{q,l} U^{ph}_{llll} \left[X^z_q \right]_{llll} - \frac{1}{4} \sum_{q,l} U^{ph}_{llll} \langle n^d_{ll} \rangle^2$$

$$- \frac{1}{2} \sum_{l_1,l_2} (1 - \delta_{l_1,l_2}) \left\{ U^{ph}_{l_1 l_2 l_1 l_2} \langle n^d_{l_1 l_1} \rangle - \frac{1}{2} U^{ph}_{l_1 l_2 l_2 l_1} \left(X^{ch}_{l_2 l_1 l_1 l_2} + X^z_{l_2 l_1 l_1 l_2} - \frac{1}{2} \langle n^d_{l_1 l_2} \rangle^2 \right) \right\}$$

$$- \frac{1}{2} \sum_{q,\{l\}} \left[V^{ch}_{\mathbf{q}} \right]_{l_3 l_4 l_1 l_2} \left[X^{ch}_q \right]_{l_1 l_2 l_3 l_4} - \frac{3}{2} \sum_{q,\{l\}} \left[V^z_{\mathbf{q}} \right]_{l_3 l_4 l_1 l_2} \left[X^z_q \right]_{l_1 l_2 l_3 l_4}$$

(6.18)

6.1.4 Scheme of a D-TRILEX calculation

The computational workflow is divided into several parts, as shown in Fig 6.2. The first step (St.1) consists in solving the reference system, e.g. the DMFT impurity problem. This produces the inputs necessary for the initialization of the diagrammatic part of the calculation. Hence, the inner steps are denoted with (Init.). The second step (St.2) takes care of the self-consistent dressing of the dual Green's function $\tilde{G}$ and the renormalized interaction $\tilde{W}$. The inner steps (I.) of the self-consistent diagrammatic iteration are highlighted below. After the dressed dual quantities are determined, the single- and two-particle quantities for the initial (lattice) problem are evaluated at the third step (St.3). Here, we assume a paramagnetic calculation, so we can omit spin indices in fermionic quantities as well as the matrix channel dependence that appears in the bosonic quantities if an off-diagonal spin
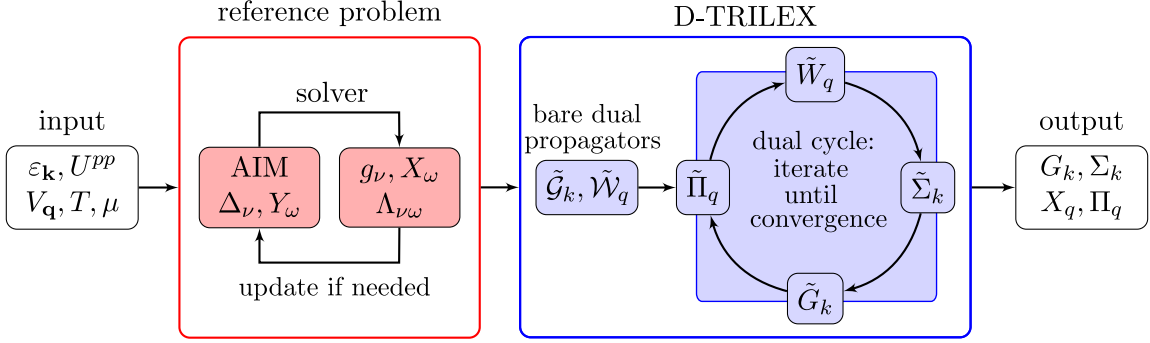
FIGURE 6.2: Workflow of the D-TRILEX method. The input consists in the parameters of the electronic lattice problem (Init.1-2 in the main text). The red box indicates the solution of the reference impurity problem (Init.3), that in some case has to be updated until self-consistency is reached (for instance in DMFT, EDMFT and cluster DMFT). The blue box contains the operations performed in the dual space, i.e. the calculation of the bare dual propagators (Init.4) and the self-consistency cycle on the dual quantities (St.2). The output consists in the Green's function, self-energy, susceptibility and polarization operator of the lattice problem, obtained by applying the exact relations between lattice and dual quantities (St.3).

dependence appears in the Hamiltonian. The computational workflow has the following form:

(St.1) Input initialization:

    (Init.1) Specify the single-particle term $\varepsilon_{\mathbf{k},ll'}$, the interactions $U^{pp/ph}_{l_1 l_2 l_3 l_4}$ and $V^{\varsigma}_{q,l_1 l_2,l_3 l_4}$, and the temperature T that enter the initial action (3.14).

    (Init.2) Define the chemical potential μ and the hybridization function $\Delta_{\nu,ll'}$.

    (Init.3) Solve the reference system and get the corresponding Green's function $g_{\nu,ll'}$, the susceptibility $\chi^{\varsigma}_{\omega,l_1 l_2,l_3 l_4}$, and the vertex function $\Lambda^{\varsigma}_{\nu\omega,l_1,l_2,l_3 l_4}$.

    (Init.4) Compute the bare fermionic $\tilde{\mathcal{G}}_{k,ll'}$ and bosonic $\tilde{\mathcal{W}}^{\varsigma}_{q,l_1 l_2,l_3 l_4}$ propagators of the effective partially bosonized dual action (4.49) according to Eqs. (4.50) and (4.51), respectively.

(St.2) Self-consistent calculation of D-TRILEX diagrams:

    (I.1) Compute the dual polarization operator $\tilde{\Pi}$ using Eq. (6.5).

        At the first iteration only: Compute the exchange interaction $\mathcal{J}^{\varsigma}_{q,l_1 l_2,l_3 l_4}$ via Eq. (6.13).

    (I.2) Compute the dual renormalized interaction $\tilde{W}$ using Eq. (4.62).

    (I.3) Compute the diagrams $\tilde{\Sigma}^{\mathrm{TP}}$ and $\tilde{\Sigma}^{GW}$ for the dual self-energy (6.4).

(I.4) Compute the dressed dual Green's function $\tilde{G}$ using Eq. (4.61).

(I.5) If the desired accuracy δ for the self-consistent condition is reached, go to (St.3). Otherwise go back to (I.1).

(St.3) Evaluation of lattice quantities:

Compute the dressed Green's function $G_{k,ll'}$ (6.8), the self-energy $\Sigma_{k,ll'}$ (4.67), the susceptibility $X^{\varsigma}_{q,l_1l_2,l_3l_4}$ (6.11), and the polarization operator $\Pi^{\varsigma}_{q,l_1l_2,l_3l_4}$ (6.12) for the lattice problem (3.14). From these quantities determine the orbital-resolved average density $\langle n_l \rangle$ (6.14) and the average energy $\langle E \rangle$ of the system (6.15) and (6.16). If one aims at the specific density $\langle n \rangle$, it is possible to update the chemical potential μ and go back to the beginning of the outer loop. In that case, go to (St.1 of Init.2) and fix the new μ and update the hybridization function $\Delta_{\nu,ll'}$ if needed.

6.1.5 Details of the calculation

The complexity of the diagrammatic part of the D-TRILEX calculation is estimated as

$$O\left(N_\nu N_\omega\right) O\left(N_{\text{imp}}^2 \times \sum_{i=1}^{N_{\text{imp}}} N_{l_i}^8\right) O\left(N_k \log N_k\right) \tag{6.19}$$

where $N_{\nu(\omega)}$ is the number of fermionic (bosonic) Matsubara frequencies, N_{imp} is the number of impurities in the reference system, N_{l_i} is the number of orbitals for the i-th impurity and N_k is the total number of $\mathbf{k}$-points. In this context, N_{imp} is the number of independent impurities in the unit cell of the reference problem. Note that the case of $N_{\text{imp}} > 1$ corresponds to a collection of impurities, as explained in Ref. [260], and not to a cluster of N_{imp} sites. If the impurities are all identical, then the reference system reduces to a single site impurity problem. If some of them are different, it is sufficient to solve an impurity problem only for the non-equivalent ones. In the multi-impurity case, fluctuations between the impurities are taken into account diagrammatically in the framework of D-TRILEX approach. On the other hand, a cluster reference system corresponds to a multi-orbital problem with $N_{\text{imp}} = 1$. In this case, N_l is the total number of orbitals and sites of the considered cluster. The separation between orbitals and sites that we introduce is useful to reduce the computational complexity when addressing problems with several atoms in the unit cells.

The scaling as a function of $\mathbf{k}$-points is determined from the fact that we utilise the fast-Fourier transform (FFT) algorithm for computing convolutions in momentum space. This shows that the multi-impurity calculation has a quadratic scaling with respect to the

number of impurities. In our current implementation, the local Coulomb matrix is considered as a non-sparse matrix within each site subspace, hence the scaling to the 6th power in the number of orbitals. However, before running the actual calculations, we introduced a check to assess which components of the vertices are zero. These components are automatically skipped in order to avoid unnecessary calculations and to automatically take advantage of a possible sparsity of the Coulomb matrix, effectively reducing the complexity (6.19) in most cases. The summation over frequencies and band indices can be efficiently parallelized both in a shared-memory framework (as done in the current implementation) and in an message-passing interface (MPI) framework.

To measure the accuracy at the n-th iteration of the self-consistent cycle, we use the relative Frobenius norm of the Green's function $F = \|\tilde{G}_n - \tilde{G}_{n-1}\|/\|\tilde{G}_{n-1}\|$ as a metric, where $\|...\|$ is the square root of the squared sum over all the components of the array. If F is smaller than some predefined accuracy value δ, the self-consistent cycle stops. The cycle stops also if a specified maximum number of iterations is reached. The stability of the bosonic Dyson equation (4.62) can be problematic in regimes of parameters, where one or more of the eigenvalues of the quantity $\tilde{\Pi} \cdot \tilde{W}$ become equal or larger than 1. In particular, this happens when the system is close to a phase transition or if the correlation length in some channel of instability exceeds a critical value. This issue appears in similar forms in other diagrammatic extensions of DMFT (see, e.g., Ref. [254]). In one- and two-dimensional systems, where Mermin-Wagner theorem forbids the breaking of continuous symmetries [255], the issue can be mitigated by imposing that the eigenvalues λ_i of the $\tilde{\Pi} \cdot \tilde{W}$ matrix in the orbital space for a physical meaningful solution are always smaller than 1. In our implementation, we check whether any eigenvalue $\lambda_i \geq 1$ ($i \in \{k, \varsigma\}$). If this happens, the eigenvalue can be rescaled as described in Ref. [254] in order to improve convergence.

Several strategies can be used to improve the stability of the self-consistent procedure in the general case. The first strategy is implemented when updating the D-TRILEX self-energy. The updated dual self-energy at the n-th iteration is computed as $\tilde{\Sigma}_n = (1 - \xi)\tilde{\Sigma}_{n-1} + \xi\tilde{\Sigma}$ for $\xi \in (0, 1)$, where $\tilde{\Sigma}_{n-1}$ is the value of the dual self-energy computed at the previous $(n - 1)$ iteration, and $\tilde{\Sigma}$ is computed using the propagators $\tilde{G}_{n-1}$ and $\tilde{W}_{n-1}$ obtained at the previous iteration. This procedure was shown to improve stability in GW-like theories [318]. A similar mixing scheme can be applied to the dual polarization. To the same aim, we also introduce multiplicative factors for the dual self-energy and the dual polarization at the first iteration. Of course, no rescaling is expected to work in the presence of the symmetry breaking due to a true phase transition. The latter case should be addressed using a suitable cluster or multi-impurity reference problem.

It is worth mentioning that the efficiency of the whole scheme is strongly affected by the computational cost of the impurity solver. In our tests, the time needed to solve the impurity problem and to obtain the required correlation functions of the reference system using continuous time quantum Monte Carlo solvers [83, 140, 143, 273] always exceeds

the computational cost for the diagrammatic part of the calculation, even by several orders of magnitude. For example, a single iteration of the self-consistent diagrammatic cycle for a two-orbital Hubbard-Kanamori model on a two-dimensional lattice with 64×64 points in the momentum-space, 64 fermionic and 32 bosonic frequencies takes only few minutes.

6.2 Implementation of the D-TRILEX code

A large part of the work for this theses aimed at the development of a general and effective D-TRILEX code to solve a generic multi-orbital and multi-impurity problem. In order to do that, it is important to balance several different aspects. In order of importance, the crucial aspects to consider are:

1. Efficiency both in CPU time and in memory usage.

2. Flexibility due to the rather general formulation of the problem to address (see Eq. (3.14) in Chapter 3).

3. Need to create an interface with existing impurity solvers.

4. Simplicity of use and readability. The user should be able to run the code straight away without any issue related to the compilation.

It turns out that the set of D-TRILEX equations in a many-body framework involves convolutions in both **k**-space and Matsubara frequency, as well as summation over the internal orbitals. The direct implementation of all these summations with a large lattice is hopeless without parallelization and optimization, even by using copiled languages such as C++.

However, the poblem can be efficiently addressed even in an interpreted language as Python, by using the correct combination of libraries for vector operations, parallelization techniques and optimization in order to avoid any unnecessary calculation. Based on this consideration, we implement the whole program package in Python 3, slightly sacrificing the performances when `for`-loops are involved, but improving all the other points listed above.

6.2.1 Requirements

Our implementation exploits the following libraries:

- `numpy`: any quantity is stored in a `numpy.ndarray` object. This allows to perform efficient operations without the use of slow loops. The use of this library allows to perform operations on arrays almost at the same speed of C with a small overhead,

but with very optimized libraries. In particular, we use the `numpy.linalg` module based on the LAPACK routines for matrix inversion and computation of eigenvalues and `numpy.fft` module as an implementation of the FFT algorithm.

- `multiprocessing`: we employ a shared-memory parallelization scheme to spam processes to the available CPUs. It is possible to do this by using a custom function based on the `multiprocessing.Process` class. Using this library is also convenient for distributing the code since it is readily available in most standard Python distributions.

- `h5py`: Input/output is managed by this library that uses the hierarchical `hdf5` format for storing the data. It also allows to compress the output data, that would require a too large storage capacity on small clusters or regular laptops.

Currently, our implementation relies on the w2dynamics software package for the impurity calculation base on the hybridization expansion [274]. The reason for this choice is that w2dynamics allows for a large flexbility in the system that can be treated and additionally provides an internal implementation of the calculation of the three-point vertices. However, the dependence on the w2dynamics package appears in the loading subroutine only. Currenly, the interested users can refer to the loading subroutine for w2dynamics to implement their own script to load from a custom impurity solver.

6.2.2   Input files

In order to run a w2dynamics calculation, the user must specify a model or an Hamiltonian. In order to use the w2dynamics output as an input to our code, it is necessary to specify an Hamiltonian file in the wannier90 format as explained in the w2dynamics wiki (for details see [322]). Our code will automatically read the name and path of the Hamiltonian file from the w2dynamics file. It is very important to consider that currently the Hamiltonian has to start from the Γ point, so $k = (0, 0, 0)$ and has to be periodic in all directions, because the FFT algorithm is used as is without specifying the geometry of the problem. This is not an issue in lattices with orthogonal axis, but might require some unitary transformation in non-orthogonal systems. This additionally requirement on the specified Hamiltonian requires some additional pre-processing, but removes any explicit dependence on the lattice type within the code. As an example, for a linear chain the momentum along the x-direction can be specified as

```python
# generate an array with Nkx equally space points
# between 0 and 2*pi
kx = np.linspace(0, 2*pi, Nkx, endpoint=False)
```

but NOT as

```
# generate an array with Nkx equally space points
# between -pi and pi
kx = np.linspace(-pi, pi, Nkx, endpoint=False)
```

It is also possible to specify the full local Coulomb matrix for the impurity problem. In this case, the `Atoms` section of the w2dynamics input files have to be modified adding the lines

```
Hamiltonian = ReadNormalUmatrix
umatrix = u_matrix.dat
```

and provide a file `u_matrix.dat` with the structure as follows.

```
2 BANDS # example with kanamori interaction
1 1 1 1 4.0
1 2 1 2 2.0
1 2 2 1 1.0
1 1 2 2 1.0
2 2 1 1 1.0
2 1 1 2 1.0
2 1 2 1 2.0
2 2 2 2 4.0
```

Our code requires three different `hdf5` files obtained using the DMFT python script provided with w2dynamics:

- a `DMFT` calculation: contains the local single-particle quantities for each impurity.

- a `p2iw` calculation based on the `DMFT`: contains the two-point bosonic correlators needed to compute the impurity susceptibilities X_ω.

- a `p3iw` calculation based on the `DMFT`: contains the three-point correlators needed to compute the impurity three-point vertices $\Lambda_{\nu\omega}$.

It is important to recall that w2dynamics uses a specific encoding for the components of two-particle objects, such as the two- and the three-point correlators. These have to be specified in the field `WormComponents` in the `p2iw` and `p3iw` input files. More information can be found in the `examples` folder of our project (currently available upon request). It is important to check whether all the relevant components are computed by w2dynamics. Our code loads all spin components and then averages over equivalent spin components.

In the `run_w2dynamics` folder of our project, we provide a file `check_index.py` to compute all the required components with/without SU(2) spin-symmetry and with/without

Z_2 symmetry for the local Hamiltonian in orbital space, which corresponds to the Hubbard-Kanamori interaction.

In addition to the Hamiltonian file (plain text file in wannier90 format) and the three output files from w2dynamics, the user might want to include a file for the non-local interaction. The non-local interaction is not used in the impurity problem. In the case of calculations with non-local interactions, it is necessary to add the key `nonloc_potential` to the input file for the D-TRILEX code `Parameters_DTRILEX.py`. This key should be associated with a `hdf5` file containing a group `nonloc_potential` with two datasets `charge` and `spin` containing the non-local V_q in each of the channels. These two datasets should have the dimension of a bosonic quantity except for the channel index, so (2 * BOSONIC_FREQS+1, Nk_x, Nk_y, Nk_z, l1, l2, l3, l4) as they can contain frequency dependent interactions.

6.2.3 Structure of the code

The structure of the code we developed in the version available during the writing of this theses is depicted in Fig.6.3.

The main runfile of the code can be summarized in very few lines of code and looks like the following:

```python
# Loading DMFT calculation
DMFT = PrepareTRILEX(Parameters)
# Actual D-TRILEX calculation
gwrun = GW_CYCLE(DMFT, Parameters)

# Get dual quantities from the gwrun
GF = gwrun.DTRILEX.GF
W = gwrun.DTRILEX.W
Pi = gwrun.Pi
sigma = gwrun.Sigma
Vq = gwrun.vq

# Get lattice quantities from the latticeQuantities subroutine
lattice_GF = Lattice_GreenFunction(DMFT, gwrun.Sigma)
lattice_sigma = Lattice_SelfEnergy(DMFT, gwrun.Sigma)
lattice_pol = Lattice_Polarization(DMFT, gwrun.Pi, Vq)
lattice_chi = Lattice_Susceptibility(DMFT, gwrun.Pi, Vq)
```

Here, we attach a sample of the code for the calculation of the dual self-energy $\tilde{\Sigma}_k$ in the absence of spin-orbit coupling. The function is written in a form that can be independently distributed for any fermionic `nu` among different processors without any communication

between the processes. As mentioned before this is done using the `multiprocesses.Process`. This happens only inside the calculation of the diagrams, where the calculation of $\tilde{\Sigma}_k$ and of the dual polarization $\tilde{\Pi}_q$ is split among different processes.

```python
def computeSelfEnergy_no_SpinOrbit(self, nu):
    """
    Returns the self-energy at frequency nu optimized for the case
    without spin-orbit
    """
    # 2 because spin channel has to be computed only once
    sigma_nu = np.zeros(self.Nkpoints + 2 * (self.Nb, ), complex)
    for omega in np.arange(-self.Nwb, self.Nwb+1):
        nupom = nu+omega
        for ch in [0, 1]:
            ch_vtx = 'charge' if ch == 0 else 'spin'
            for orb_right in self.comb_orbs_pi:
                for orb_left in self.comb_orbs_pi:
                    i1, l1, l2, l3 = orb_right
                    i2, l4, l5, l6 = orb_left
                    vtx = self.Lambda_b(
                        nu, omega, (i1, l1, l2, l3), ch_vtx)
                    vtx_conj = self.Lambda_b(
                        nu+omega, -omega, (l6, i2, l5, l4), ch_vtx)
                    if (abs(vtx) < 1e-6) or (abs(vtx_conj) < 1e-6):
                        continue
                    GFnupom = self.symm(self.GF[..., l1, l6], nupom)
                    W = self.W[omega+self.Nwb, :, :, :, l2, l3, l4, l5,
                        ch]
                    bubble = convolution_fft(GFnupom, W, axis=(0, 1, 2))
                    sigma_nu[:, :, :, i1,
                            i2] -= (2.*ch+1.)*vtx*bubble*vtx_conj
    return sigma_nu
```
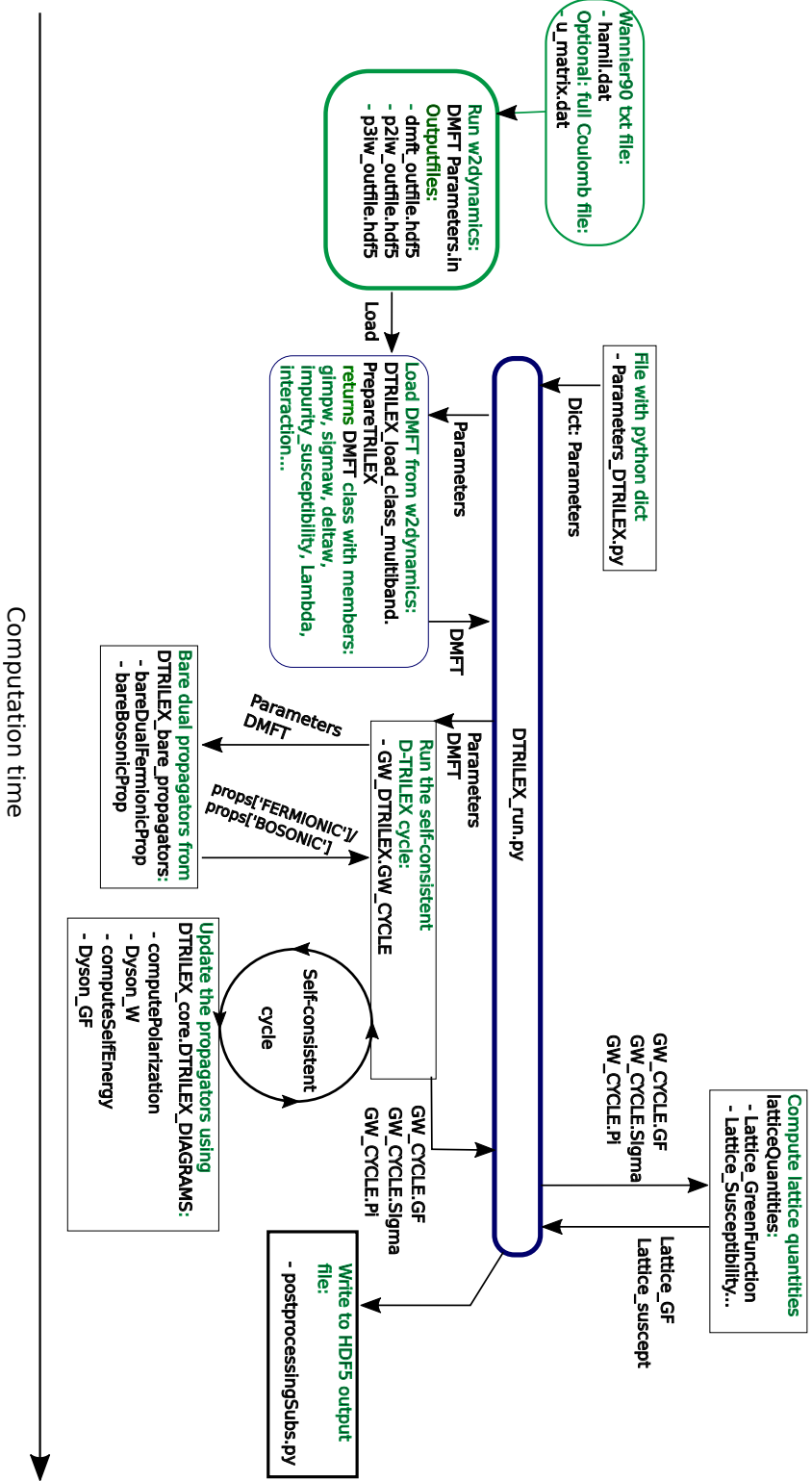
FIGURE 6.3: Scheme of the D-TRILEX scheme in the available version while writing this theses. The horizontal axis highlights that all the steps from left to right are in chronological order.

6.3 Benchmark for the single-orbital Hubbard model on the square lattice

In this section, we investigate the performances of the D-TRILEX approximation in several single-orbital examples. This step is crucial to understand which contributions are effectively missing and in which regimes the method is not expected to work well. Additionally, there are many available methods that can deal with the single-orbital Hubbard model. An extensive review of these methods in the weak-coupling regime can be found in Ref. [236]. Each of the subsections treats a different system.

6.3.1 D-TRILEX vs DiagMC@DB on the square lattice with Hubbard interaction

The first system considered here is the Hubband model of Eq. (3.21) for the $d = 2$ case on the square lattice. The dispersion of the system is chosen to be the simple nearest-neighbor tight-binding form of Eq. (5.31) in Chapter 5

$$\epsilon_{\mathbf{k}} = -2t\left(\cos k_x + \cos k_y\right). \tag{6.20}$$

We start by considering a scan over a broad range of local Coulomb interactions U at half-filling. We remind the reader that DMFT predicts the Néel transition at a finite temperature in two-dimensions, even though any transition with symmetry breaking is forbidden by Mermin-Wagner theorem [255] and thus it is an artefact of the method. In this benchmark, we compare results for in the D-TRILEX approximation with ladder dual fermion (LDF), DiagMC@DF and the DiagMC results obtained with two different partially bosonized dual approximations for the fermion-fermion vertex (PBDT), called DiagMC@PBDT and DiagMC@PBDT-s. The vertex function in both approximations is obtained using Eq. (4.34).

The difference consists in the fact that the DiagMC@PBDT contains all the constributions including the exchange of bosons in the singlet channel, while this term is neglected in the DiagMC@PBDT-s approximation. The DiagMC solution with the two approximations for the fermion-fermion vertex corresponds to the exact solution of the partially bosonized dual action (4.49) with or without the particle-particle channels in the interacting term $\mathcal{F}[f, b]$ (4.57). Considering all these different approaches, that exclude different classes of diagrams, is important to understand which contributions are negligible and in
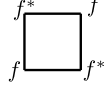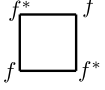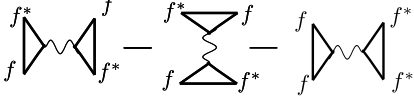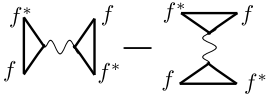
	Interaction vertex	Diagrams
DiagMC@DF		all
LDF		ladder only
DiagMC @PBDB		all
DiagMC @PBDB-s		all
D-TRILEX		ladder only

FIGURE 6.4: Summary of the diagrammatic contributions included in each of the methods considered in this Section. The DiagMC@DF corresponds to the exact solution of the dual action at the two-particle level. The order in which the methods are presented reflects the degree of approximation of the local fermion-fermion vertex Γ, from exact to more approximated.

what regimes. A sketch of the approximations and diagrams for each method in summarized in Fig. 6.4.

Since the DiagMC@DF method uses the DMFT impurity problem as a starting point for the diagrammatic expansion, the DiagMC@DF theory shows difficult convergence or even divergent result close to the DMFT Néel point [220, 221]. The same convergence issues appear at a somewhat smaller temperature in LDF calculations(large β) [236] and D-TRILEX [232]. It is known that at any finite temperature considering a sufficiently large number of k-points N_k and Matsubara frequencies in the LDF method ensures that Mermin-Wagner theorem at low temeprature. The number of k-points N_k necessary to get sensible results at low temperature increases too quickly to be viable in practical calculations [254]. A similar study for D-TRILEX is currently still missing. As a consequence, calculations are performed at the inverse temperature $\beta = T^{-1} = 2$, so that the DiagMC results are not affected by any convergence issue. In Fig. 6.5 we show results for the lattice self-energy (4.67) calculated for all the different approaches at different values of the Hubbard interation U. The results are obtained for the first Matsubara frequency $\nu_0 = \pi/\beta$ along the high symmetry path connecting $\Gamma = (0,0)$, X $= (0,\pi)$, and M $= (\pi,\pi)$ points
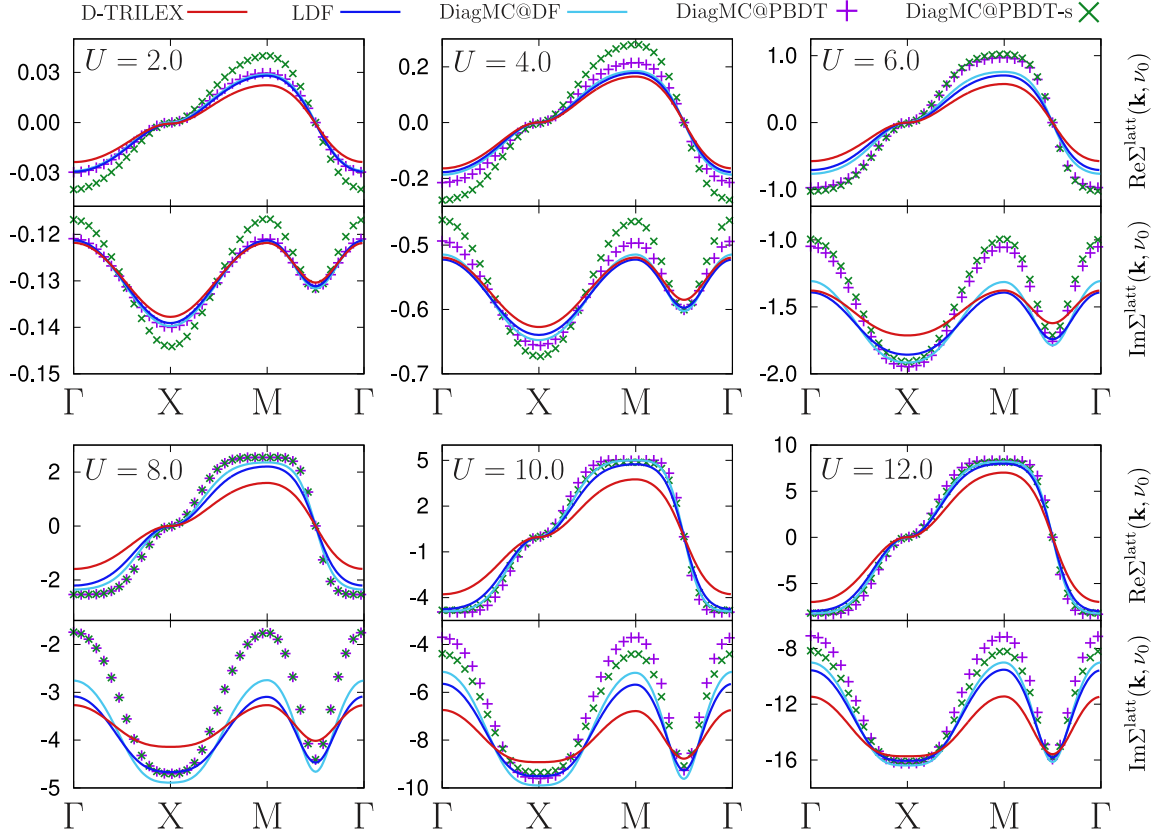
FIGURE 6.5: The lattice self-energy $\Sigma_{\mathbf{k},\nu}^{\text{latt}}$ obtained for the first Matsubara frequency $\nu_0 = \pi/\beta$ for the inverse temperature $\beta = 2$ along the high symmetry path in momentum space $\mathbf{k}$. The value of the on-site Coulomb potential U for which the calculation was performed is specified in panels. Upper and lower part of each panel corresponds to real and imaginary part of the self energy, respectively. Results are obtained using D-TRILEX (red line), LDF (dark blue line), DiagMC@DF (light blue line), DiagMC@PBDT (purple crosses), and DiagMC@PBDT-s (green crosses) methods. Figure reproduced from Ref. [232].

in momentum space $\mathbf{k} = (k_x, k_y)$. We use a mesh of 128×128 k-points in the Brillouin Zone. The self-energy does not contain the constant Hartree part that is equal to $U/2$ at half-filling.

We take advantage of the diferences between the different methods to investigate which contributions are important in which regimes. The first important contribution to investigate is the effect of the irreducible part of the four-point vertex. The impact of this contribution can be obtained by looking at the difference between the self-energy of DiagMC@DF (light blue line) and DiagMC@PBDT (purple crosses) approaches shown in Fig. 6.5. We find that at $U = 2$ both methods produce identical results, which means that in a weakly-correlated regime the irreducible contributions to the vertex do not affect the

self-energy in a relevant way. The discrepancy between these two methods also increases as the interaction strength U is incresed and is particularly large in the strongly-correlated regime at $U = 8$, which is equal to the bandwidth. After that, at very large interactions $U = 10$ and $U = 12$ the real part of the DiagMC@PBDT self-energy again nearly coincides with the one of the DiagMC@DF approach. The agreement in the imaginary part of the self-energy also improves, but the discrepancy between these two methods remains visible and not negligible.

To quantify the difference between the given self-energy and the exact solution of the dual theory given by DiagMC@DF, we calculate the following normalized deviation

$$\delta = \sum_{\mathbf{k}} \left| \frac{\Sigma^{\text{ref}}_{\mathbf{k},\nu_0} - \Sigma_{\mathbf{k},\nu_0}}{\Sigma^{\text{ref}}_{\mathbf{k},\nu_0}} \right|. \tag{6.21}$$

A similar quantity but for only one k-point was introduced in Ref. [230]. The corresponding result for all considered approaches is presented in Fig. 6.6. We find that the normalized deviation of the DiagMC@PBDT method reaches its maximum value $\delta = 15\%$ at $U = 8$. As has been pointed out in the Section 4.3.1, the irreducible part can be excluded from the renormalized four-point vertex only in the ladder approximation. In the strongly-correlated regime diagrams in a non-ladder form become relevant [220, 221, 230], which is also confirmed by the increase of the normalized deviation of the LDF approach (blue line in Fig. 6.6). Consequently, the contribution of the irreducible part of the vertex to the electronic self-energy also becomes noticeable. We would like to emphasise that the strength of electronic correlations does not depend on the strength of the interaction U only, but also on the proximity of the system to an instability. Indeed, it has been shown that close to a transition the fluctuations become strongly non-linear [323]. The strength of antiferromagnetic fluctuations, that are the sources of instability in this regime, can be estimated by the leading eigenvalue (l.e.) of the Bethe-Salpeter equation of the LDF theory [222, 254] (black line in Fig. 6.6).

The next class of diagrams that we can investigate contains the diagrams with singlet contributions in the partially bosonized four-point vertex (4.34). We investigate the effect of the additional exclusion of all singlet contributions by comparing the DiagMC@PBDT-s and the DiagMC@PBDT results. At small ($U = 2$) and moderate ($U = 4$) interactions, this exclusion immediately leads to a large discrepancy between DiagMC@PBDT-s (green crosses) and DiagMC@PBDT (purple crosses) results for the self-energy presented in Fig. 6.5. In addition, from Fig. 6.6 we find that for these values of the interaction the DiagMC@PBDT-s strongly differs from the reference result, while the DiagMC@PBDT performs reasonably well. Therefore, one can conclude that singlet fluctuations play an important role in weakly- and moderately-correlated regime when all the diagrams are considered. This observation seems to contradict the statement that particle-particle fluctuations are believed to be negligibly small at standard fillings [324]. This point is clarified
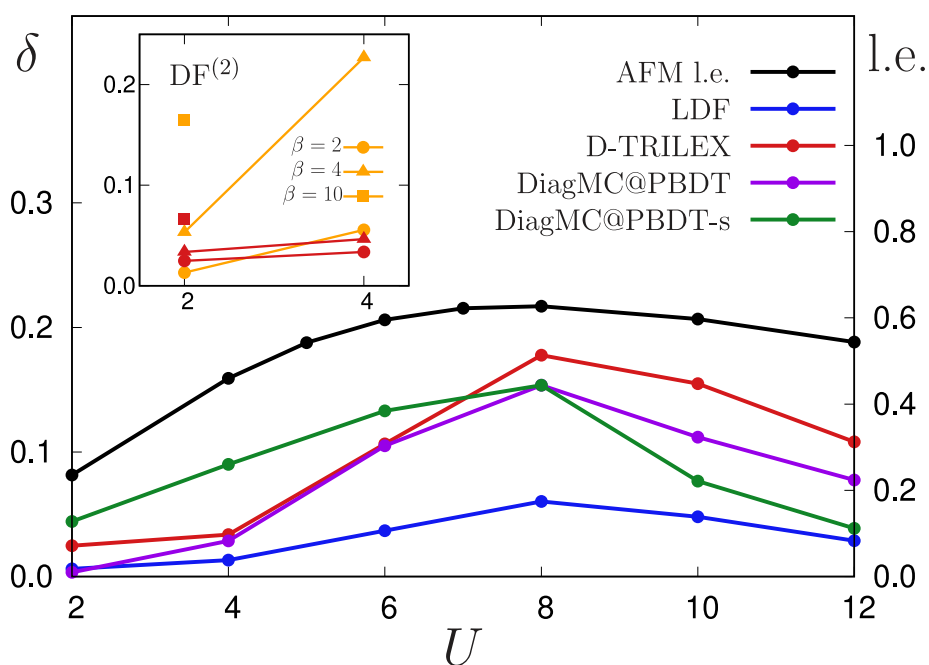
FIGURE 6.6: The normalized deviation δ calculated for LDF (blue), D-TRILEX (red), DiagMC@PBDT (purple), and DiagMC@PBDT-s (green) approximations with respect to the reference Diag@DF result. The black line shows the leading eigenvalue (l.e.) of AFM fluctuations. The vertical left axis shows the scale for the normalized deviation, while the vertical right axis displays values for the leading eigenvalue. The inset compares δ obtained for D-TRILEX and second-order DF ($DF^{(2)}$, orange) approaches for different inverse temperatures $\beta = 2$ (circles), $\beta = 4$ (triangles), and $\beta = 10$ (squares). The figure is taken from Ref. [232].

below when we discuss the result of the D-TRILEX approach. Increasing the interaction to $U = 6$, makes the discrepancy between DiagMC@PBDT and DiagMC@PBDT-s results rapidly decrease, and in the strongly-correlated regime ($U = 8$) both methods produce almost identical results, signalling that the singlet contribution is negligibly small in that regime. Remarkably, for $U = 10$ and $U = 12$ the DiagMC@PBDT-s method shows the best agreement with the DiagMC@DF result among all considered DiagMC-based approximations. This result suggests that in the regime of very large interactions contributions to the self-energy that stem from the irreducible and singlet parts of the renormalized four-point vertex, which are not considered in the DiagMC@PBDT-s theory, nearly cancel each other. This analysis shows that the partially bosonized theory should be handled with care and the exclusion of the singlet contributions should be considered depending on the regime of interest. In general, this shows that inclusing more diagrammatic contributions in the theory does not necessarily mean that the reuslt will improve, especially in fermionic systems, where cancellations between different diagrams play a crucial role in

the convergence properties of the series [300].

Finally, we consider the D-TRILEX method that can be obtained as the first diagrammatic contribution of the partially bosonized action. Alternatively, we can look at it as an approximation to the LDF theory where the irreducible part and transverse particle-hole and particle-particle fluctuations ae neglected from the exact local impurity four-point vertex. As shown in Fig. 6.5, the best agreement between the D-TRILEX (red line) and the reference DiagMC@DF (light blue line) results for the imaginary part of the self-energy occurs at $U = 2$. At small and moderate values of U, the D-TRILEX self-energy seems to be pinned to the LDF result (dark blue line) at Γ and M points. Therefore, the difference between these two methods is mostly visible around local minima located at antinodal AN $= (0, \pi)$ and nodal N $= (\pi/2, \pi/2)$ points. This difference increases with the interaction, and the observed trend persists up to $U = 6$. At larger interactions, when the value of the self-energy at local minima becomes similar, the D-TRILEX result shifts downwards, and at $U = 12$ becomes pinned to the LDF result at N and AN points.

The discrepancy between the D-TRILEX and the reference results for the real part of the self-energy also increases with the interaction up to $U = 8$, and after that decreases again for very large interaction strengths. However, here the best agreement with the exact result is achieved at $U = 4$ (see red line in Fig. 6.5). It can be explained by the fact, that in the perturbative regime of small interactions ($U = 2$) and high temperatures ($\beta = 2$) the second-order dual self-energy $\tilde{\Sigma}^{(2)}$ gives the main contribution to the nonlocal part of the total self-energy [220, 221, 230, 300]. The D-TRILEX theory is not based on a perturbation expansion, because it takes into account only a particular (GW-like) subset of diagrams. For this reason, this simple theory does not fully reproduce the second-order self-energy $\tilde{\Sigma}^{(2)}$ [232]. On the contrary, the D-TRILEX approach correctly accounts for the screening of the interaction that is represented by longitudinal part of the infinite two-particle ladder in all bosonic channels. At lower temperatures and/or larger interactions, when the system enters the correlated regime, these types of diagrams become more important than the second-order self-energy. To illustrate this point, we also obtained the normalized deviation for the D-TRILEX approach for $\beta = 4$ (for $U = 2$ and $U = 4$) and $\beta = 10$ (for $U = 2$), and compared it with δ calculated for the second-order DF (DF$^{(2)}$) approximation that considers only $\tilde{\Sigma}^{(2)}$ contribution to the dual self-energy. The corresponding result is shown in the inset of Fig. 6.6. As expected, the accuracy of the DF$^{(2)}$ approximation rapidly decreases with the temperature and becomes $\delta = 16.5\%$ (for $\beta = 10$ and $U = 2$) and $\delta = 22.5\%$ (for $\beta = 4$ and $U = 4$) in the regime, which is yet above the DMFT Néel point $\beta_N \simeq 12.5$ for $U = 2$ and $\beta_N \simeq 4.3$ for $U = 4$. At the same time, the D-TRILEX theory remains in a reasonable agreement with the reference result.

Fig. 6.6 shows that in the regime of weak and moderate interactions the D-TRILEX self-energy is relatively close to the DiagMC@DF result ($\delta = 2\%$ for $U = 2$ and $\delta = 3\%$ for $U = 4$). This fact looks paradoxical at a first glance, because the D-TRILEX method

does not take into account singlet fluctuations that were found to be important in this regime of interactions. To explain this result, let us first note that at $U \leq 4$ the LDF method is in a very good agreement with the DiagMC@DF theory. Therefore, in the weakly- and moderately-correlated regime ladder diagrams provide the most important contribution to the self-energy. This fact allows for a direct comparison of the self-energies produced by ladder DF and D-TRILEX methods with the result of DiagMC@ methods that account for all diagrammatic contributions. Note however, that all DiagMC-based schemes with approximated interactions tend to overestimate the reference result, while ladder-like approaches underestimate it. Therefore, the normalized deviation presented in Fig. 6.6 should be compared cautiously. Fig. 6.5 shows that D-TRILEX and DiagMC@PBDT self-energies obtained at $U = 2$ and $U = 4$ are very close to the reference result. Both methods do not take into account the irreducible part of the four-point vertex function, but the D-TRILEX approach additionally neglects all transverse particle-hole and particle-particle modes. Keeping in mind that for these interaction strengths the exclusion of only singlet fluctuations leads to a large overestimation of the self-energy, we can conclude that transverse particle-hole and particle-particle fluctuations partially screen each other. This means that the exclusion of both types of vertical insertions in diagrams, as it is done in the D-TRILEX theory, turns out to be a good approximation in the weakly- and moderately-correlated regime. On the other hand, excluding only one channel leaves the other channel unscreened, which results in a large contribution to the self-energy.

Remarkably, the normalized deviation for all considered approximations shown in Fig. 6.6 resembles the behavior of the leading eigenvalue of the magnetic channel (black line). For instance, the D-TRILEX and LDF methods show the largest discrepancy with the DiagMC@DF result exactly in the region where the l.e. is maximal. As has been pointed out in Ref. [323], approaching an instability leads to collective fluctuations becoming strongly anharmonic, which cannot be captured by considering only a single class of diagrammatic contributions. Consequently, in this regime transverse momentum-dependent fluctuations are expected to be important. At $U = 10$ and $U = 12$ the agreement of the D-TRILEX theory with the DiagMC@DF result improves again. Above we have found that at very large interaction strengths contributions to the self-energy that stem from singlet and irreducible parts of the vertex partially cancel each other. This result suggests that the effect of remaining transverse particle-hole fluctuations becomes weaker at very large interactions, which again justifies the applicability of the D-TRILEX theory.

6.3.2 Beyond half-filling: doped model close to a pseudogap

The doped two-dimensional Hubbard model on a square lattice with nearest-neighbor t and next-nearest-neighbor t' hopping amplitudes is widely known as a prototype model for high-temperature superconducting cuprate compounds, even though it is still under debate whether this model is sufficient to explain the physics observed in these materials.
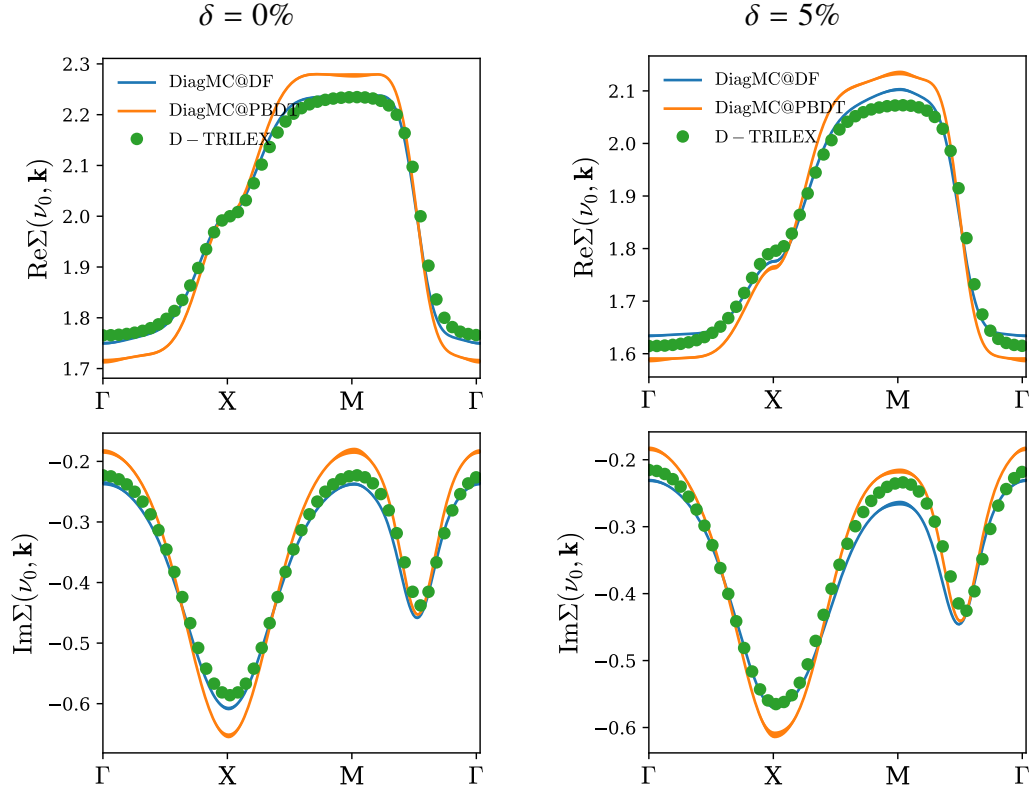
FIGURE 6.7: Lattice self-energy $\Sigma_{\nu_0 \mathbf{k}}$ of the doped Hubbard model along the high-symmetry path in the Brillouin zone. The upper panel shows the real part and the lower panel the imaginary part. D-TRILEX method (green dots) compared with DiagMC@DF and DiagMC@PBDT at half-filling and the small value of hole-doping $\delta = 5\%$. Results show that in this regime the D-TRILEX diagrams capture the main physics occurring in the system and reproduce very well the exact benchmark for the dual theory. The other parameters are $t = 1$, $t' = 0$, $U = 4$ and $\beta = 4$.

In this model, the dispersion acquires an additional term due to the next-nearest neighbor hopping if compared with the nearest neighbor dispersion, and becomes

$$\epsilon_{\mathbf{k}} = -2t \left(\cos k_x + \cos k_y \right) - 4t' \cos k_x \cos k_y. \tag{6.22}$$

We start the discussion of this benchmark by assessing the range of validity of D-TRILEX as a function of doping only and, to that aim, we initially we set $t' = 0$. We study the discrepancy between the D-TRILEX method and the reference DiagMC@DF, that represents the exact solution of the dual action. Additionally, we use the DiagMC@PBDT method to obtain an exact solution of the partially bosonized action, in order to clarify
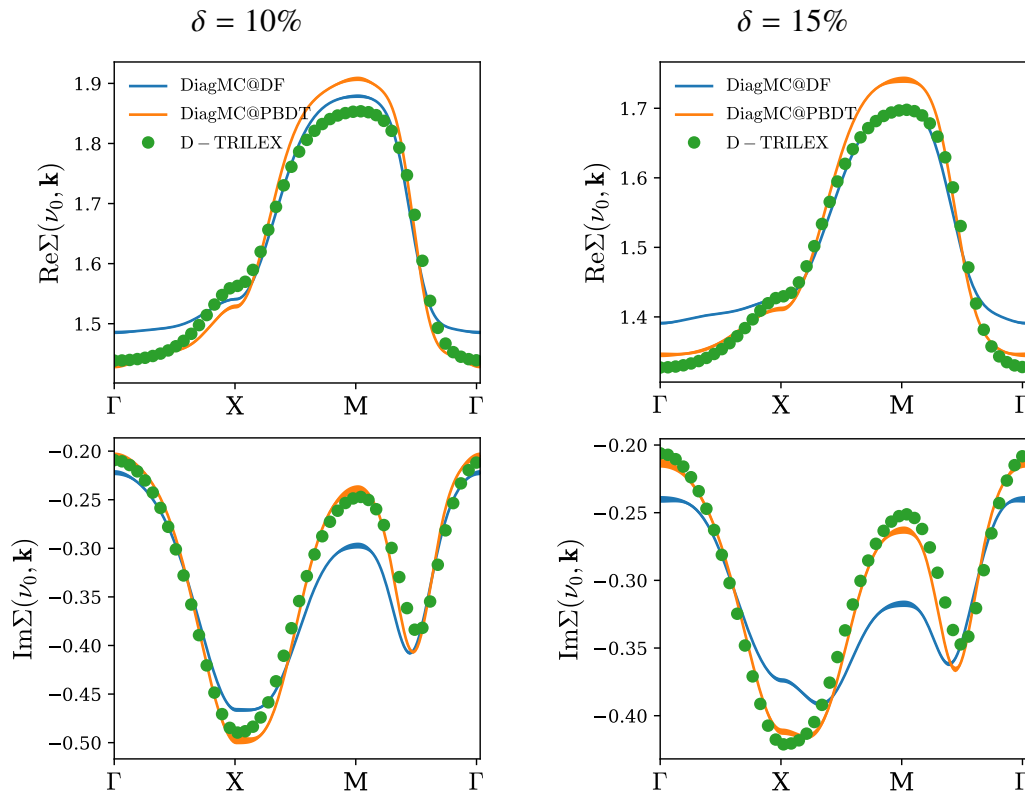
FIGURE 6.8: Lattice self-energy $\Sigma_{\nu_0 \mathbf{k}}$ of the doped Hubbard model along the high-symmetry path in the Brillouin zone. D-TRILEX method (green dots) compared with DiagMC@DF and DiagMC@PBDT at intermediate values of hole-doping $\delta = 10\%$ and $\delta = 15\%$. The other parameters are $t = 1$, $t' = 0$, $U = 4$ and $\beta = 4$.

the source of the mismatch with DiagMC@DF. In Figures 6.7-6.9, we show the lattice self-energy for the parameters $t = 1$, $t' = 0$, $U = 4$ and $\beta = 4$ and different levels of hole-doping δ. A mesh of 64×64 k-points is used. Since the model is particle-hole symmetric for $t' = 0$, these findings are valid also for the electron-doped case. The green dots represent the D-TRILEX results, while the shaded blue and orange areas repesent DiagMC@DF and DiagMC@PBDT respectively. The width of the shaded are represent the stochastic error on the data. The results were obtained summing all the diagrams up to 6th order for both DiagMC schemes.

Results in Fig. 6.7 show that in the regime close to half-filling the D-TRILEX diagrams describes accurately the main physics of the system. In this regime D-TRILEX even outperforms the result obtained by summing up all the diagrams of the partially bosonized action in DiagMC@PBDT. This result can be explained by noting that the partially bosonized action was derived as an approximation to the ladder approximation. As such, we do not

$$\delta = 20\%$$
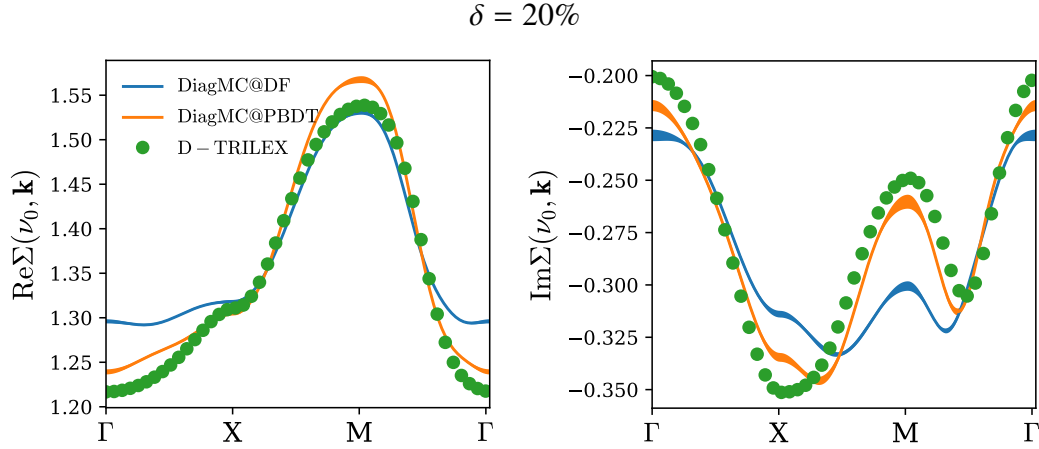
FIGURE 6.9: Lattice self-energy $\Sigma_{\nu_0 \mathbf{k}}$ of the doped Hubbard model along the high-symmetry path in the Brillouin zone. D-TRILEX method (green dots) compared with DiagMC@DF and DiagMC@PBDT at the large value of hole-doping $\delta = 20\%$. The other parameters are $t = 1$, $t' = 0$, $U = 4$ and $\beta = 4$.

expect this approximation to be always accurate when non-ladder diagrams are included. It is certainly true that including only selected subsets of diagrams can lead to wrong results away from regimes where the choice is physically well-motivated in general [300]. Additionally, the inclusion of additional vertex corrections does not always result in an improvement of the results. Sometimes, vertex corrections can be screened by terms that are not taken into account in the considered classes of diagrams leading to the paradoxical situation that considering more diagrams results in a worse accuracy [325].

In the small-doping regime, the minimum of the imaginary self-energy lies at the X point and a secondary minimum appears the nodal point N, lying in the middle between M and Γ. This picture changes for larger values of doping. Indeed, for doping between $\delta = 10\%$ and $\delta = 15\%$, the exact solution of the dual action displays a change in the position of the imaginary self-energy minimum, which is shifted in an intermediate incommensurate position between X- and M-points. The partially bosonized action mimics the behavior even if the effect is smaller, while the D-TRILEX result fails to capture this effect and it has a minimum at the X-point. Apart from the small shift in the minimu around the X-point, D-TRILEX and DiagMC@PBDT appear to be in quantitative good agreement up to $\delta = 15\%$. The behavior of ImΣ at the M-point is strongly different from DiagMC@DF in both the methods based on the partially bosonized action. The same kind of trend appears in the largest doping $\delta = 20\%$ considered here in Fig. 6.9. There, the picture is very similar to the case $\delta = 15\%$, but it becomes more clear that the minimu in the ImΣ in the DiagMC@PBDT method follows the correct trend predicted by DiagMC@DF, while

D-TRILEX still predicts a minimum at the X-point.

These results show that the D-TRILEX method appears to be in good agreement with DiagMC@DF up to some value of doping, around $10 - 15\%$. In this regime, horizontal spin fluctuations are the largest contribution to the self-energy. This is signalled by a large value of the leading AFM eigenvalue of the dual Dyson equation, which goes from $\lambda_d = 0.81$ at half-filling to $\lambda_d = 0.72$ at $\delta = 10\%$. The AFM eigenvalue drops significantly above this value of doping and becomes $\lambda_d = 0.62$ at $\delta = 15\%$ and $\lambda_d = 0.48$ at $\delta = 20\%$, signalling that horizontal spin fluctuations are probably not so large anymore. The discrepancy between the DiagMC@DF and DiagMC@PBDT suggests that non-local transverse fluctuations are responsible for the shift of the minimum away from the X point, but are not sufficient to accurately describe the behavior of the imaginary self-energy at the M-point. Probably, the mismatch at the M point is related to irreducible contributions to the fermion-fermion vertex.

Preliminary results show that the disagreement with the benchmark methods is followed by a complete breakdown on the theory at even larger doping levels ($\delta \sim 30\%$). In that regime, D-TRILEX which predicts an instability in the charge channel which is absent in the ladder approximation, at least at the same values of temperature/doping. For this reason, we argue that this behavior might be related to the absence of irreducible contributions or perhaps local transverse fluctuations that would screen the horizontal charge fluctuations. When left unscreened, the horizontal fluctuations cause the divergence of the method. More extensive studies of the $U-$doping parameters for which this breakdown appears and possible solutions to avoid it are subject of current research.

These results show that our method can be applied in the vicinity of the pseudogap regime where spin fluctuations are large. This regime is the most difficult regime to perform calculations with weak coupling methods like FLEX. The opening of a pseudogap and the dichotomy between the N and AN points in this model has been studied recently in Ref. [326] in the framework of the exact DiagMC method.

There, the authors considered the following set of model parameters $t' = -0.3$, $U = 5.6$, $\beta = 5$, and 4% hole-doping that leads to a largest onset temperature for the pseudogap. In our work of Ref. [232], we addressed this physically interesting regime for a comparable hole doping level of 3.4% within the D-TRILEX and DiagMC@DF approaches. For this calculation, we could not converge a D-TRILEX calculation based on the DMFT impurity problem. As a consequence, we introduced an additional outer loop to update self-consistently the parameters of the impurity problem. To stress this difference with the other calculations, we introduce the label scD-TRILEX for this specific calculation. The obtained self-energies are compared with the exact result of DiagMC method that was provided by the authors of the Ref. [326]. For the sake of consistency, the DiagMC@DF expansion was performed based on the impurity problem determined with the scD-TRILEX
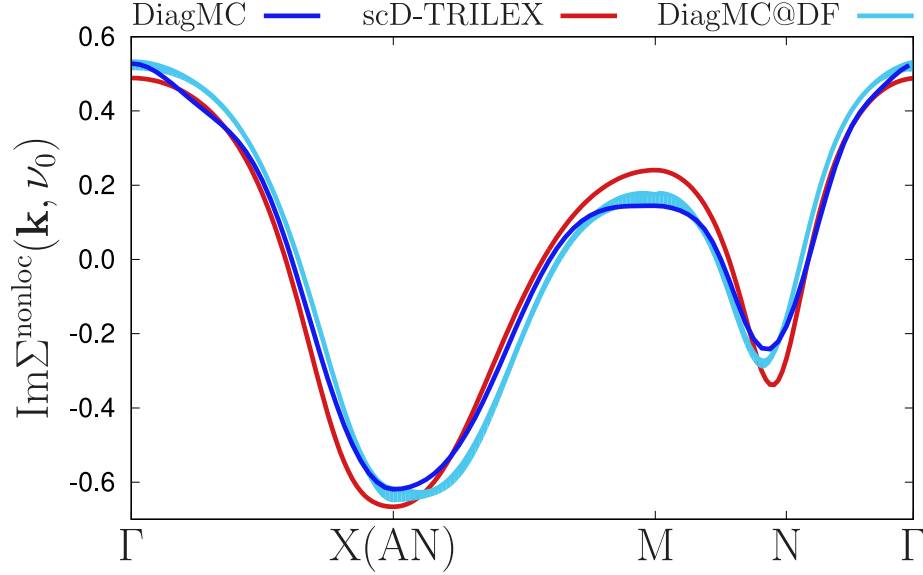
FIGURE 6.10:   Imaginary part of the nonlocal self-energy obtained for the zeroth Matsubara frequency $\nu_0 = \pi/\beta$ along the high symmetry path in momentum space $\mathbf{k}$. Calculations are performed for $U = 5.6$, $t' = -0.3$, and $\beta = 5$ using scD-TRILEX (red line) and DiagMC@DF (light blue line) methods for 3.4% hole-doping. The DiagMC result (dark blue line) for 4% doping is provided by the authors of Ref. [326]. The figure is taken from Ref. [232].

approach.

In Fig. 6.10 we compare the imaginary part of the nonlocal self-energy $\Sigma^{\mathrm{nonloc}}_{\mathbf{k},\nu_0}$ calculated for the first Matsubara frequency along the high-symmetry path in momentum-space for all three approaches. To obtain this quantity we subtract the local part $\Sigma^{\mathrm{loc}}_{\mathbf{k},\nu_0}$ from the lattice self energy $\Sigma^{\mathrm{latt}}_{\mathbf{k},\nu_0}$, where $\Sigma^{\mathrm{loc}}_{\mathbf{k},\nu_0} = \sum_{\mathbf{k}} \Sigma^{\mathrm{latt}}_{\mathbf{k},\nu_0}$. Due to the lack of reference DiagMC data, the sum over the Brillouin zone in this expression is approximated by the sum over the high-symmetry path in momentum space. We find that the nonlocal part of the DiagMC@DF self-energy is in a very good agreement with the reference DiagMC result. The scD-TRILEX approach also performs remarkably good in this physically non-trivial regime, especially given that the considered value of the local Coulomb interaction $U = 5.6$ exceeds the half of the bandwidth. This good agreement in Im $\Sigma^{\mathrm{nonloc}}_{\mathbf{k},\nu_0}$ indicates that the simple ladder-like scD-TRILEX method accurately captures the N/AN dichotomy in the formation of a pseudogap in this regime [326]. This fact additionally confirms our finding that going away from the Slater regime allows to use less sophisticated methods to capture the effect of collective fluctuations.

At the same time we find that the DiagMC@DF and the scD-TRILEX methods do not provide a good value for the local part of the lattice self-energy. Indeed, Im $\Sigma^{\mathrm{loc}}_{\mathbf{k},\nu_0}$ of the DiagMC@DF calculated for the zeroth Matsubara frequency is equal to -0.77. The

corresponding value for the scD-TRILEX approach is -0.80, while the exact DiagMC result reads -1.04. This discrepancy can again be explained by the fact that DMFT impurity problem does not provide a good starting point for a diagrammatic expansion already for moderate interactions. To address this issue, we exploited the dual self-consistency condition to update the fermionic hybridization as an attempt for the improvement of the reference system. However, the result obtained in this Section clearly demonstrates the need for an even better starting point, which should be able to provide more accurate local quantities to reproduce the exact result.

6.4 Detecting instabilities with D-TRILEX

So far, we have discussed the impact of the partially bosonized approximation and D-TRILEX method on the single-particle observables. However, the method also allows to investigate two-particle observables. As we have discussed previously, two-particle observables are related to ordering of the system. In particular, a diverging susceptibility in one channel signals a symmetry-breaking phase transition in that channel. The aim of this Section is to show that D-TRILEX is able to capture the tendency towards an instability and even predict the corresponding transition point, in the presence of a physical phase transition. To this aim, the plain two-dimensional Hubbard model is not a suitable candidate, since symmetry-breaking phase transitions are in principle forbidden. On the other hand, the Hubbard model on the cubic lattice and the extended Hubbard model are very interesting systems in this regard, as they show an AFM phase transition and a CDW phase transition respectively.

6.4.1 Antiferromagnetic transition in the Hubbard model on a cubic lattice

The second benchmark we investigated is the Hubbard model on a cubic lattice. The dispersion is taken to be the tight-binding dispersion with only nearest-neighbors, which explicitly reads

$$\epsilon_{\mathbf{k}} = -2t \left(\cos k_x + \cos k_y + \cos k_z \right) \tag{6.23}$$

We set the value of the nearest-neighbor hopping to $t = 1$, so that the half-bandwidth is $D = 6t = 6$. This system is expected to undergo a second-order phase transition to an AFM state, as in a 3D case the Mermin-Wagner theorem does not hold. This phase transition clearly appears in mean-field methods such as Hartree-Fock calculations [327]. In addition to that, DMFT is able to describe the transition [328], but clearly overestimates the Néel temperature at any $U \geq 5$. Indeed, the presence of this transition is confirmed by more
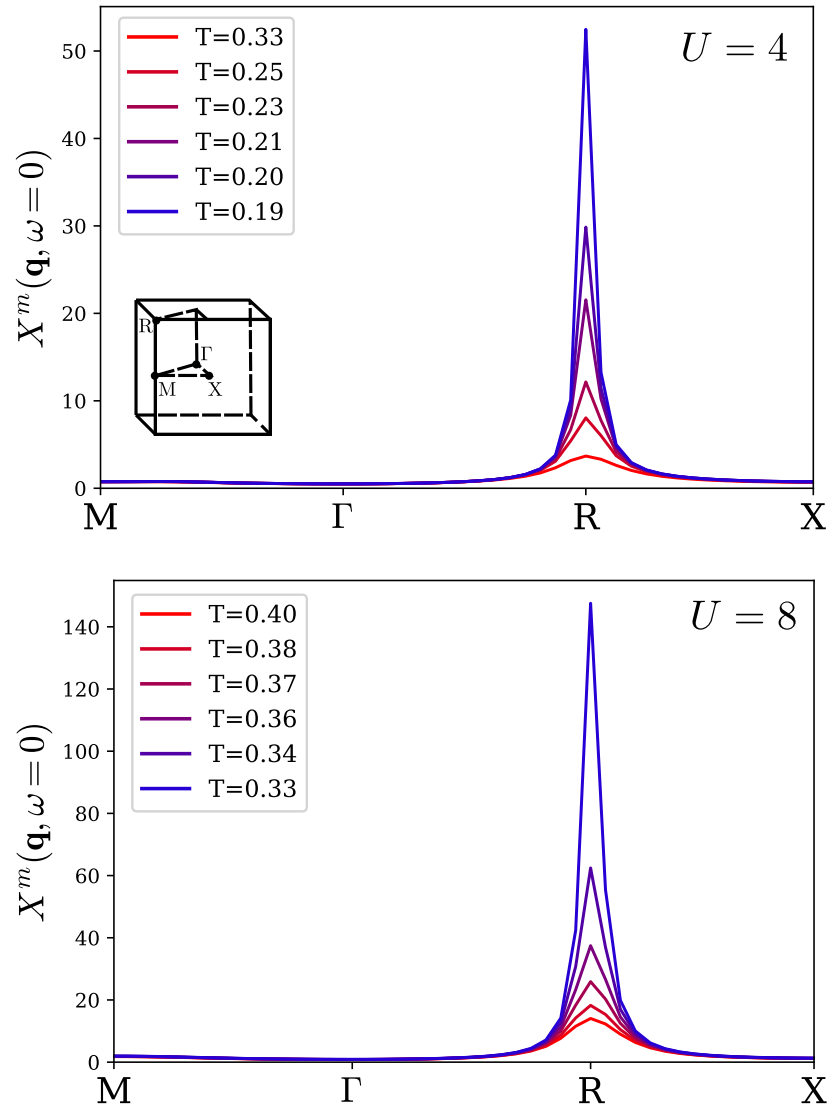
FIGURE 6.11: The plot shows the static magnetic susceptibility $X^m(\mathbf{q}, \omega = 0)$ along the high-symmetry path in the BZ of the cubic lattice (sketched in the upper panel). The upper panel is computed at the value of the Hubbard interaction $U = 4$, the lower panel at $U = 8$. Different colors correspond to different temperatures. The peak at $\mathbf{q} = R$ is clearly visible.

accurate and exact methods as shown in Fig. 6.13. However, this is not enough to state *a priori* that D-TRILEX is able to even capture this transition.

To confirm that D-TRILEX accurately describes the AFM phase transition on a cubic
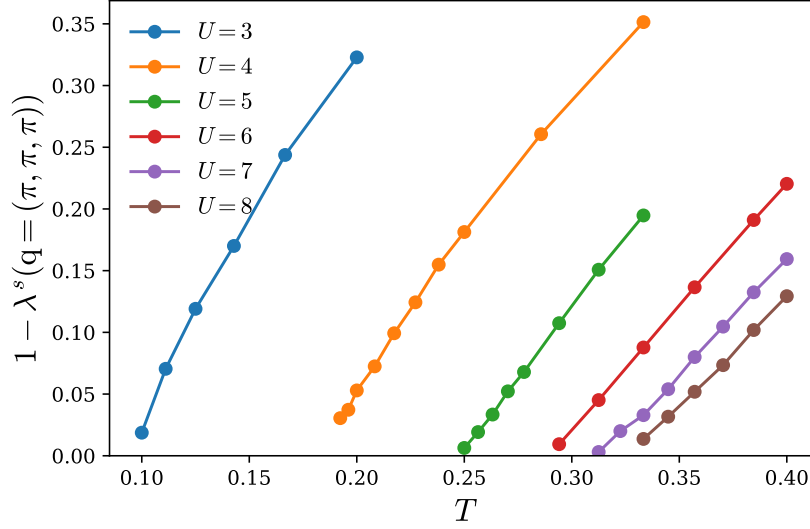
FIGURE 6.12: The plot shows the quantity $1 - \lambda^s$, where λ^s is the leading eigenvalue of the dual Dyson equation, computed for the cubic lattice Hubbard model at half-filling for different values of the Hubbard interaction U plotted as a function of temperature T. The curves show a clear trend towards 0, signalling a divergence of the effective interaction $\tilde{W}$ at the point $R = (\pi, \pi, \pi)$, that corresponds to the AFM ordering.

lattice, we performed calculations for few values of the Hubbard interaction U to investigate how accurate the D-TRILEX method is in describing the phase boundary of this transition. In our calculations, we use a $32 \times 32 \times 32$ mesh in the Brillouin Zone, 48 fermionic frequencies and 32 bosonic frequencies. In Figure 6.12, we show that indeed D-TRILEX captures the AFM transition. In a cubic lattice, the AFM transition corresponds to an ordering vector corresponding with the so-called R point, so $\mathbf{q}_{AFM} = R = (\pi, \pi, \pi)$. The magnetic ordering of the system can be revealed by looking at the static magnetic susceptibility $X^m_{\mathbf{q}, \omega=0}$. Indeed, we show in Fig. 6.11 that plotting this susceptibility in the BZ reveals the expected behavior. The D-TRILEX method gives an alternative and simple way of analysing the transition. Since the $\tilde{W}^{\varsigma}_q$ is obtained by inverting the Dyson's equation of Eq. (4.62), we can look at the divergent behavior of this equation to identify phase transitions. The divergence occurs when the eigenvalue $1 - \lambda^{\varsigma}$ of the denominator vanishes in some channel $\varsigma = d, m$.

In this simple single-band case, the bosonic Dyson equation is not a matrix-valued equation so the eigenvalue simply corresponds to plotting the maximum over the Brillouin zone of the quantity

$$\lambda^m(\mathbf{q}) = \tilde{W}_{\omega=0, \mathbf{q}} \tilde{\Pi}_{\omega=0, \mathbf{q}}. \tag{6.24}$$
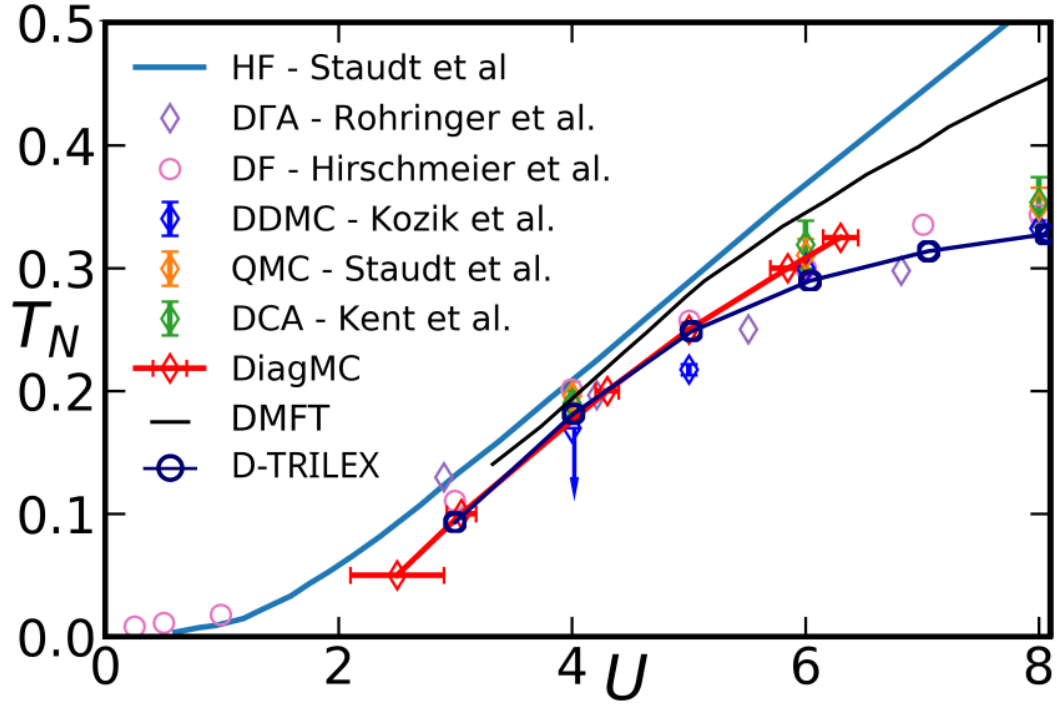
FIGURE 6.13: AFM bounary for the Hubbard model on a cubic lattice in the $U - T$ plane. The D-TRILEX values obtained for the critical temperature for the Néel transition T_N as a result of our calulations have been added on top of the figure taken from Ref. [302] and are indicated by blue-navy circles connected with full lines. We have additionally superimposed DMFT data (black line) taken from Ref. [256]. The source of the other data are cited in the main text and summarized in the legend. Results from the D-TRILEX method compare very well with exact methods such as DiagMC and QMC.

When the maximum of this quantity reaches unity, the bosonic Dyson equation becomes unstable and the method breaks. Indeed, in Ref. [232], we showed that the $\tilde{W}_q$ diverges at the same point as the physical susceptibility X_q, hence the eigenvalue is an alternative way of assessing a divergence of the susceptibility. The parameters for which this happens are typically the critical values associated with a phase transition. Indeed, by inspecting the plot, it is clear that the quantity $1 - \lambda^m(\mathbf{q})$ goes to 0 as the temperature is decreased. For this model, the transition occues at any finite value of U, so there is no critical value U_c. On the other hand, at each value of U, the transition occurs at a critical Néel temperature T_N, so it makes sense to investigate the behavior $T_N = T_N(U)$.

The values are obtaied from a linear fitting of the eigenvalue λ^m in the range of temperatures close to where it crosses $\lambda^m = 1$. The results of the T_N obtained from the D-TRILEX data as a function of U are sumarized in the table below.

U	T_N
3.0	0.093 ±0.016
4.0	0.181 ±0.006
5.0	0.248 ±0.005
6.0	0.289 ±0.009
7.0	0.313 ±0.014
8.0	0.327 ±0.014

Errorbars contain the contribution from the fitting procedure, assuming that the Monte Carlo errors in the calculation of the impurity quantities is normally distributed and equal among all the calculations.

Our aim is to compare these results with approximate calculations based on dynamical cluster approximation (DCA) [329] and DΓA calculations [330] as well as by numerically exact results obtained with QMC [327] , DDMC [331] and DiagMC [302]. Additionally, it is known that the LDF (ladder dual fermion) method is able to accurately capture this transition, as shown by the results presented in Ref. [256]. In Fig. 6.13, we adapt a figure originally presented in Ref. [302], that collects the Néel temperatures obtained with the methods presented in all these references. On top of the previous results, we add the transition temperature obtained from our D-TRILEX calculations. The figure show that the T_N predicted by D-TRILEX is in very good agreement with the exact methods (QMC, DDMC and DiagMC) within the stochastic error bars of these methods as well as with the LDF method. This fact is not surprising, as the AFM transition is well-described by horizontal spin fluctuations which are accounted for in D-TRILEX. D-TRILEX consistently improves the DMFT results even in the most correlated regime. For instance, in Ref. [328] it is shown that T_N predicted by DMFT at $U = 8$ is around $T_N \approx 0.45$ [256], while D-TRILEX predicts a value much closer to the more advanced methods. These findings confirm the previously made statement that it is not necessary to have an exact theory in the $d = \infty$ at the two-particle level to accurately describe a phase transition at finite dimensions.

6.4.2 Benchmark in the single-orbital extended Hubbard model

Previous works on D-TRILEX [231–233] suggest that the method is able to account for the effect of the non-local interactions. However, no thorough benchmarking of the results for the extended Hubbard model has been performed so far. For this reason, in this work we investigate the performance of D-TRILEX in the case of a single-orbital extended Hubbard model on a square lattice with the local U and the nearest-neighbor V^d interactions between electronic densities (3.14). To simplify notations, in the following the superscript "d" for the non-local interaction is again omitted. The single-particle dispersion for this

model for the case of a nearest-neighbor hopping amplitude reads

$$\epsilon_{\mathbf{k}} = -2t \left(\cos k_x + \cos k_y \right) \tag{6.25}$$

Similarly, the momentum-space representation for the non-local interaction is

$$V_{\mathbf{q}} = 2V \left(\cos q_x + \cos q_y \right) \tag{6.26}$$

We set the value of the nearest-neighbor hopping to $t = 1$, so that the half-bandwidth is $D = 4t = 4$. To benchmark our results, we compare the lattice self-energy Σ calculated using D-TRILEX approach with the result of the dual boson diagrammatic Monte Carlo (DiagMC@DB) method presented in Ref. [230]. DiagMC@DB allows for the exact solution of an effective dual boson action (4.10), where the renormalized interaction is truncated at the two-particle level (4.15). Note that the dual boson action is derived within the exact analytical transformation of the initial lattice problem (3.14) (see Section 4.2.1). In addition, diagrammatic Monte Carlo methods applied to dual theories show a very good agreement with the exact results [221, 232] and the results of the cluster methods [307, 312].

We perform calculations at half-filling for different strengths of the Hubbard interaction $U = 2$, $U = 4$, and $U = 6$. For each value of U we consider three different values of the nearest-neighbor Coulomb interaction $V = 0$, $V = U/8$, and $V = U/4$. As in Ref. [230], for $U = 2$ and $U = 4$ the temperature is set to $T = 0.25$, for $U = 6$ to $T = 0.50$. The obtained results for the lattice self-energy are shown in Fig. 6.14. We find that for the smallest value of the Hubbard interaction $U = 2$ the agreement between the two methods is almost perfect. A slight difference appears only in the imaginary part of the self-energy in the vicinity of the $X = (\pi, 0)$ point for $V = 0.25$ and near the $\Gamma = (0, 0)$ point for $V = 0.5$. When the interaction reaches the value of the half-bandwidth $U = 4$, the real part of the D-TRILEX self-energy remains very close to the DiagMC@DB result for all values of V considered here. On the other hand, we observe a constant shift in the imaginary part of the self-energy that increases with the strength of the non-local interaction V. A constant but smaller shift was also observed between DF and DiagMC@DF results [221, 232], hence it does not seem to be a feature of only the D-TRILEX method. Finally, at $U = 6.0$ we observe that D-TRILEX does not agree with DiagMC@DB as accurately as for smaller values of the interaction. In the real part, the difference between the two methods is not very large and appears to be independent on the value of V. On the contrary, the imaginary part of the self-energy displays a rather large mismatch already at $V = 0$, and the agreement seems to become worse as V increases. This result comes as no surprise and agrees with the findings of Refs. [221, 230, 232] that the ladder-like dual approximations become less accurate in the regime of strong magnetic fluctuations. The reason is that magnetic fluctuations become strongly non-linear close to a magnetic instability (see, e.g., Ref. [323]).
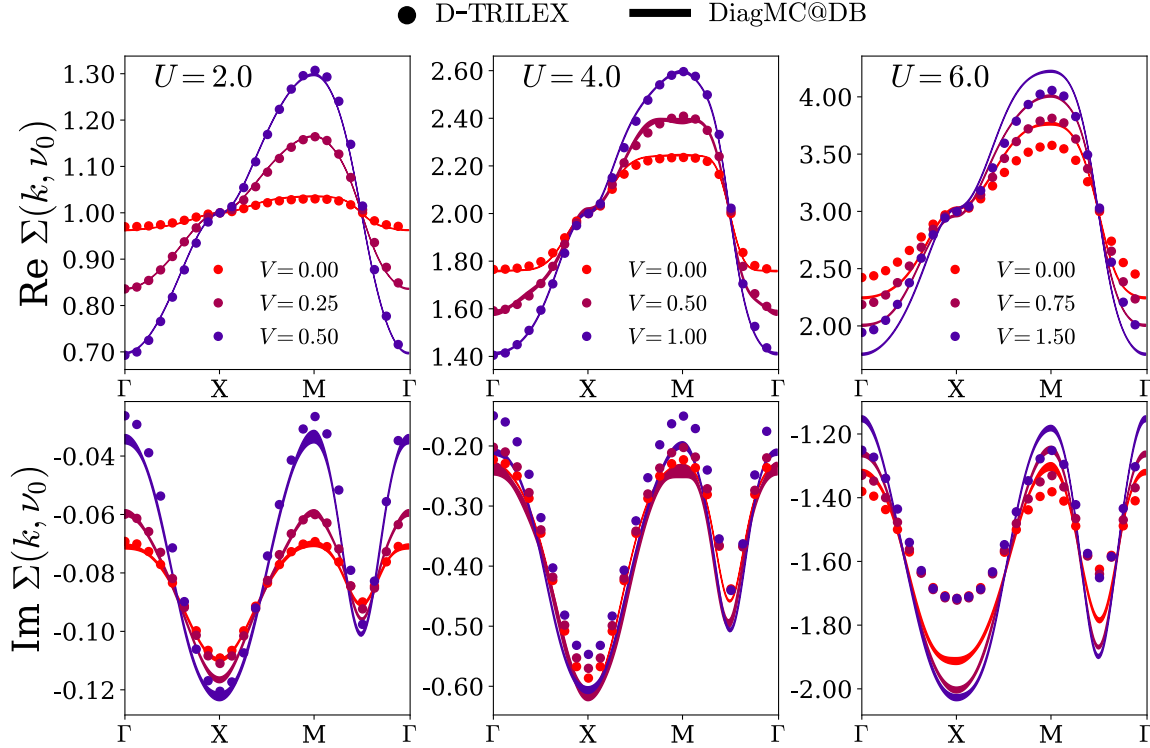
FIGURE 6.14: Real (top row) and imaginary (bottom row) parts of the lattice self-energy for the half-filled single-band extended Hubbard model on a square lattice. The result is obtained for $U = 2.0$ (left column), $U = 4.0$ (middle column), and $U = 6.0$ (right column) for three different values of the nearest-neighbor interaction $V = 0.0$ (light red), $V = U/8$ (dark red), and $V = U/4$ (purple). The D-TRILEX result is depicted by dots. The DiagMC@DB data is taken from Ref. [230] and is represented by solid lines with the width that corresponds to the estimated stochastic error. Reproduced from Ref. [96].

This non-linear behavior originates from the mutual interplay between different bosonic modes as well as from an anharmonic fluctuation of the single mode itself. The description of these effects requires to consider much more complex diagrammatic structures that account for vertical (transverse) insertions of momentum- and frequency-dependent bosonic fluctuations, which are present in the DiagMC@DB approach but are not considered in ladder-like dual approximations including the D-TRILEX approach. However, despite the quantitative disagreement, at $U = 6.0$ D-TRILEX qualitatively captures the correct momentum dependence of the self-energy, which is completely missing in DMFT.

In addition to single-particle quantities, D-TRILEX also provides two-particle quantities, namely the susceptibility and the polarization operator of the lattice problem. These quantities are calculated as momentum- and frequency-dependent functions, which allows one to get the information about the full energy spectrum of the charge and spin
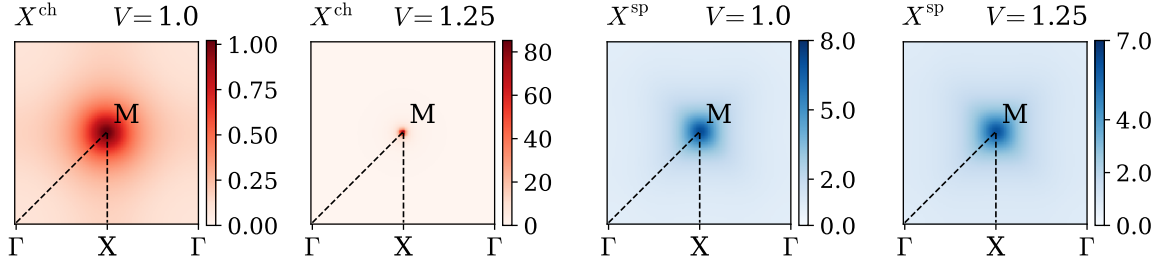
FIGURE 6.15: Static charge (red panels) and spin (blue panels) susceptibilities $X^{\mathrm{ch/sp}}(\mathbf{q}, \omega = 0)$ in the Brillouin zone. Calculations are performed for the half-filled single-band extended Hubbard model on a square lattice for $U = 4$ and $\beta = 4$. The value of the non-local interaction V is indicated above each panel. Reproduced from Ref. [96].

excitations in the system. In Fig. 6.15, we show the static ($\omega = 0$) charge and spin susceptibilities $X^{\mathrm{ch/sp}} = -X^{d/m}$ in the Brillouin zone (BZ) computed for the same model at $U = 4$, $T = 0.25$, and different values of the non-local interaction $V = 1.0$ and $V = 1.25$. Both, charge and spin susceptibilities display a maximum value at the $M = (\pi, \pi)$ point of the BZ, which signals that corresponding order parameters tend to have a checkerboard configuration on a square lattice. From the physical point of view, this means that in this parameter range the system has a tendency towards the charge density wave (CDW) for large values of V and the antiferromagnetic (AFM) ordering at small values of V. The enormous increase in the value of the charge susceptibility indicates that the system is very close to the CDW transition point, that corresponds to a divergence of the charge susceptibility. On the contrary, the spin susceptibility does not change significantly, and its value is slightly reduced upon increasing V. This reduction is expectable, since in this particular case the spin fluctuations are screened by strong charge fluctuations.

If we analyse more quantitatively the behavior of the charge susceptibility at the M point, we find that the inverse X^{ch} at that k-point exhibits a typical linear behavior for large values of V and crosses the zero axis close to $V = 1.25$, which means a divergence of the value of susceptibility X^{ch}, as shown in Fig. 6.16. A linear fitting close to the crossing point gives an estimation of the critical interaction $V_{\mathrm{CDW}} = 1.25(2)$. The static spin susceptibility X^{sp}, on the other hand, has a rather large value at small values of V. This value is weakly, but noticeably reduced by the large charge fluctuations thanks to the self-consistency condition. This screening appears to be linear up to a value of $V = 1.2$. Close to the divergence in correspondence to the CDW phase, this screening becomes clearly non-linear.

It is commonly believed that in strongly-correlated systems the non-local interactions have to be treated in the framework of the extended DMFT by introducing a bosonic hybridization function in the impurity problem [162–165, 267]. However, the diagrammatic
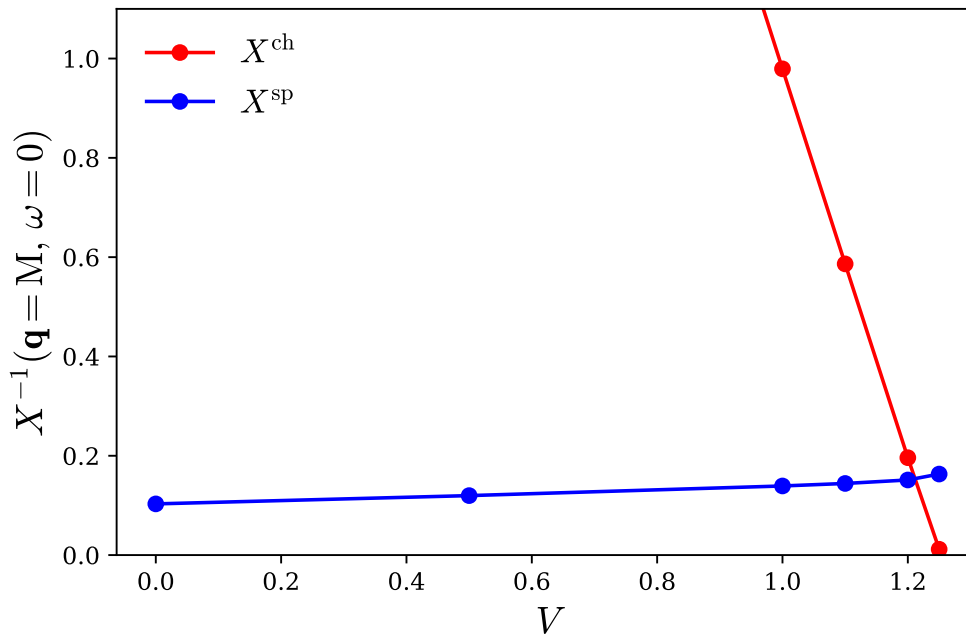
FIGURE 6.16: Values of the static charge (red dots) and spin (blue dots) susceptibilities $X^{\mathrm{ch/sp}}(\mathbf{q} = \mathrm{M} = (\pi, \pi), \omega = 0)$ as a function of the non-local iteraction V. The inverse of the susceptibility is shown to emphasise the linear behavior near the transition point to the CDW phase. A linear fitting of $X^{-1,\mathrm{ch}}$ close to the point where it crosses the value $X^{-1} = 0$ gives a value $V_{\mathrm{CDW}} = 1.25(2)$ for the CDW transition point. Calculations are performed for the half-filled single-band extended Hubbard model on a square lattice for $U = 4$ and $\beta = 4$. The value of the non-local interaction V is indicated above each panel.

expansion in dual theories can be performed for of an arbitrary reference system. In particular, the results of this section demonstrate that the D-TRILEX approach can accurately treat the non-local interactions on the basis of the DMFT impurity problem. The latter does not contain the bosonic hybridization function and thus is easier to solve numerically. In addition, in D-TRILEX the non-local collective electronic fluctuations are not restricted in the range, which is a big advantage over cluster extensions of DMFT. Moreover, the D-TRILEX method is able to capture the interplay between the collective electronic fluctuations in different channels through the self-consistent procedure that involves single-particle quantities. As a matter of fact, the bosonic propagators from all channels contribute to the self-energy. Therefore, a large value of the bosonic propagator in one channel considerably increases the value of the self-energy, hence it reduces the value of the Green's function. In turn, the reduced value of the Green's function leads to a smaller value of the dual polarization for app channels, which is the main ingredient for computing

the physical susceptibility and the polarization operator. This feature is not provided by DMFT calculations of the susceptibility with dynamical vertex corrections [45, 47, 332] that are performed non-self-consistently.

6.5 Benchmarks for the two-orbital Hubbard model

After assessing the performances of the D-TRILEX method in the single-orbital case and finding the regimes of problematic behavior, namely the regime of intermediate coupling strength $6 \leq U \leq 8$ and the large-doping regime, we are ready to address the first multi-orbital systems.

6.5.1 The exactly-solvable Hubbard-Kanamori dimer

The first case-study we discuss is a two-site model, also known as dimer. Due to a small size of this system, the exact solution for the dimer problem for small number of orbitals can be achieved by ED. This makes the dimer an ideal platform to benchmark various approximate methods. To test our multi-orbital D-TRILEX implementation, we consider a particular case of a Hubbard-Kanamori dimer, where each of the two identical sites has two degenerate orbitals. The single-particle part of the corresponding Hamiltonian reads:

$$H_0 = -t \sum_{l,\sigma} \sum_{j \neq j'} c^\dagger_{j\sigma l} c_{j'\sigma l} \tag{6.27}$$

The single-particle Hamiltonian (6.27) can be diagonalized in the site-space. After that, the dimer problem can be effectively considered as a periodic system with the dispersion

$$\varepsilon_{\mathbf{k},ll'} = -2t \cos(\mathbf{k}) \, \delta_{ll'} \tag{6.28}$$

defined for $N_k = 2$ points in momentum space that correspond to $\mathbf{k} = 0$ (symmetric solution) and $\mathbf{k} = \pi$ (anti-symmetric solution). Based on this consideration, we can apply our multi-band D-TRILEX method, that is designed for solving periodic lattice models, to this benchmark system. The interacting part is considered in the Kanamori form (3.19) discussed above.

We chose the single-site two-orbital impurity problem of DMFT as the reference system for the D-TRILEX calculation. Since interorbital hoping processes are not taken into account, different orbitals do not hybridize. For the case of degenerate orbitals considered here it implies that the Green's function is diagonal in the orbital space and has identical components for both orbitals ($G_{ll'} = G\delta_{ll'}$). To compare the D-TRILEX result with the exact solution for the dimer problem we perform ED calculations using the pomerol
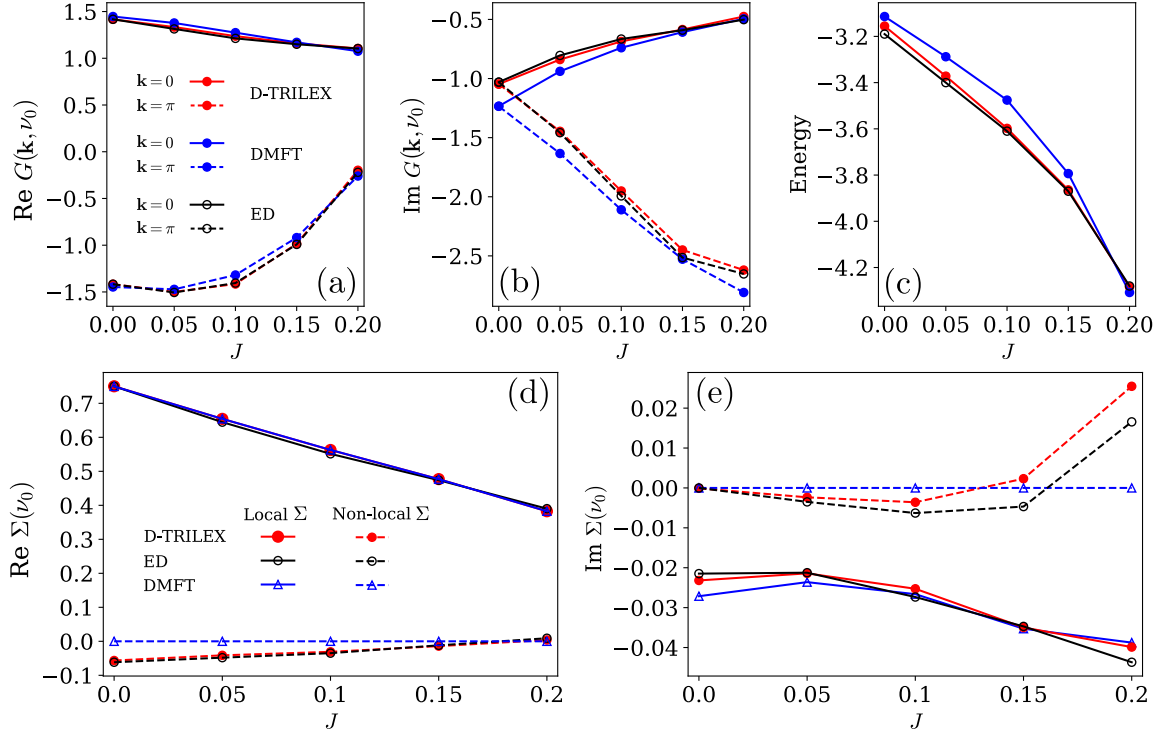
FIGURE 6.17: Panels (a) and (b) respectively show the real and the imaginary parts of the Green's function for the Hubbard-Kanamori dimer calculated for the frequency $\nu_0 = \pi/\beta$ at momenta $\mathbf{k} = 0$ (solid line) and $\mathbf{k} = \pi$ (dashed line). The panel (c) shows the average energy of the system. Panels (d) and (e) respectively show the real and the imaginary parts of the self-energy Σ for the frequency $\nu_0 = \pi/\beta$. The local component is denoted by a think line, while the non-local component is represented by a dashed line. Non-local components are identically zero for DMFT, but are displayed for consistency. Results obtained using D-TRILEX (red), DMFT (blue), and ED (black) methods for different values of the Hund's coupling J. Model parameters for these calculations are $t = 0.2$, $U = 0.5$, $\beta = 10$, and $\mu = 0.75$, and are equal across all panels.

package [76]. The total number of degrees of freedom for the two-orbital Hubbard-Kanamori dimer for the ED calculation is $2N_l N_{\mathrm{imp}} = 8$ and the total number of states is $N_{\mathrm{tot}} = 2^8 = 256$. This makes the ED calculation numerically inexpensive.

First, we focus on the effect of the Hund's exchange coupling J. To this aim we perform calculations for different values of J fixing other model parameters to $t = 0.2$, $U = 0.5$, $\beta = 10$, and $\mu = 0.75$. A very similar set of model parameters for a single-orbital dimer problem was recently used in Ref. [237] to benchmark another diagrammatic extension of DMFT. In Fig.6.17, we show the real (Re G, left panel) and imaginary (Im G, middle panel) parts of the Green's function produced by D-TRILEX (red), DMFT (blue), and ED

(black) methods. We find that the D-TRILEX result for the Re G lies on top of the exact solution in the whole range of values for the Hund's coupling considered here. DMFT is also rather accurate in calculating the real part of the Green's function, but the discrepancy between the DMFT and ED results is noticeable. The D-TRILEX solution for Im G is very close to the one provided by ED, while the DMFT result becomes substantially different from the exact solution, especially for small values of J. A very good agreement between D-TRILEX and ED methods is also confirmed by analyzing the result for the average energy $\langle E \rangle$ (right panel in Fig. 6.17). The average energy for ED is obtained as $\langle E \rangle_{\text{ED}} = \sum_i (E_i - \mu) e^{-\beta(E_i - \mu)}$ where the index i runs over the eigenstates of the system. The average energy in D-TRILEX is calculated using Eq. (6.18). The DMFT energy $\langle E \rangle_{\text{DMFT}}$ has been computed using the same formula (6.18) by setting $\tilde{\Sigma} = 0$ and $\tilde{\Pi} = 0$. We show that the mismatch in D-TRILEX and ED results for the energy is 1.1% ($\delta E = 0.034$) at $J = 0$ and decreases as J increases. The largest difference between DMFT and ED results is found at $J = 0.1$ and amounts to 3.7% ($\delta E = 0.134$), which is approximately four times larger than the one of the D-TRILEX approach. Nevertheless, we observe that in this case DMFT is surprisingly close to the exact result. The reason is that for the considered set of model parameters the system lies very far away from half-filling, hence the non-local fluctuations between the two sites of the dimer are suppressed. This fact can be confirmed by looking at the self-energy Σ shown in panels (d) and (e) of Fig. 6.17. The local contribution to the self-energy $2\Sigma^{\text{local}} = \Sigma(\mathbf{k} = 0) + \Sigma(\mathbf{k} = \pi)$ is dominant and is in a very good agreement among all three methods. The non-local part $2\Sigma^{\text{non-local}} = \Sigma(\mathbf{k} = 0) - \Sigma(\mathbf{k} = \pi)$, which is completely missing in DMFT, is relatively small and is also well reproduced by D-TRILEX approach.

At half-filling, DMFT ceases to be a good approximation. To illustrate that D-TRILEX is able to improve and even to cure a wrong behavior of the DMFT result, we perform calculations for $t = 0.5$ and $\beta = 10$ for different values of the Hubbard interaction U for a fixed ratio $U/J = 4$. The chemical potential is set to $\mu = (3U - 5J)/2$ in order to ensure half-filling [333]. Panel (a) of Fig. 6.18 shows the imaginary part of the local Green's function as a function of the Matsubara frequency. The result is obtained in a weak ($U = 0.5$, dots) and strong coupling ($U = 2.0$, triangles) regimes of the interaction. At $U = 0.5$, the D-TRILEX result coincides with the exact solution in the whole frequency range. The DMFT result is also very accurate and only slightly deviates from the ED solution at lowest frequencies. This situation changes completely at $U = 2.0$, where the exact Im G provided by ED is strongly reduced at low frequencies. Remarkably, DMFT does not capture this change and predicts approximately the same result for the Im G for both values of the interaction. Instead, the D-TRILEX solution lies very close to exact result and reproduces the correct behavior of the Im G. To confirm this fact, we compute the normalized difference from the ED result for D-TRILEX and DMFT as

$$\delta \left[\text{Im} \, G(\nu_n) \right] = \text{Im} \left[G(\nu_n) - G_{\text{ED}}(\nu_n) \right] / \text{Im} \, G_{\text{ED}}(\nu_n) \qquad (6.29)$$
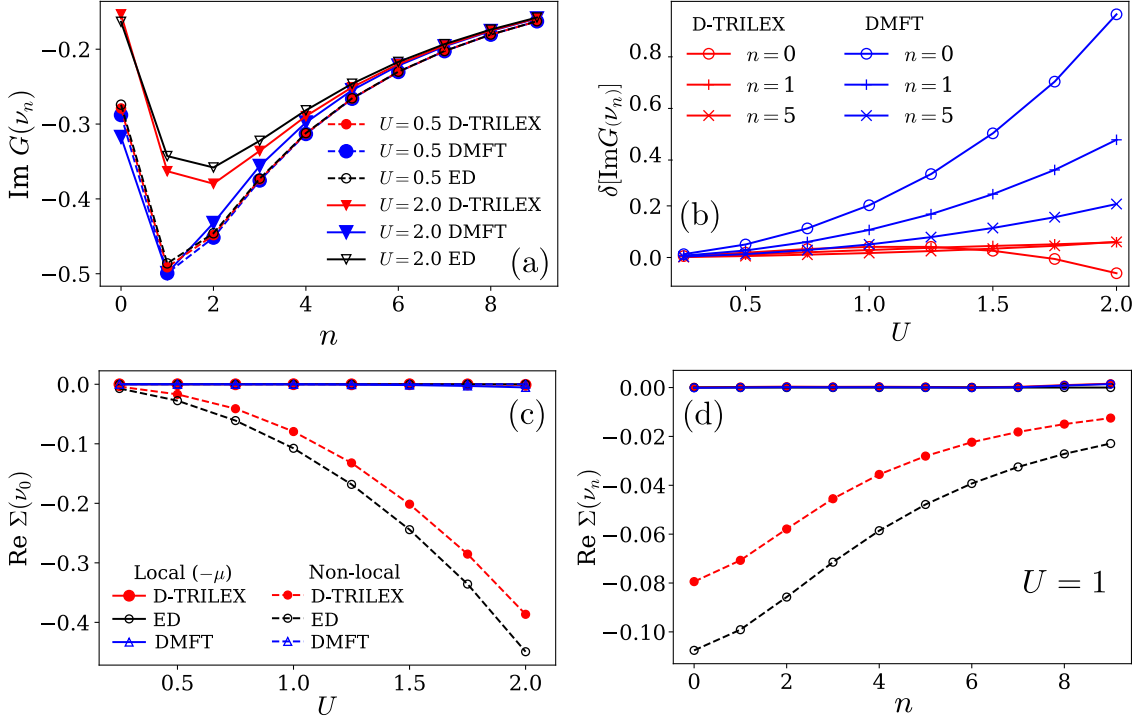
FIGURE 6.18: (a) Imaginary part of the local Green's function $\text{Im}\,G(\nu_n)$ calculated as a function of the Mastubara frequency index n for two values of the interaction $U = 0.5$ (dashed lines) and $U = 2.0$ (solid lines). The result is obtained at half-filling for $t = 0.5, \beta = 10$, and $J = U/4$ using the D-TRILEX (red), the DMFT (blue), and the ED (black) methods. (b) Normalized difference $\delta\,[\text{Im}\,G(\nu_n)]$ (6.21) with respect to the ED solution calculated for D-TRILEX (red), the DMFT (blue) methods as a function of U. The result is obtained for three difference Matsubara frequencies with indices $n = 0$ (empty circles), $n = 1$ (pluses), and $n = 5$ (crosses). (c) Real part of the self-energy Σ as a function of the interaction U at the first Matsubara frequency ν_0. (d) Real part of the self-energy $\Sigma(\nu_n)$ as a function of the Matsubara index obtained at $U = 1$. In panels (c) and (d), the local and non-local parts are shown and the chemical potential μ is subtracted from the local part.

The corresponding result obtained for three different frequencies as a function of U is shown is the panel (b) of Fig. 6.18. We find that the normalized difference for DMFT is relatively large and drastically increases upon increasing the interaction strength. At $U = 2.0$, the $\text{Im}\,G(\nu)$ calculated at the zeroth and the first Matsubara frequency using DMFT is respectively almost two and 1.5 times larger than the exact result. On the contrary, the $\text{Im}\,G(\nu)$ of D-TRILEX lies very close to the ED result. Indeed, the normalized difference for D-TRILEX calculated for the first and the fifth frequency does not exceed 2%. The difference for D-TRILEX calculated for the zeroth frequency becomes larger than 2% at
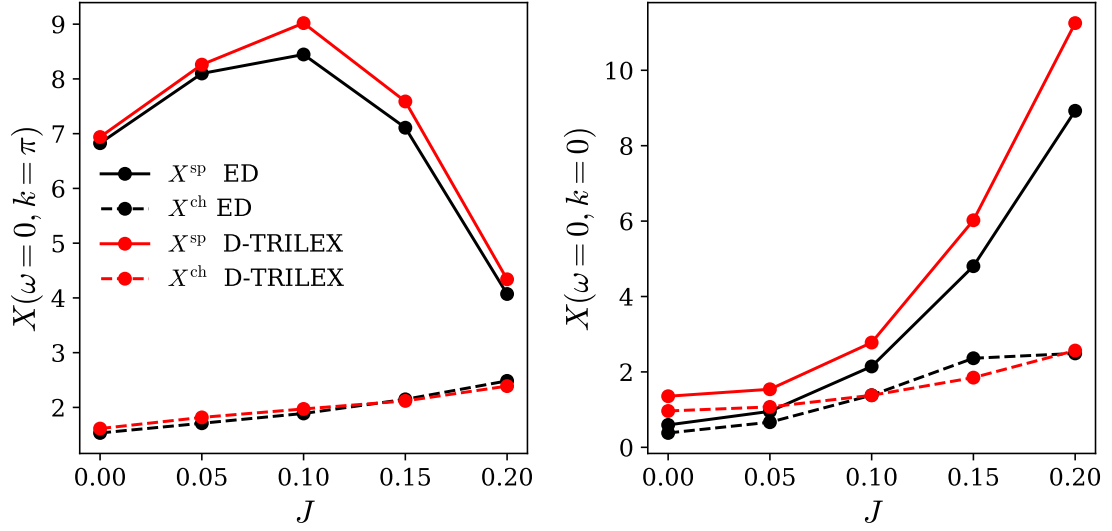
FIGURE 6.19: Spin (full lines) and charge (dashed lines) static ($\omega = 0$) susceptibility X. Left panel shows results computed at the $\mathbf{q} = \pi$ point, right panel at the $\mathbf{q} = 0$ point. Results are obtained obtained using D-TRILEX (red) and ED (black) methods for different values of the Hund's coupling J. Model parameters for these calculations are $t = 0.2$, $U = 0.5$, $\beta = 10$, and $\mu = 0.75$, and are equal across both panels.

$U > 1.5$ and reaches the maximum value of 7.6% at $U = 2.0$. We find that the DMFT result strongly deviates from the considered benchmark at moderate and large values of U. By looking at the real part of the self-energy ReΣ (panels (c) and (d) in Fig. 6.18), we can immediately understand the origin of the large mismatch between ED and DMFT. As a matter of fact, the real part of the self-energy at moderate to large U is dominated by the non-local contributions (dashed lines), which are completely missing in DMFT, while local contributions (solid lines) are approximately zero. D-TRILEX does not exactly reproduce all the contributions to the non-local self-energy, as they correspond to roughly 25% of the value of self-energy at $U = 1$. However, it follows the same trend as the ED result and this ensures the correct behavior of the Green's function as U is increased. We do not show the imaginary part of the self-energy, since it is at least an order of magnitude smaller than the real part in the whole range of parameters considered here.

In addition to single-particle quantities we calculate the charge and spin susceptibilities defined as $X^{\text{ch/sp}} = -\sum_{ll'} X^{d/m}_{ll'l'}$. Fig. 6.20 shows the corresponding results for the static susceptibilities $X^{\text{ch/sp}}(\mathbf{q}, \omega = 0)$ obtained at the $\mathbf{q} = \pi$ point. The susceptibilities at the $\mathbf{q} = 0$ point are very small in the whole range of considered parameters and are not shown here. In the left panel of Fig. 6.20, we illustrate the results for the half-filled Hubbard-Kanamori dimer considered above. We find that the susceptibilities of the D-TRILEX
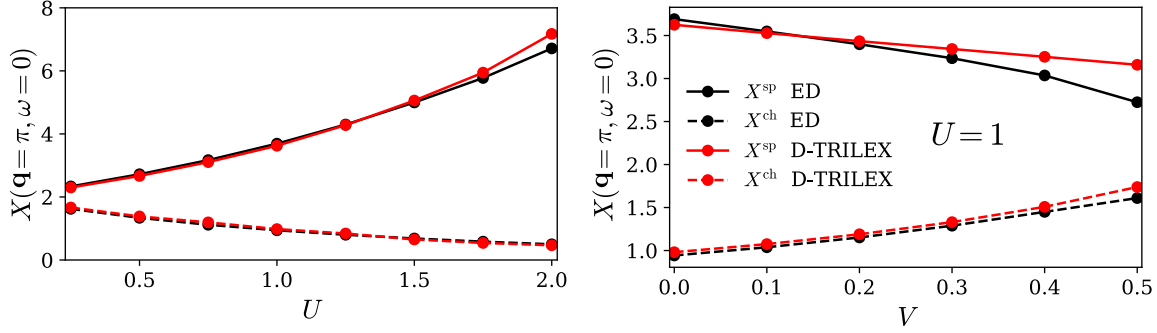
FIGURE 6.20: Spin (full lines) and charge (dashed lines) static ($\omega = 0$) susceptibility X obtained at the $\mathbf{q} = \pi$ point for the half-filled system with model parameters $t = 0.5$, $J = U/4$, and $\beta = 10$. The left panel shows the result as a function of the local interaction strengths U in the absence of the non-local interaction ($V = 0$). The right panel illustrates the susceptibility as a function of V calculated for the fixed value of the local interaction $U = 1$.

approach are in a very good agreement with the exact ED solution in the whole range of local interaction strength $0.25 \leq U \leq 2$. In the right panel, we demonstrate the dependence of the static charge and spin susceptibilities on the value of the non-local interaction V^d between electronic densities on neighboring sites $\langle i, j \rangle$ (3.14). More explicitly, we consider the non-local interaction in the form

$$\frac{V^d}{2} \sum_{ll',i\neq j} \rho^d_{i,ll} \rho^d_{j,l'l'} \tag{6.30}$$

To simplify notations, in the following the superscript "d" for the non-local interaction is omitted. We find that in the presence of the non-local interaction the susceptibilities obtained using ED and D-TRILEX methods are nearly identical up to $V = 0.3$. Above that threshold, the D-TRILEX susceptibility starts to deviate from the exact ED result. At $V > 0.3$ the D-TRILEX spin susceptibility continues to decrease almost linearly with increasing the value of V, while the exact result shows a stronger non-linear damping. This trend continues also above $V = 0.5$, where the difference between the D-TRILEX result and the exact result continues to increase. This behavior can be explained by the fact that the strong non-local interaction favors either full or zero occupancy of a lattice site. This charge density wave instability strongly suppresses magnetic fluctuations. In this regime the D-TRILEX calculations break down, because they are performed on the basis of the DMFT impurity problem, which does not incorporate any effect of the non-local interaction. The inclusion of the bosonic hybridization function in the spirit of EDMFT could improve the result, because in this case some contributions of the non-local interaction would be taken into account in the impurity problem via the bosonic hybridization.

These findings show that D-TRILEX improves the DMFT results in all considered

regimes. Additionally, D-TRILEX reproduces the trends observed in ED calculations in all the cases, even when DMFT fails. This fact suggests that for the considered system the difference between DMFT and ED mostly stems from non-local correlations that have the form accounted for in the D-TRILEX diagrams. These results are particularly remarkable taking into account that DMFT approximation is not very accurate in low dimensions, hence the DMFT impurity problem is probably not an optimal reference system for a diagrammatic expansion in this case.

6.5.2 Comparison with ladder DΓA
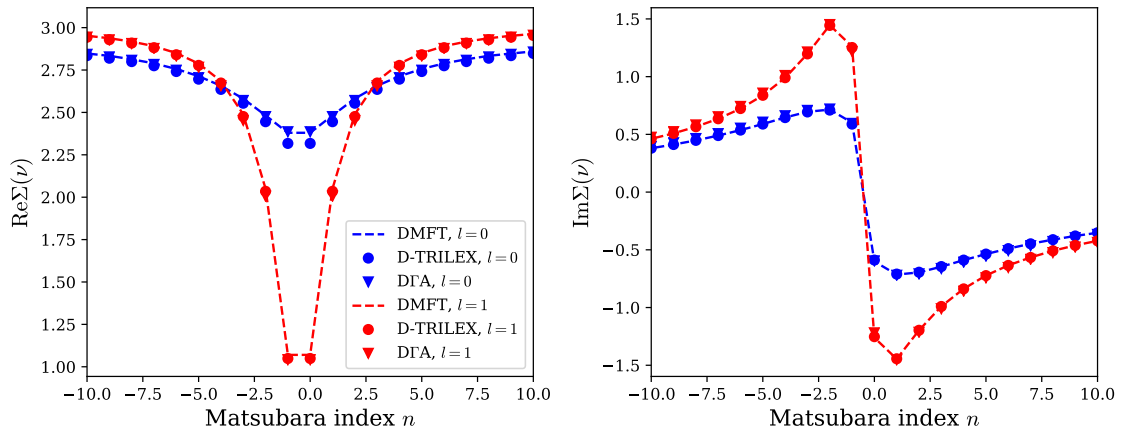
FIGURE 6.21: Real (left panel) and imaginary (right panel) parts of the local self-energy as a function of the index n of the Matsubara frequency. Dashed lines correspond to DMFT, dots to D-TRILEX and triangles to ladder DΓA results. the blue (red) color corresponds to the $l = 0$ ($l = 1$) orbital.

The next system we are going to address is a Hubbard-Kanamori model on a square lattice. Unfortunately, benchmark methods for this system are rare and we have to compar with non-exact methods, making it difficult to assess which approximation should be trusted in which regime. In spite of the difficult interpretation of the results, we believe it is instructive and potentially useful as a future reference to compare with another approximate method. In particular, we compare the D-TRILEX approach with data provided by Josef Kaufmann obtained using the ladder DΓA method. While comparing the two methods, we have to keep in mind that both methods are diagrammatic extensions of DMFT base on ladder diagrams, but the approximations involved at the level of the local vertex are almost opposite. Indeed, DΓA builds the diagrammatic expansion on top of the two-article irreducible vertex, while D-TRILEX completely neglects it. The model has two-orbitals $l = 0$ and $l = 1$ characterized by the same local Kanamori interaction with $U = 4$, $U' = 2$,

$J = 1$. The two orbitals differ by their half-bandwidths D_l, which are $D_0 = 4$ and $D_1 = 1$ with nearest-neighbor dispersion

$$\varepsilon_{\mathbf{k},ll'} = -2t_l \left(\cos k_x + \cos k_y \right) \delta_{ll'} \tag{6.31}$$

in terms of the hopping-amplitude $t_l = D_l/4$. The inverse temperature is set to $\beta = 5$.
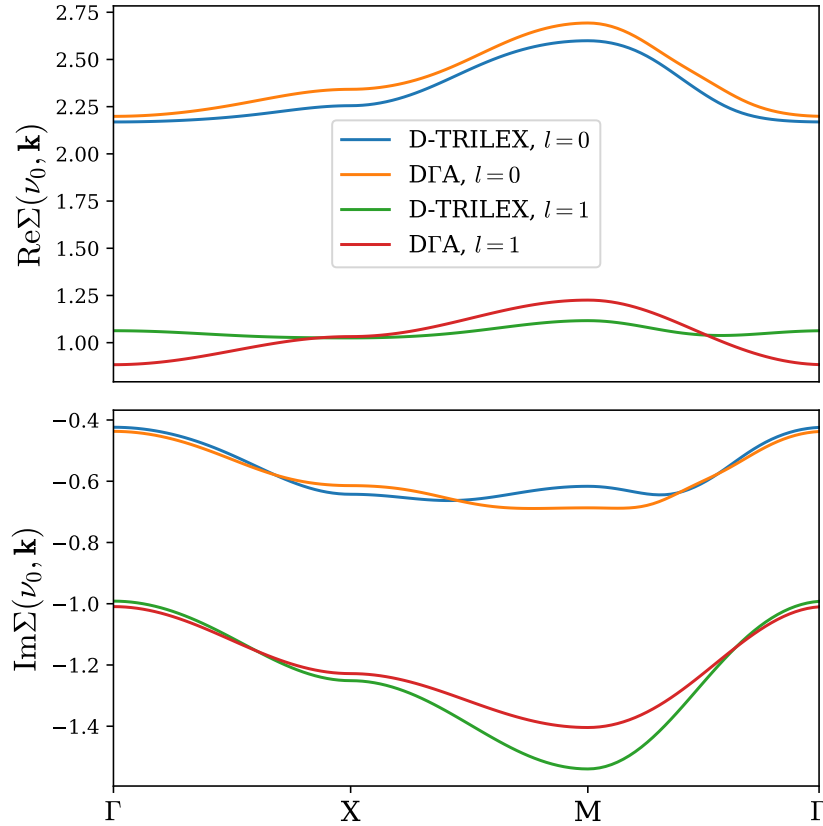
FIGURE 6.22: Real (upper panel) and imaginary (lower panel) parts of the self-energy along the high-symmetry path of the BZ. Blue and Green lines describe the D-TRILEX results for the $l = 0$ and $l = 1$ orbitals respectively. Similarly, the orange and red lines correspond to the DΓA results.

Additionally, the model is doped with filling $n = 1.7$ electrons per site ($n = 2$ would be half-filling), which coresponds to a doping $\delta = 15\%$. The chemical potential of the impurity problem was adjusted in DΓA to ensure the desired filling. In our case, we ran D-TRILEX on top of the same impurity problem obtained by DΓA, hence the two methods have the same chemical potential $\mu = 1.8158$. Since we are not addressing a specific

physical system, we can just stick to a comparison at fix chemical potential. However, we obviously get a slightly different filling $n = 1.75$ in the D-TRILEX calculation.

As a consequence, it comes as no surprise that the local self-energy shown in Fig. 6.21 is slightly different and we get the fillings for the two orbitals $n_0 = 0.794$ and $n_1 = 0.952$, instead of the values $n_0 = 0.766$ and $n_1 = 0.934$ obtained in DΓA. Despite this rather small difference, the overall agreement between the local self-energies as a function of frequency is very good for both orbitals $l = 0, 1$ and both methods remain very close to the DMFT results.
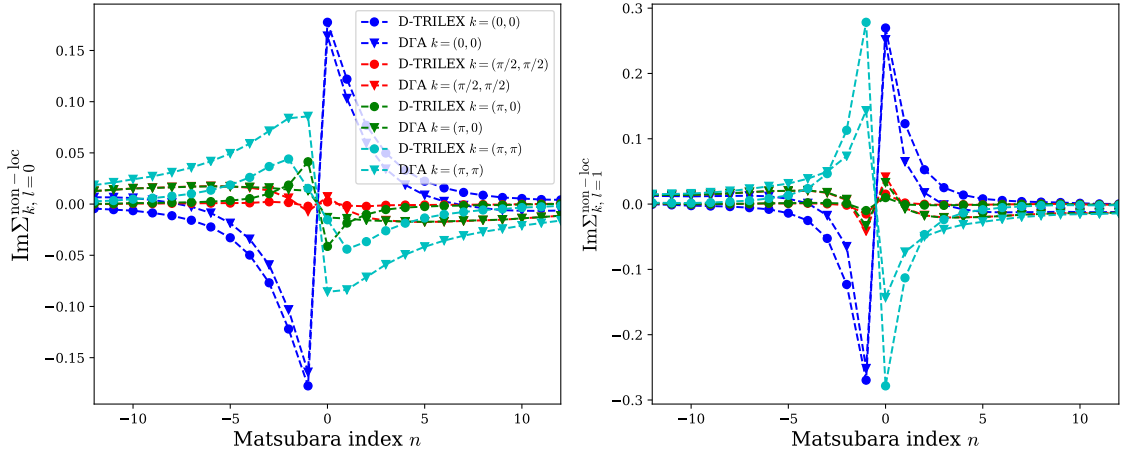
FIGURE 6.23: Imaginary part of the self-energy for $l = 0$ (left panel) and $l = 1$ (right panel) as a function of the Matsubara index n. Dots correspond to D-TRILEX results, triangles to ladder DΓA results. Different k-points are highlighted by different colors. The local self-energy is subtracted to emphasise the differences between the two methods.

Of course, it is much more significant to compare non-local quantities to assess the difference between the two methods. We start by investigating the lattice self-energy Σ_k in the Brillouin Zone for the two orbitals. In Fig. 6.22, we show a comparison between the methods. As we can see, the momentum dependences of ReΣ and ImΣ for the orbital $l = 0$ are both very similar to each other, with the exception of the behavior around the M-point in the imaginary part. The overall difference is rather small, especially if we keep in mind the underlying opposite approximations involved. If we consider the orbital $l = 1$, on the other hand, the differences between the two methods are larger. However, we can immediately notice that ReΣ is very flat and can be approximated as constant, hence its impact is not crucial. The imaginary part ImΣ shows a quantitative difference around the M-point but the overall qualitative behavior remains very similar between the two methods.
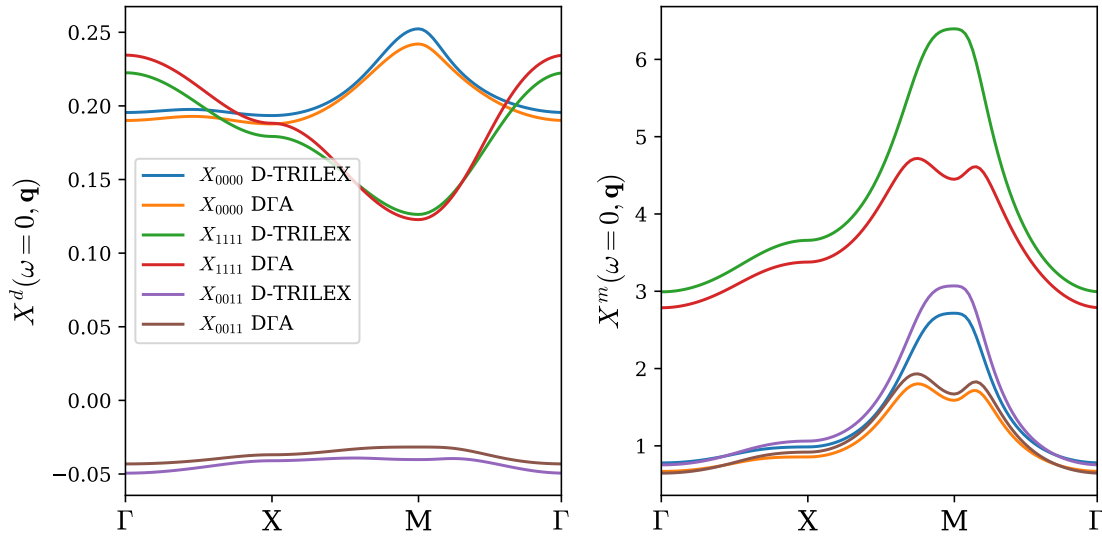
FIGURE 6.24: Static susceptibility $X(\omega = 0, \mathbf{q})$ in the density (left panel) and magnetic (right panel) channels along the high-symmetry path of the BZ. Colors for different components can be found in the legend on the plot.

The same behavior appears also at higher frequency, as it can be seen be found by plotting the ImΣ as a function of the Matsubara frequency for the different k-points. Results for this case are shown in Fig. 6.23, where we subtract the local part of the self-energy for better visibility of the features. Even though, there is a clear quantitative difference between the methods, these differences do not show any dramatic change at larger frequencies.

In addition to single-particle quantities, both methods give access to the density and magnetic susceptibilities $X_q^{d/m}$ of the system. Since the susceptibilities are different for each orbital, we plot the static susceptibility for each orbital separately in Fig. 6.24. The left panel of the figure represents the density channel. In this channel, we fid a very good agreement between the two methods for all the considered orbital components. In particular, we notice that the band with the largest bandwidth $l = 0$, hence the weakly interacting orbital, has a peak at M-point in the X_{0000}^d, while the strongly interacting orbital has a peak at Γ. On the contrary, we find an interesting qualitative difference in the magnetic channel. For all the components, the D-TRILEX has a peak at the M-point, hence it shows that magnetic flucuations are very strong. However, the peak is rather broad and far away from the usually very sharp peak that signals an AFM instability. DΓA exhibits an apparently different behavior: X^m has four distinct pokets around the M-point in the direction of the X-point for all the considered components. This behavior signals the formation of an incommensurate spin density wave. This is clearly visualized as a splitting of the peak around the M-point in Fig. 6.24. Since we are comparing two approximate methods, it

is perfectly possible that the difference between the two methods is only quantitative and not qualitative, since also the D-TRILEX peak is rather broad and could signal a splitting for a slightly different choice of the parameters. On the other hand, we know that D-TRILEX overestimates the horizontal fluctuations and has issues at large doping. As a consequence, the peak might be reduced and split, due to irreducible vertex corrections included in DΓA but not properly accounted for in the D-TRILEX method. However, we have to keep in mind that ladder DΓA is also not an exact method, so we should not expect a perfect agreement between the two. Further investigations by changing doping and temperature are required to understand if the two methods agree, but lead to slightly different parameters for the formation of the spin density wave, or if D-TRILEX does not capture this behavior.

Despite this difference, these results show that the D-TRILEX results are in reasonable agreement with ladder DΓA.

7 Theoretical study of Pb adatoms on the Si(111) surface

Chapter based on:
M. Vandelli, A. Galler, A. Rubio, A. I. Lichtenstein, S. Biermann and E. A. Stepanov
The origin of the rich variety of phases in a system of Pb adatoms on Si(111) surface
(*in preparation*)

7.1 Systems of adatoms on surfaces as a platform for tunable systems

Recent advances in scanning tunneling microscopy allow extensive control and manipulation of single atoms placed on surfaces [334]. These techniques can open the way to a new class of synthetic two-dimensional materials constituted by atomic structures organized in precise geometries on top of different substrates, such as tin (Sn) and lead (Pb) adatoms disposed on silicon Si(111), germanium Ge(111) or SiC(0001) surfaces. The possibility of tuning the structure and the chemical composition in these artificial systems allows to directly modify the properties of these two-dimensional materials in a similar way to what has been achieved in systems of cold atoms, with the potential advantage of having a much more stable platform. In this regard, control over the geometry and the type of atoms arranged on these surfaces allows to achieve an effect analogous to varying the twisting angle in Moiré bilayer heterostructures as proposed in Ref. [335]. As a consequence, these systems of adatoms atomically arranged on surfaces are also a promising new platform for "a condensed-matter quantum simulator", mimicking the title of Ref. [335].

In addition to the tunability of their properties, systems of adatoms arranged in triangular structures were proposed as suitable candidates to host topological superconductivity [336–338]. Experiments on a doped system of adatoms on Si(111) revealed the validity of these predictions [339].

Despite early suggestions that this kind of systems can be effectively described by a simple single-site Hubbard model, experimental findings showed a much more complicated picture. These include the effects of nonlocal Coulomb correlations, magnetic frustration, as well as strong spin-orbit coupling in case of heavy adsorbants (Sn, Pb,

etc). Among various distinctive features, these artificial surface systems reveal unexpected magnetic properties. This breakthrough result showed that the magnetism is not limited to *d*-electron materials, but can be found in *sp*- and *p*-systems as well. Unfortunately, the theoretical description of these effects belongs to the class of the most challenging problems of condensed matter physics.

Most of the theoretical studies in this field are focused on a single-particle description, without considering collective effects of the electronic or magnetic subsystems. As an exception to that, a study based on the combination of DMFT, variational cluster approximation (VCA) and dual fermions predicts the formation of row-wise collinear order that is stabilized in Sn:Si(111) due to hopping processes beyond the nearest-neighbors was reported in Ref.[340].

For our studies, we can use D-TRILEX method described in Chapter 6 to address the problem. By means of this method, we can consistently address the problem collective of excitations and charge/magnetic orders appearing as a result of symmetry breaking in this kind of systems, even including long-range non-local interactions and the effect of spin-orbit coupling.

7.1.1   Rich phase diagram and ultra-strong spin-orbit coupling in Pb on Si(111)
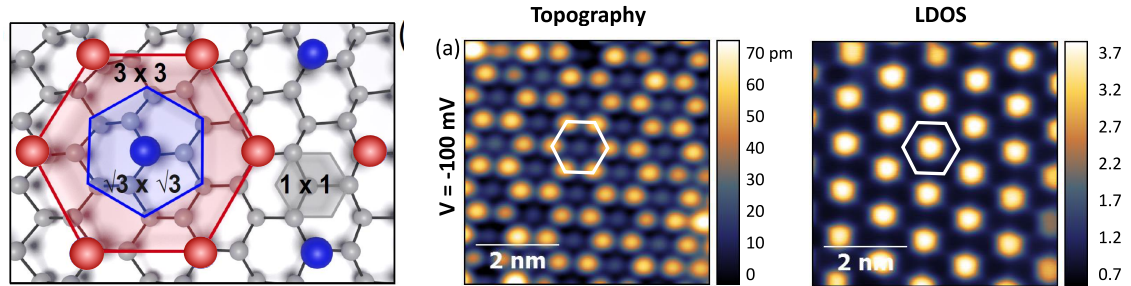
FIGURE 7.1: The right panel shows the ideal structure of the Pb:Si(111) system, adapted from Ref. [341]. The arrangement of the Pb adatoms forms a lattice that displays a rotation of 30° with respect to the host Si. With red and blue colors we indicate the atoms that are equivalent in the $\sqrt{3} \times \sqrt{3}$-phase and that become inequivalent in the 3×3-phase. The middle and right panels show results of an STS scan for the topology and local density of states (LDOS) in the 3×3-phase, reproduced from Ref. [341].

In this work, we focus on adatom systems on top on Si(111) surfaces. This choice is based on the fact that Pb on Si(111) has attracted wide interest in the past few years due to the large variety of phases that can be experimentally observed in such system [342]. The Pb adatoms arrange themselves to form patches of triangular geometry rotated of 30°

with respect to the substrate, as shown in Fig. 7.1. Indeed, the peculiarity of triangular lattices is a high degree of frustration, that can lead to highly non-trivial competition between different ordering phenomena. In addition to the usual frustration of the triangular lattice, this class of systems displays both very strong onsite interaction and very large values of the non-local interaction between nearest-neighbor adatoms. These characteristics make the system an ideal candidate to study competition between charge and spin excitations. When the type of adatoms is chosen to have a sufficiently large atomic number Z, additional effects appear due to spin-orbit coupling. These effects can indeed be experimentally observed when lead adatoms (Pb, $Z = 82$) are chosen, and they consist in a split of the Fermi surface and in ordered states with non-commensurate ordering vectors. Additionally, spin-orbit coupling is responsible for the Dzyaloshinskii–Moriya interaction, hence skyrmion lattices or chiral phases could appear in the system [343].

Experimentally, it was observed by using scanning tunnelling microscopy (STM) that the system develops structural instabilities, a charge density wave and that the quasi-particle interference patterns are influenced by the strong value of spin-orbit coupling [341, 342]. Several different arragements of the atoms on the surface were identified, namely a $\sqrt{3} \times \sqrt{3}$ phase with respect to the underlying Si surface, a 3×3 phase and a $\sqrt{7} \times \sqrt{3}$ phase, that becomes superconductive at very low temperatures [344, 345]. Among those, the origin of the CDW phase is the most debated, as two completely different mechanisms have been proposed as a driving mechanism for it. Indeed, many experiments confirm that the system exhibits a structural transition to a charge ordered phase at a temperature of 86 K. However, it is still a matter of on-going research to understand whether this transition has to be attributed to a Peierls-like transition, an intrinsic asymmetry induced by the substrate or to strong electronic correlations. The reason why it is so difficult to investigate this transition is that the 3×3 pahse of Pb:Si(111) forms very small domains, which cannot be investigated by usual optical measurements. The most widely used experimental technique for this system is STM, which is not suitable for determining whether the order occurs due to single-particle effects or collective fluctuations. At this point, it is also important to stress that the experimental control over doping conditions in this kind of systems is not an easy task. The reason is the fact that adatoms can attract dopants from the the bulk. Another reason is that STM measurements require a finite conductance in the system. As we explain in the next sections, these sources of doping may play an important role in the physics of this material. It is worth noticing that a similar effect appears in other similar systems of adatoms, notably in Pb:Ge(111) and Sn:Ge(111) [346, 347], but not in the Sn:Si(111) compound.

The interpretation of the experimental results for Pb:Si(111) as well as for Pb:Ge(111) found in literature is mostly based on density functional theory, in particular DFT+U calculations [342, 348]. Notable exceptions are the *GW*+DMFT method used in Ref. [349] and an extended version of the VCA method, called XVCA, used to interpret the experimental result in Ref. [341]. However, in both cases calculations were performed without

spin-orbit coupling. Additionally, the use of *GW*+DMFT predicted that this material lies very close to a coexistence region of Mott insulating phase and metallic charge density wave phase. Of course, this picture is very unstable and can be easily modified if vertex corrections are included or the Fermi surface is modified by the addition of the spin-orbit coupling. On the other hand, the XVCA calculation of Ref. [341] cannot take into account any kind of long-range interaction or fluctuation.

In this thesis, we show that the physics of the system cannot be fully captured by a simple extended Hubbard model on a triangular lattice, as previously pointed out in Ref. [348]. Many concurrent factors affect the physics of this material. Namely the presence of strong non-local interactions causes the emergence of long-range correlations, while a strong hybridization with the substrate effectively destroys the symmetry between the sites and the large value of the spin-orbit coupling introduces a split between the single-particle bands. By disentangling and investigating separately each contributions, we can highlight the role that each factor plays in the physics of the material. Indeed, each of them plays an important role in specific regions of the phase diagram and induces the formations of a large variety of different magnetic as well as charge-ordered phases. In particular, we will point out what could be a cause of the charge ordering and what are the ordering mechanisms in the low temperature magnetic phases.

7.1.2   Model for the system with spin-orbit and non-local interactions
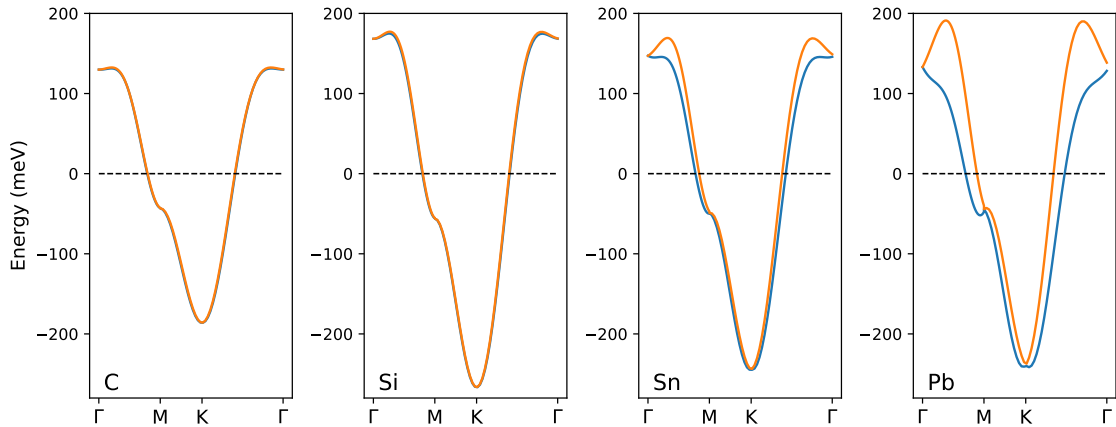
FIGURE 7.2: Non-interacting bandstructure of the adatom systems of IV-group elements deposited on Si(111) with geometry $\sqrt{3} \times \sqrt{3}$, as obtained using the parameters taken from Ref. [343] along the high-symmetry path of the BZ of the triangular lattice. The different colors indicate the different spin-orbital-resolved bands. Among these, Pb exhibits a noticeable splitting between the bands even at the Fermi surface $E = 0$.

The model that we use to study this system is the extended Hubbard model with spin-orbit coupling in the form of Rashba interaction, as introduced when discussing Eq. (3.14). According to DFT calculations, this system is characterized by a single band in the vicinity of the Fermi surface and localized on the Pb atoms while the other bands corresponding to the substrate are gapped and are rather well-separated by the Pb band. As a consequence, we can describe this system within a single-orbital to a high degree of accuracy [343].

The Hamiltonian for this model reads

$$\hat{H} = \sum_{ij, \sigma\sigma'} c_{i\sigma}^{\dagger} \left(t_{ij}\, \delta_{\sigma\sigma'} + i\, \boldsymbol{\gamma}_{ij} \cdot \boldsymbol{\sigma}_{\sigma\sigma'} \right) c_{j\sigma'} + U \sum_{i} n_{i\uparrow} n_{i\downarrow}$$
$$+ \frac{1}{2} \sum_{i \neq j,} V_{ij}\, n_i\, n_j + \frac{1}{2} \sum_{i \neq j} J_{ij}\, \mathbf{S}_i \cdot \mathbf{S}_j. \tag{7.1}$$

where $\boldsymbol{\gamma}_{ij} = \gamma_{|i-j|} \left(\hat{r}_{ij} \times \hat{z} \right)$ is the Rashba interaction, U describes the usual Hubbard interaction, V_{ij} is the regular density-density Coulomb interaction and J_{ij} represents the exchange interaction among the electrons. In this work, we use the same parameters estimated from DFT calculations in Ref. [343] in the $\sqrt{3} \times \sqrt{3}$-phase. From a Wannier projection on the localized orbitals, the nearest-neighbor and next-nearest-neighbor hoppings are estimated to be $t = t_{01} = 31.3$ meV and $t' = t_{02} = -19.2$ meV in this material. The Rashba parameters wer found to be $\gamma_{01} = 16.7$ meV and $\gamma_{02} = 2.1$ meV. The parameters of the model were obtained using cRPA in the same work. The Hubbard interaction is taken to be $U = 900$ meV, the nearest-neightbor interaction is $V_{01} = 500$ meV and the exchange integral reads $J_{01} = 1.67$ meV. These parameters are rather similar to those computed in Ref. [349] with a similar method. In the momentum-space, we can write the Fourier transform of the single-particle term as $\varepsilon_{\mathbf{k},ll'}^{\sigma\sigma'} = \varepsilon_{\mathbf{k},ll'}\delta_{\sigma\sigma'} + i\, \vec{\gamma}_{\mathbf{k},ll'} \cdot \vec{\sigma}_{\sigma\sigma'}$ with $l^{(')}$ indicating the site within the unit cell, as discussed in Eq. (3.14) of Chapter 3.

In the $\sqrt{3} \times \sqrt{3}$ phase each site is equivalent with $l = l' = 1$, so $\epsilon_{ll',\mathbf{k}}$ becomes the next-nearest neighbor dispersion for the triangular lattice $\epsilon_{\mathbf{k}}$ and similarly for the Rashba term. In the 3×3 phase, the unit cell contains three atoms. Experiments show that these three Pb atoms are not equivalent to each other and display a 1-up-2-down configuration. For this reason, we perform DFT calculation displacing one of the Pb atoms upwards in the cell and letting all the atoms relax to the equilibrium configuration. As in previous DFT studies [104, 342, 343, 350, 351], the surface is simulated by a slab geometry consisting of a 1/3 monolayer of Pb adatoms on top of three Si bi-layers. The Pb adatoms occupy the T_4 positions. The dangling bonds of the bottom Si bilayer are compensated by hydrogen capping, and 19 Å of vacuum are included in the simulation. For all structural relaxations we employ the WIEN2k [352, 353] program package, a full-potential linear-augmented plane-wave code. A k-grid with $6 \times 6 \times 1$ k-points in the reducible Brillouin zone was used and internal coordinates were relaxed until forces were less than 2 mRy/bohr. In all DFT calculations, we employed the generalized gradient approximation (PBE), spin-orbit
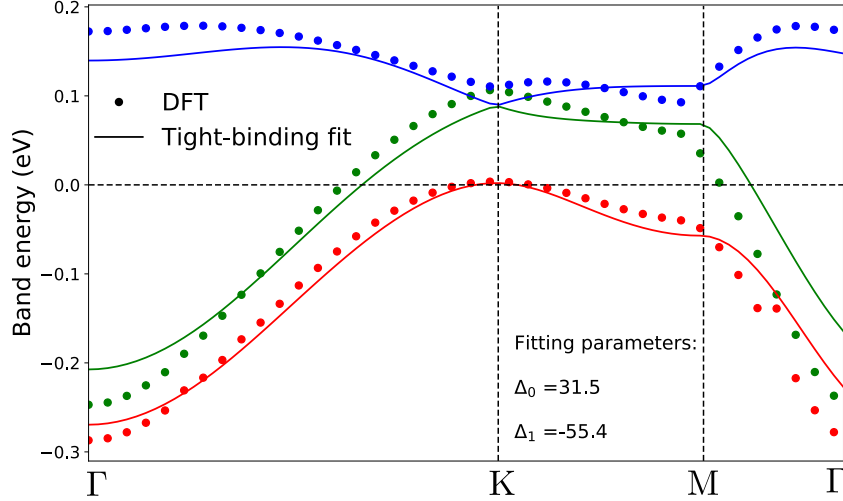
FIGURE 7.3: Comparison between the DFT band structure obtained using the generalized gradient approximation with the PBE functional for the 3×3 structure and the corresponding tight-binding obtained as a result of the fitting by just varying the values of the local shift on each atom Δ_l.

coupling was neglected. In agreement with experiment, we find the stabilisation of a 3×3 reconstruction, where one Pb adatom is vertically displaced by 0.22Å compared to the other two Pb adatoms in the supercell. The energy gain of this 1-up-2-down structural reconstruction is found to be 9.5 meV with respect to a flat adatom layer. This leads to a situation where the sites are not all equivalent. In particular, the two sites in the down configuration are equivalent to each other and the one in the up position is inequivalent.

We model this behavior in a tight-binding model with three atoms in the unit cell with the same parameters as in the single-site case, but with a different local component of the single-particle Hamiltonian matrix Δ_l (not to be confused with the hybridization function in the impurity model) for each site l in the unit cell. Since the values found for Δ_l are rather small, we can safely neglect the modification of the Coulomb interaction. The resulting tight-binding model becomes $\varepsilon_{\mathbf{k},ll'} = \varepsilon^{1s}_{\mathbf{k},ll'} + \Delta_l$ under the constraint that $\Delta_0 = \Delta_1 \neq \Delta_2$, where $\varepsilon^{1s}_{\mathbf{k},ll'}$ is the tight-binding Hamiltonian of three sites using the same parameters as the single-site case. We fit the DFT band-structure obtained for the 3×3 phase using the two fitting parameters Δ_0 and Δ_1. The result of this fitting is displayed in Fig. 7.3. The tight-binding model obtained with the fitting exhibits a very good agreement with the DFT result close to the Fermi surface and a rather good agreement elsewhere. We perform DMFT calculations using the w2dynamics package [274]. The D-TRILEX solution is based on the numerical implementation described in Ref. [96]. The local density of states (DOS) is obtained from the corresponding local Green's functions via analytical continuation using

the ana_cont package [22], based on the maximum entropy method.

7.2   The $\sqrt{3} \times \sqrt{3}$ phase with nearest-neighbor interactions only
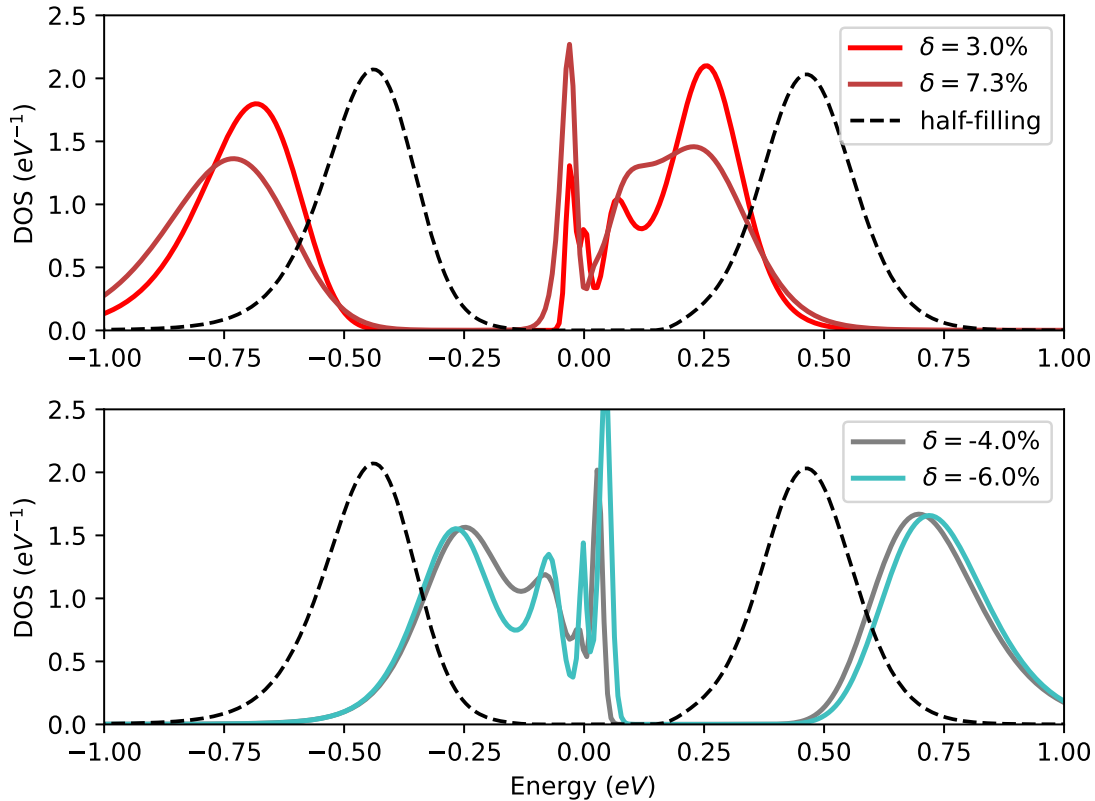
FIGURE 7.4: D-TRILEX spectral function $\sqrt{3} \times \sqrt{3}$ phase with nearest-neighbor interactions at $T = 65\,\text{K}$ obtained with the ana_cont package [22]. Upper panel shows electron doping, lower panel hole doping.

7.2.1   The spectral function of a protoypical Mott insulator

In order to disentangle the different sources that can lead to the observed CDW transition, we start by considering the $\sqrt{3} \times \sqrt{3}$ phase with only nearest-neighbor interactions. We consider single-particle observables first, in particular the interacting density of states

(DOS) of the system, which contains information about the conduction properties of the system.
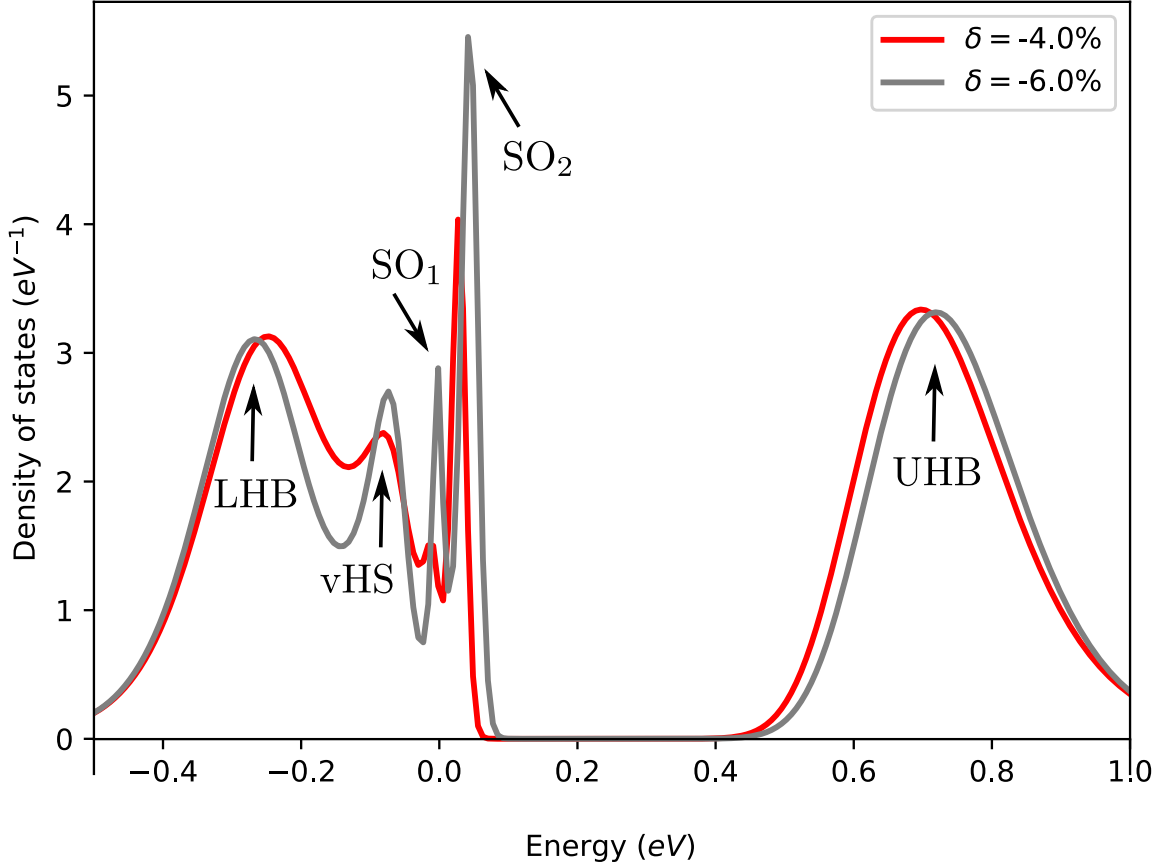
FIGURE 7.5: D-TRILEX spectral function at $T = 65$ K obtained with the ana_cont package [22]. Upper panel shows electron doping, lower panel hole doping.

We first notice that the system lies rather deep in the Mott phase, no matter if we include spin-orbit coupling or not. Using the dispersion obtained from the downfolding of DFT calculations and local Hubbard interaction obtained by cRPA calculations in Ref. [343], the ratio between the interaction and bandwidth is about $U/W \sim 3$, which is large enough to motivate this behavior. As a matter of fact, the results obtained in Ref [343] with a mean-field Hartree approximation predict a Mott insulating ground state for the system. Since the value of the interaction is very large, we expect the Hartree calculations to predict roughly the correct spectrum. A very small value of doping in the system causes a phase transition to a metallic behavior with a very clear quasi-particle peak at the Fermi level, no matter whether it is *p*- or *n*-doping. This behavior is a characteristic manifestation of the physics of a doped Mott insulator. We additionally analyse the spectral function

of the system for different values of doping δ in Fig. 7.4. The upper panel shows the electron (n-)doping for the values $\delta = 3\%$ and $\delta = 7.3\%$, while the lower panel shows the electron (n-)doping for the values $\delta = 4\%$ and $\delta = 6\%$. The black dashed line shows the result at half-filling which corresponds to a simple Mott insulator with two Hubbard sub-bands located roughly at $\pm U/2$. The two are separated by a large Mott gap, where no single-particle excitations can occur. On the contrary, at any value of the doping the system is metallic and shows the typical features of a doped Mott insulator, i.e. a quasi-particle weight in the correspondence of the Fermi surface and the two Hubbard subbands, that are shifted in energy of a value corresponding to the chemical potential at the given doping $\mu = \mu(\delta)$. Interestingly, these are not the only features appearing in the density of states of this system. We additionally observe other features such as an intermediate peak between the quasi-particle peak and the closest Hubbard subband and a smaller replica of the quasi-particle peak. We explain these peaks by taking a closer look at the DOS in the hole-doped case in Fig. 7.5. These additional peaks correspond to the signature of the van Hove singularity (vHS in the figure) that appears in tight-binding dispersion of the system at zero temperature and the spin-orbit splitting ($SO_{1/2}$ in the figure) respectively. The LHB and UHB in the figure indicate the lower Hubbard subband and the upper Hubbard subband. We note that the spectra presented here appear to be similar to what has been measured for the $p-$doper Sn:Si(111) in Refs. [339, 354], which is characterized by similar parameters to the Pb:Si(111).

7.2.2 Phase diagram

The phase diagram of the system in the $\sqrt{3} \times \sqrt{3}$ phase obtained with a single-shot D-TRILEX calculation is shown in Fig. 7.6. The model exhibits a Mott insulating (MI) phase denoted in black in plot, which exists only at half-filling at high-temperature. As soon as a doping $|\delta| > 0$ is introduced, there is a transition to a metallic phase as discussed for the DOS. In addition to these phases, we also observe symmetry-breaking transitions in the magnetic and/or in the density sector. In our method, we are not able to access the region of broken symmetry, but we can do calculations in the disordered phase and monitor the susceptibilities $X_{\mathbf{q},\omega=0}^{\varsigma\varsigma'}$ with $\varsigma(') = \{d, s_x, s_y, s_z\}$ to look for a divergence. Depending on the momentum at which it occurs, we can understand the ordering vector $\mathbf{Q}$ of the geometry in the broken-symmetry phase. In the magnetic channel, we observe two different kinds of magnetic phases that differ for the ordering vector. We call them *chiral M* and *chiral K* phases for reasons explained below. The chiral M phase appears with the typical dome structure in the vicinity of half-filling, while the chiral K phase occurs at larger electron doping. Both phases exhibit a top of their respective dome structure at around $T = 60$ K. Both in the $n-$ and $p-$doped regimes, we find a CDW instability that appears around $\delta = \pm 7.5\%$ by means of a dynamical symmetry breaking. Interestingly, for this model the CDW phase has a peak at the $\mathbf{Q} = K$ and it occurs independently on the temperature. We
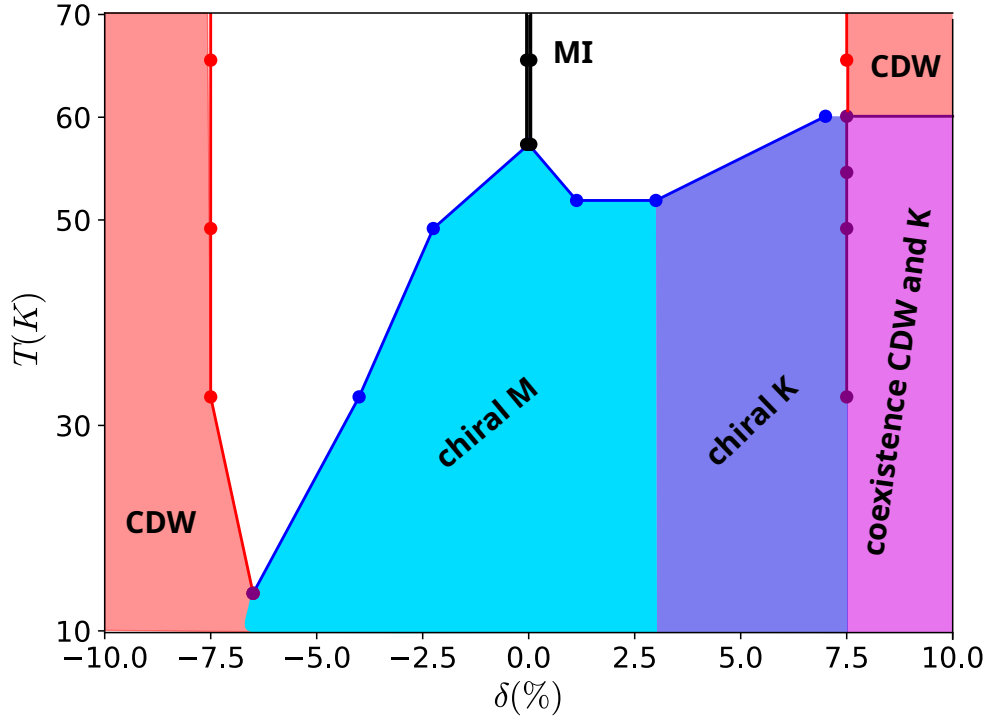
FIGURE 7.6: Phase diagram of the system with only nearest-neighbor interactions in the $\sqrt{3} \times \sqrt{3}$-phase as a function of the doping δ and the temperature T, obtained with single-shot D-TRILEX calculations. The ordered phases are highlighted in colors, while the white area describes the regular metallic phase phase. The dots signal the middle point between the last point in a phase and the first in the next phase.

repeated calculations without spin-orbit coupling and the results did not qualitatively differ from what is shown here, except that the chiral M and chiral K phases turn into a row-wise order with $\mathbf{Q} = M$ and a 120°-Néel ordering with $\mathbf{Q} = K$ respectively. The the take-away messages are that, under these approximations, the system does not exhibit a dynamical CDW only at finite-doping and not at half-filling, but it shows a variety of chiral phases with incommensurate ordering vector $\mathbf{Q}$.

7.2.3   Effects of spin-orbit on the order of the system

In the previous subsection, we discussed the different phases occurring in the system. Here, we show the susceptibilities for the phases discussed above. In Fig. 7.7, we compare the susceptibilities obtained without (left column) and with (right column) the spin-orbit coupling in the calculations. The top row corresponds to the magnetic susceptibilities at half-filling. The lowest row shows the magnetic susceptibility at $\delta = 7.4\%$. Even though
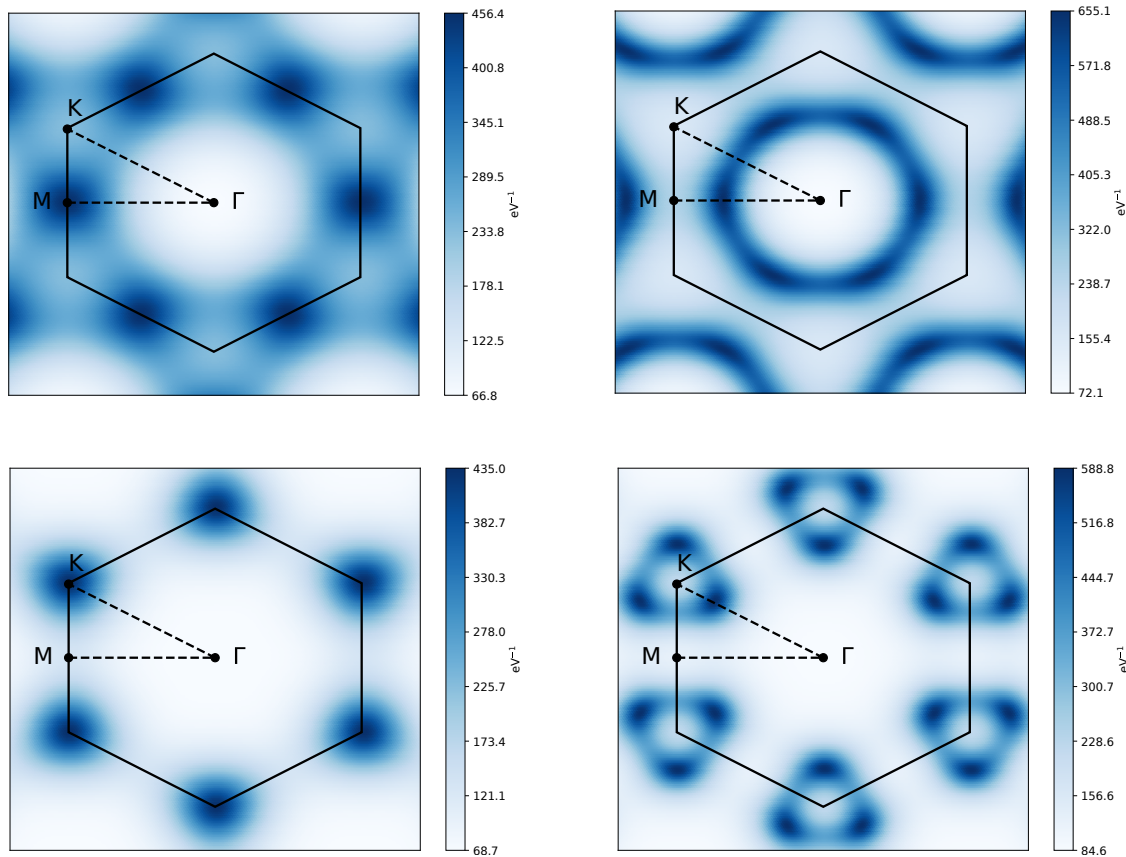
FIGURE 7.7: Comparison between the largest eigenvalue of the static spin susceptibility $X^{\varsigma\varsigma'}_{\mathbf{q},\omega=0}$ with $\varsigma(') = \{s_x, s_y, s_z\}$. The panels show the cases without (left) and with spin-orbit coupling (right). The two upper panels show the $\delta = 0\%$ case, while the lower panels are computed at $\delta = 7.4\%$ for spin (blue) and charge (red) respectively. The temperature is chosen to be $T = 65$K.

the susceptibility has not diverged yet, peaks appearing at specific points in the BZ clearly signal the ordering vectors characterizing the symmetry-broken phases.

Without spin-orbit coupling, at half-filling the strongest magnetic fluctuations correspond to the commensurate row-wise antiferromagnetic modes with peaks located at the ordering vector $\mathbf{Q} = $ M, in accordance with mean-field results [343], while in the doped case at $\delta = 7.4\%$ the magnetic susceptibility exhibits a large peak at $\mathbf{Q} = $ K which corresponds to the 120°-Néel phase. A discussion of these different phases can be found, for instance, in Refs. [343, 355]. The spin-orbit coupling partially changes this picture, by splitting the peaks into three different peaks located at different points of the BZ. These points are located on the line connecting M/K and Γ and are close to $\mathbf{Q} \approx \frac{2}{3}$ M for the
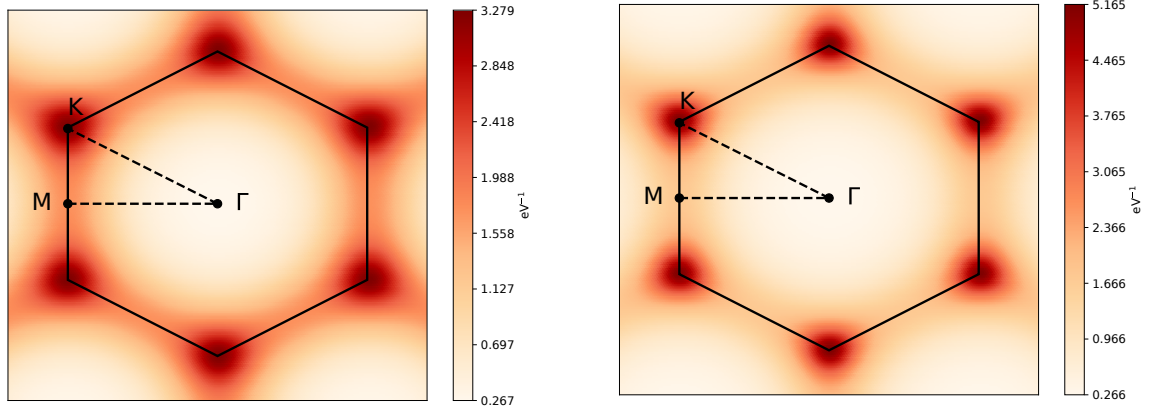
FIGURE 7.8: Comparison between the static density susceptibility $X^d_{\mathbf{q},\omega=0}$ without (left) and with spin-orbit coupling (right) at $\delta = 7.4\%$.

so-called chiral M phase and close to $\mathbf{Q} \approx \frac{3}{4} \mathrm{K}$ for the chiral K phase. The new location of the peaks between the corresponding M/K ordering to a point in the BZ between M/K and Γ signals the emergence of an incommensurate spin spiral in both cases. As discussed in Ref. [343], the presence of these spin spirals is very attractive from the point of view of applications, as it can be exploited to realize skyrmion lattices. Despite this important physical difference, it is worth noticing that the position of the boundaries between the phases remains roughly unchanged and the quantitative picture exhibits only a small shift in the magnetic phases towards a slightly larger critical temperature.

A similar displacement of the ordering vector was observed in Ref. [340] varying the Hubbard interaction in the Sn:Si(111) system. This is again due to the high degree of frustration of lattice. In the absence of spin-orbit coupling, indeed our spin susceptibility strongly resembles the one computed for the largest value of the Hubbard interaction presented in the reference. We point out that cluster methods consider a plaquette with few atoms or, alternatively, a rather coarse grid in momentum-space. This means that, while they are able to capture ordering appearing at the high-symmetry points in the BZ, they can hardly capture this kind of features that appear at incommensurate points in the BZ.

On the other hand, the charge susceptibility does not change dramatically if we include spin-orbit coupling. In the lowest row of Fig 7.8, we show the charge susceptibility at $\delta = 7.4\%$, hence quite close to the CDW phase boundary in the electron-doping sector. The main instability in the charge channel remains $\mathbf{Q} = \mathrm{K}$ in all the regimes investigated in this study. This is consistent with the presence of the very strong nearest neighbour interaction. We do not show the density susceptibility at half-filling since it is basically negligible and does not exhibit any characteristic peak.

7.2.4 Exchange interactions
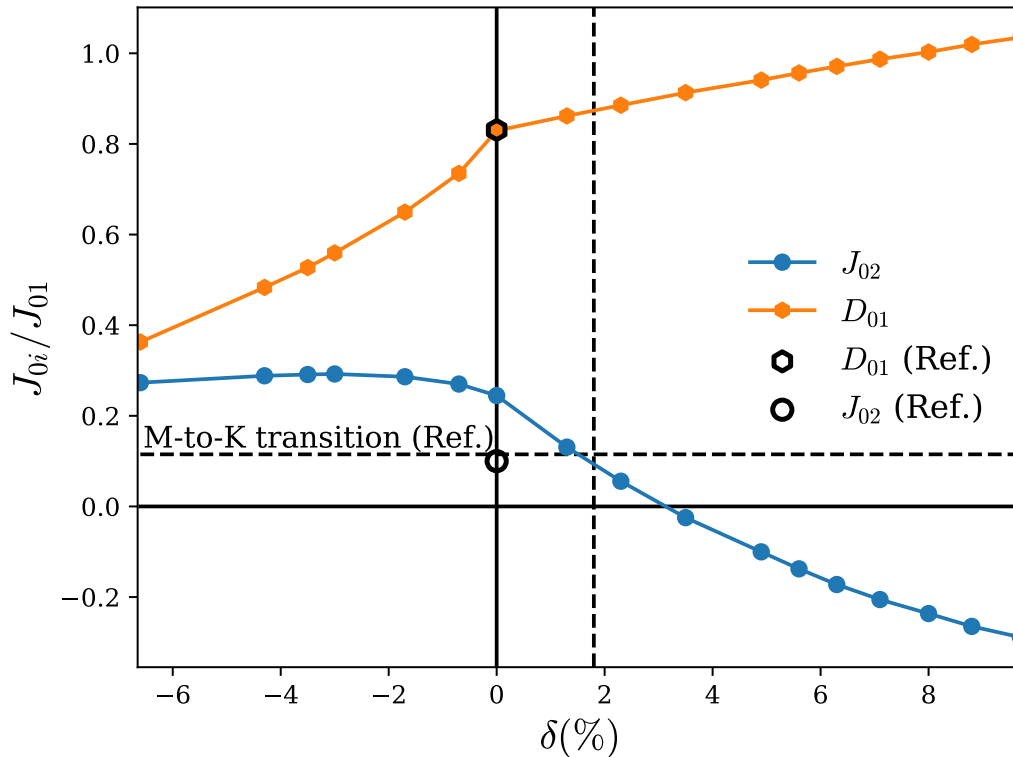
FIGURE 7.9: Exchange interactions as a function of doping divided by the nearest-neighbor exchange coupling J_{01}. D_{01} is the nearest-neighbor Dzyaloshinskii–Moriya interaction (orange line with dots) and J_{02} is the next-nearest-neighbor exchange (blue line with dots). The vertical dashed line indicates the transition from chiral M to chiral K phases according to our calculations. The black hexagon and dot represent the value at half-filling computed in Ref. [343], using the Hartree approximation. The horizontal dashed line represents the prediction for the M-to-K transition in the antiferromagnetic Heisenberg model with J_{01} and J_{02} obtained from Monte Carlo calculations in Ref. [356].

An additional quantity which is accessible from D-TRILEX calculations is the exchange interaction $\mathcal{J}^{s}_{q, l_1 l_2, l_3 l_4}$ of an effective Heisenberg model using Eq. (6.13), that can be computed with a single iteration of the method. The calculation of this quantity helps to shed a light on the different behaviors observed in the magnetic susceptibility as a function of doping.

In particular, we consider the exchange coupling terms that appear in the effective spin Hamiltonian

$$H_{\text{Heis}} = J_{01} \sum_{\langle ij \rangle} \mathbf{S}_i \cdot \mathbf{S}_j + J_{02} \sum_{\langle\langle ij \rangle\rangle} \mathbf{S}_i \cdot \mathbf{S}_j + D_{01} \sum_{\langle ij \rangle} \hat{z} \cdot \left(\mathbf{S}_i \times \mathbf{S}_j \right) \tag{7.2}$$

where $\langle ij \rangle$ represents summation over nearest-neighbors and $\langle\langle ij \rangle\rangle$ represents summation over next-nearest-neighbors. We refer to J_{01} as exchange coupling, to J_{02} as the next-nearest-neighbor exchange coupling, and D_{01} as the nearest-neighbor Dzyaloshinskii–Moriya interaction, which appears in our system as a consequence of the spin-orbit coupling.

In Fig. 7.9, we plot the J_{02} (blue line with dots) and D_{01} (orange line with hexagons) normalized by the value of J_{01} as a function of the doping δ. It is important to notice that the value of D_{01} is very large and of magnitude comparable with the exchange coupling. This explains why we observe a clear shift of the intensity from the high-symmetry point to an incommensurate position in the magnetic susceptibility in Fig. 7.7. This results in a superposition of spin spirals with period that extends over several lattice sites. Additionally, it has a roughly linear dependence on doping in both the $p-$ and $n-$doped regimes, with different slopes in the two different doping regions. Interestingly, its value is very similar to the value predicted by Hartree mean-field calculations at half-filling reported in Ref. [343], which again shows that the system lies deep in the Mott insulating phase, where a t^2/U estimation for the exchange interaction used in that work is justified.

The calculation of the J_{02} exchange coupling also helps understanding the M-to-K shift in the magnetic ordering observed in our calculations. The magnitude of this coupling constant is rather small compared to J_{01} and D_{01}. However, it is not negligible and in our calulations we obtain a larger value of the J_{02} coupling compared to mean-field estimates. An important feature is that J_{02}/J_{01} is roughly constant in the $p-$doped regime while D_{01} is strongly modified. Hence, D_{01} is responsible for the formation of the chiral phase. Conversely, in the $n-$doped regime the value of J_{02}/J_{01} decreases and it even changes sign, while D_{01} increases again linearly. We attribute the shift of the magnetic susceptibility from M to K to the variation in the magnitude of the J_{02}/J_{01} coefficient. This is consistent with Monte Carlo calculations of the phase diagram of the Heisenberg model with both J_{01} and J_{02} on a triangular lattice that show a transition from a row-wise AFM configuration (peak at M point) to a 120°-Néel when $J_{02}/J_{01} \approx 0.12$ [356], as highlighted in Fig. 7.9. In the figure we additionally mark the mean-point between the last calculated point with peak at M and the first point with peak at K.

7.3 Preliminary results with full Coulomb coupling

7.3.1 CDW phase: $1/r$ tail and 3×3 phase

In the previous section, we gained a general understanding of the properties of this system, under the simplifying assumption of next-nearest-neighbor interaction. In this section, we generalize these findings to a realistic case by performing calculations of the phase diagram using the long-range potential with the full $1/r$ tail [349]. The aim of this Section is to try to understand the origin of the CDW phase observed in experiments.

As previously discussed, the Pb:Si(111) system exhibits a 3×3-phase at low temperature. The mechanism that leads to the formation of this phase has been highly debated, since several mechanisms can be responsible for its formation. The most accredited hypotheses are either an electronic instability that leads to a spontaneous symmetry-breaking or a purely structural deformation appearing due to the surface-substrate interaction. The facts that the 1-up-2-down configuration with one displaced atom has a lower energy already in DFT calculations and that we do not observe a CDW at half-filling with only nearest-neighbor interaction, favor the second hypothesis.

However, the $1/r$ tail can have a noticeable effect on the CDW instability. Additionally, the local contribution Δ_l that differs from atom to atom in the 3×3-phase can act as an effective doping and can strongly affect results in that phase. To this aim, we compute the phase diagram obtained with the unit cell containing three atoms to investigate the 3×3-phase, using the tight-binding Hamiltonian introduced when discussing Fig. 7.3 in the 1-up-2-down configuration. A discussion of the CDW and superconductivity as a function of doping and temperature in a very similar model can be found there. The non-local interaction strength can be written in real space as

$$V_{\mathbf{q}} = V \sum_{j \neq 0} \frac{e^{-i\mathbf{q} \cdot \mathbf{R}_{j0}}}{|\mathbf{R}_{j0}|/a} \tag{7.3}$$

where V is the nearest-neighbor interaction strength, R_{ij} is the distance between atoms i and j. The long-range non-local interaction is computed using an Ewald-type to obtain a smooth curve in the same way as in Ref. [338]. The only complication when computing the 3×3-phase is the presence three atoms in the unit cell, instead of a single atom as for the $\sqrt{3} \times \sqrt{3}$. In this section, we are mainly interested in understanding the origin of the CDW and we can simplify our calculations by neglecting spin-orbit coupling for that phase. In the previous calculations, we showed that the effect of spin-orbit coupling in the Rashba form is to simply tilt the direction of the localized spins, inducing the formation of a spin spiral instead of the corresponding row-wise or 120°-Néel AFM structures. The charge ordering in the system is hardly affected by the inclusion of the Rashba term in

the calculations. For this reason, we slightly simplify our model for calculations in the 3×3-phase by neglecting the spin-orbit coupling.

7.3.2   Preliminary results for the phase diagram
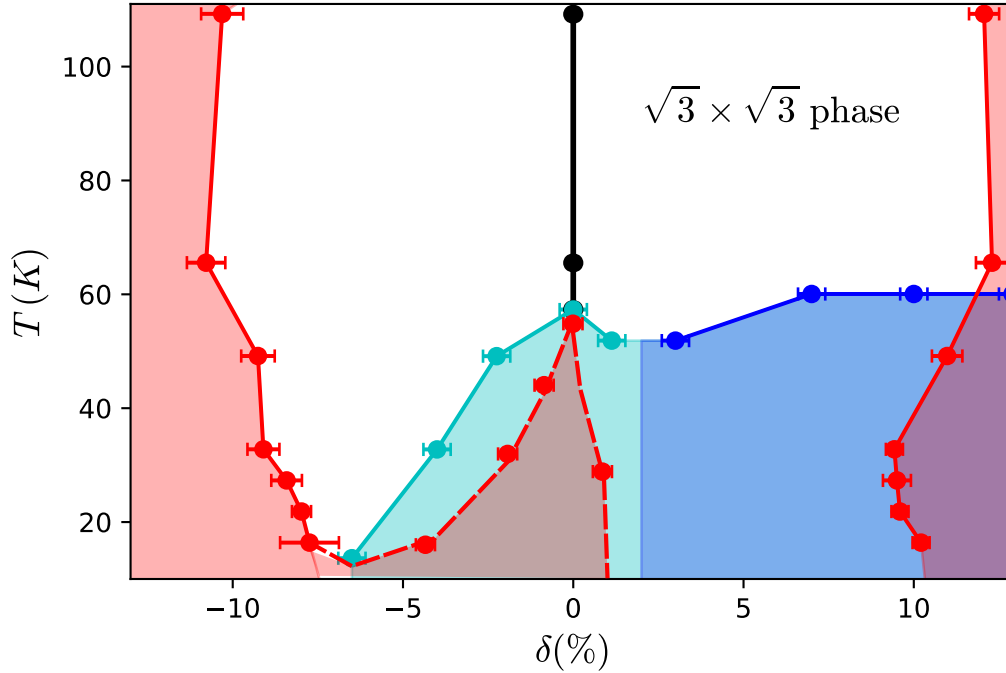
FIGURE 7.10: Phase diagram of the system as a function of the doping δ and the temperature T, obtained with single-shot D-TRILEX calculations. The ordered phases are highlighted in colors, while the white area describes the regular Fermi liquid phase. The black area represents the Mott insulating phase, the red area the CDW phase, the cyan area is the row-wise magnetic phase (or chiral M phase when spin-orbit is included) and dark blue indicates the 120°-Néel phase (or chiral K with spin-orbit).

In this subsection, we report results for the (n, T)-phase diagram in the two cases with one atom and three inequivalent atoms in the unit cell with the full potential. Since the number of calculations required to precisely draw the phase boundary is very large, we present here only preliminary results to discuss the effect of introducing the full $1/r$ tail of the Coulomb interaction. The dots connected with full lines in the plots 7.10 and 7.11 describe the lines which are known with sufficient accuracy, highlighted by the error bars. The dashed lines and the points on that line represent the phase boundary extrapolated with

only the currently available calculations and need to be refined. These last points could be even strongly modified as a result of further calculations.

The known points are located at the mean point between the last point outside and the first point within a certain phase. The error bars are related to the fact that we do calculations on a grid of chemical potentials μ and then compute the density $n = 1 + \delta$. Addtionally, the stochastic error appearing in the CT-HYB solver for the impurity affects the susceptibility (despite the relatively large number of measurements is $N_{meas} = 10^7$) and leads to a certain uncertainty even on the single point, especially at low temperature T. For this reason, an arbitrary accuracy could not be reached for all the points.
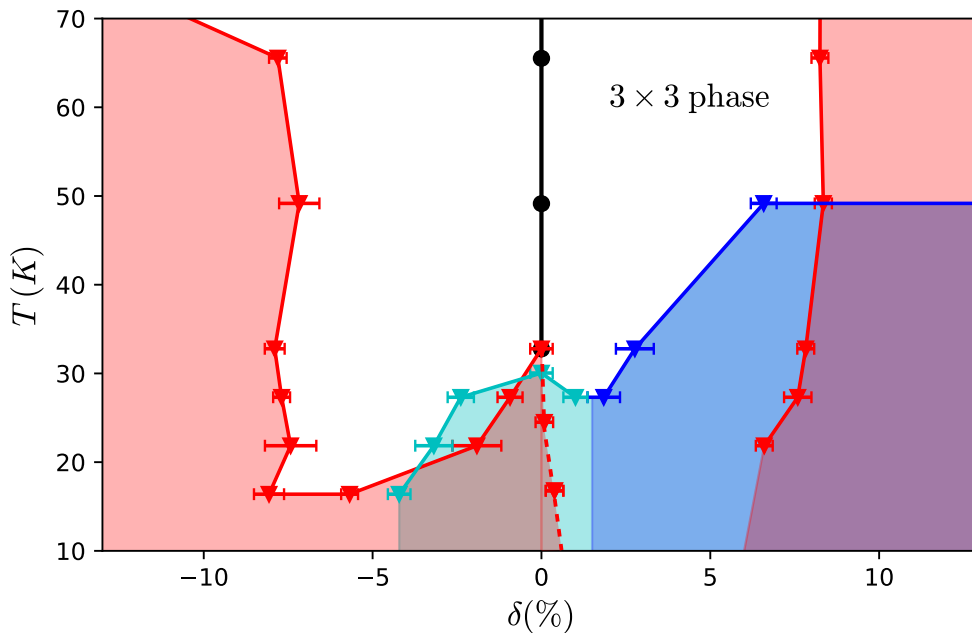
FIGURE 7.11: Phase diagram of the system as a function of the doping δ and the temperature T, obtained with single-shot D-TRILEX calculations. The ordered phases are highlighted in colors, while the white area describes the regular Fermi liquid phase. The black area represents the Mott insulating phase, the red area the CDW phase, the cyan area is the row-wise magnetic phase (or chiral M phase when spin-orbit is included) and dark blue indicates the 120°-Néel phase (or chiral K with spin-orbit).

In Fig. 7.10, we show the phase diagrams for the $\sqrt{3} \times \sqrt{3}$ configuration.

The inclusion of the realistic long-range potential has a noticeable effect on the phase boundaries compared to the nearest-neighbor interaction of Fig. 7.6. If the boundaries of the CDW at large doping are only slightly deformed, the creation of a cusp structure close

to half-filling with an asymmetric structure signals a clear difference from the previously calculated phase diagram.

In Fig. 7.11 we show the results for the 3×3 unit cell obtained using the dispersion of Fig. 7.3. At this stage, the result for the $\sqrt{3} \times \sqrt{3}$-phase does not differ qualitatively from the 3×3 reconstructed phase. The reason is that the value of the chemical potential needed to dope the system is around 200 meV both in the case of electron and hole doping. The on-site potential Δ_l with $l = 0, 1, 2$ that breaks the symmetry can be interpreted as an on-site doping that differs from site to site. However, the value of the local on-site potential is much smaller than the critical chemical potential needed to induce a non-negligible doping level in the system. As a consequence, the net result a simple lowering of the transition temperature of the SDW phase compared to the $\sqrt{3} \times \sqrt{3}$-phase.

7.3.3 Charge ordering: effect of interactions or driven by the substrate?

It is clear from the results shown in the previous sections, that they do not provide a definitive answer to the problem of the origin of charge ordering in the system. As the STM is a single-particle probe, one has to proceed with care since the observed pattern can emerge both from a dynamical transition as a consequence of a spontaneous symmetry-breaking followed by a Peierls mechanism [341] or from a structural relaxation as argued in Ref. [348]. From the STM spectrum, it appears that the material exhibits a modulation of the electron density and a pseudo-gap behavior at low temperatures. It is possible that this pseudogap is related to the CDW and to the simultaneous presence of strong magnetic fluctuations, as predicted by our calculations. However, by looking at the STM spectrum of Ref. [341], the atomic configuration is clearly that of a 1-up-2-down configuration. In our calculations, the predicted CDW has a row-wise structure at half-filling and appears at temperature of around $T = 60$ K. From our calculations, two arguments are in favor of a simple structural relaxation.

The first argument is that the structure observed in experiments does not seem to have a symmetry which is favored by a spontaneous symmetry-breaking of the potential $V_{\mathbf{q}}$ of Eq. 7.3, since that potential has a minimum at the K-point and the M-point has an energy very close to K. Additionally, the polarization operator in our calculations has its lagest absolute value close to the M and K points. This structure seem to favor either a 120°-Néel broken-symmetry phase with three inequivalent sites in the unit cell or a row-wise structure rather than a 3×3 unit cell with a single inequivalent atom.

The second argument is that interactions with an environment and phonons in real systems usually tend to reduce the temperature of the phase transition compared to theoretical

predictions. Since the measured $T_{\text{CDW}}^{\text{exp}} = 86$ K [357, 358], there should be a physical mechanism that dramatically increases the T_{CDW} in the experiments compared to the predicted one.

On the other hand, the analysis of the STM data does not provide any information on collective excitations of the system, but rather on the local density of states. The only way to determine with confidence if the origin of this transition is related to the CDW, is to use a probe which is sensitive to the symmetry-breaking. Experiments on the transition temperature seem to reproduce quite closely the model of the order-disorder phase transition suggested in Ref. [359] for a reconstruction of Sn on a germanium substrate rather than the CDW model [357]. However, the existence of a CDW at half-filling in calculations in both phases at low temperature does not allow us to completely rule out that this is the source of the phase transition.

In addition to these considerations, the other very important aspect to assess is the determination of doping. According to our calculations, it would be desirable to have a detailed control over the doping in the system, since a different doping might result in a completely different physical phase. The control over the doping of the surface states can be tricky to control and requires some fine calibration of the experimental setup of a similar system with Sn adatoms instead of Pb [339, 354]. All the experiments report some degree of doping occurring in the system, which is needed in order to have any conduction and thus to measure the STM spectrum. For instance, Ref. [341] reports the use of a $p-$doped Si substrate, while a heavily n-doped substrate was used in Ref. [342], according to its Supplemental Material. The precise estimation of the doping and the possibility to tune it would be really useful in better understanding the processes occurring in the system.

7.4   Conclusion

We performed D-TRILEX calculations for the system consisting in Pb adatoms on a Si(111) substrate, including spin-orbit coupling and non-local interactions. By including fluctuations in both charge and spin-channels, we found a rich variety of different magnetic phases in the low temperature regime by varying the doping level. Different magnetic phases appear both in the presence and without the inclusion of spin-orbit coupling, one with a typical dome structure around the half-filling and the other localized at large electronic doping. The spin-orbit coupling introduces a distortion of the spin structures that leads to non-commensurate spin spirals and is compatible with the formation of skyrmions, as highlighted in previous theoretical calculations. The effect of the spin-orbit coupling could be investigated thanks to the use of the diagrammatic D-TRILEX method and it is unlikely to be captured in cluster calculations, due to its incommensurate nature. Our findings support the idea that Pb on Si(111) has potential applications in the creation of skyrmionic lattices with different structures.

We observe the formation of a CDW at large doping levels. This occurs both for electron and hole dopings. We additionally report the CDW at half-filling if we include the full tail of the Coulomb interaction in our calculations. This preliminary result has to be analysed more in detail to reveal the precise ordering occuring in the system in that regime. Since a CDW transition takes place also at large doping, according to our calculations, it is important to determine the intrinsic doping level occurring in the system due to the use of a $p-$ or $n-$doped Si substrate. Due to the smaller transition temperature found in the preliminary results for this system compared to the experimental one, the spatial charge modulation observed in experiments seems to be imputable to the vertical displacement of the Pb atoms, induced by the substrate, rather than to the CDW.

8 Coexistence of metallic and insulating phases in a two-orbital model

The following Chapter contains the preprint **M. Vandelli** *et al., arXiv*:2204.02116 (2022). The author of this thesis contribution to this work consisted in the development of the D-TRILEX code used to obtain the results, in the collection and analysis of the results and in writing the manuscript.

In this preprint, we study a two-orbital model with crystal-field splitting on a cubic lattice and Hubbard-Kanamori interactions using D-TRILEX. We report the simultaneous presence of two different phases, a metallic and an insulating one for a large range of the Hubbard interaction U. This region of metastability is not present in DMFT.

These results show that non-local fluctuations in the system can lead to a redistribution of density between different orbitals and between above and below the Fermi energy. It is a clear demonstration that the picture provided by DMFT can change dramatically if non-local correlations are included.

These findings might appear surprising, especially in three-dimensions where DMFT is widely expected to provide a good approximation. However, we believe that we can apply D-TRILEX in this regime without incurring in any problem related to the reduced accuracy as doping is increased described in the benchmarking section. The reason is that the model chosen here as an almost empty band, so it is weakly correlated, and an other band which is almost at half-filling, where we have shown that D-TRILEX generally provides good results.

The considered model describes the low-energy physics of vanadates [38] and of fulleride molecular crystals [360–364]. Our results could explain experimental reports of phase coexistence in VO_2 thin-film samples [365, 366].

8.1   Extended regime of coexisting metallic and insulating phases in a two-orbital electronic system

Introduction

There are two main mechanisms responsible for the formation of an insulating phase in electronic materials: a gap at the Fermi energy in the non-interacting band structure and the many-body localization induced by strong electronic interactions, as for instance the Mott scenario [24, 25]. The interplay between these different mechanisms can strongly affect the degree of electronic correlations and therefore the phase diagram of the material [367]. Both these effects are especially important when a subset of doubly- or triply-degenerate localized orbitals appears in the electronic spectrum at Fermi energy. Usually, the charge distribution on neighboring atoms lifts this degeneracy, which results in a local splitting of the orbitals called crystal field splitting. Strong electronic correlations may greatly renormalize the electronic spectral distribution, thus affecting the orbital splitting [39, 368–370]. The crystal field splitting also has a strong influence on the Mott transition in several materials, as it favors orbital polarization and orbital selective phenomena [38, 371–383].

The dynamical mean field theory (DMFT) [118] is currently the most-widely used theoretical method for describing the Mott transition in realistic materials [107, 127]. For instance, this method captures the coexistence of metallic and insulating phases that accompanies the Mott transition in both, single-band [150–156] and multi-orbital [157–161] systems. However, in some cases DMFT is insufficient, because this theory accounts only for local correlation effects. Considering even short-range correlations beyond DMFT significantly modifies the coexistence region and drastically reduces the critical value of the interaction [155]. Long-range correlations can have even more dramatic consequences [171]. Therefore, an important leap towards an accurate theoretical description of correlated materials would be to understand the effect of non-local collective electronic fluctuations on the spectral function. Unfortunately, most of the available theoretical methods for multi-orbital systems are either limited to a weakly correlated regime [92, 185–188, 190, 191], or do not take into account all desired physical ingredients, such as long-range correlations [174–177] or spatial magnetic fluctuations [40, 193, 194, 196–198, 202, 204, 206, 207]. Attempts to go beyond these assumptions using diagrammatic methods lead to expensive numerical calculations [45, 47, 211–213, 332, 384, 385], while unbiased quantum Monte Carlo methods are so far limited to specific parameter regimes or symmetries due to the fermionic sign problem [179–184].

In this work, we investigate the effect of non-local correlations on the Mott transition in a two-orbital model with the crystal field splitting and the density-density approximation for the interaction. This model is relevant for investigating the low-energy physics of

some transition metal oxides [38] and of fulleride molecular crystals [360–364]. More importantly, this model is the simplest multi-orbital system, where the influence of the orbital splitting on the Mott transition was studied in details using DMFT [369]. We challenge this solution of the problem by utilizing a relatively inexpensive diagrammatic extension of DMFT [1] – the dual triply irreducible local expansion (D-TRILEX) method [48, 96, 231, 232]. This approach accounts for the effect of the non-local collective electronic fluctuations on the spectral function in a self-consistent manner [232, 233, 235]. We find that, despite the apparent simplicity, the considered model displays a non-trivial behavior around the Mott transition. In particular, considering the non-local correlations beyond DMFT reveals a broad coexistence region of meta-stable metallic and Mott insulating phases that extends from approximately the bandwidth to more than twice the bandwidth in the value of the interaction. Our results might guide the understanding of the memristive effects experimentally observed in VO_2 thin-film samples [365, 366].

Method

The Hamiltonian of the considered two-orbital model on a cubic lattice

$$H = \sum_{jj',l,\sigma} c^\dagger_{jl\sigma} \left(t^l_{jj'} + \Delta_l \, \delta_{jj'} \right) c_{j'l\sigma} + \frac{U}{2} \sum_{j,ll'} n_{jl} \, n_{jl'}$$

contains three contributions. We restrict the hopping to the nearest-neighbor lattice sites and set it to $t^l_{\langle jj' \rangle} = 1/6$ for each of the two orbitals $l \in \{1, 2\}$. Hereinafter, the energy is expressed in units of the half-bandwidth of the cubic dispersion $W/2 = 6t = 1$. The interaction U between electronic densities $n_{jl} = \sum_\sigma c^\dagger_{jl\sigma} c_{jl\sigma}$ describes both the intra- and interorbital Coulomb repulsion. Calculations are performed at quarter-filling, which corresponds to the average density of $\langle n \rangle = 1$ electron per two orbitals. In order to induce an orbital polarization $\delta n = (\langle n_2 \rangle - \langle n_1 \rangle)/\langle n \rangle$, we take a relatively large value for the crystal field splitting $\Delta = 2\Delta_1 = -2\Delta_2 = 0.3$. This case was studied in details in Ref. [369] using DMFT. It was demonstrated, that local electronic correlations enlarge the orbital splitting, resulting in a high degree of orbital polarization. Consequently, the single electron mostly populates the lower orbital ($l = 2$) that undergoes the Mott transition at a critical value of the electronic interaction. A similar interplay between the orbital polarization and Mott physics is also found in actual materials such as V_2O_3 [38] and $SrVO_3$ [203, 386, 387], where it is important for the Mott transition.

In order to investigate how non-local correlations affect the DMFT scenario of the Mott transition, we employ the D-TRILEX method [96, 231, 232], where collective electronic fluctuations are treated diagrammatically beyond DMFT. This method was derived as an approximation to the dual boson theory [224–230, 264–266], one of the most commonly

---

[1]For a review on diagrammatic extensions of DMFT see [208].

used diagrammatic extensions of DMFT, cf. [208–211, 213, 215–219, 222, 223, 236, 258, 388, 389]. The D-TRILEX method stands out for its lowered complexity, which allows one to address multi-band problems [48, 96, 235], cf. [211, 212], and its capability of correctly reproducing the results of more elaborate theories. The reduction of the critical interaction for the Mott transition compared to DMFT [231] is very similar to cluster DMFT [155]. Additionally, it shows a precise agreement with exact benchmarks for some single- and multi-band systems [96, 232].

If the system exhibits strong magnetic fluctuations, as frequently happens at half-filling, the Mott transition usually lies inside the antiferromagnetic (AFM) phase. In this case, addressing the Mott transition requires to perform calculations in a symmetry broken phase, which is problematic. Going away from half-filling suppresses the magnetic fluctuations and allows one to access the Mott transition from the paramagnetic phase. According to our calculations, the highest critical temperature for the Néel transition for the considered quarter-filled model lies below $T = 0.06$. For this reason, we set the inverse temperature to $T^{-1} = 15$, which ensures that the system is located outside the AFM phase but close to its boundary to observe strong magnetic fluctuations. We perform DMFT calculations using the w2dynamics package [274]. The D-TRILEX solution is based on the numerical implementation described in Ref. [96]. The local density of states (DOS) is obtained from the corresponding local Green's functions via analytical continuation using the ana_cont package [22].
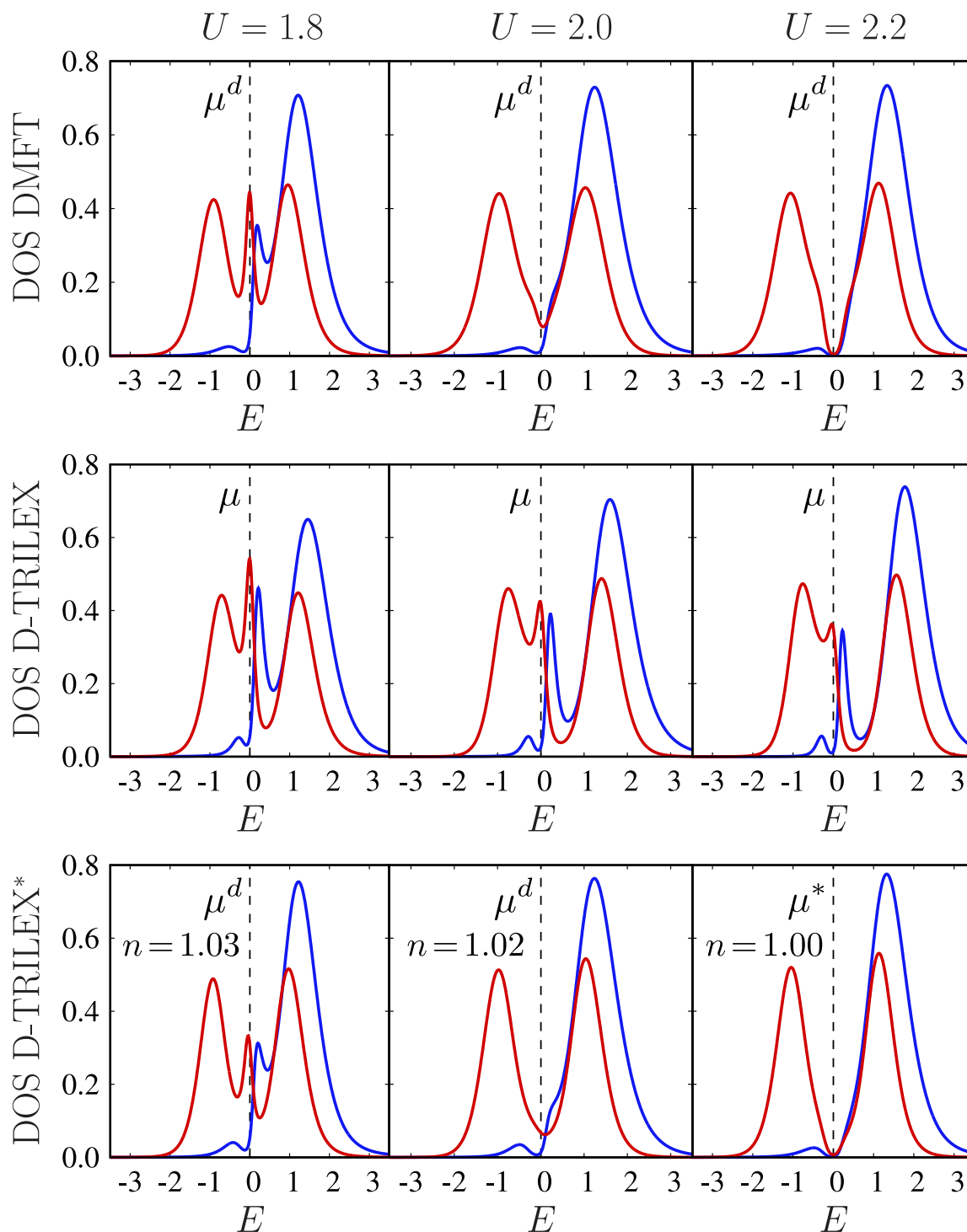
FIGURE 8.1: DOS for the upper ($l = 1$, blue line) and lower ($l = 2$, red line) orbitals calculated for different interactions $U = 1.8$ (left column), $U = 2.0$ (middle column), and $U = 2.2$ (right column). Top row: DMFT solution at quarter-filling that corresponds to the chemical potential μ^d. Middle row: quarter-filled metallic D-TRILEX solution for the chemical potential μ. Bottom row: a further D-TRILEX* calculation based on the DMFT solution. Calculations for $U = 1.8$ and $U = 2.0$ are performed for μ^d. The resulting $\langle n \rangle > 1$ is specified in panels. At $U = 2.2$ the quarter-filled D-TRILEX* solution appears at $\mu^* \simeq \mu^d$ and corresponds to the Mott insulating state.

Results

To illustrate the effect of non-local correlations on the Mott transition, we compare the DOS predicted by DMFT and D-TRILEX methods. The result of these calculations is shown in Fig. 8.1 for three different values of the interaction $U = 1.8$, $U = 2.0$, and $U = 2.2$. First, let us focus on the quarter-filled calculations presented in the two upper rows of this figure. We find that the results of the DMFT and D-TRILEX methods are different already at $U = 1.8$. In both cases, the DOS is metallic. The lower orbital ($l = 2$, red line) displays a three-peak structure consisting of the quasi-particle peak at Fermi energy $E = 0$ and two side peaks that correspond to lower and upper Hubbard bands (LHB and UHB). The upper orbital ($l = 1$, blue line) also exhibits the quasi-particle peak in the DOS that appears close to the Fermi energy at $E \simeq \Delta$. However, the three-peak structure predicted by DMFT possesses a high degree of electron-hole symmetry. Instead, the DOS of obtained for the same orbital ($l = 1$) using the D-TRILEX approach resembles the DOS of a hole-doped Mott insulator with the quasi-particle peak being shifted closer to the LHB [118]. The quasi-particle peaks in the DOS of DMFT vanish simultaneously between $U = 1.8$ and $U = 2.0$, which signals the tendency towards a Mott insulating state in a multi-orbital system at finite temperature. A further increase of the interaction decreases the electronic density at Fermi energy $A(E = 0)$. The latter reaches zero at $U_c^* \simeq 2.2$ (blue line in Fig. 8.2), and the DMFT solution enters the Mott insulating phase. On the contrary, the D-TRILEX solution remains metallic for the discussed values of the interaction (middle row in Fig. 8.1). Thus, even at U_c^* it reveals pronounced quasi-particle peaks in the DOS for both orbitals. Fig. 8.2 shows that $A(E = 0)$ in the metallic D-TRILEX solution also decreases upon increasing the interaction. However, this solution turns into a Mott insulator only at a very strong critical interaction $U_c \simeq 4.5$, which is larger than twice the bandwidth. This result seems surprising, since in the single-orbital case the non-local correlations lead to a more insulating electronic behavior [155], as correctly captured by the D-TRILEX method [231].

To explain the observed effect, we note that quarter-filling in DMFT and D-TRILEX corresponds to different values of the chemical potential. The left panel of Fig. 8.3 shows that at $U \geq 1.5$ the chemical potential μ of D-TRILEX (red dots) significantly deviates from μ^d of DMFT (blue dots), and this difference increases with increasing the interaction. We point out that D-TRILEX calculations are based on the DMFT solution of the local impurity problem that plays a role of the reference system [231, 232]. We find that the quarter-filled metallic D-TRILEX solution originates from the metallic reference system that has smaller average density. Fig. 8.4 shows that due to $\langle n \rangle < 1$ the reference system (dashed lines) remains metallic even at U_c^*. At the same time, the DOS predicted by D-TRILEX (solid lines) is not dramatically different from the one of the reference system. This fact suggests that for a given value of the chemical potential the effect of non-local collective electronic fluctuations in the metallic regime consists in moving the spectral
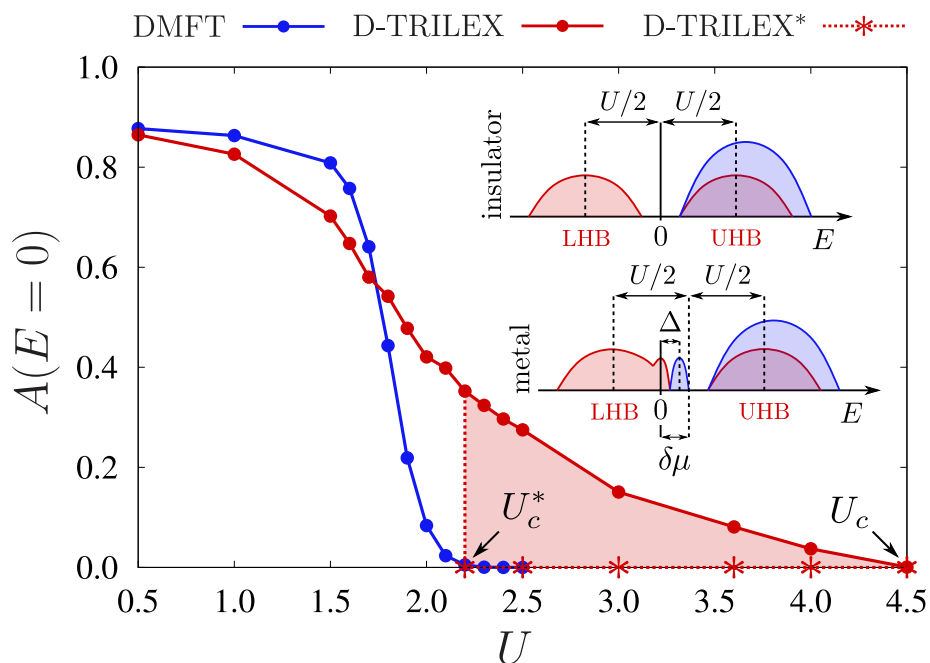
FIGURE 8.2: Electronic density at Fermi energy $A(E = 0)$ for the lower orbital ($l = 2$) as a function of the interaction U. The result is obtained from DMFT (blue dots), metallic D-TRILEX (red dots), and insulating D-TRILEX* (red asterisks) solutions. The red shaded area highlights the simultaneous existence of the metallic and the Mott insulating solutions. The inset sketches the difference in the DOS between the insulating (top) and metallic (bottom) D-TRILEX solutions. In the insulating case, the Fermi energy lies between the LHB and UHB that are split approximately by U. In the metallic case, the difference in the chemical potential $\delta\mu = \mu^* - \mu$ brings the upper part of the LHB to the Fermi energy, which results in the formation of the quasi-particle peak at $E = 0$. The splitting between the quasi-particle peaks coincides with the value of the crystal field splitting $\simeq \Delta$.

weight from above to below the Fermi energy, which brings the filling of the system to $\langle n \rangle = 1$.

To confirm this statement, we perform D-TRILEX calculations for the chemical potential μ^d of the quarter-filled DMFT solution. The corresponding result is shown in the bottom row of Fig. 8.1 and is referred to as the D-TRILEX* calculation in order not to confuse it with the metallic solution. We observe that the obtained DOS is again practically identical to the one of DMFT (bottom *vs.* top row in Fig. 8.1). However, the D-TRILEX* calculations performed in the regime $1.0 \lesssim U < 2.2$, where DMFT solution is metallic, correspond to $\langle n \rangle > 1$. Moreover, no quarter-filled D-TRILEX* solution is found near μ^d in this regime of interactions. This fact supports our previous finding that in the metallic regime non-local correlations increase the average density of the considered system.
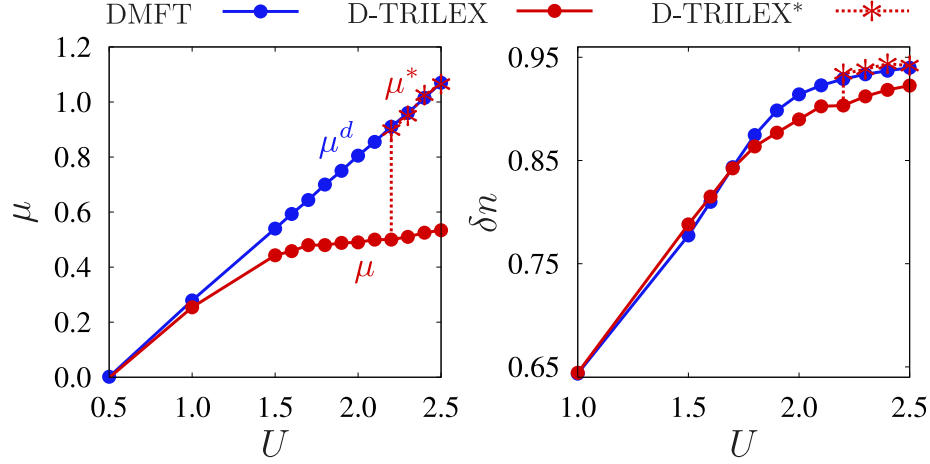
FIGURE 8.3: Chemical potential (left panel) and orbital polarization (right panel) for the quarter-filled DMFT (blue dots), metallic D-TRILEX (red dots), and insulating D-TRILEX (red asterisks) solutions. The result is obtained for different values of the interaction U. Chemical potentials for the insulating D-TRILEX (μ^*) and DMFT (μ^d) solutions nearly coincide. For $1.0 \lesssim U < 2.2$ no quarter-filled D-TRILEX solution exists near μ^d. The chemical potential μ for the metallic D-TRILEX solution strongly deviates from μ^d at $U \geq 1.5$.

This physical picture changes when the DMFT solution becomes Mott insulating. We find that the corresponding D-TRILEX* solution undergoes the Mott transition at the same critical interaction U_c^* as in DMFT (bottom right panel of Fig. 8.1). Moreover, at $U \geq U_c^*$ the average density for the D-TRILEX* solution becomes $\langle n \rangle = 1$ for $\mu^* \simeq \mu^d$ (bottom left panel of Fig. 8.1). The right panel of Fig. 8.3 shows that the insulating DMFT and D-TRILEX* solutions are almost fully polarized and have approximately the same value of δn, which results in electron-hole symmetric DOS for the lower orbital (top and bottom left panels of Fig. 8.3). Consequently, the upper orbital becomes nearly unoccupied and thus cannot strongly interact with the lower one. Therefore, no transfer of the spectral weight between the orbitals by means of the non-local fluctuations occurs in the insulating regime. Remarkably, the metallic D-TRILEX solution has a lower δn compared to DMFT.

At $U \geq U_c^*$ the D-TRILEX* solution remains quarter-filled and Mott insulating, which is confirmed by the zero electronic density at Fermi energy (red asterisks in Fig. 8.2). Therefore, both, the DMFT and the D-TRILEX methods predict the Mott transition for the considered system at the same value of the critical interaction U_c^*. However, including non-local collective electronic fluctuations beyond DMFT allows one to additionally capture the metallic solution that coexists with the Mott insulating one up to the second critical interaction U_c. For $U > U_c$ any value of the chemical potential inside the Mott gap gives the same average density, and the two solutions corresponding to μ and μ^* can be considered equivalent. A more detailed discussion of the hysteresis curve appearing in

Fig. 8.3 can be found in Supplemental Material (SM) [390].
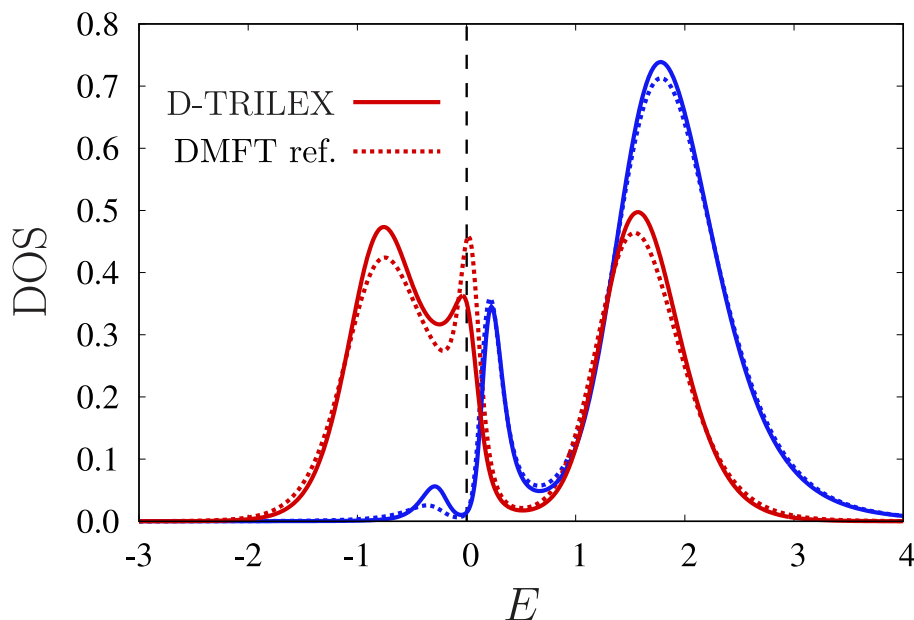
FIGURE 8.4: DOS for the metallic D-TRILEX solution (solid lines) and its DMFT reference system (dashed lines) obtained for the same value of the chemical potential μ at the critical interaction U_c^*. The reference system is a doped Mott insulator with $\langle n \rangle = 0.96$.

Coexisting solutions with the same average density but different values of the chemical potential have also been found in the DMFT solution of the Hubbard-Kanamori model for small doping around half-filling [391–395], and for different parameters using a strong-coupling expansion [393]. Since the quarter-filled model considered in our work displays a strong orbital polarization, it can be expected that taking into account the Hund's rule coupling J, which is present in the Kanamori parametrization of the electronic interaction [107, 396], should not qualitatively change the observed results. To confirm this point, we perform calculations for the case of $J = U/6$ and find that the meta-stability discussed above survives also in this case, as shown in SM [390].

Conclusion

We investigated the effect of non-local collective electronic fluctuations on the Mott transition in a two-orbital quarter-filled model with density-density interaction by comparing the results of the D-TRILEX and DMFT methods. At the considered temperature, the DMFT solution of the problem remains metallic below the critical interaction $U_c^* = 2.2$,

and at this value of the interaction undergoes the Mott transition. We find that the inclusion of non-local correlations by means of the D-TRILEX approach stabilizes the metallic phase up to the very large critical interaction $U_c = 4.5$. The D-TRILEX method also captures the appearance of Mott insulating phase at U_c^* as a second meta-stable solution. This leads to a remarkably broad coexistence region between the metallic and the Mott insulating phases that exist at the same filling, but with different values of the chemical potential between the U_c^* and the U_c critical interactions. Our results show, that for a simple two-orbital model, DMFT cannot correctly interpolate between the moderately- and strongly-interacting regimes, in analogy with the single-orbital case. This fact brings further evidence that non-local correlations may lead to non-trivial effects due to the presence of additional channels for collective electronic fluctuations also in multi-orbital systems.

8.2   Supplemental material of the previous pre-print

8.2.1   Charge compressibility and meta-stability

The meta-stability of the two solutions is signalled by the appearance of two different values of the chemical potential μ and μ^* leading to the same average density $\langle n \rangle$, as demonstrated in the left panel of Fig. 3 in the main text. As shown there, the presence of two meta-stable solutions manifest itself with the appearance of an hysteresis loop. The branch of the hysteresis chosen by the system depends on whether the corresponding reference system is metallic or Mott insulating. As a matter of fact, if we follow the $\mu(U)$ curve that gives $\langle n \rangle = 1$ in the weak coupling regime (red dots), we obtain the metallic solution until it continuously turns into an insulating phase at U_c. Above this threshold, any value of the chemical potential inside the Mott gap gives the same average density, and the two solutions corresponding to μ and μ^* can be considered equivalent from there on. On the other hand, if we start from the chemical potential μ^* that corresponds to the insulating phase and decrease the interaction following the condition $\langle n \rangle = 1$, we obtain the insulating solution (red asterisks). The latter exists until the critical interaction U_c^* below which no solution for $\mu^* \simeq \mu^d$ is available at quarter-filling. This behavior means that the function $\langle n \rangle(\mu)$ is not monotonic and exhibits a region of negative charge compressibility $\kappa = \frac{1}{\langle n \rangle^2} \frac{d \langle n \rangle}{d\mu}$. According to our calculations, the metallic and insulating D-TRILEX solutions are both characterized by $\kappa > 0$, hence they are thermodynamically meta-stable. Since the density is the same for both phases, they have to be separated by a region of chemical potentials associated with a negative charge compressibility.

From the perspective of applications, this region of negative charge compressibility between the two meta-stable solutions could forbid the spontaneous switch between the two solutions. In this case, the application of a static electric field should be sufficient to drive the transition between the metallic and Mott insulating phases, as this perturbation would

effectively change the chemical potential from μ to μ^* or *vice versa*. A similar switching between two meta-stable phases as a function of an electric field was investigated in Ref. [397], where a similar regime of parameters with coexisting metallic and Mott insulating meta-stable solutions was reported. One can speculate that the observed presence of two meta-stable phases could be exploited in the realization of Mott-based electronic switches or transistors. Indeed, the experimental realization of Mott field effect transistors (MottFET) was shown to be practically viable [386, 398, 399]. The simultaneous presence of metallic and Mott insulating states could be detected experimentally, for example by measuring dielectric properties of the system [400].
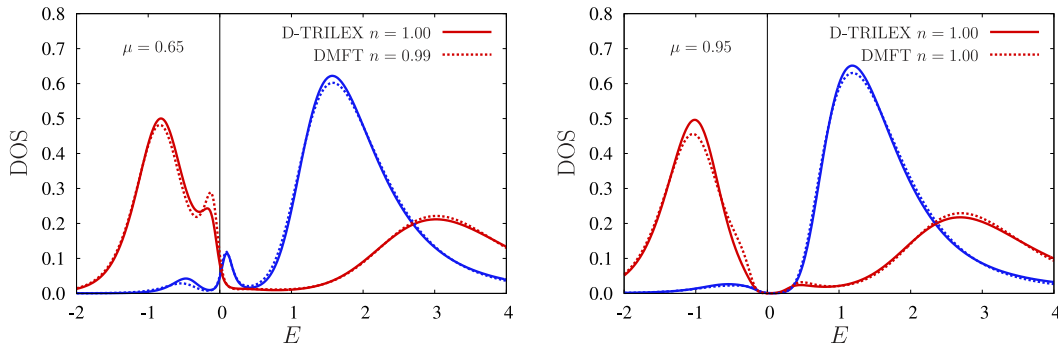
FIGURE 8.5: DOS for the upper ($l = 1$, blue line) and lower ($l = 2$, red line) orbitals obtained for $U = 4.2$ and $J = U/6$ using D-TRILEX (solid lines) and DMFT (dashed lines) methods. Left panel corresponds to the chemical potential $\mu = 0.65$ at which the D-TRILEX solution is metallic and quarter-filled ($\langle n \rangle = 1.00$). Right panel corresponds to the chemical potential $\mu = 0.95$ at which both, D-TRILEX and DMFT solutions are Mott insulating and quarter-filled.

8.2.2 Calculations for a non-zero Hund's coupling

The quarter-filled ($\langle n \rangle = 1$ electrons per lattice site) two-orbital model considered in the main text has a relatively big value of the crystal-field splitting. This leads to a large orbital polarization that appears already in the metallic regime before the system undergoes the Mott transition. The latter means that the single electron at each lattice site mostly populates the lower orbital ($l = 2$), and the upper orbital ($l = 1$) stays nearly unoccupied. In this case, it can be expected that including the Hund's rule coupling J in the electronic interaction should not qualitatively change the physical effect observed in the absence of J. To confirm this point, we perform calculations for the local density of states (DOS) for two different interaction strength $U = 2.4$ (Fig. 8.6) and $U = 4.2$ (Fig. 8.5) for a non-zero value of the Hund's coupling $J = U/6$.
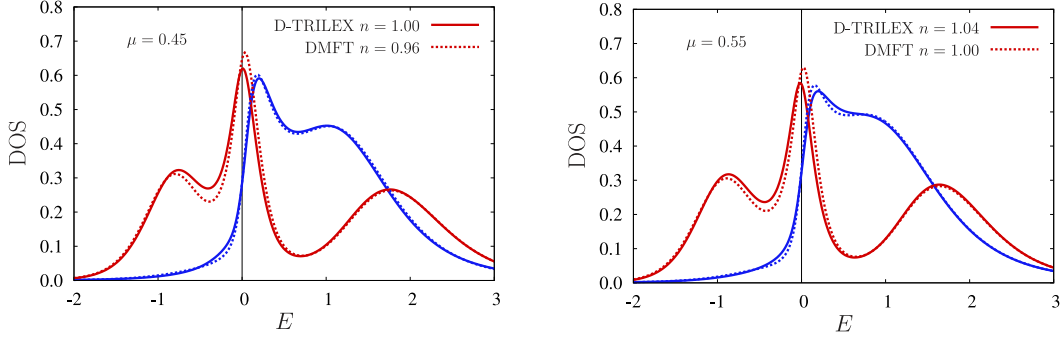
FIGURE 8.6: DOS for the upper ($l = 1$, blue line) and lower ($l = 2$, red line) orbitals obtained for $U = 2.4$ and $J = U/6$ using D-TRILEX (solid lines) and DMFT (dashed lines) methods. Left panel corresponds to the chemical potential $\mu = 0.45$ at which the D-TRILEX solution is quarter-filled ($\langle n \rangle = 1.00$). Right panel corresponds to the chemical potential $\mu = 0.55$ of the quarter-filled DMFT solution.

Due to the effect of J, the system is still metallic at $U = 2.4$ in contrast to the $J = 0$ case, and we find a single value of the chemical potential μ for which the D-TRILEX solution has an average density $\langle n \rangle = 1$. As in the case of $J = 0$ discussed in the main text, the quarter filling in DMFT and D-TRILEX methods corresponds to different values of the chemical potential. At $\mu = 0.45$ (left panel in Fig. 8.6), when the D-TRILEX solution is quarter-filled, the average density in DMFT is $\langle n \rangle = 0.96$ electrons per lattice site. The chemical potential $\mu = 0.55$ (right panel in Fig. 8.6) corresponds to the quarter-filled DMFT solution, while the average density in D-TRILEX is $\langle n \rangle = 1.04$. We find that both methods predict a rather similar DOS for each of the two values of the chemical potential. However, the average density of D-TRILEX is always larger than in DMFT. This observation is in agreement with the results reported in the main text for the case of $J = 0$ and illustrates that in the metallic regime the role of the non-local fluctuations in the considered system consists in redistributing the spectral weight between the orbitals.

At $U = 4.2$ the quarter-filled DMFT solution that corresponds to $\mu = 0.95$ lies in the Mott insulating regime (right panel in Fig. 8.5). For this value of the chemical potential the D-TRILEX solution is also quarter-filled and Mott insulating, because no spectral weight redistribution induced by the non-local fluctuations occurs in the insulating regime. Finally, at smaller value of the chemical potential $\mu = 0.65$ (left panel in Fig. 8.5) the D-TRILEX reveals the second quarter-filled solution, which is metallic. The DOS predicted by DMFT for this value of the chemical potential is again similar to the one of D-TRILEX, but the DMFT solution does not reside at quarter filling and corresponds to $\langle n \rangle = 0.99$. Therefore, we find that when the DMFT solution becomes Mott insulating D-TRILEX reveals two different quarter-filled solutions even for the case of a non-zero value of the Hund's coupling.

9 General conclusions

In this thesis, we have shown that dual theories represent a very promising tool for the description of multi-orbital and multi-site problems. Additionally, we argued that their use is by far not limited to the case of single-orbital (extended) Hubbard model to which they were mostly applied before.

An important aspect of this thesis was to highlight the connection of dual theories with quantum embedding methods. We can employ the intrinsically multi-scale nature of dual theories to split an otherwise intractable problem with strong electronic correlations into a relatively small impurity problem, that can be solved using exact methods, and a weakly correlated remaining system. This strongly reduces the size of the effective system to be solved, correspondingly reducing the computational cost of the simulations. Interactions among the collection of strongly interacting impurities are mediated by the weakly correlated system, in a way similar to the strong coupling perturbation theory, but with the advantage that dual methods return reliable results also in the weak and intermediate coupling regimes.

The multi-band formulation of the problem is crucial in drawing this connection, as the usual application of the dual theories only to the Hubbard model in different flavors could be responsible for the wrong assumption that dual theories can be applied only to a small class of model systems. This is certainly not the case, as we prove in this thesis. The use of multi-orbital or multi-site reference problems has been proven a viable route and it paves the way to the possibility of using cluster reference systems, that could even describe broken-symmetry phases. In our opinion, this is a fascinating development of dual theories that cold be soon combined with quantum Monte Carlo methods or quantum hardware to include long range interactions and correlations that exceed the size of the cluster used in these methods.

We would like to stress once again that the work of code development and implementation was a crucial aspect of this thesis. Arguments about the applicability of the dual techniques to many-orbital systems would not have been as convincing without the working python implementation used in the applications presented here.

Analogously, advancing beyond the current standard approximation based on the single-orbital ladder dual boson approximation was very important to extend our understanding of the approximations involved in the dual techniques. As a matter of fact, an equally important part of this work was devoted to the implementation of the DiagMC@DB starting

point. Even though this method has not shown any significant advantage in the application to physically relevant systems compared to previous approximations, it has proven a very valuable tool for understanding the limits of applicability of dual theories as well as for benchmarking approximations.

Another important part of this work has been devoted to finding and understanding the limitations of the D-TRILEX method. The final result is that D-TRILEX performs very well in the regime where a single main channel of fluctuations or few non-interfering channels are present. This is the case, for example, of the (extended) Hubbard model at half-filling and it is very likely to be the case in most multi-orbital or multi-band systems, where correlations tend to be weaker than in a single-band system. When all the sorts of channels of fluctuations, including transverse ones, are important, the theory starts to show the first cracks when compared with more advanced methods. This happens mainly in the case of large doping in the system, and it is certainly something that has to be investigated in more detail in the future.

Additionally, even in cases where the method does not produce very accurate results, it might be possible to modify the reference impurity problem to improve the results.

The use of cluster starting points could allow to study broken-symmetry phases and superconductive states directly by inducing the symmetry breaking at the cluster level, even though this is still under debate and it is a very interesting direction for further research.

A final comment concerns the applications of the D-TRILEX theory presented here. Both the main applications, namely the study of the Pb adatoms on Si(111) and the two-orbital model, resulted in exciting results that hint towards physics well beyond the standard approximations, but it is currently not so clear what their implications are from the point of view of real materials.

Access to new experimental data based on the current theoretical developments is crucial in understanding whether the new findings can explain the physics observed in those systems, at least partially. Certainly, some observations seem to confirm the picture that we have outlined for the Pb:Si(111) system, where our results suggest a CDW related to a surface-substrate interaction rather than to a dynamical symmetry breaking induced by correlations. We propose that measuring the density and magnetic susceptibility of this system could give a definitive answer to this intricate problem.

Bibliography

[1] C. Ahn, A. Cavalleri, A. Georges, S. Ismail-Beigi, A. J. Millis, and J.-M. Triscone. "Designing and controlling the properties of transition metal oxide quantum materials". *Nature Materials* 20.11 (Nov. 1, 2021), pp. 1462–1468. ISSN: 1476-4660. DOI: 10.1038/s41563-021-00989-2. URL: https://doi.org/10.1038/s41563-021-00989-2.

[2] P. A. M. Dirac and R. H. Fowler. "Quantum mechanics of many-electron systems". *Proceedings of the Royal Society of London. Series A, Containing Papers of a Mathematical and Physical Character* 123.792 (1929), pp. 714–733. DOI: 10.1098/rspa.1929.0094.

[3] E. Dagotto. "Complexity in Strongly Correlated Electronic Systems". *Science* 309.5732 (2005), pp. 257–262. DOI: 10.1126/science.1107559. URL: https://www.science.org/doi/abs/10.1126/science.1107559.

[4] M. Troyer and U.-J. Wiese. "Computational Complexity and Fundamental Limitations to Fermionic Quantum Monte Carlo Simulations". *Phys. Rev. Lett.* 94 (17 May 2005), p. 170201. DOI: 10.1103/PhysRevLett.94.170201. URL: https://link.aps.org/doi/10.1103/PhysRevLett.94.170201.

[5] R. P. Feynman. "Simulating physics with computers". *International Journal of Theoretical Physics* 21.6 (June 1982), pp. 467–488. ISSN: 1572-9575. DOI: 10.1007/BF02650179. URL: https://doi.org/10.1007/BF02650179.

[6] D. Wecker, M. B. Hastings, N. Wiebe, B. K. Clark, C. Nayak, and M. Troyer. "Solving strongly correlated electron models on a quantum computer". *Phys. Rev. A* 92 (6 Dec. 2015), p. 062318. DOI: 10.1103/PhysRevA.92.062318. URL: https://link.aps.org/doi/10.1103/PhysRevA.92.062318.

[7] B. Bauer, D. Wecker, A. J. Millis, M. B. Hastings, and M. Troyer. "Hybrid Quantum-Classical Approach to Correlated Materials". *Phys. Rev. X* 6 (3 Sept. 2016), p. 031045. DOI: 10.1103/PhysRevX.6.031045. URL: https://link.aps.org/doi/10.1103/PhysRevX.6.031045.

[8] J. M. Leinaas and J. Myrheim. "On the theory of identical particles". *Il Nuovo Cimento B (1971-1996)* 37.1 (Jan. 1977), pp. 1–23. ISSN: 1826-9877. DOI: 10.1007/BF02727953. URL: https://doi.org/10.1007/BF02727953.

[9] G. Moore and N. Read. "Nonabelions in the fractional quantum hall effect". *Nuclear Physics B* 360.2 (1991), pp. 362–396. ISSN: 0550-3213. DOI: https://doi.org/10.1016/0550-3213(91)90407-O. URL: https://www.sciencedirect.com/science/article/pii/055032139190407O.

[10] F. Wilczek. "Quantum Mechanics of Fractional-Spin Particles". *Phys. Rev. Lett.* 49 (14 Oct. 1982), pp. 957–959. DOI: 10.1103/PhysRevLett.49.957. URL: https://link.aps.org/doi/10.1103/PhysRevLett.49.957.

[11] C. Nayak, S. H. Simon, A. Stern, M. Freedman, and S. Das Sarma. "Non-Abelian anyons and topological quantum computation". *Rev. Mod. Phys.* 80 (3 Sept. 2008), pp. 1083–1159. DOI: 10.1103/RevModPhys.80.1083. URL: https://link.aps.org/doi/10.1103/RevModPhys.80.1083.

[12] G. D. Mahan. *Many-Particle Physics*. Springer US, 2000. DOI: 10.1007/978-1-4757-5714-9. URL: https://doi.org/10.1007/978-1-4757-5714-9.

[13] A. Altland and B. D. Simons. *Condensed matter field theory*. Cambridge University Press, 2010.

[14] E. Noether. "Invariant variation problems". *Transport Theory and Statistical Physics* 1.3 (1971), pp. 186–207. DOI: 10.1080/00411457108231446. URL: https://doi.org/10.1080/00411457108231446.

[15] A. A. Abrikosov, I. Dzyaloshinskii, L. P. Gorkov, and R. A. Silverman. *Methods of quantum field theory in statistical physics*. New York, NY: Dover, 1975. URL: https://cds.cern.ch/record/107441.

[16] A. Kamenev. *Field Theory of Non-Equilibrium Systems*. Cambridge University Press, 2011. DOI: 10.1017/CBO9781139003667.

[17] J. A. Sobota, Y. He, and Z.-X. Shen. "Angle-resolved photoemission studies of quantum materials". *Rev. Mod. Phys.* 93 (2 May 2021), p. 025006. DOI: 10.1103/RevModPhys.93.025006. URL: https://link.aps.org/doi/10.1103/RevModPhys.93.025006.

[18] T. Ayral. "Nonlocal Coulomb Interactions and Electronic Correlations: Novel Many-Body Approaches". Theses. Ecole Polytechnique, Sept. 2015. URL: https://hal.archives-ouvertes.fr/tel-01247625.

[19] M. Jarrell and J. Gubernatis. "Bayesian inference and the analytic continuation of imaginary-time quantum Monte Carlo data". *Physics Reports* 269.3 (1996), pp. 133–195. ISSN: 0370-1573. DOI: https://doi.org/10.1016/0370-1573(95)00074-7. URL: https://www.sciencedirect.com/science/article/pii/0370157395000747.

[20] O. Goulko, A. S. Mishchenko, L. Pollet, N. Prokof'ev, and B. Svistunov. "Numerical analytic continuation: Answers to well-posed questions". *Phys. Rev. B* 95 (1 Jan. 2017), p. 014102. DOI: 10.1103/PhysRevB.95.014102. URL: https://link.aps.org/doi/10.1103/PhysRevB.95.014102.

[21] I. Krivenko and M. Harland. "TRIQS/SOM: Implementation of the stochastic optimization method for analytic continuation". *Computer Physics Communications* 239 (2019), pp. 166–183. ISSN: 0010-4655. DOI: https://doi.org/10.1016/j.cpc.2019.01.021. URL: https://www.sciencedirect.com/science/article/pii/S0010465519300402.

[22] J. Kaufmann and K. Held. "ana_cont: Python package for analytic continuation". *arXiv* (2021). DOI: 10.48550/ARXIV.2105.11211. URL: https://arxiv.org/abs/2105.11211.

[23] J. Schwinger. "The Theory of Quantized Fields. V". *Phys. Rev.* 93 (3 Feb. 1954), pp. 615–628. DOI: 10.1103/PhysRev.93.615. URL: https://link.aps.org/doi/10.1103/PhysRev.93.615.

[24] N. F. Mott. *Metal-insulator transitions*. London: Taylor & Francis, 1974.

[25] M. Imada, A. Fujimori, and Y. Tokura. "Metal-insulator transitions". *Rev. Mod. Phys.* 70 (4 Oct. 1998), pp. 1039–1263. DOI: 10.1103/RevModPhys.70.1039. URL: https://link.aps.org/doi/10.1103/RevModPhys.70.1039.

[26] J. C. Slater. "Magnetic Effects and the Hartree-Fock Equation". *Phys. Rev.* 82 (4 May 1951), pp. 538–541. DOI: 10.1103/PhysRev.82.538. URL: https://link.aps.org/doi/10.1103/PhysRev.82.538.

[27] M. Gell-Mann and F. Low. "Bound States in Quantum Field Theory". *Phys. Rev.* 84 (2 Oct. 1951), pp. 350–354. DOI: 10.1103/PhysRev.84.350. URL: https://link.aps.org/doi/10.1103/PhysRev.84.350.

[28] Y.M. Vilk and A.-M.S. Tremblay. "Non-Perturbative Many-Body Approach to the Hubbard Model and Single-Particle Pseudogap". *J. Phys. I France* 7.11 (1997), pp. 1309–1368. DOI: 10.1051/jp1:1997135. URL: http://dx.doi.org/10.1051/jp1:1997135.

[29] A.-M. S. Tremblay, B. Kyung, and D. Sénéchal. "Pseudogap and high-temperature superconductivity from weak to strong coupling. Towards a quantitative theory (Review Article)". *Low Temperature Physics* 32.4 (2006), pp. 424–451. DOI: 10.1063/1.2199446. URL: https://doi.org/10.1063/1.2199446.

[30] O. Gunnarsson, T. Schäfer, J. P. F. LeBlanc, E. Gull, J. Merino, G. Sangiovanni, G. Rohringer, and A. Toschi. "Fluctuation Diagnostics of the Electron Self-Energy: Origin of the Pseudogap Physics". *Phys. Rev. Lett.* 114 (23 June 2015), p. 236402. DOI: 10.1103/PhysRevLett.114.236402. URL: https://link.aps.org/doi/10.1103/PhysRevLett.114.236402.

[31] P. W. Anderson. "Is There Glue in Cuprate Superconductors?" *Science* 316.5832 (2007), pp. 1705–1707. DOI: 10.1126/science.1140970. URL: https://www.science.org/doi/abs/10.1126/science.1140970.

[32] E. Dagotto. "Correlated electrons in high-temperature superconductors". *Rev. Mod. Phys.* 66 (3 July 1994), pp. 763–840. DOI: 10.1103/RevModPhys.66.763. URL: https://link.aps.org/doi/10.1103/RevModPhys.66.763.

[33] D. J. Scalapino. "A common thread: The pairing interaction for unconventional superconductors". *Rev. Mod. Phys.* 84 (4 Oct. 2012), pp. 1383–1417. DOI: 10.1103/RevModPhys.84.1383. URL: https://link.aps.org/doi/10.1103/RevModPhys.84.1383.

[34] F. C. Zhang and T. M. Rice. "Effective Hamiltonian for the superconducting Cu oxides". *Phys. Rev. B* 37 (7 Mar. 1988), pp. 3759–3761. DOI: 10.1103/PhysRevB.37.3759. URL: https://link.aps.org/doi/10.1103/PhysRevB.37.3759.

[35] P. A. Lee, N. Nagaosa, and X.-G. Wen. "Doping a Mott insulator: Physics of high-temperature superconductivity". *Rev. Mod. Phys.* 78 (1 Jan. 2006), pp. 17–85. DOI: 10.1103/RevModPhys.78.17. URL: https://link.aps.org/doi/10.1103/RevModPhys.78.17.

[36] O. K. Andersen, A. I. Liechtenstein, O. Jepsen, and F. Paulsen. "LDA energy bands, low-energy hamiltonians, t', t'', $t_\perp(k)$, and $J_\perp$". *Journal of Physics and Chemistry of Solids* 56.12 (1995). Proceedings of the Conference on Spectroscopies in Novel Superconductors, pp. 1573–1591. ISSN: 0022-3697. DOI: https://doi.org/10.1016/0022-3697(95)00269-3. URL: https://www.sciencedirect.com/science/article/pii/0022369795002693.

[37] L. F. Feiner, J. H. Jefferson, and R. Raimondi. "Effective single-band models for the high-T_c cuprates. I. Coulomb interactions". *Phys. Rev. B* 53 (13 Apr. 1996), pp. 8751–8773. DOI: 10.1103/PhysRevB.53.8751. URL: https://link.aps.org/doi/10.1103/PhysRevB.53.8751.

[38] G. Keller, K. Held, V. Eyert, D. Vollhardt, and V. I. Anisimov. "Electronic structure of paramagnetic V_2O_3: Strongly correlated metallic and Mott insulating phase". *Phys. Rev. B* 70 (20 Nov. 2004), p. 205116. DOI: 10.1103/PhysRevB.70.205116. URL: https://link.aps.org/doi/10.1103/PhysRevB.70.205116.

[39] A. I. Poteryaev, J. M. Tomczak, S. Biermann, A. Georges, A. I. Lichtenstein, A. N. Rubtsov, T. Saha-Dasgupta, and O. K. Andersen. "Enhanced crystal-field splitting and orbital-selective coherence induced by strong correlations in V_2O_3". *Phys. Rev. B* 76 (8 Aug. 2007), p. 085127. DOI: 10.1103/PhysRevB.76.085127. URL: https://link.aps.org/doi/10.1103/PhysRevB.76.085127.

[40] J. M. Tomczak, M. Casula, T. Miyake, F. Aryasetiawan, and S. Biermann. "Combined GW and dynamical mean-field theory: Dynamical screening effects in transition metal oxides". *EPL (Europhysics Letters)* 100.6 (Dec. 2012), p. 67001. DOI: 10.1209/0295-5075/100/67001. URL: https://doi.org/10.1209%2F0295-5075%2F100%2F67001.

[41] Z. Zhong, M. Wallerberger, J. M. Tomczak, C. Taranto, N. Parragh, A. Toschi, G. Sangiovanni, and K. Held. "Electronics with Correlated Oxides: $SrVO_3$/$SrTiO_3$ as a Mott Transistor". *Phys. Rev. Lett.* 114 (24 June 2015), p. 246401. DOI: 10.1103/PhysRevLett.114.246401. URL: https://link.aps.org/doi/10.1103/PhysRevLett.114.246401.

[42] D. F. Agterberg, T. M. Rice, and M. Sigrist. "Orbital Dependent Superconductivity in Sr_2RuO_4". *Phys. Rev. Lett.* 78 (17 Apr. 1997), pp. 3374–3377. DOI: 10.1103/PhysRevLett.78.3374. URL: https://link.aps.org/doi/10.1103/PhysRevLett.78.3374.

[43] A. P. Mackenzie and Y. Maeno. "The superconductivity of Sr_2RuO_4 and the physics of spin-triplet pairing". *Rev. Mod. Phys.* 75 (2 May 2003), pp. 657–712. DOI: 10.1103/RevModPhys.75.657. URL: https://link.aps.org/doi/10.1103/RevModPhys.75.657.

[44] A. P. Mackenzie, T. Scaffidi, C. W. Hicks, and Y. Maeno. "Even odder after twenty-three years: the superconducting order parameter puzzle of Sr_2RuO_4". *npj Quantum Materials* 2.1 (July 2017), p. 40. ISSN: 2397-4648. DOI: 10.1038/s41535-017-0045-4. URL: https://doi.org/10.1038/s41535-017-0045-4.

[45] L. Boehnke, P. Werner, and F. Lechermann. "Multi-orbital nature of the spin fluctuations in Sr_2RuO_4". *EPL (Europhysics Letters)* 122.5 (July 2018), p. 57001. DOI: 10.1209/0295-5075/122/57001. URL: https://doi.org/10.1209/0295-5075/122/57001.

[46] P. Steffens, Y. Sidis, J. Kulda, Z. Q. Mao, Y. Maeno, I. I. Mazin, and M. Braden. "Spin Fluctuations in Sr_2RuO_4 from Polarized Neutron Scattering: Implications for Superconductivity". *Phys. Rev. Lett.* 122 (4 Feb. 2019), p. 047004. DOI: 10.1103/PhysRevLett.122.047004. URL: https://link.aps.org/doi/10.1103/PhysRevLett.122.047004.

[47]   H. U. R. Strand, M. Zingl, N. Wentzell, O. Parcollet, and A. Georges. "Magnetic response of Sr_2RuO_4: Quasi-local spin fluctuations due to Hund's coupling". *Phys. Rev. B* 100 (12 Sept. 2019), p. 125120. DOI: 10.1103/PhysRevB.100.125120. URL: https://link.aps.org/doi/10.1103/PhysRevB.100.125120.

[48]   E. A. Stepanov, Y. Nomura, A. I. Lichtenstein, and S. Biermann. "Orbital Isotropy of Magnetic Fluctuations in Correlated Electron Materials Induced by Hund's Exchange Coupling". *Phys. Rev. Lett.* 127 (20 Nov. 2021), p. 207205. DOI: 10.1103/PhysRevLett.127.207205. URL: https://link.aps.org/doi/10.1103/PhysRevLett.127.207205.

[49]   D. Li, K. Lee, B. Y. Wang, M. Osada, S. Crossley, H. R. Lee, Y. Cui, Y. Hikita, and H. Y. Hwang. "Superconductivity in an infinite-layer nickelate". *Nature* 572.7771 (Aug. 2019), pp. 624–627. ISSN: 1476-4687. DOI: 10.1038/s41586-019-1496-5. URL: https://doi.org/10.1038/s41586-019-1496-5.

[50]   A. S. Botana and M. R. Norman. "Similarities and Differences between $LaNiO_2$ and $CaCuO_2$ and Implications for Superconductivity". *Phys. Rev. X* 10 (1 Feb. 2020), p. 011024. DOI: 10.1103/PhysRevX.10.011024. URL: https://link.aps.org/doi/10.1103/PhysRevX.10.011024.

[51]   F. Lechermann. "Late transition metal oxides with infinite-layer structure: Nickelates versus cuprates". *Phys. Rev. B* 101 (8 Feb. 2020), p. 081110. DOI: 10.1103/PhysRevB.101.081110. URL: https://link.aps.org/doi/10.1103/PhysRevB.101.081110.

[52]   J. Karp, A. S. Botana, M. R. Norman, H. Park, M. Zingl, and A. Millis. "Many-Body Electronic Structure of $NdNiO_2$ and $CaCuO_2$". *Phys. Rev. X* 10 (2 June 2020), p. 021061. DOI: 10.1103/PhysRevX.10.021061. URL: https://link.aps.org/doi/10.1103/PhysRevX.10.021061.

[53]   F. Lechermann. "Multiorbital Processes Rule the $Nd_{1-x}Sr_xNiO_2$ Normal State". *Phys. Rev. X* 10 (4 Oct. 2020), p. 041002. DOI: 10.1103/PhysRevX.10.041002. URL: https://link.aps.org/doi/10.1103/PhysRevX.10.041002.

[54]   W. E. Pickett. "The dawn of the nickel age of superconductivity". *Nature Reviews Physics* 3.1 (Jan. 2021), pp. 7–8. ISSN: 2522-5820. DOI: 10.1038/s42254-020-00257-3. URL: https://doi.org/10.1038/s42254-020-00257-3.

[55]   B. Kang, C. Melnick, P. Semon, S. Ryee, M. J. Han, G. Kotliar, and S. Choi. "Infinite-layer nickelates as Ni-eg Hund's metals". *arXiv e-prints*, arXiv:2007.14610 (July 2020), arXiv:2007.14610.

[56] M. Aichhorn, L. Pourovskii, V. Vildosola, M. Ferrero, O. Parcollet, T. Miyake, A. Georges, and S. Biermann. "Dynamical mean-field theory within an augmented plane-wave framework: Assessing electronic correlations in the iron pnictide LaFeAsO". *Phys. Rev. B* 80 (8 Aug. 2009), p. 085101. DOI: 10.1103/PhysRevB.80.085101. URL: https://link.aps.org/doi/10.1103/PhysRevB.80.085101.

[57] K. Haule and G. Kotliar. "Coherence–incoherence crossover in the normal state of iron oxypnictides and importance of Hund's rule coupling". *New Journal of Physics* 11.2 (Feb. 2009), p. 025021. DOI: 10.1088/1367-2630/11/2/025021. URL: https://doi.org/10.1088/1367-2630/11/2/025021.

[58] M. Aichhorn, S. Biermann, T. Miyake, A. Georges, and M. Imada. "Theoretical evidence for strong correlations and incoherent metallic state in FeSe". *Phys. Rev. B* 82 (6 Aug. 2010), p. 064504. DOI: 10.1103/PhysRevB.82.064504. URL: https://link.aps.org/doi/10.1103/PhysRevB.82.064504.

[59] M. D. Watson, T. K. Kim, A. A. Haghighirad, N. R. Davies, A. McCollam, A. Narayanan, S. F. Blake, Y. L. Chen, S. Ghannadzadeh, A. J. Schofield, M. Hoesch, C. Meingast, T. Wolf, and A. I. Coldea. "Emergence of the nematic electronic state in FeSe". *Phys. Rev. B* 91 (15 Apr. 2015), p. 155106. DOI: 10.1103/PhysRevB.91.155106. URL: https://link.aps.org/doi/10.1103/PhysRevB.91.155106.

[60] S.-H. Baek, D. V. Efremov, J. M. Ok, J. S. Kim, J. van den Brink, and B. Büchner. "Orbital-driven nematicity in FeSe". *Nature Materials* 14.2 (Feb. 2015), pp. 210–214. ISSN: 1476-4660. DOI: 10.1038/nmat4138. URL: https://doi.org/10.1038/nmat4138.

[61] P. O. Sprau, A. Kostin, A. Kreisel, A. E. Böhmer, V. Taufour, P. C. Canfield, S. Mukherjee, P. J. Hirschfeld, B. M. Andersen, and J. C. Séamus Davis. "Discovery of orbital-selective Cooper pairing in FeSe". *Science* 357.6346 (2017), pp. 75–80. DOI: 10.1126/science.aal1575. URL: https://www.science.org/doi/abs/10.1126/science.aal1575.

[62] D. V. Evtushinsky, M. Aichhorn, Y. Sassa, Z. .-. Liu, J. Maletz, T. Wolf, A. N. Yaresko, S. Biermann, S. V. Borisenko, and B. Buchner. "Direct observation of dispersive lower Hubbard band in iron-based superconductor FeSe". *arXiv* (2016). DOI: 10.48550/ARXIV.1612.02313. URL: https://arxiv.org/abs/1612.02313.

[63] J. Fink, E. D. L. Rienks, S. Thirupathaiah, J. Nayak, A. van Roekeghem, S. Biermann, T. Wolf, P. Adelmann, H. S. Jeevan, P. Gegenwart, S. Wurmehl, C. Felser, and B. Büchner. "Experimental evidence for importance of Hund's exchange interaction for incoherence of charge carriers in iron-based superconductors". *Phys.*

Rev. B 95 (14 Apr. 2017), p. 144513. DOI: 10.1103/PhysRevB.95.144513. URL: https://link.aps.org/doi/10.1103/PhysRevB.95.144513.

[64]   M. D. Watson, S. Backes, A. A. Haghighirad, M. Hoesch, T. K. Kim, A. I. Coldea, and R. Valentí. "Formation of Hubbard-like bands as a fingerprint of strong electron-electron interactions in FeSe". *Phys. Rev. B* 95 (8 Feb. 2017), p. 081106. DOI: 10.1103/PhysRevB.95.081106. URL: https://link.aps.org/doi/10.1103/PhysRevB.95.081106.

[65]   K. Zantout, S. Backes, and R. Valentí. "Effect of Nonlocal Correlations on the Electronic Structure of LiFeAs". *Phys. Rev. Lett.* 123 (25 Dec. 2019), p. 256401. DOI: 10.1103/PhysRevLett.123.256401. URL: https://link.aps.org/doi/10.1103/PhysRevLett.123.256401.

[66]   C. Weber, A. Läuchli, F. Mila, and T. Giamarchi. "Orbital Currents in Extended Hubbard Models of High-T_c Cuprate Superconductors". *Phys. Rev. Lett.* 102 (1 Jan. 2009), p. 017005. DOI: 10.1103/PhysRevLett.102.017005. URL: https://link.aps.org/doi/10.1103/PhysRevLett.102.017005.

[67]   T. Yanagisawa, M. Miyazaki, and K. Yamaji. "Incommensurate Antiferromagnetism Coexisting with Superconductivity in Two-Dimensional d–p Model". *Journal of the Physical Society of Japan* 78.1 (2009), p. 013706. DOI: 10.1143/JPSJ.78.013706. URL: https://doi.org/10.1143/JPSJ.78.013706.

[68]   C. Weber, C. Yee, K. Haule, and G. Kotliar. "Scaling of the transition temperature of hole-doped cuprate superconductors with the charge-transfer energy". *EPL (Europhysics Letters)* 100.3 (Nov. 2012), p. 37001. DOI: 10.1209/0295-5075/100/37001. URL: https://doi.org/10.1209/0295-5075/100/37001.

[69]   C. Weber, T. Giamarchi, and C. M. Varma. "Phase Diagram of a Three-Orbital Model for High-T_c Cuprate Superconductors". *Phys. Rev. Lett.* 112 (11 Mar. 2014), p. 117001. DOI: 10.1103/PhysRevLett.112.117001. URL: https://link.aps.org/doi/10.1103/PhysRevLett.112.117001.

[70]   Z.-Z. Li, W.-S. Wang, and Q.-H. Wang. "Competing orders in a three-orbital model of cuprates: Is there a loop-current order?" *Physica C: Superconductivity and its Applications* 507 (2014), pp. 103–106. ISSN: 0921-4534. DOI: https://doi.org/10.1016/j.physc.2014.10.011. URL: https://www.sciencedirect.com/science/article/pii/S0921453414003347.

[71]   A. Go and A. J. Millis. "Spatial Correlations and the Insulating Phase of the High-T_c Cuprates: Insights from a Configuration-Interaction-Based Solver for Dynamical Mean Field Theory". *Phys. Rev. Lett.* 114 (1 Jan. 2015), p. 016402. DOI: 10.1103/PhysRevLett.114.016402. URL: https://link.aps.org/doi/10.1103/PhysRevLett.114.016402.

[72] D. Rybicki, M. Jurkutat, S. Reichardt, C. Kapusta, and J. Haase. "Perspective on the phase diagram of cuprate high-temperature superconductors". *Nature Communications* 7.1 (May 2016), p. 11413. ISSN: 2041-1723. DOI: 10.1038/ncomms11413. URL: https://doi.org/10.1038/ncomms11413.

[73] Y. F. Kung, C.-C. Chen, Y. Wang, E. W. Huang, E. A. Nowadnick, B. Moritz, R. T. Scalettar, S. Johnston, and T. P. Devereaux. "Characterizing the three-orbital Hubbard model with determinant quantum Monte Carlo". *Phys. Rev. B* 93 (15 Apr. 2016), p. 155166. DOI: 10.1103/PhysRevB.93.155166. URL: https://link.aps.org/doi/10.1103/PhysRevB.93.155166.

[74] M. Zegrodnik, A. Biborski, M. Fidrysiak, and J. Spałek. "Superconductivity in the three-band model of cuprates: Variational wave function study and relation to the single-band case". *Phys. Rev. B* 99 (10 Mar. 2019), p. 104511. DOI: 10.1103/PhysRevB.99.104511. URL: https://link.aps.org/doi/10.1103/PhysRevB.99.104511.

[75] M. Zegrodnik, A. Biborski, M. Fidrysiak, and J. Spałek. "Superconductivity in the three-band model of cuprates: nodal direction characteristics and influence of intersite interactions". *Journal of Physics: Condensed Matter* 33.41 (Aug. 2021), p. 415601. DOI: 10.1088/1361-648x/abcff6. URL: https://doi.org/10.1088/1361-648x/abcff6.

[76] I. Krivenko, A. Antipov, S. Iskakov, and J. Otsuki. *pomerol: An exact diagonalization code written in C++*. Version 2.0. Nov. 2021. DOI: 10.5281/zenodo.5739623. URL: https://doi.org/10.5281/zenodo.5739623.

[77] S. Iskakov and M. Danilov. "Exact diagonalization library for quantum electron models". *Computer Physics Communications* 225 (2018), pp. 128–139. ISSN: 0010-4655. DOI: https://doi.org/10.1016/j.cpc.2017.12.016. URL: https://www.sciencedirect.com/science/article/pii/S0010465517304216.

[78] M. Danilov, E. G. C. P. van Loon, S. Brener, S. Iskakov, M. I. Katsnelson, and A. I. Lichtenstein. "Degenerate plaquette physics as key ingredient of high-temperature superconductivity in cuprates". *npj Quantum Materials* 7.1 (Apr. 2022), p. 50. ISSN: 2397-4648. DOI: 10.1038/s41535-022-00454-6. URL: https://doi.org/10.1038/s41535-022-00454-6.

[79] S. Trotzky, L. Pollet, F. Gerbier, U. Schnorrberger, I. Bloch, N. V. Prokof'ev, B. Svistunov, and M. Troyer. "Suppression of the critical temperature for superfluidity near the Mott transition". *Nature Physics* 6.12 (Dec. 2010), pp. 998–1004. ISSN: 1745-2481. DOI: 10.1038/nphys1799. URL: https://doi.org/10.1038/nphys1799.

[80] R. Blankenbecler, D. J. Scalapino, and R. L. Sugar. "Monte Carlo calculations of coupled boson-fermion systems. I". *Phys. Rev. D* 24 (8 Oct. 1981), pp. 2278–2286. DOI: `10.1103/PhysRevD.24.2278`. URL: `https://link.aps.org/doi/10.1103/PhysRevD.24.2278`.

[81] E. Y. Loh, J. E. Gubernatis, R. T. Scalettar, S. R. White, D. J. Scalapino, and R. L. Sugar. "Sign problem in the numerical simulation of many-electron systems". *Phys. Rev. B* 41 (13 May 1990), pp. 9301–9307. DOI: `10.1103/PhysRevB.41.9301`. URL: `https://link.aps.org/doi/10.1103/PhysRevB.41.9301`.

[82] A. N. Rubtsov. *Quantum Monte Carlo determinantal algorithm without Hubbard-Stratonovich transformation: a general consideration.* 2003. DOI: `10.48550/ARXIV.COND-MAT/0302228`. URL: `https://arxiv.org/abs/cond-mat/0302228`.

[83] A. N. Rubtsov, V. V. Savkin, and A. I. Lichtenstein. "Continuous-time quantum Monte Carlo method for fermions". *Phys. Rev. B* 72 (3 July 2005), p. 035122. DOI: `10.1103/PhysRevB.72.035122`. URL: `https://link.aps.org/doi/10.1103/PhysRevB.72.035122`.

[84] E. Burovski, N. Prokof'ev, B. Svistunov, and M. Troyer. "The Fermi–Hubbard model at unitarity". *New Journal of Physics* 8.8 (Aug. 2006), pp. 153–153. DOI: `10.1088/1367-2630/8/8/153`. URL: `https://doi.org/10.1088/1367-2630/8/8/153`.

[85] H. J. M. van Bemmel, D. F. B. ten Haaf, W. van Saarloos, J. M. J. van Leeuwen, and G. An. "Fixed-Node Quantum Monte Carlo Method for Lattice Fermions". *Phys. Rev. Lett.* 72 (15 Apr. 1994), pp. 2442–2445. DOI: `10.1103/PhysRevLett.72.2442`. URL: `https://link.aps.org/doi/10.1103/PhysRevLett.72.2442`.

[86] S. Chandrasekharan and U.-J. Wiese. "Meron-Cluster Solution of Fermion Sign Problems". *Phys. Rev. Lett.* 83 (16 Oct. 1999), pp. 3116–3119. DOI: `10.1103/PhysRevLett.83.3116`. URL: `https://link.aps.org/doi/10.1103/PhysRevLett.83.3116`.

[87] E. Huffman and S. Chandrasekharan. "Solution to sign problems in models of interacting fermions and quantum spins". *Phys. Rev. E* 94 (4 Oct. 2016), p. 043311. DOI: `10.1103/PhysRevE.94.043311`. URL: `https://link.aps.org/doi/10.1103/PhysRevE.94.043311`.

[88] C. T. Hann, E. Huffman, and S. Chandrasekharan. "Solution to the sign problem in a frustrated quantum impurity model". *Annals of Physics* 376 (2017), pp. 63–75. ISSN: 0003-4916. DOI: `https://doi.org/10.1016/j.aop.2016.11.006`. URL: `https://www.sciencedirect.com/science/article/pii/S0003491616302494`.

[89] Z.-X. Li and H. Yao. "Sign-Problem-Free Fermionic Quantum Monte Carlo: Developments and Applications". *Annual Review of Condensed Matter Physics* 10.1 (2019), pp. 337–356. DOI: 10.1146/annurev-conmatphys-033117-054307. URL: https://doi.org/10.1146/annurev-conmatphys-033117-054307.

[90] D. Hangleiter, I. Roth, D. Nagaj, and J. Eisert. "Easing the Monte Carlo sign problem". *Science Advances* 6.33 (2020), eabb8341. DOI: 10.1126/sciadv.abb8341. URL: https://www.science.org/doi/abs/10.1126/sciadv.abb8341.

[91] J. Yoo, S. Chandrasekharan, R. K. Kaul, D. Ullmo, and H. U. Baranger. "On the sign problem in the Hirsch-Fye algorithm for impurity problems". *Journal of Physics A: Mathematical and General* 38.48 (Nov. 2005), pp. 10307–10310. DOI: 10.1088/0305-4470/38/48/004. URL: https://doi.org/10.1088/0305-4470/38/48/004.

[92] G. Onida, L. Reining, and A. Rubio. "Electronic excitations: density-functional versus many-body Green's-function approaches". *Rev. Mod. Phys.* 74 (2 June 2002), pp. 601–659. DOI: 10.1103/RevModPhys.74.601. URL: https://link.aps.org/doi/10.1103/RevModPhys.74.601.

[93] P. Hohenberg and W. Kohn. "Inhomogeneous Electron Gas". *Phys. Rev.* 136 (3B Nov. 1964), B864–B871. DOI: 10.1103/PhysRev.136.B864. URL: https://link.aps.org/doi/10.1103/PhysRev.136.B864.

[94] W. Kohn and L. J. Sham. "Self-Consistent Equations Including Exchange and Correlation Effects". *Phys. Rev.* 140 (4A Nov. 1965), A1133–A1138. DOI: 10.1103/PhysRev.140.A1133. URL: https://link.aps.org/doi/10.1103/PhysRev.140.A1133.

[95] N. Schuch and F. Verstraete. "Computational complexity of interacting electrons and fundamental limitations of density functional theory". *Nature Physics* 5.10 (Oct. 1, 2009), pp. 732–735. ISSN: 1745-2481. DOI: 10.1038/nphys1370. URL: https://doi.org/10.1038/nphys1370.

[96] M. Vandelli, J. Kaufmann, M. El-Nabulsi, V. Harkov, A. I. Lichtenstein, and E. A. Stepanov. "Multi-band D-TRILEX approach to materials with strong electronic correlations". *SciPost Phys.* 13 (2022), p. 036. DOI: 10.21468/SciPostPhys.13.2.036. URL: https://scipost.org/10.21468/SciPostPhys.13.2.036.

[97] Y. A. Bychkov and E. I. Rashba. "Properties of a 2D electron gas with lifted spectral degeneracy". *JETP Lett.* 39 (2 1984). [Pis'ma Zh. Eksp. Teor. Fiz. **39**, 66-69 (1984)], p. 78.

[98]   T. Yildirim, A. B. Harris, A. Aharony, and O. Entin-Wohlman. "Anisotropic spin Hamiltonians due to spin-orbit and Coulomb exchange interactions". *Phys. Rev. B* 52 (14 Oct. 1995), pp. 10239–10267. DOI: 10.1103/PhysRevB.52.10239. URL: https://link.aps.org/doi/10.1103/PhysRevB.52.10239.

[99]   N. Marzari and D. Vanderbilt. "Maximally localized generalized Wannier functions for composite energy bands". *Phys. Rev. B* 56 (20 Nov. 1997), pp. 12847–12865. DOI: 10.1103/PhysRevB.56.12847. URL: https://link.aps.org/doi/10.1103/PhysRevB.56.12847.

[100]   I. Souza, N. Marzari, and D. Vanderbilt. "Maximally localized Wannier functions for entangled energy bands". *Phys. Rev. B* 65 (3 Dec. 2001), p. 035109. DOI: 10.1103/PhysRevB.65.035109. URL: https://link.aps.org/doi/10.1103/PhysRevB.65.035109.

[101]   G. Pizzi, V. Vitale, R. Arita, S. Blügel, F. Freimuth, G. Géranton, M. Gibertini, D. Gresch, C. Johnson, T. Koretsune, J. Ibañez-Azpiroz, H. Lee, J.-M. Lihm, D. Marchand, A. Marrazzo, Y. Mokrousov, J. I. Mustafa, Y. Nohara, Y. Nomura, L. Paulatto, S. Poncé, T. Ponweiser, J. Qiao, F. Thöle, S. S. Tsirkin, M. Wierzbowska, N. Marzari, D. Vanderbilt, I. Souza, A. A. Mostofi, and J. R. Yates. "Wannier90 as a community code: new features and applications". *Journal of Physics: Condensed Matter* 32.16 (Jan. 2020), p. 165902. DOI: 10.1088/1361-648x/ab51ff. URL: https://doi.org/10.1088/1361-648x/ab51ff.

[102]   F. Aryasetiawan, M. Imada, A. Georges, G. Kotliar, S. Biermann, and A. I. Lichtenstein. "Frequency-dependent local interactions and low-energy effective models from electronic structure calculations". *Phys. Rev. B* 70 (19 Nov. 2004), p. 195104. DOI: 10.1103/PhysRevB.70.195104. URL: https://link.aps.org/doi/10.1103/PhysRevB.70.195104.

[103]   L. Vaugier, H. Jiang, and S. Biermann. "Hubbard *U* and Hund exchange *J* in transition metal oxides: Screening versus localization trends from constrained random phase approximation". *Phys. Rev. B* 86 (16 Oct. 2012), p. 165105. DOI: 10.1103/PhysRevB.86.165105. URL: https://link.aps.org/doi/10.1103/PhysRevB.86.165105.

[104]   P. Hansmann, L. Vaugier, H. Jiang, and S. Biermann. "What about *U* on surfaces? Extended Hubbard models for adatom systems from first principles". *Journal of Physics: Condensed Matter* 25.9 (Feb. 2013), p. 094005. DOI: 10.1088/0953-8984/25/9/094005. URL: https://doi.org/10.1088/0953-8984/25/9/094005.

[105] S. Acharya, D. Pashov, A. N. Rudenko, M. Rösner, M. van Schilfgaarde, and M. I. Katsnelson. "Importance of charge self-consistency in first-principles description of strongly correlated systems". *npj Computational Materials* 7.1 (Dec. 2021), p. 208. ISSN: 2057-3960. DOI: 10.1038/s41524-021-00676-5. URL: https://doi.org/10.1038/s41524-021-00676-5.

[106] J. Kanamori. "Electron Correlation and Ferromagnetism of Transition Metals". *Prog. Theor. Phys.* 30.3 (Sept. 1963), pp. 275–289. ISSN: 0033-068X. DOI: 10.1143/PTP.30.275. URL: https://doi.org/10.1143/PTP.30.275.

[107] A. Georges, L. d. Medici, and J. Mravlje. "Strong Correlations from Hund's Coupling". *Annual Review of Condensed Matter Physics* 4.1 (2013), pp. 137–178. DOI: 10.1146/annurev-conmatphys-020911-125045. URL: https://doi.org/10.1146/annurev-conmatphys-020911-125045.

[108] J. Hubbard. "Electron Correlations in Narrow Energy Bands". *Proc. R. Soc. A.* 276.1365 (1963), pp. 238–257. DOI: 10.1098/rspa.1963.0204. URL: http://rspa.royalsocietypublishing.org/content/276/1365/238.abstract.

[109] J. Hubbard. "Electron Correlations in Narrow Energy Bands. III. An Improved Solution". *Proc. R. Soc. A.* 281.1386 (1964), pp. 401–419. DOI: 10.1098/rspa.1964.0190. URL: http://rspa.royalsocietypublishing.org/content/281/1386/401.abstract.

[110] Q. Sun and G. K.-L. Chan. "Quantum Embedding Theories". *Accounts of Chemical Research* 49.12 (2016). PMID: 27993005, pp. 2705–2712. DOI: 10.1021/acs.accounts.6b00356. URL: https://doi.org/10.1021/acs.accounts.6b00356.

[111] L. O. Jones, M. A. Mosquera, G. C. Schatz, and M. A. Ratner. "Embedding Methods for Quantum Chemistry: Applications from Materials to Life Sciences". *Journal of the American Chemical Society* 142.7 (Feb. 2020), pp. 3281–3295. ISSN: 0002-7863. DOI: 10.1021/jacs.9b10780. URL: https://doi.org/10.1021/jacs.9b10780.

[112] L. Muechler, D. I. Badrtdinov, A. Hampel, J. Cano, M. Rösner, and C. E. Dreyer. "Quantum embedding methods for correlated excited states of point defects: Case studies and challenges". *Phys. Rev. B* 105 (23 June 2022), p. 235104. DOI: 10.1103/PhysRevB.105.235104. URL: https://link.aps.org/doi/10.1103/PhysRevB.105.235104.

[113] G. Knizia and G. K.-L. Chan. "Density Matrix Embedding: A Simple Alternative to Dynamical Mean-Field Theory". *Phys. Rev. Lett.* 109 (18 Nov. 2012), p. 186404. DOI: 10.1103/PhysRevLett.109.186404. URL: https://link.aps.org/doi/10.1103/PhysRevLett.109.186404.

[114]   G. Knizia and G. K.-L. Chan. "Density Matrix Embedding: A Strong-Coupling Quantum Embedding Theory". *Journal of Chemical Theory and Computation* 9.3 (Mar. 2013), pp. 1428–1432. ISSN: 1549-9618. DOI: 10.1021/ct301044e. URL: https://doi.org/10.1021/ct301044e.

[115]   R. Frésard and P. Wölfle. "Unified Slave Boson Representation of Spin and Charge Degrees of Freedom for Strongly Correlated Fermi Systems". *International Journal of Modern Physics B* 06.05n06 (1992), pp. 685–704. DOI: 10.1142/S0217979292000414. URL: https://doi.org/10.1142/S0217979292000414.

[116]   F. Lechermann, A. Georges, G. Kotliar, and O. Parcollet. "Rotationally invariant slave-boson formalism and momentum dependence of the quasiparticle weight". *Phys. Rev. B* 76 (15 Oct. 2007), p. 155102. DOI: 10.1103/PhysRevB.76.155102. URL: https://link.aps.org/doi/10.1103/PhysRevB.76.155102.

[117]   T.-H. Lee, T. Ayral, Y.-X. Yao, N. Lanata, and G. Kotliar. "Rotationally invariant slave-boson and density matrix embedding theory: Unified framework and comparative study on the one-dimensional and two-dimensional Hubbard model". *Phys. Rev. B* 99 (11 Mar. 2019), p. 115129. DOI: 10.1103/PhysRevB.99.115129. URL: https://link.aps.org/doi/10.1103/PhysRevB.99.115129.

[118]   A. Georges, G. Kotliar, W. Krauth, and M. J. Rozenberg. "Dynamical mean-field theory of strongly correlated fermion systems and the limit of infinite dimensions". *Rev. Mod. Phys.* 68 (1 Jan. 1996), pp. 13–125. DOI: 10.1103/RevModPhys.68.13. URL: https://link.aps.org/doi/10.1103/RevModPhys.68.13.

[119]   A. A. Kananenka, E. Gull, and D. Zgid. "Systematically improvable multiscale solver for correlated electron systems". *Phys. Rev. B* 91 (12 Mar. 2015), p. 121111. DOI: 10.1103/PhysRevB.91.121111. URL: https://link.aps.org/doi/10.1103/PhysRevB.91.121111.

[120]   D. Zgid and E. Gull. "Finite temperature quantum embedding theories for correlated systems". *New Journal of Physics* 19.2 (Feb. 2017), p. 023047. DOI: 10.1088/1367-2630/aa5d34. URL: https://doi.org/10.1088/1367-2630/aa5d34.

[121]   A. A. Rusakov, S. Iskakov, L. N. Tran, and D. Zgid. "Self-Energy Embedding Theory (SEET) for Periodic Systems". *Journal of Chemical Theory and Computation* 15.1 (2019). PMID: 30540474, pp. 229–240. DOI: 10.1021/acs.jctc.8b00927. URL: https://doi.org/10.1021/acs.jctc.8b00927.

[122]   J. Kondo. "Resistance Minimum in Dilute Magnetic Alloys". *Progress of Theoretical Physics* 32.1 (July 1964), pp. 37–49. ISSN: 0033-068X. DOI: 10.1143/PTP.32.37. URL: https://academic.oup.com/ptp/article/32/1/37/1834632.

[123] R. Hanson, L. P. Kouwenhoven, J. R. Petta, S. Tarucha, and L. M. K. Vandersypen. "Spins in few-electron quantum dots". *Rev. Mod. Phys.* 79 (4 Oct. 2007), pp. 1217–1265. DOI: 10.1103/RevModPhys.79.1217. URL: https://link.aps.org/doi/10.1103/RevModPhys.79.1217.

[124] P. W. Anderson. "Localized Magnetic States in Metals". *Phys. Rev.* 124 (1 Oct. 1961), pp. 41–53. DOI: 10.1103/PhysRev.124.41. URL: https://link.aps.org/doi/10.1103/PhysRev.124.41.

[125] T. Ayral, T.-H. Lee, and G. Kotliar. "Dynamical mean-field theory, density-matrix embedding theory, and rotationally invariant slave bosons: A unified perspective". *Phys. Rev. B* 96 (23 Dec. 2017), p. 235139. DOI: 10.1103/PhysRevB.96.235139. URL: https://link.aps.org/doi/10.1103/PhysRevB.96.235139.

[126] G. H. Booth and G. K.-L. Chan. "Spectral functions of strongly correlated extended systems via an exact quantum embedding". *Phys. Rev. B* 91 (15 Apr. 2015), p. 155107. DOI: 10.1103/PhysRevB.91.155107. URL: https://link.aps.org/doi/10.1103/PhysRevB.91.155107.

[127] G. Kotliar, S. Y. Savrasov, K. Haule, V. S. Oudovenko, O. Parcollet, and C. A. Marianetti. "Electronic structure calculations with dynamical mean-field theory". *Rev. Mod. Phys.* 78 (3 Aug. 2006), pp. 865–951. DOI: 10.1103/RevModPhys.78.865. URL: https://link.aps.org/doi/10.1103/RevModPhys.78.865.

[128] K. Held. "Electronic structure calculations using dynamical mean field theory". *Advances in Physics* 56.6 (2007), pp. 829–926. DOI: 10.1080/00018730701619647. URL: https://doi.org/10.1080/00018730701619647.

[129] V. I. Anisimov, A. I. Poteryaev, M. A. Korotin, A. O. Anokhin, and G. Kotliar. "First-principles calculations of the electronic structure and spectra of strongly correlated systems: dynamical mean-field theory". *Journal of Physics: Condensed Matter* 9.35 (Sept. 1997), pp. 7359–7367. DOI: 10.1088/0953-8984/9/35/010. URL: https://doi.org/10.1088/0953-8984/9/35/010.

[130] A. I. Lichtenstein and M. I. Katsnelson. "Ab initio calculations of quasiparticle band structure in correlated systems: LDA++ approach". *Phys. Rev. B* 57 (12 Mar. 1998), pp. 6884–6895. DOI: 10.1103/PhysRevB.57.6884. URL: https://link.aps.org/doi/10.1103/PhysRevB.57.6884.

[131] W. Metzner and D. Vollhardt. "Correlated Lattice Fermions in $d = \infty$ Dimensions". *Phys. Rev. Lett.* 62 (3 Jan. 1989), pp. 324–327. DOI: 10.1103/PhysRevLett.62.324. URL: https://link.aps.org/doi/10.1103/PhysRevLett.62.324.

[132]   M. Caffarel and W. Krauth. "Exact diagonalization approach to correlated fermions in infinite dimensions: Mott transition and superconductivity". *Phys. Rev. Lett.* 72 (10 Mar. 1994), pp. 1545–1548. DOI: `10.1103/PhysRevLett.72.1545`. URL: `https://link.aps.org/doi/10.1103/PhysRevLett.72.1545`.

[133]   M. Capone, L. de'Medici, and A. Georges. "Solving the dynamical mean-field theory at very low temperatures using the Lanczos exact diagonalization". *Phys. Rev. B* 76 (24 Dec. 2007), p. 245116. DOI: `10.1103/PhysRevB.76.245116`. URL: `https://link.aps.org/doi/10.1103/PhysRevB.76.245116`.

[134]   C. Lupo, F. Jamet, W. H. T. Tse, I. Rungger, and C. Weber. "Maximally localized dynamical quantum embedding for solving many-body correlated systems". *Nature Computational Science* 1.6 (June 2021), pp. 410–420. ISSN: 2662-8457. DOI: `10.1038/s43588-021-00090-3`. URL: `https://doi.org/10.1038/s43588-021-00090-3`.

[135]   J. E. Hirsch and R. M. Fye. "Monte Carlo Method for Magnetic Impurities in Metals". *Phys. Rev. Lett.* 56 (23 June 1986), pp. 2521–2524. DOI: `10.1103/PhysRevLett.56.2521`. URL: `https://link.aps.org/doi/10.1103/PhysRevLett.56.2521`.

[136]   A. N. Rubtsov and A. I. Lichtenstein. "Continuous-time quantum Monte Carlo method for fermions: Beyond auxiliary field framework". *Journal of Experimental and Theoretical Physics Letters* 80.1 (July 2004), pp. 61–65. ISSN: 1090-6487. DOI: `10.1134/1.1800216`. URL: `https://doi.org/10.1134/1.1800216`.

[137]   S. Rombouts, K. Heyde, and N. Jachowicz. "A discrete Hubbard-Stratonovich decomposition for general, fermionic two-body interactions". *Physics Letters A* 242.4 (1998), pp. 271–276. ISSN: 0375-9601. DOI: `https://doi.org/10.1016/S0375-9601(98)00197-2`. URL: `https://www.sciencedirect.com/science/article/pii/S0375960198001972`.

[138]   S. M. A. Rombouts, K. Heyde, and N. Jachowicz. "Quantum Monte Carlo Method for Fermions, Free of Discretization Errors". *Phys. Rev. Lett.* 82 (21 May 1999), pp. 4155–4159. DOI: `10.1103/PhysRevLett.82.4155`. URL: `https://link.aps.org/doi/10.1103/PhysRevLett.82.4155`.

[139]   E. Gull, P. Werner, O. Parcollet, and M. Troyer. "Continuous-time auxiliary-field Monte Carlo for quantum impurity models". *EPL (Europhysics Letters)* 82.5 (May 2008), p. 57003. DOI: `10.1209/0295-5075/82/57003`. URL: `https://doi.org/10.1209/0295-5075/82/57003`.

[140] P. Werner, A. Comanac, L. de'Medici, M. Troyer, and A. J. Millis. "Continuous-Time Solver for Quantum Impurity Models". *Phys. Rev. Lett.* 97 (7 Aug. 2006), p. 076405. DOI: 10.1103/PhysRevLett.97.076405. URL: https://link.aps.org/doi/10.1103/PhysRevLett.97.076405.

[141] P. Werner and A. J. Millis. "Hybridization expansion impurity solver: General formulation and application to Kondo lattice and two-orbital models". *Phys. Rev. B* 74 (15 Oct. 2006), p. 155107. DOI: 10.1103/PhysRevB.74.155107. URL: https://link.aps.org/doi/10.1103/PhysRevB.74.155107.

[142] H. Hafermann, P. Werner, and E. Gull. "Efficient implementation of the continuous-time hybridization expansion quantum impurity solver". *Computer Physics Communications* 184.4 (2013), pp. 1280–1286. ISSN: 0010-4655. DOI: https://doi.org/10.1016/j.cpc.2012.12.013. URL: http://www.sciencedirect.com/science/article/pii/S0010465512004092.

[143] E. Gull, A. J. Millis, A. I. Lichtenstein, A. N. Rubtsov, M. Troyer, and P. Werner. "Continuous-time Monte Carlo methods for quantum impurity models". *Rev. Mod. Phys.* 83 (2 May 2011), pp. 349–404. DOI: 10.1103/RevModPhys.83.349. URL: https://link.aps.org/doi/10.1103/RevModPhys.83.349.

[144] J. Li, M. Wallerberger, and E. Gull. "Diagrammatic Monte Carlo method for impurity models with general interactions and hybridizations". *Phys. Rev. Research* 2 (3 Aug. 2020), p. 033211. DOI: 10.1103/PhysRevResearch.2.033211. URL: https://link.aps.org/doi/10.1103/PhysRevResearch.2.033211.

[145] E. Eidelstein, E. Gull, and G. Cohen. "Multiorbital Quantum Impurity Solver for General Interactions and Hybridizations". *Phys. Rev. Lett.* 124 (20 May 2020), p. 206405. DOI: 10.1103/PhysRevLett.124.206405. URL: https://link.aps.org/doi/10.1103/PhysRevLett.124.206405.

[146] R. Bulla, T. A. Costi, and T. Pruschke. "Numerical renormalization group method for quantum impurity systems". *Rev. Mod. Phys.* 80 (2 Apr. 2008), pp. 395–450. DOI: 10.1103/RevModPhys.80.395. URL: https://link.aps.org/doi/10.1103/RevModPhys.80.395.

[147] S. Nishimoto, F. Gebhard, and E. Jeckelmann. "Dynamical mean-field theory calculation with the dynamical density-matrix renormalization group". *Physica B: Condensed Matter* 378-380 (2006). Proceedings of the International Conference on Strongly Correlated Electron Systems, pp. 283–285. ISSN: 0921-4526. DOI: https://doi.org/10.1016/j.physb.2006.01.104. URL: https://www.sciencedirect.com/science/article/pii/S0921452606001372.

[148]   S. R. White. "Density matrix formulation for quantum renormalization groups". *Phys. Rev. Lett.* 69 (19 Nov. 1992), pp. 2863–2866. DOI: 10.1103/PhysRevLett.69.2863. URL: https://link.aps.org/doi/10.1103/PhysRevLett.69.2863.

[149]   L. Kohn and G. E. Santoro. "Efficient mapping for Anderson impurity problems with matrix product states". *Phys. Rev. B* 104 (1 July 2021), p. 014303. DOI: 10.1103/PhysRevB.104.014303. URL: https://link.aps.org/doi/10.1103/PhysRevB.104.014303.

[150]   X. Y. Zhang, M. J. Rozenberg, and G. Kotliar. "Mott transition in the d=∞ Hubbard model at zero temperature". *Phys. Rev. Lett.* 70 (11 Mar. 1993), pp. 1666–1669. DOI: 10.1103/PhysRevLett.70.1666. URL: https://link.aps.org/doi/10.1103/PhysRevLett.70.1666.

[151]   A. Georges and W. Krauth. "Physical properties of the half-filled Hubbard model in infinite dimensions". *Phys. Rev. B* 48 (10 Sept. 1993), pp. 7167–7182. DOI: 10.1103/PhysRevB.48.7167. URL: https://link.aps.org/doi/10.1103/PhysRevB.48.7167.

[152]   M. J. Rozenberg, G. Kotliar, and X. Y. Zhang. "Mott-Hubbard transition in infinite dimensions. II". *Phys. Rev. B* 49 (15 Apr. 1994), pp. 10181–10193. DOI: 10.1103/PhysRevB.49.10181. URL: https://link.aps.org/doi/10.1103/PhysRevB.49.10181.

[153]   R. Bulla. "Zero Temperature Metal-Insulator Transition in the Infinite-Dimensional Hubbard Model". *Phys. Rev. Lett.* 83 (1 July 1999), pp. 136–139. DOI: 10.1103/PhysRevLett.83.136. URL: https://link.aps.org/doi/10.1103/PhysRevLett.83.136.

[154]   M. Eckstein, M. Kollar, M. Potthoff, and D. Vollhardt. "Phase separation in the particle-hole asymmetric Hubbard model". *Phys. Rev. B* 75 (12 Mar. 2007), p. 125103. DOI: 10.1103/PhysRevB.75.125103. URL: https://link.aps.org/doi/10.1103/PhysRevB.75.125103.

[155]   H. Park, K. Haule, and G. Kotliar. "Cluster Dynamical Mean Field Theory of the Mott Transition". *Phys. Rev. Lett.* 101 (18 Oct. 2008), p. 186403. DOI: 10.1103/PhysRevLett.101.186403. URL: https://link.aps.org/doi/10.1103/PhysRevLett.101.186403.

[156]   H. U. R. Strand, A. Sabashvili, M. Granath, B. Hellsing, and S. Östlund. "Dynamical mean field theory phase-space extension and critical properties of the finite temperature Mott transition". *Phys. Rev. B* 83 (20 May 2011), p. 205136. DOI: 10.1103/PhysRevB.83.205136. URL: https://link.aps.org/doi/10.1103/PhysRevB.83.205136.

[157] M. J. Rozenberg. "Integer-filling metal-insulator transitions in the degenerate Hubbard model". *Phys. Rev. B* 55 (8 Feb. 1997), R4855–R4858. DOI: 10.1103/PhysRevB.55.R4855. URL: https://link.aps.org/doi/10.1103/PhysRevB.55.R4855.

[158] S. Florens and A. Georges. "Quantum impurity solvers using a slave rotor representation". *Phys. Rev. B* 66 (16 Oct. 2002), p. 165111. DOI: 10.1103/PhysRevB.66.165111. URL: https://link.aps.org/doi/10.1103/PhysRevB.66.165111.

[159] G. Kotliar, S. Murthy, and M. J. Rozenberg. "Compressibility Divergence and the Finite Temperature Mott Transition". *Phys. Rev. Lett.* 89 (4 July 2002), p. 046401. DOI: 10.1103/PhysRevLett.89.046401. URL: https://link.aps.org/doi/10.1103/PhysRevLett.89.046401.

[160] Y. Ōno, M. Potthoff, and R. Bulla. "Mott transitions in correlated electron systems with orbital degrees of freedom". *Phys. Rev. B* 67 (3 Jan. 2003), p. 035119. DOI: 10.1103/PhysRevB.67.035119. URL: https://link.aps.org/doi/10.1103/PhysRevB.67.035119.

[161] J. Steinbauer, L. de'Medici, and S. Biermann. "Doping-driven metal-insulator transition in correlated electron systems with strong Hund's exchange coupling". *Phys. Rev. B* 100 (8 Aug. 2019), p. 085104. DOI: 10.1103/PhysRevB.100.085104. URL: https://link.aps.org/doi/10.1103/PhysRevB.100.085104.

[162] Q. Si and J. L. Smith. "Kosterlitz-Thouless Transition and Short Range Spatial Correlations in an Extended Hubbard Model". *Phys. Rev. Lett.* 77 (16 Oct. 1996), pp. 3391–3394. DOI: 10.1103/PhysRevLett.77.3391. URL: http://link.aps.org/doi/10.1103/PhysRevLett.77.3391.

[163] J. L. Smith and Q. Si. "Spatial correlations in dynamical mean-field theory". *Phys. Rev. B* 61 (8 Feb. 2000), pp. 5184–5193. DOI: 10.1103/PhysRevB.61.5184. URL: http://link.aps.org/doi/10.1103/PhysRevB.61.5184.

[164] R. Chitra and G. Kotliar. "Effect of Long Range Coulomb Interactions on the Mott Transition". *Phys. Rev. Lett.* 84 (16 Apr. 2000), pp. 3678–3681. DOI: 10.1103/PhysRevLett.84.3678. URL: https://link.aps.org/doi/10.1103/PhysRevLett.84.3678.

[165] R. Chitra and G. Kotliar. "Effective-action approach to strongly correlated fermion systems". *Phys. Rev. B* 63 (11 Mar. 2001), p. 115110. DOI: 10.1103/PhysRevB.63.115110. URL: http://link.aps.org/doi/10.1103/PhysRevB.63.115110.

[166] M. H. Hettler, A. N. Tahvildar-Zadeh, M. Jarrell, T. Pruschke, and H. R. Krish-
       namurthy. "Nonlocal dynamical correlations of strongly interacting electron sys-
       tems". *Phys. Rev. B* 58 (12 Sept. 1998), R7475–R7479. DOI: 10.1103/PhysRevB.
       58.R7475. URL: https://link.aps.org/doi/10.1103/PhysRevB.58.
       R7475.

[167] A. I. Lichtenstein and M. I. Katsnelson. "Antiferromagnetism and d-wave super-
       conductivity in cuprates: A cluster dynamical mean-field theory". *Phys. Rev. B*
       62 (14 Oct. 2000), R9283–R9286. DOI: 10.1103/PhysRevB.62.R9283. URL:
       https://link.aps.org/doi/10.1103/PhysRevB.62.R9283.

[168] T. Maier, M. Jarrell, T. Pruschke, and M. H. Hettler. "Quantum cluster theories".
       Rev. Mod. Phys. 77 (3 Oct. 2005), pp. 1027–1080. DOI: 10.1103/RevModPhys.
       77.1027. URL: https://link.aps.org/doi/10.1103/RevModPhys.77.
       1027.

[169] G. Kotliar, S. Y. Savrasov, G. Pálsson, and G. Biroli. "Cellular Dynamical Mean
       Field Approach to Strongly Correlated Systems". *Phys. Rev. Lett.* 87 (18 Oct.
       2001), p. 186401. DOI: 10.1103/PhysRevLett.87.186401. URL: https://
       link.aps.org/doi/10.1103/PhysRevLett.87.186401.

[170] M. Harland, M. I. Katsnelson, and A. I. Lichtenstein. "Plaquette valence bond
       theory of high-temperature superconductivity". *Phys. Rev. B* 94 (12 Sept. 2016),
       p. 125133. DOI: 10.1103/PhysRevB.94.125133. URL: https://link.aps.
       org/doi/10.1103/PhysRevB.94.125133.

[171] T. Schäfer, F. Geles, D. Rost, G. Rohringer, E. Arrigoni, K. Held, N. Blümer, M.
       Aichhorn, and A. Toschi. "Fate of the false Mott-Hubbard transition in two dimen-
       sions". *Phys. Rev. B* 91 (12 Mar. 2015), p. 125109. DOI: 10.1103/PhysRevB.91.
       125109. URL: https://link.aps.org/doi/10.1103/PhysRevB.91.125109.

[172] F. Šimkovic, R. Rossi, and M. Ferrero. *The Weak, the Strong and the Long Cor-
       relation Regimes of the Two-Dimensional Hubbard Model at Finite Temperature.*
       2021. DOI: 10.48550/ARXIV.2110.05863. URL: https://arxiv.org/abs/
       2110.05863.

[173] E. Gorelov, T. O. Wehling, A. N. Rubtsov, M. I. Katsnelson, and A. I. Lichtenstein.
       "Relevance of the complete Coulomb interaction matrix for the Kondo problem:
       Co impurities in Cu hosts". *Phys. Rev. B* 80 (15 Oct. 2009), p. 155132. DOI: 10.
       1103/PhysRevB.80.155132. URL: https://link.aps.org/doi/10.1103/
       PhysRevB.80.155132.

[174] H. Lee, Y.-Z. Zhang, H. O. Jeschke, and R. Valentí. "Orbital-selective phase transition induced by different magnetic states: A dynamical cluster approximation study". *Phys. Rev. B* 84 (2 July 2011), p. 020401. DOI: 10.1103/PhysRevB.84.020401. URL: https://link.aps.org/doi/10.1103/PhysRevB.84.020401.

[175] Y. Nomura, S. Sakai, and R. Arita. "Multiorbital cluster dynamical mean-field theory with an improved continuous-time quantum Monte Carlo algorithm". *Phys. Rev. B* 89 (19 May 2014), p. 195146. DOI: 10.1103/PhysRevB.89.195146. URL: https://link.aps.org/doi/10.1103/PhysRevB.89.195146.

[176] Y. Nomura, S. Sakai, and R. Arita. "Nonlocal correlations induced by Hund's coupling: A cluster DMFT study". *Phys. Rev. B* 91 (23 June 2015), p. 235107. DOI: 10.1103/PhysRevB.91.235107. URL: https://link.aps.org/doi/10.1103/PhysRevB.91.235107.

[177] Y. Nomura, S. Sakai, and R. Arita. "Fermi Surface Expansion above Critical Temperature in a Hund Ferromagnet". *Phys. Rev. Lett.* 128 (20 May 2022), p. 206401. DOI: 10.1103/PhysRevLett.128.206401. URL: https://link.aps.org/doi/10.1103/PhysRevLett.128.206401.

[178] S. N. Iskakov, V. V. Mazurenko, M. V. Valentyuk, and A. I. Lichtenstein. "Valence fluctuations and empty-state resonance for Fe adatom on a surface". *Phys. Rev. B* 92 (24 Dec. 2015), p. 245135. DOI: 10.1103/PhysRevB.92.245135. URL: https://link.aps.org/doi/10.1103/PhysRevB.92.245135.

[179] K. Bouadim, G. G. Batrouni, and R. T. Scalettar. "Determinant Quantum Monte Carlo Study of the Orbitally Selective Mott Transition". *Phys. Rev. Lett.* 102 (22 June 2009), p. 226402. DOI: 10.1103/PhysRevLett.102.226402. URL: https://link.aps.org/doi/10.1103/PhysRevLett.102.226402.

[180] Z. Cai, H.-H. Hung, L. Wang, and C. Wu. "Quantum magnetic properties of the $SU(2N)$ Hubbard model in the square lattice: A quantum Monte Carlo study". *Phys. Rev. B* 88 (12 Sept. 2013), p. 125108. DOI: 10.1103/PhysRevB.88.125108. URL: https://link.aps.org/doi/10.1103/PhysRevB.88.125108.

[181] T. Ma, H.-Q. Lin, and J. Hu. "Quantum Monte Carlo Study of a Dominant *s*-Wave Pairing Symmetry in Iron-Based Superconductors". *Phys. Rev. Lett.* 110 (10 Mar. 2013), p. 107002. DOI: 10.1103/PhysRevLett.110.107002. URL: https://link.aps.org/doi/10.1103/PhysRevLett.110.107002.

[182] H. Hao, B. M. Rubenstein, and H. Shi. "Auxiliary field quantum Monte Carlo for multiband Hubbard models: Controlling the sign and phase problems to capture Hund's physics". *Phys. Rev. B* 99 (23 June 2019), p. 235142. DOI: 10.1103/PhysRevB.99.235142. URL: https://link.aps.org/doi/10.1103/PhysRevB.99.235142.

[183]   M. H. Christensen, X. Wang, Y. Schattner, E. Berg, and R. M. Fernandes. "Model-
        ing Unconventional Superconductivity at the Crossover between Strong and Weak
        Electronic Interactions". *Phys. Rev. Lett.* 125 (24 Dec. 2020), p. 247001. DOI: `10.`
        `1103/PhysRevLett.125.247001`. URL: `https://link.aps.org/doi/10.`
        `1103/PhysRevLett.125.247001`.

[184]   X.-X. Huang, B. Moritz, M. Claassen, and T. P. Devereaux. "Sign-free determinant
        quantum Monte Carlo study of excitonic density orders in a two-orbital Hubbard-
        Kanamori model". *Phys. Rev. B* 105 (16 Apr. 2022), p. 165124. DOI: `10.1103/`
        `PhysRevB.105.165124`. URL: `https://link.aps.org/doi/10.1103/`
        `PhysRevB.105.165124`.

[185]   L. Hedin. "New Method for Calculating the One-Particle Green's Function with
        Application to the Electron-Gas Problem". *Phys. Rev.* 139 (3A Aug. 1965), A796–
        A823. DOI: `10.1103/PhysRev.139.A796`. URL: `http://link.aps.org/doi/`
        `10.1103/PhysRev.139.A796`.

[186]   F. Aryasetiawan and O. Gunnarsson. "The *GW* method". *Reports on Progress in
        Physics* 61.3 (1998), p. 237. URL: `http://stacks.iop.org/0034-4885/61/`
        `i=3/a=002`.

[187]   L. Hedin. "On correlation effects in electron spectroscopies and the *GW* approxi-
        mation". *Journal of Physics: Condensed Matter* 11.42 (1999), R489. URL: `http:`
        `//stacks.iop.org/0953-8984/11/i=42/a=201`.

[188]   N. E. Bickers. "Self-Consistent Many-Body Theory for Condensed Matter Sys-
        tems". *Theoretical Methods for Strongly Correlated Electrons*. Ed. by D. Sénéchal,
        A.-M. Tremblay, and C. Bourbonnais. New York, NY: Springer New York, 2004,
        pp. 237–296. ISBN: 978-0-387-21717-8. DOI: `10.1007/0-387-21717-7_6`. URL:
        `https://doi.org/10.1007/0-387-21717-7_6`.

[189]   V. Drchal, V. Janiš, J. Kudrnovský, V. S. Oudovenko, X. Dai, K. Haule, and G.
        Kotliar. "Dynamical correlations in multiorbital Hubbard models: fluctuation ex-
        change approximations". *Journal of Physics: Condensed Matter* 17.1 (Dec. 2004),
        pp. 61–74. DOI: `10.1088/0953-8984/17/1/007`. URL: `https://doi.org/10.`
        `1088/0953-8984/17/1/007`.

[190]   T. Takimoto, T. Hotta, and K. Ueda. "Strong-coupling theory of superconductivity
        in a degenerate Hubbard model". *Phys. Rev. B* 69 (10 Mar. 2004), p. 104504. DOI:
        `10.1103/PhysRevB.69.104504`. URL: `https://link.aps.org/doi/10.`
        `1103/PhysRevB.69.104504`.

[191]   K. Kubo. "Pairing symmetry in a two-orbital Hubbard model on a square lattice".
        Phys. Rev. B 75 (22 June 2007), p. 224509. DOI: `10.1103/PhysRevB.75.224509`.
        URL: `https://link.aps.org/doi/10.1103/PhysRevB.75.224509`.

[192] N. Witt, E. G. C. P. van Loon, T. Nomoto, R. Arita, and T. O. Wehling. "Efficient fluctuation-exchange approach to low-temperature spin fluctuations and superconductivity: From the Hubbard model to $Na_xCoO_2 \cdot yH_2O$". *Phys. Rev. B* 103 (20 May 2021), p. 205148. DOI: 10.1103/PhysRevB.103.205148. URL: https://link.aps.org/doi/10.1103/PhysRevB.103.205148.

[193] S. Biermann, F. Aryasetiawan, and A. Georges. "First-Principles Approach to the Electronic Structure of Strongly Correlated Systems: Combining the *GW* Approximation and Dynamical Mean-Field Theory". *Phys. Rev. Lett.* 90 (8 Feb. 2003), p. 086402. DOI: 10.1103/PhysRevLett.90.086402. URL: https://link.aps.org/doi/10.1103/PhysRevLett.90.086402.

[194] J. M. Tomczak, M. van Schilfgaarde, and G. Kotliar. "Many-Body Effects in Iron Pnictides and Chalcogenides: Nonlocal Versus Dynamic Origin of Effective Masses". *Phys. Rev. Lett.* 109 (23 Dec. 2012), p. 237010. DOI: 10.1103/PhysRevLett.109.237010. URL: https://link.aps.org/doi/10.1103/PhysRevLett.109.237010.

[195] T. Ayral, S. Biermann, and P. Werner. "Screening and nonlocal correlations in the extended Hubbard model from self-consistent combined *GW* and dynamical mean field theory". *Phys. Rev. B* 87 (12 Mar. 2013), p. 125149. DOI: 10.1103/PhysRevB.87.125149. URL: https://link.aps.org/doi/10.1103/PhysRevB.87.125149.

[196] C. Taranto, M. Kaltak, N. Parragh, G. Sangiovanni, G. Kresse, A. Toschi, and K. Held. "Comparing quasiparticle *GW*+DMFT and LDA+DMFT for the test bed material $SrVO_3$". *Phys. Rev. B* 88 (16 Oct. 2013), p. 165119. DOI: 10.1103/PhysRevB.88.165119. URL: https://link.aps.org/doi/10.1103/PhysRevB.88.165119.

[197] R. Sakuma, P. Werner, and F. Aryasetiawan. "Electronic structure of $SrVO_3$ within *GW*+DMFT". *Phys. Rev. B* 88 (23 Dec. 2013), p. 235110. DOI: 10.1103/PhysRevB.88.235110. URL: https://link.aps.org/doi/10.1103/PhysRevB.88.235110.

[198] J. M. Tomczak, M. Casula, T. Miyake, and S. Biermann. "Asymmetry in band widening and quasiparticle lifetimes in $SrVO_3$: Competition between screened exchange and local correlations from combined *GW* and dynamical mean-field theory *GW* + DMFT". *Phys. Rev. B* 90 (16 Oct. 2014), p. 165138. DOI: 10.1103/PhysRevB.90.165138. URL: https://link.aps.org/doi/10.1103/PhysRevB.90.165138.

[199] L. Huang, T. Ayral, S. Biermann, and P. Werner. "Extended dynamical mean-field study of the Hubbard model with long-range interactions". *Phys. Rev. B* 90 (19 Nov. 2014), p. 195114. DOI: 10.1103/PhysRevB.90.195114. URL: https://link.aps.org/doi/10.1103/PhysRevB.90.195114.

[200] P. Sun and G. Kotliar. "Many-Body Approximation Scheme beyond GW". *Phys. Rev. Lett.* 92 (19 May 2004), p. 196402. DOI: 10.1103/PhysRevLett.92.196402. URL: https://link.aps.org/doi/10.1103/PhysRevLett.92.196402.

[201] T. Ayral, P. Werner, and S. Biermann. "Spectral Properties of Correlated Materials: Local Vertex and Nonlocal Two-Particle Correlations from Combined *GW* and Dynamical Mean Field Theory". *Phys. Rev. Lett.* 109 (22 Nov. 2012), p. 226401. DOI: 10.1103/PhysRevLett.109.226401. URL: http://link.aps.org/doi/10.1103/PhysRevLett.109.226401.

[202] A. van Roekeghem, T. Ayral, J. M. Tomczak, M. Casula, N. Xu, H. Ding, M. Ferrero, O. Parcollet, H. Jiang, and S. Biermann. "Dynamical Correlations and Screened Exchange on the Experimental Bench: Spectral Properties of the Cobalt Pnictide $BaCo_2As_2$". *Phys. Rev. Lett.* 113 (26 Dec. 2014), p. 266403. DOI: 10.1103/PhysRevLett.113.266403. URL: http://link.aps.org/doi/10.1103/PhysRevLett.113.266403.

[203] L. Boehnke, F. Nilsson, F. Aryasetiawan, and P. Werner. "When strong correlations become weak: Consistent merging of *GW* and DMFT". *Phys. Rev. B* 94 (20 Nov. 2016), 201106(R). DOI: 10.1103/PhysRevB.94.201106. URL: https://link.aps.org/doi/10.1103/PhysRevB.94.201106.

[204] L. Sponza, P. Pisanti, A. Vishina, D. Pashov, C. Weber, M. van Schilfgaarde, S. Acharya, J. Vidal, and G. Kotliar. "Self-energies in itinerant magnets: A focus on Fe and Ni". *Phys. Rev. B* 95 (4 Jan. 2017), 041112(R). DOI: 10.1103/PhysRevB.95.041112. URL: https://link.aps.org/doi/10.1103/PhysRevB.95.041112.

[205] T. Ayral, S. Biermann, P. Werner, and L. Boehnke. "Influence of Fock exchange in combined many-body perturbation and dynamical mean field theory". *Phys. Rev. B* 95 (24 June 2017), p. 245130. DOI: 10.1103/PhysRevB.95.245130. URL: https://link.aps.org/doi/10.1103/PhysRevB.95.245130.

[206] S. Acharya, C. Weber, E. Plekhanov, D. Pashov, A. Taraphder, and M. Van Schilfgaarde. "Metal-Insulator Transition in Copper Oxides Induced by Apex Displacements". *Phys. Rev. X* 8 (2 May 2018), p. 021038. DOI: 10.1103/PhysRevX.8.021038. URL: https://link.aps.org/doi/10.1103/PhysRevX.8.021038.

[207] S. Ryee, P. Sémon, M. J. Han, and S. Choi. "Nonlocal Coulomb interaction and spin-freezing crossover as a route to valence-skipping charge order". *npj Quantum Mater.* 5 (1 Mar. 2020), p. 19. DOI: 10.1038/s41535-020-0221-9. URL: https://doi.org/10.1038/s41535-020-0221-9.

[208] G. Rohringer, H. Hafermann, A. Toschi, A. A. Katanin, A. E. Antipov, M. I. Katsnelson, A. I. Lichtenstein, A. N. Rubtsov, and K. Held. "Diagrammatic routes to nonlocal correlations beyond dynamical mean field theory". *Rev. Mod. Phys.* 90 (2 May 2018), p. 025003. DOI: 10.1103/RevModPhys.90.025003. URL: https://link.aps.org/doi/10.1103/RevModPhys.90.025003.

[209] A. Toschi, A. A. Katanin, and K. Held. "Dynamical vertex approximation: A step beyond dynamical mean-field theory". *Phys. Rev. B* 75 (4 Jan. 2007), p. 045118. DOI: 10.1103/PhysRevB.75.045118. URL: https://link.aps.org/doi/10.1103/PhysRevB.75.045118.

[210] A. A. Katanin, A. Toschi, and K. Held. "Comparing pertinent effects of antiferromagnetic fluctuations in the two- and three-dimensional Hubbard model". *Phys. Rev. B* 80 (7 Aug. 2009), p. 075104. DOI: 10.1103/PhysRevB.80.075104. URL: https://link.aps.org/doi/10.1103/PhysRevB.80.075104.

[211] A. Galler, P. Thunström, P. Gunacker, J. M. Tomczak, and K. Held. "Ab initio dynamical vertex approximation". *Phys. Rev. B* 95 (11 Mar. 2017), p. 115107. DOI: 10.1103/PhysRevB.95.115107. URL: https://link.aps.org/doi/10.1103/PhysRevB.95.115107.

[212] A. Galler, J. Kaufmann, P. Gunacker, M. Pickem, P. Thunström, J. M. Tomczak, and K. Held. "Towards ab initio Calculations with the Dynamical Vertex Approximation". *Journal of the Physical Society of Japan* 87.4 (2018), p. 041004. DOI: 10.7566/JPSJ.87.041004. URL: https://doi.org/10.7566/JPSJ.87.041004.

[213] J. Kaufmann, C. Eckhardt, M. Pickem, M. Kitatani, A. Kauch, and K. Held. "Self-consistent ladder dynamical vertex approximation". *Phys. Rev. B* 103 (3 Jan. 2021), p. 035120. DOI: 10.1103/PhysRevB.103.035120. URL: https://link.aps.org/doi/10.1103/PhysRevB.103.035120.

[214] J. Kaufmann, K. Steiner, R. T. Scalettar, K. Held, and O. Janson. "How correlations change the magnetic structure factor of the kagome Hubbard model". *Phys. Rev. B* 104 (16 Oct. 2021), p. 165127. DOI: 10.1103/PhysRevB.104.165127. URL: https://link.aps.org/doi/10.1103/PhysRevB.104.165127.

[215] T. Ayral and O. Parcollet. "Mott physics and spin fluctuations: A unified framework". *Phys. Rev. B* 92 (11 Sept. 2015), p. 115109. DOI: 10.1103/PhysRevB.92.115109. URL: https://link.aps.org/doi/10.1103/PhysRevB.92.115109.

[216]   T. Ayral and O. Parcollet. "Mott physics and spin fluctuations: A functional view-point". *Phys. Rev. B* 93 (23 June 2016), p. 235124. DOI: 10.1103/PhysRevB.93.235124. URL: https://link.aps.org/doi/10.1103/PhysRevB.93.235124.

[217]   T. Ayral, J. Vučičević, and O. Parcollet. "Fierz Convergence Criterion: A Controlled Approach to Strongly Interacting Systems with Small Embedded Clusters". *Phys. Rev. Lett.* 119 (16 Oct. 2017), p. 166401. DOI: 10.1103/PhysRevLett.119.166401. URL: https://link.aps.org/doi/10.1103/PhysRevLett.119.166401.

[218]   A. N. Rubtsov, M. I. Katsnelson, and A. I. Lichtenstein. "Dual fermion approach to nonlocal correlations in the Hubbard model". *Phys. Rev. B* 77 (3 Jan. 2008), p. 033101. DOI: 10.1103/PhysRevB.77.033101. URL: https://link.aps.org/doi/10.1103/PhysRevB.77.033101.

[219]   A. N. Rubtsov, M. I. Katsnelson, A. I. Lichtenstein, and A. Georges. "Dual fermion approach to the two-dimensional Hubbard model: Antiferromagnetic fluctuations and Fermi arcs". *Phys. Rev. B* 79 (4 Jan. 2009), p. 045133. DOI: 10.1103/PhysRevB.79.045133. URL: http://link.aps.org/doi/10.1103/PhysRevB.79.045133.

[220]   S. Iskakov, A. E. Antipov, and E. Gull. "Diagrammatic Monte Carlo for dual fermions". *Phys. Rev. B* 94 (3 July 2016), p. 035102. DOI: 10.1103/PhysRevB.94.035102. URL: https://link.aps.org/doi/10.1103/PhysRevB.94.035102.

[221]   J. Gukelberger, E. Kozik, and H. Hafermann. "Diagrammatic Monte Carlo approach for diagrammatic extensions of dynamical mean-field theory: Convergence analysis of the dual fermion technique". *Phys. Rev. B* 96 (3 July 2017), p. 035152. DOI: 10.1103/PhysRevB.96.035152. URL: https://link.aps.org/doi/10.1103/PhysRevB.96.035152.

[222]   H. Hafermann, G. Li, A. N. Rubtsov, M. I. Katsnelson, A. I. Lichtenstein, and H. Monien. "Efficient Perturbation Theory for Quantum Lattice Models". *Phys. Rev. Lett.* 102 (20 May 2009), p. 206401. DOI: 10.1103/PhysRevLett.102.206401. URL: https://link.aps.org/doi/10.1103/PhysRevLett.102.206401.

[223]   S. Brener, E. A. Stepanov, A. N. Rubtsov, M. I. Katsnelson, and A. I. Lichtenstein. "Dual fermion method as a prototype of generic reference-system approach for correlated fermions". *Annals of Physics* 422 (2020), p. 168310. ISSN: 0003-4916. DOI: https://doi.org/10.1016/j.aop.2020.168310. URL: http://www.sciencedirect.com/science/article/pii/S000349162030244X.

[224] A. N. Rubtsov, M. I. Katsnelson, and A. I. Lichtenstein. "Dual boson approach to collective excitations in correlated fermionic systems". *Annals of Physics* 327.5 (2012), pp. 1320–1335. ISSN: 0003-4916. DOI: 10.1016/j.aop.2012.01.002. URL: http://www.sciencedirect.com/science/article/pii/S0003491612000164.

[225] E. G. C. P. van Loon, A. I. Lichtenstein, M. I. Katsnelson, O. Parcollet, and H. Hafermann. "Beyond extended dynamical mean-field theory: Dual boson approach to the two-dimensional extended Hubbard model". *Phys. Rev. B* 90 (23 Dec. 2014), p. 235135. DOI: 10.1103/PhysRevB.90.235135. URL: https://link.aps.org/doi/10.1103/PhysRevB.90.235135.

[226] E. A. Stepanov, E. G. C. P. van Loon, A. A. Katanin, A. I. Lichtenstein, M. I. Katsnelson, and A. N. Rubtsov. "Self-consistent dual boson approach to single-particle and collective excitations in correlated systems". *Phys. Rev. B* 93 (4 Jan. 2016), p. 045107. DOI: 10.1103/PhysRevB.93.045107. URL: https://link.aps.org/doi/10.1103/PhysRevB.93.045107.

[227] E. A. Stepanov, A. Huber, E. G. C. P. van Loon, A. I. Lichtenstein, and M. I. Katsnelson. "From local to nonlocal correlations: The Dual Boson perspective". *Phys. Rev. B* 94 (20 Nov. 2016), p. 205110. DOI: 10.1103/PhysRevB.94.205110. URL: https://link.aps.org/doi/10.1103/PhysRevB.94.205110.

[228] E. A. Stepanov, L. Peters, I. S. Krivenko, A. I. Lichtenstein, M. I. Katsnelson, and A. N. Rubtsov. "Quantum spin fluctuations and evolution of electronic structure in cuprates". *npj Quantum Materials* 3 (1 Oct. 2018), p. 54. DOI: 10.1038/s41535-018-0128-x. URL: https://doi.org/10.1038/s41535-018-0128-x.

[229] L. Peters, E. G. C. P. van Loon, A. N. Rubtsov, A. I. Lichtenstein, M. I. Katsnelson, and E. A. Stepanov. "Dual boson approach with instantaneous interaction". *Phys. Rev. B* 100 (16 Oct. 2019), p. 165128. DOI: 10.1103/PhysRevB.100.165128. URL: https://link.aps.org/doi/10.1103/PhysRevB.100.165128.

[230] M. Vandelli, V. Harkov, E. A. Stepanov, J. Gukelberger, E. Kozik, A. Rubio, and A. I. Lichtenstein. "Dual boson diagrammatic Monte Carlo approach applied to the extended Hubbard model". *Phys. Rev. B* 102 (19 Nov. 2020), p. 195109. DOI: 10.1103/PhysRevB.102.195109. URL: https://link.aps.org/doi/10.1103/PhysRevB.102.195109.

[231] E. A. Stepanov, V. Harkov, and A. I. Lichtenstein. "Consistent partial bosonization of the extended Hubbard model". *Phys. Rev. B* 100 (20 Nov. 2019), p. 205115. DOI: 10.1103/PhysRevB.100.205115. URL: https://link.aps.org/doi/10.1103/PhysRevB.100.205115.

[232] V. Harkov, M. Vandelli, S. Brener, A. I. Lichtenstein, and E. A. Stepanov. "Impact of partially bosonized collective fluctuations on electronic degrees of freedom". *Phys. Rev. B* 103 (24 June 2021), p. 245123. DOI: 10.1103/PhysRevB.103.245123. URL: https://link.aps.org/doi/10.1103/PhysRevB.103.245123.

[233] E. A. Stepanov, V. Harkov, M. Rösner, A. I. Lichtenstein, M. I. Katsnelson, and A. N. Rudenko. "Coexisting charge density wave and ferromagnetic instabilities in monolayer InSe". *npj Computational Materials* 8.1 (May 2022), p. 118. ISSN: 2057-3960. DOI: 10.1038/s41524-022-00798-4. URL: https://doi.org/10.1038/s41524-022-00798-4.

[234] M. Vandelli, J. Kaufmann, V. Harkov, A. I. Lichtenstein, K. Held, and E. A. Stepanov. "Extended regime of meta-stable metallic and insulating phases in a two-orbital electronic system". *arXiv e-prints*, arXiv:2204.02116 (2022), - under consideration in Phys. Rev. Lett.

[235] E. A. Stepanov. "Eliminating Orbital Selectivity from the Metal-Insulator Transition by Strong Magnetic Fluctuations". *Phys. Rev. Lett.* 129 (9 Aug. 2022), p. 096404. DOI: 10.1103/PhysRevLett.129.096404. URL: https://link.aps.org/doi/10.1103/PhysRevLett.129.096404.

[236] T. Schäfer, N. Wentzell, F. Šimkovic, Y.-Y. He, C. Hille, M. Klett, C. J. Eckhardt, B. Arzhang, V. Harkov, F. ç.-M. Le Régent, A. Kirsch, Y. Wang, A. J. Kim, E. Kozik, E. A. Stepanov, A. Kauch, S. Andergassen, P. Hansmann, D. Rohe, Y. M. Vilk, J. P. F. LeBlanc, S. Zhang, A.-M. S. Tremblay, M. Ferrero, O. Parcollet, and A. Georges. "Tracking the Footprints of Spin Fluctuations: A MultiMethod, MultiMessenger Study of the Two-Dimensional Hubbard Model". *Phys. Rev. X* 11 (1 Mar. 2021), p. 011058. DOI: 10.1103/PhysRevX.11.011058. URL: https://link.aps.org/doi/10.1103/PhysRevX.11.011058.

[237] E. G. C. P. van Loon. "Second-order dual fermion for multi-orbital systems". *Journal of Physics: Condensed Matter* 33.13 (Jan. 2021), p. 135601. DOI: 10.1088/1361-648x/abd9ed. URL: https://doi.org/10.1088/1361-648x/abd9ed.

[238] M. Danilov. "Anomalies in spectrum of two-dimensional Hubbard model: Exact Diagonalization and Dual Fermion study". Theses. Universität Hamburg, 2021. URL: https://ediss.sub.uni-hamburg.de/handle/ediss/9232.

[239] F. Aryasetiawan and S. Biermann. "Generalized Hedin's Equations for Quantum Many-Body Systems with Spin-Dependent Interactions". *Phys. Rev. Lett.* 100 (11 Mar. 2008), p. 116402. DOI: 10.1103/PhysRevLett.100.116402. URL: https://link.aps.org/doi/10.1103/PhysRevLett.100.116402.

[240] H. Kontani. "Optical Conductivity and Hall Coefficient in High-Tc Superconductors: Significant Role of Current Vertex Corrections". *Journal of the Physical Society of Japan* 75.1 (2006), p. 013703. DOI: 10.1143/JPSJ.75.013703. URL: https://doi.org/10.1143/JPSJ.75.013703.

[241] N. Lin, E. Gull, and A. J. Millis. "Optical conductivity from cluster dynamical mean-field theory: Formalism and application to high-temperature superconductors". *Phys. Rev. B* 80 (16 Oct. 2009), p. 161105. DOI: 10.1103/PhysRevB.80.161105. URL: https://link.aps.org/doi/10.1103/PhysRevB.80.161105.

[242] M. I. Katsnelson and A. I. Lichtenstein. "Theory of optically forbidden d–d transitions in strongly correlated crystals". *Journal of Physics: Condensed Matter* 22.38 (Sept. 2010), p. 382201. ISSN: 1361-648X. DOI: 10.1088/0953-8984/22/38/382201. URL: http://dx.doi.org/10.1088/0953-8984/22/38/382201.

[243] D. Bergeron, V. Hankevych, B. Kyung, and A.-M. S. Tremblay. "Optical and dc conductivity of the two-dimensional Hubbard model in the pseudogap regime and across the antiferromagnetic quantum critical point including vertex corrections". *Phys. Rev. B* 84 (8 Aug. 2011), p. 085128. DOI: 10.1103/PhysRevB.84.085128. URL: https://link.aps.org/doi/10.1103/PhysRevB.84.085128.

[244] J. Vučičević, J. Kokalj, R. Žitko, N. Wentzell, D. Tanasković, and J. Mravlje. "Conductivity in the Square Lattice Hubbard Model at High Temperatures: Importance of Vertex Corrections". *Phys. Rev. Lett.* 123 (3 July 2019), p. 036601. DOI: 10.1103/PhysRevLett.123.036601. URL: https://link.aps.org/doi/10.1103/PhysRevLett.123.036601.

[245] A. Kauch, P. Pudleiner, K. Astleithner, P. Thunström, T. Ribic, and K. Held. "Generic Optical Excitations of Correlated Systems: π-tons". *Phys. Rev. Lett.* 124 (4 Jan. 2020), p. 047401. DOI: 10.1103/PhysRevLett.124.047401. URL: https://link.aps.org/doi/10.1103/PhysRevLett.124.047401.

[246] O. Simard, S. Takayoshi, and P. Werner. "Diagrammatic study of optical excitations in correlated systems". *Phys. Rev. B* 103 (10 Mar. 2021), p. 104415. DOI: 10.1103/PhysRevB.103.104415. URL: https://link.aps.org/doi/10.1103/PhysRevB.103.104415.

[247] L. Hedin. "New Method for Calculating the One-Particle Green's Function with Application to the Electron-Gas Problem". *Phys. Rev.* 139 (3A Aug. 1965), A796–A823. DOI: 10.1103/PhysRev.139.A796. URL: http://link.aps.org/doi/10.1103/PhysRev.139.A796.

[248] J. Jaeckel and C. Wetterich. "Flow equations without mean field ambiguity". *Phys. Rev. D* 68 (2 July 2003), p. 025020. DOI: 10.1103/PhysRevD.68.025020. URL: https://link.aps.org/doi/10.1103/PhysRevD.68.025020.

[249]   T. Baier, E. Bick, and C. Wetterich. "Temperature dependence of antiferromagnetic order in the Hubbard model". *Phys. Rev. B* 70 (12 Sept. 2004), p. 125111. DOI: 10.1103/PhysRevB.70.125111. URL: https://link.aps.org/doi/10.1103/PhysRevB.70.125111.

[250]   J. Jaeckel. "Understanding the Fierz Ambiguity of Partially Bosonized Theories". *arXiv e-prints*, hep-ph/0205154 (May 2002), hep–ph/0205154.

[251]   V. Harkov, A. I. Lichtenstein, and F. Krien. "Parametrizations of local vertex corrections from weak to strong coupling: Importance of the Hedin three-leg vertex". *Phys. Rev. B* 104 (12 Sept. 2021), p. 125141. DOI: 10.1103/PhysRevB.104.125141. URL: https://link.aps.org/doi/10.1103/PhysRevB.104.125141.

[252]   E. G. C. P. van Loon, M. I. Katsnelson, and H. Hafermann. "Second-order dual fermion approach to the Mott transition in the two-dimensional Hubbard model". *Phys. Rev. B* 98 (15 Oct. 2018), p. 155117. DOI: 10.1103/PhysRevB.98.155117. URL: https://link.aps.org/doi/10.1103/PhysRevB.98.155117.

[253]   E. G. C. P. van Loon, H. Hafermann, A. I. Lichtenstein, A. N. Rubtsov, and M. I. Katsnelson. "Plasmons in Strongly Correlated Systems: Spectral Weight Transfer and Renormalized Dispersion". *Phys. Rev. Lett.* 113 (24 Dec. 2014), p. 246407. DOI: 10.1103/PhysRevLett.113.246407. URL: https://link.aps.org/doi/10.1103/PhysRevLett.113.246407.

[254]   J. Otsuki, H. Hafermann, and A. I. Lichtenstein. "Superconductivity, antiferromagnetism, and phase separation in the two-dimensional Hubbard model: A dual-fermion approach". *Phys. Rev. B* 90 (23 Dec. 2014), p. 235132. DOI: 10.1103/PhysRevB.90.235132. URL: http://link.aps.org/doi/10.1103/PhysRevB.90.235132.

[255]   N. D. Mermin and H. Wagner. "Absence of Ferromagnetism or Antiferromagnetism in One- or Two-Dimensional Isotropic Heisenberg Models". *Phys. Rev. Lett.* 17 (22 Nov. 1966), pp. 1133–1136. DOI: 10.1103/PhysRevLett.17.1133. URL: http://link.aps.org/doi/10.1103/PhysRevLett.17.1133.

[256]   D. Hirschmeier, H. Hafermann, E. Gull, A. I. Lichtenstein, and A. E. Antipov. "Mechanisms of finite-temperature magnetism in the three-dimensional Hubbard model". *Phys. Rev. B* 92 (14 Oct. 2015), p. 144409. DOI: 10.1103/PhysRevB.92.144409. URL: https://link.aps.org/doi/10.1103/PhysRevB.92.144409.

[257]   G. V. Astretsov, G. Rohringer, and A. N. Rubtsov. "Dual parquet scheme for the two-dimensional Hubbard model: Modeling low-energy physics of high-T_c cuprates with high momentum resolution". *Phys. Rev. B* 101 (7 Feb. 2020), p. 075109.

DOI: `10.1103/PhysRevB.101.075109`. URL: `https://link.aps.org/doi/10.1103/PhysRevB.101.075109`.

[258] F. Krien, A. Valli, P. Chalupa, M. Capone, A. I. Lichtenstein, and A. Toschi. "Boson-exchange parquet solver for dual fermions". *Phys. Rev. B* 102 (19 Nov. 2020), p. 195131. DOI: `10.1103/PhysRevB.102.195131`. URL: `https://link.aps.org/doi/10.1103/PhysRevB.102.195131`.

[259] F. Krien, A. I. Lichtenstein, and G. Rohringer. "Fluctuation diagnostic of the nodal/antinodal dichotomy in the Hubbard model at weak coupling: A parquet dual fermion approach". *Phys. Rev. B* 102 (23 Dec. 2020), p. 235133. DOI: `10.1103/PhysRevB.102.235133`. URL: `https://link.aps.org/doi/10.1103/PhysRevB.102.235133`.

[260] D. Hirschmeier, H. Hafermann, and A. I. Lichtenstein. "Multiband dual fermion approach to quantum criticality in the Hubbard honeycomb lattice". *Phys. Rev. B* 97 (11 Mar. 2018), p. 115150. DOI: `10.1103/PhysRevB.97.115150`. URL: `https://link.aps.org/doi/10.1103/PhysRevB.97.115150`.

[261] O. Parcollet, M. Ferrero, T. Ayral, H. Hafermann, I. Krivenko, L. Messio, and P. Seth. "TRIQS: A toolbox for research on interacting quantum systems". *Computer Physics Communications* 196 (2015), pp. 398–415. ISSN: 0010-4655. DOI: `http://dx.doi.org/10.1016/j.cpc.2015.04.023`. URL: `http://www.sciencedirect.com/science/article/pii/S0010465515001666`.

[262] H. Hafermann, S. Brener, A. N. Rubtsov, M. I. Katsnelson, and A. I. Lichtenstein. "Cluster dual fermion approach to nonlocal correlations". *JETP Letters* 86.10 (Jan. 2008), pp. 677–682. ISSN: 1090-6487. DOI: `10.1134/S0021364007220134`. URL: `https://doi.org/10.1134/S0021364007220134`.

[263] S. Iskakov, H. Terletska, and E. Gull. "Momentum-space cluster dual-fermion method". *Phys. Rev. B* 97 (12 Mar. 2018), p. 125114. DOI: `10.1103/PhysRevB.97.125114`. URL: `https://link.aps.org/doi/10.1103/PhysRevB.97.125114`.

[264] E. A. Stepanov, S. Brener, F. Krien, M. Harland, A. I. Lichtenstein, and M. I. Katsnelson. "Effective Heisenberg Model and Exchange Interaction for Strongly Correlated Systems". *Phys. Rev. Lett.* 121 (3 July 2018), p. 037204. DOI: `10.1103/PhysRevLett.121.037204`. URL: `https://link.aps.org/doi/10.1103/PhysRevLett.121.037204`.

[265] E. A. Stepanov, A. Huber, A. I. Lichtenstein, and M. I. Katsnelson. "Effective Ising model for correlated systems with charge ordering". *Phys. Rev. B* 99 (11 Mar. 2019), p. 115124. DOI: `10.1103/PhysRevB.99.115124`. URL: `https://link.aps.org/doi/10.1103/PhysRevB.99.115124`.

[266]   E. A. Stepanov, S. Brener, V. Harkov, M. I. Katsnelson, and A. I. Lichtenstein. "Spin dynamics of itinerant electrons: Local magnetic moment formation and Berry phase". *Phys. Rev. B* 105 (15 Apr. 2022), p. 155151. DOI: 10.1103/PhysRevB.105.155151. URL: https://link.aps.org/doi/10.1103/PhysRevB.105.155151.

[267]   A. M. Sengupta and A. Georges. "Non-Fermi-liquid behavior near a T=0 spin-glass transition". *Phys. Rev. B* 52 (14 Oct. 1995), pp. 10295–10302. DOI: 10.1103/PhysRevB.52.10295. URL: https://link.aps.org/doi/10.1103/PhysRevB.52.10295.

[268]   T. Ribic, P. Gunacker, S. Iskakov, M. Wallerberger, G. Rohringer, A. N. Rubtsov, E. Gull, and K. Held. "Role of three-particle vertex within dual fermion calculations". *Phys. Rev. B* 96 (23 Dec. 2017), p. 235127. DOI: 10.1103/PhysRevB.96.235127. URL: https://link.aps.org/doi/10.1103/PhysRevB.96.235127.

[269]   E. G. C. P. van Loon, F. Krien, H. Hafermann, A. I. Lichtenstein, and M. I. Katsnelson. "Fermion-boson vertex within dynamical mean-field theory". *Phys. Rev. B* 98 (20 Nov. 2018), p. 205148. DOI: 10.1103/PhysRevB.98.205148. URL: https://link.aps.org/doi/10.1103/PhysRevB.98.205148.

[270]   B. Bauer, L. D. Carr, H. G. Evertz, A. Feiguin, J. Freire, S. Fuchs, L. Gamper, J. Gukelberger, E. Gull, S. Guertler, A. Hehn, R. Igarashi, S. V. Isakov, D. Koop, P. N. Ma, P. Mates, H. Matsuo, O. Parcollet, G. Pawłowski, J. D. Picon, L. Pollet, E. Santos, V. W. Scarola, U. Schollwöck, C. Silva, B. Surer, S. Todo, S. Trebst, M. Troyer, M. L. Wall, P. Werner, and S. Wessel. "The ALPS project release 2.0: open source software for strongly correlated systems". *Journal of Statistical Mechanics: Theory and Experiment* 2011.05 (May 2011), P05001. DOI: 10.1088/1742-5468/2011/05/p05001. URL: https://doi.org/10.1088%2F1742-5468%2F2011%2F05%2Fp05001.

[271]   S. Biermann, A. Poteryaev, A. I. Lichtenstein, and A. Georges. "Dynamical Singlets and Correlation-Assisted Peierls Transition in VO_2". *Phys. Rev. Lett.* 94 (2 Jan. 2005), p. 026404. DOI: 10.1103/PhysRevLett.94.026404. URL: https://link.aps.org/doi/10.1103/PhysRevLett.94.026404.

[272]   G. Carleo and M. Troyer. "Solving the quantum many-body problem with artificial neural networks". *Science* 355.6325 (2017), pp. 602–606. DOI: 10.1126/science.aag2302. URL: https://www.science.org/doi/abs/10.1126/science.aag2302.

[273]   P. Werner and A. J. Millis. "Dynamical Screening in Correlated Electron Materials". *Phys. Rev. Lett.* 104 (14 Apr. 2010), p. 146401. DOI: 10.1103/PhysRevLett.104.146401. URL: https://link.aps.org/doi/10.1103/PhysRevLett.104.146401.

[274] M. Wallerberger, A. Hausoel, P. Gunacker, A. Kowalski, N. Parragh, F. Goth, K. Held, and G. Sangiovanni. "w2dynamics: Local one- and two-particle quantities from dynamical mean field theory". *Computer Physics Communications* 235 (2019), pp. 388–399. ISSN: 0010-4655. DOI: https://doi.org/10.1016/j.cpc.2018.09.007. URL: https://www.sciencedirect.com/science/article/pii/S0010465518303217.

[275] J. Kaufmann, P. Gunacker, and K. Held. "Continuous-time quantum Monte Carlo calculation of multiorbital vertex asymptotics". *Phys. Rev. B* 96 (3 July 2017), p. 035114. DOI: 10.1103/PhysRevB.96.035114. URL: https://link.aps.org/doi/10.1103/PhysRevB.96.035114.

[276] N. V. Prokof'ev and B. V. Svistunov. "Polaron Problem by Diagrammatic Quantum Monte Carlo". *Phys. Rev. Lett.* 81 (12 Sept. 1998), pp. 2514–2517. DOI: 10.1103/PhysRevLett.81.2514. URL: https://link.aps.org/doi/10.1103/PhysRevLett.81.2514.

[277] J. P. F. LeBlanc, A. E. Antipov, F. Becca, I. W. Bulik, G. K.-L. Chan, C.-M. Chung, Y. Deng, M. Ferrero, T. M. Henderson, C. A. Jiménez-Hoyos, E. Kozik, X.-W. Liu, A. J. Millis, N. V. Prokofév, M. Qin, G. E. Scuseria, H. Shi, B. V. Svistunov, L. F. Tocchio, I. S. Tupitsyn, S. R. White, S. Zhang, B.-X. Zheng, Z. Zhu, and E. Gull. "Solutions of the Two-Dimensional Hubbard Model: Benchmarks and Results from a Wide Range of Numerical Algorithms". *Phys. Rev. X* 5 (4 Dec. 2015), p. 041041. DOI: 10.1103/PhysRevX.5.041041. URL: https://link.aps.org/doi/10.1103/PhysRevX.5.041041.

[278] M. Iazzi, A. A. Soluyanov, and M. Troyer. "Topological origin of the fermion sign problem". *Phys. Rev. B* 93 (11 Mar. 2016), p. 115102. DOI: 10.1103/PhysRevB.93.115102. URL: https://link.aps.org/doi/10.1103/PhysRevB.93.115102.

[279] R. Rossi, F. Werner, N. Prokof'ev, and B. Svistunov. "Shifted-action expansion and applicability of dressed diagrammatic schemes". *Phys. Rev. B* 93 (16 Apr. 2016), 161102(R). DOI: 10.1103/PhysRevB.93.161102. URL: https://link.aps.org/doi/10.1103/PhysRevB.93.161102.

[280] D. P. Landau and K. Binder. *A Guide to Monte Carlo Simulations in Statistical Physics*. 4th ed. Cambridge University Press, 2014. DOI: 10.1017/CBO9781139696463.

[281] L. Tierney. "Markov Chains for Exploring Posterior Distributions". *The Annals of Statistics* 22.4 (1994), pp. 1701–1728. DOI: 10.1214/aos/1176325750. URL: https://doi.org/10.1214/aos/1176325750.

[282]   H. Suwa and S. Todo. "Markov Chain Monte Carlo Method without Detailed Bal-ance". *Phys. Rev. Lett.* 105 (12 Sept. 2010), p. 120603. DOI: `10.1103/PhysRevLett.105.120603`. URL: `https://link.aps.org/doi/10.1103/PhysRevLett.105.120603`.

[283]   N. Metropolis, A. W. Rosenbluth, M. N. Rosenbluth, A. H. Teller, and E. Teller. "Equation of State Calculations by Fast Computing Machines". *The Journal of Chemical Physics* 21.6 (1953), pp. 1087–1092. DOI: `10.1063/1.1699114`. URL: `https://doi.org/10.1063/1.1699114`.

[284]   W. K. Hastings. "Monte Carlo sampling methods using Markov chains and their applications". *Biometrika* 57.1 (Apr. 1970), pp. 97–109. ISSN: 0006-3444. DOI: `10.1093/biomet/57.1.97`. URL: `https://doi.org/10.1093/biomet/57.1.97`.

[285]   N. Prokof'ev and B. Svistunov. "Fermi-polaron problem: Diagrammatic Monte Carlo method for divergent sign-alternating series". *Phys. Rev. B* 77 (2 Jan. 2008), 020408(R). DOI: `10.1103/PhysRevB.77.020408`. URL: `https://link.aps.org/doi/10.1103/PhysRevB.77.020408`.

[286]   M. Maček, P. T. Dumitrescu, C. Bertrand, B. Triggs, O. Parcollet, and X. Waintal. "Quantum Quasi-Monte Carlo Technique for Many-Body Perturbative Expansions". *Phys. Rev. Lett.* 125 (4 July 2020), p. 047702. DOI: `10.1103/PhysRevLett.125.047702`. URL: `https://link.aps.org/doi/10.1103/PhysRevLett.125.047702`.

[287]   K. V. Houcke, E. Kozik, N. Prokofév, and B. Svistunov. "Diagrammatic Monte Carlo". *Physics Procedia* 6 (2010). Computer Simulations Studies in Condensed Matter Physics XXI, pp. 95–105. ISSN: 1875-3892. DOI: `https://doi.org/10.1016/j.phpro.2010.09.034`. URL: `http://www.sciencedirect.com/science/article/pii/S1875389210006498`.

[288]   E. Kozik, K. V. Houcke, E. Gull, L. Pollet, N. Prokof'ev, B. Svistunov, and M. Troyer. "Diagrammatic Monte Carlo for correlated fermions". *EPL (Europhysics Letters)* 90.1 (Apr. 2010), p. 10004. DOI: `10.1209/0295-5075/90/10004`. URL: `https://doi.org/10.1209%2F0295-5075%2F90%2F10004`.

[289]   F. J. Dyson. "Divergence of Perturbation Theory in Quantum Electrodynamics". *Phys. Rev.* 85 (4 Feb. 1952), pp. 631–632. DOI: `10.1103/PhysRev.85.631`. URL: `https://link.aps.org/doi/10.1103/PhysRev.85.631`.

[290]   G. Benfatto, A. Giuliani, and V. Mastropietro. "Low Temperature Analysis of Two-Dimensional Fermi Systems with Symmetric Fermi Surface". *Annales Henri Poincaré* 4.1 (Mar. 2003), pp. 137–193. ISSN: 1424-0661. DOI: `10.1007/s00023-003-0125-9`. URL: `https://doi.org/10.1007/s00023-003-0125-9`.

[291] F. Šimkovic. "Understanding Electron Correlations through Advances in Diagrammatic Monte Carlo". PhD thesis. 2018.

[292] F. B. Kugler. "Counting Feynman diagrams via many-body relations". *Phys. Rev. E* 98 (2 Aug. 2018), p. 023303. DOI: `10.1103/PhysRevE.98.023303`. URL: `https://link.aps.org/doi/10.1103/PhysRevE.98.023303`.

[293] J. Gukelberger. "From non-unitary anyons to unconventional superfluidity". Ph.D. thesis. 2015. DOI: `10.3929/ethz-a-010451939`.

[294] R. Rossi. "Determinant Diagrammatic Monte Carlo Algorithm in the Thermodynamic Limit". *Phys. Rev. Lett.* 119 (4 July 2017), p. 045701. DOI: `10.1103/PhysRevLett.119.045701`. URL: `https://link.aps.org/doi/10.1103/PhysRevLett.119.045701`.

[295] F. Šimkovic and E. Kozik. "Determinant Monte Carlo for irreducible Feynman diagrams in the strongly correlated regime". *Phys. Rev. B* 100 (12 Sept. 2019), 121102(R). DOI: `10.1103/PhysRevB.100.121102`. URL: `https://link.aps.org/doi/10.1103/PhysRevB.100.121102`.

[296] A. Moutenet, W. Wu, and M. Ferrero. "Determinant Monte Carlo algorithms for dynamical quantities in fermionic systems". *Phys. Rev. B* 97 (8 Feb. 2018), p. 085117. DOI: `10.1103/PhysRevB.97.085117`. URL: `https://link.aps.org/doi/10.1103/PhysRevB.97.085117`.

[297] R. Rossi. "Direct sampling of the self-energy with Connected Determinant Monte Carlo". *arXiv:1802.04743* (Feb. 2018). URL: `https://arxiv.org/abs/1802.04743`.

[298] A. J. Kim, F. Simkovic, and E. Kozik. "Spin and Charge Correlations across the Metal-to-Insulator Crossover in the Half-Filled 2D Hubbard Model". *Phys. Rev. Lett.* 124 (11 Mar. 2020), p. 117602. DOI: `10.1103/PhysRevLett.124.117602`. URL: `https://link.aps.org/doi/10.1103/PhysRevLett.124.117602`.

[299] R. Rossi, N. Prokof'ev, B. Svistunov, K. V. Houcke, and F. Werner. "Polynomial complexity despite the fermionic sign". *EPL (Europhysics Letters)* 118.1 (Apr. 2017), p. 10004. DOI: `10.1209/0295-5075/118/10004`. URL: `https://doi.org/10.1209/0295-5075/118/10004`.

[300] J. Gukelberger, L. Huang, and P. Werner. "On the dangers of partial diagrammatic summations: Benchmarks for the two-dimensional Hubbard model in the weak-coupling regime". *Phys. Rev. B* 91 (23 June 2015), p. 235114. DOI: `10.1103/PhysRevB.91.235114`. URL: `https://link.aps.org/doi/10.1103/PhysRevB.91.235114`.

[301] R. Rossi, F. Šimkovic, and M. Ferrero. "Renormalized perturbation theory at large expansion orders". *EPL (Europhysics Letters)* 132.1 (Nov. 2020), p. 11001. DOI: 10.1209/0295-5075/132/11001. URL: https://doi.org/10.1209/0295-5075/132/11001.

[302] C. Lenihan, A. J. Kim, F. Šimkovic, and E. Kozik. "Evaluating Second-Order Phase Transitions with Diagrammatic Monte Carlo: Néel Transition in the Doped Three-Dimensional Hubbard Model". *Phys. Rev. Lett.* 129 (10 Aug. 2022), p. 107202. DOI: 10.1103/PhysRevLett.129.107202. URL: https://link.aps.org/doi/10.1103/PhysRevLett.129.107202.

[303] J., Kuneš. "Efficient treatment of two-particle vertices in dynamical mean-field theory". *Phys. Rev. B* 83 (8 Feb. 2011), p. 085102. DOI: 10.1103/PhysRevB.83.085102. URL: https://link.aps.org/doi/10.1103/PhysRevB.83.085102.

[304] A. S. Mishchenko, N. V. Prokof'ev, A. Sakamoto, and B. V. Svistunov. "Diagrammatic quantum Monte Carlo study of the Fröhlich polaron". *Phys. Rev. B* 62 (10 Sept. 2000), pp. 6317–6336. DOI: 10.1103/PhysRevB.62.6317. URL: https://link.aps.org/doi/10.1103/PhysRevB.62.6317.

[305] W. Wu, M. Ferrero, A. Georges, and E. Kozik. "Controlling Feynman diagrammatic expansions: Physical nature of the pseudogap in the two-dimensional Hubbard model". *Phys. Rev. B* 96 (4 July 2017), 041105(R). DOI: 10.1103/PhysRevB.96.041105. URL: https://link.aps.org/doi/10.1103/PhysRevB.96.041105.

[306] A. A. Katanin. "Extended dynamical mean field theory combined with the two-particle irreducible functional renormalization-group approach as a tool to study strongly correlated systems". *Phys. Rev. B* 99 (11 Mar. 2019), p. 115112. DOI: 10.1103/PhysRevB.99.115112. URL: https://link.aps.org/doi/10.1103/PhysRevB.99.115112.

[307] J. Paki, H. Terletska, S. Iskakov, and E. Gull. "Charge order and antiferromagnetism in the extended Hubbard model". *Phys. Rev. B* 99 (24 June 2019), p. 245146. DOI: 10.1103/PhysRevB.99.245146. URL: https://link.aps.org/doi/10.1103/PhysRevB.99.245146.

[308] H. Terletska, T. Chen, J. Paki, and E. Gull. "Charge ordering and nonlocal correlations in the doped extended Hubbard model". *Phys. Rev. B* 97 (11 Mar. 2018), p. 115117. DOI: 10.1103/PhysRevB.97.115117. URL: https://link.aps.org/doi/10.1103/PhysRevB.97.115117.

[309] M. Schüler, M. Rösner, T. O. Wehling, A. I. Lichtenstein, and M. I. Katsnelson. "Optimal Hubbard Models for Materials with Nonlocal Coulomb Interactions: Graphene, Silicene, and Benzene". *Phys. Rev. Lett.* 111 (3 July 2013), p. 036601. DOI: 10.1103/PhysRevLett.111.036601. URL: https://link.aps.org/doi/10.1103/PhysRevLett.111.036601.

[310] O. Gunnarsson, J. Merino, T. Schäfer, G. Sangiovanni, G. Rohringer, and A. Toschi. "Complementary views on electron spectra: From fluctuation diagnostics to real-space correlations". *Phys. Rev. B* 97 (12 Mar. 2018), p. 125134. DOI: 10.1103/PhysRevB.97.125134. URL: https://link.aps.org/doi/10.1103/PhysRevB.97.125134.

[311] G. A. Baker Jr. "Application of the Padé Approximant Method to the Investigation of Some Magnetic Properties of the Ising Model". *Phys. Rev.* 124 (3 Nov. 1961), pp. 768–774. DOI: 10.1103/PhysRev.124.768. URL: https://link.aps.org/doi/10.1103/PhysRev.124.768.

[312] H. Terletska, T. Chen, and E. Gull. "Charge ordering and correlation effects in the extended Hubbard model". *Phys. Rev. B* 95 (11 Mar. 2017), p. 115149. DOI: 10.1103/PhysRevB.95.115149. URL: https://link.aps.org/doi/10.1103/PhysRevB.95.115149.

[313] C.-O. Almbladh, U. v. Barth, and R. v. Leeuwen. "Variational total energies from Φ- and Ψ- Derivable Theories". *International Journal of Modern Physics B* 13.05n06 (1999), pp. 535–541. DOI: 10.1142/S0217979299000436. URL: https://doi.org/10.1142/S0217979299000436.

[314] J. M. Luttinger and J. C. Ward. "Ground-State Energy of a Many-Fermion System. II". *Phys. Rev.* 118 (5 June 1960), pp. 1417–1427. DOI: 10.1103/PhysRev.118.1417. URL: https://link.aps.org/doi/10.1103/PhysRev.118.1417.

[315] G. Baym and L. P. Kadanoff. "Conservation Laws and Correlation Functions". *Phys. Rev.* 124 (2 Oct. 1961), pp. 287–299. DOI: 10.1103/PhysRev.124.287. URL: https://link.aps.org/doi/10.1103/PhysRev.124.287.

[316] M. Potthoff. "Self-energy-functional approach to systems of correlated electrons". *The European Physical Journal B - Condensed Matter and Complex Systems* 32.4 (Apr. 2003), pp. 429–436. ISSN: 1434-6036. DOI: 10.1140/epjb/e2003-00121-8. URL: https://doi.org/10.1140/epjb/e2003-00121-8.

[317] C.-H. Pao and N. E. Bickers. "Renormalization-group acceleration of self-consistent field solutions: Two-dimensional Hubbard model". *Phys. Rev. B* 49 (3 Jan. 1994), pp. 1586–1599. DOI: 10.1103/PhysRevB.49.1586. URL: https://link.aps.org/doi/10.1103/PhysRevB.49.1586.

[318] F. Tandetzky, J. K. Dewhurst, S. Sharma, and E. K. U. Gross. "Multiplicity of solutions to GW-type approximations". *Phys. Rev. B* 92 (11 Sept. 2015), p. 115125. DOI: 10.1103/PhysRevB.92.115125. URL: https://link.aps.org/doi/10.1103/PhysRevB.92.115125.

[319] H. Hafermann, K. R. Patton, and P. Werner. "Improved estimators for the self-energy and vertex function in hybridization-expansion continuous-time quantum Monte Carlo simulations". *Phys. Rev. B* 85 (20 May 2012), p. 205106. DOI: 10.1103/PhysRevB.85.205106. URL: http://link.aps.org/doi/10.1103/PhysRevB.85.205106.

[320] P. Gunacker, M. Wallerberger, T. Ribic, A. Hausoel, G. Sangiovanni, and K. Held. "Worm-improved estimators in continuous-time quantum Monte Carlo". *Phys. Rev. B* 94 (12 Sept. 2016), p. 125153. DOI: 10.1103/PhysRevB.94.125153. URL: https://link.aps.org/doi/10.1103/PhysRevB.94.125153.

[321] J. Kaufmann, P. Gunacker, A. Kowalski, G. Sangiovanni, and K. Held. "Symmetric improved estimators for continuous-time quantum Monte Carlo". *Phys. Rev. B* 100 (7 Aug. 2019), p. 075119. DOI: 10.1103/PhysRevB.100.075119. URL: https://link.aps.org/doi/10.1103/PhysRevB.100.075119.

[322] URL: https://github.com/w2dynamics/w2dynamics/wiki/Density-density-and-Kanamori-interacting:-a-two-orbital-model.

[323] A. N. Rubtsov, E. A. Stepanov, and A. I. Lichtenstein. "Collective magnetic fluctuations in Hubbard plaquettes captured by fluctuating local field method". *Phys. Rev. B* 102 (22 Dec. 2020), p. 224423. DOI: 10.1103/PhysRevB.102.224423. URL: https://link.aps.org/doi/10.1103/PhysRevB.102.224423.

[324] C.-H. Pao and N. E. Bickers. "Renormalization-group acceleration of self-consistent field solutions: Two-dimensional Hubbard model". *Phys. Rev. B* 49 (3 Jan. 1994), pp. 1586–1599. DOI: 10.1103/PhysRevB.49.1586. URL: https://link.aps.org/doi/10.1103/PhysRevB.49.1586.

[325] S. Vacondio, D. Varsano, A. Ruini, and A. Ferretti. "Numerically Precise Benchmark of Many-Body Self-Energies on Spherical Atoms". *Journal of Chemical Theory and Computation* 18.6 (2022). PMID: 35561415, pp. 3703–3717. DOI: 10.1021/acs.jctc.2c00048. URL: https://doi.org/10.1021/acs.jctc.2c00048.

[326] W. Wu, M. Ferrero, A. Georges, and E. Kozik. "Controlling Feynman diagrammatic expansions: Physical nature of the pseudogap in the two-dimensional Hubbard model". *Phys. Rev. B* 96 (4 July 2017), p. 041105. DOI: 10.1103/PhysRevB.96.041105. URL: https://link.aps.org/doi/10.1103/PhysRevB.96.041105.

[327] R. Staudt, M. Dzierzawa, and A. Muramatsu. "Phase diagram of the three-dimensional Hubbard model at half filling". *The European Physical Journal B - Condensed Matter and Complex Systems* 17.3 (Oct. 2000), pp. 411–415. ISSN: 1434-6036. DOI: 10.1007/s100510070120. URL: https://doi.org/10.1007/s100510070120.

[328] L. Del Re and G. Rohringer. "Fluctuations analysis of spin susceptibility: Néel ordering revisited in dynamical mean field theory". *Phys. Rev. B* 104 (23 Dec. 2021), p. 235128. DOI: 10.1103/PhysRevB.104.235128. URL: https://link.aps.org/doi/10.1103/PhysRevB.104.235128.

[329] P. R. C. Kent, M. Jarrell, T. A. Maier, and T. Pruschke. "Efficient calculation of the antiferromagnetic phase diagram of the three-dimensional Hubbard model". *Phys. Rev. B* 72 (6 Aug. 2005), p. 060411. DOI: 10.1103/PhysRevB.72.060411. URL: https://link.aps.org/doi/10.1103/PhysRevB.72.060411.

[330] G. Rohringer, A. Toschi, A. Katanin, and K. Held. "Critical Properties of the Half-Filled Hubbard Model in Three Dimensions". *Phys. Rev. Lett.* 107 (25 Dec. 2011), p. 256402. DOI: 10.1103/PhysRevLett.107.256402. URL: https://link.aps.org/doi/10.1103/PhysRevLett.107.256402.

[331] E. Kozik, E. Burovski, V. W. Scarola, and M. Troyer. "Néel temperature and thermodynamics of the half-filled three-dimensional Hubbard model by diagrammatic determinant Monte Carlo". *Phys. Rev. B* 87 (20 May 2013), p. 205102. DOI: 10.1103/PhysRevB.87.205102. URL: https://link.aps.org/doi/10.1103/PhysRevB.87.205102.

[332] L. Boehnke and F. Lechermann. "Competing orders in Na_xCoO_2 from strong correlations on a two-particle level". *Phys. Rev. B* 85 (11 Mar. 2012), p. 115128. DOI: 10.1103/PhysRevB.85.115128. URL: https://link.aps.org/doi/10.1103/PhysRevB.85.115128.

[333] L. de'Medici. "Hund's coupling and its key role in tuning multiorbital correlations". *Phys. Rev. B* 83 (20 May 2011), p. 205112. DOI: 10.1103/PhysRevB.83.205112. URL: https://link.aps.org/doi/10.1103/PhysRevB.83.205112.

[334] O. Custance, R. Perez, and S. Morita. "Atomic force microscopy as a tool for atom manipulation". *Nature Nanotechnology* 4.12 (Dec. 2009), pp. 803–810. ISSN: 1748-3395. DOI: 10.1038/nnano.2009.347. URL: https://doi.org/10.1038/nnano.2009.347.

[335] D. M. Kennes, M. Claassen, L. Xian, A. Georges, A. J. Millis, J. Hone, C. R. Dean, D. N. Basov, A. N. Pasupathy, and A. Rubio. "Moiré heterostructures as a condensed-matter quantum simulator". *Nature Physics* 17.2 (Feb. 2021), pp. 155–163. ISSN: 1745-2481. DOI: 10.1038/s41567-020-01154-3. URL: https://doi.org/10.1038/s41567-020-01154-3.

[336] M. Vojta and E. Dagotto. "Indications of unconventional superconductivity in doped and undoped triangular antiferromagnets". *Phys. Rev. B* 59 (2 Jan. 1999), R713–R716. DOI: 10.1103/PhysRevB.59.R713. URL: https://link.aps.org/doi/10.1103/PhysRevB.59.R713.

[337] C. Weber, A. Läuchli, F. Mila, and T. Giamarchi. "Magnetism and superconductivity of strongly correlated electrons on the triangular lattice". *Phys. Rev. B* 73 (1 Jan. 2006), p. 014519. DOI: 10.1103/PhysRevB.73.014519. URL: https://link.aps.org/doi/10.1103/PhysRevB.73.014519.

[338] X. Cao, T. Ayral, Z. Zhong, O. Parcollet, D. Manske, and P. Hansmann. "Chiral *d*-wave superconductivity in a triangular surface lattice mediated by long-range interaction". *Phys. Rev. B* 97 (15 Apr. 2018), p. 155145. DOI: 10.1103/PhysRevB.97.155145. URL: https://link.aps.org/doi/10.1103/PhysRevB.97.155145.

[339] X. Wu, F. Ming, T. S. Smith, G. Liu, F. Ye, K. Wang, S. Johnston, and H. H. Weitering. "Superconductivity in a Hole-Doped Mott-Insulating Triangular Adatom Layer on a Silicon Surface". *Phys. Rev. Lett.* 125 (11 Sept. 2020), p. 117001. DOI: 10.1103/PhysRevLett.125.117001. URL: https://link.aps.org/doi/10.1103/PhysRevLett.125.117001.

[340] G. Li, M. Laubach, A. Fleszar, and W. Hanke. "Geometrical frustration and the competing phases of the Sn/Si(111) $\sqrt{3} \times \sqrt{3}R30°$ surface systems". *Phys. Rev. B* 83 (4 Jan. 2011), p. 041104. DOI: 10.1103/PhysRevB.83.041104. URL: https://link.aps.org/doi/10.1103/PhysRevB.83.041104.

[341] F. Adler, S. Rachel, M. Laubach, J. Maklar, A. Fleszar, J. Schäfer, and R. Claessen. "Correlation-Driven Charge Order in a Frustrated Two-Dimensional Atom Lattice". *Phys. Rev. Lett.* 123 (8 Aug. 2019), p. 086401. DOI: 10.1103/PhysRevLett.123.086401. URL: https://link.aps.org/doi/10.1103/PhysRevLett.123.086401.

[342] C. Tresca, C. Brun, T. Bilgeri, G. Menard, V. Cherkez, R. Federicci, D. Longo, F. Debontridder, M. D'angelo, D. Roditchev, G. Profeta, M. Calandra, and T. Cren. "Chiral Spin Texture in the Charge-Density-Wave Phase of the Correlated Metallic Pb/Si(111) Monolayer". *Phys. Rev. Lett.* 120 (19 May 2018), p. 196402. DOI: 10.1103/PhysRevLett.120.196402. URL: https://link.aps.org/doi/10.1103/PhysRevLett.120.196402.

[343] D. I. Badrtdinov, S. A. Nikolaev, M. I. Katsnelson, and V. V. Mazurenko. "Spin-orbit coupling and magnetic interactions in Si(111):C,Si,Sn,Pb". *Phys. Rev. B* 94 (22 Dec. 2016), p. 224418. DOI: 10.1103/PhysRevB.94.224418. URL: https://link.aps.org/doi/10.1103/PhysRevB.94.224418.

[344] C. Brun, T. Cren, and D. Roditchev. "Review of 2D superconductivity: the ultimate case of epitaxial monolayers". *Superconductor Science and Technology* 30.1 (Nov. 2016), p. 013003. DOI: 10.1088/0953-2048/30/1/013003. URL: https://doi.org/10.1088/0953-2048/30/1/013003.

[345] C. Brun, T. Cren, V. Cherkez, F. Debontridder, S. Pons, D. Fokin, M. C. Tringides, S. Bozhko, L. B. Ioffe, B. L. Altshuler, and D. Roditchev. "Remarkable effects of disorder on superconductivity of single atomic layers of lead on silicon". *Nature Physics* 10.6 (June 2014), pp. 444–450. ISSN: 1745-2481. DOI: 10.1038/nphys2937. URL: https://doi.org/10.1038/nphys2937.

[346] J. M. Carpinelli, H. H. Weitering, E. W. Plummer, and R. Stumpf. "Direct observation of a surface charge density wave". *Nature* 381.6581 (May 1996), pp. 398–400. ISSN: 1476-4687. DOI: 10.1038/381398a0. URL: https://doi.org/10.1038/381398a0.

[347] J. M. Carpinelli, H. H. Weitering, M. Bartkowiak, R. Stumpf, and E. W. Plummer. "Surface Charge Ordering Transition: α Phase of Sn/Ge(111)". *Phys. Rev. Lett.* 79 (15 Oct. 1997), pp. 2859–2862. DOI: 10.1103/PhysRevLett.79.2859. URL: https://link.aps.org/doi/10.1103/PhysRevLett.79.2859.

[348] C. Tresca and M. Calandra. "Charge density wave in single-layer Pb/Ge(111) driven by Pb-substrate exchange interaction". *Phys. Rev. B* 104 (4 July 2021), p. 045126. DOI: 10.1103/PhysRevB.104.045126. URL: https://link.aps.org/doi/10.1103/PhysRevB.104.045126.

[349] J. Wu, P. Phillips, and A. H. Castro Neto. "Theory of the Magnetic Moment in Iron Pnictides". *Phys. Rev. Lett.* 101 (12 Sept. 2008), p. 126401. DOI: 10.1103/PhysRevLett.101.126401. URL: https://link.aps.org/doi/10.1103/PhysRevLett.101.126401.

[350] G. Profeta and E. Tosatti. "Triangular Mott-Hubbard Insulator Phases of Sn/Si(111) and Sn/Ge(111) Surfaces". *Phys. Rev. Lett.* 98 (8 Feb. 2007), p. 086401. DOI: 10.1103/PhysRevLett.98.086401. URL: https://link.aps.org/doi/10.1103/PhysRevLett.98.086401.

[351] S. Schuwalow, D. Grieger, and F. Lechermann. "Realistic modeling of the electronic structure and the effect of correlations for Sn/Si(111) and Sn/Ge(111) surfaces". *Phys. Rev. B* 82 (3 July 2010), p. 035116. DOI: 10.1103/PhysRevB.82.035116. URL: https://link.aps.org/doi/10.1103/PhysRevB.82.035116.

[352] P. Blaha, K. Schwarz, G. Madsen, D. Kvasnicka, J. Luitz, R. Laskowski, F. Tran, and L. D. Marks. *WIEN2k, An augmented Plane Wave + Local Orbitals Program for Calculating Crystal Properties*. Karlheinz Schwarz, Techn. Universität Wien, Austria,ISBN 3-9501031-1-2, 2018.

[353] P. Blaha, K. Schwarz, F. Tran, R. Laskowski, G. K. H. Madsen, and L. D. Marks. "WIEN2k: An APW+lo program for calculating the properties of solids". *The Journal of Chemical Physics* 152.7 (2020), p. 074101. DOI: 10.1063/1.5143061. URL: https://doi.org/10.1063/1.5143061.

[354] F. Ming, S. Johnston, D. Mulugeta, T. S. Smith, P. Vilmercati, G. Lee, T. A. Maier, P. C. Snijders, and H. H. Weitering. "Realization of a Hole-Doped Mott Insulator on a Triangular Silicon Lattice". *Phys. Rev. Lett.* 119 (26 Dec. 2017), p. 266802. DOI: 10.1103/PhysRevLett.119.266802. URL: https://link.aps.org/doi/10.1103/PhysRevLett.119.266802.

[355] P. Kurz, G. Bihlmayer, K. Hirai, and S. Blügel. "Three-Dimensional Spin Structure on a Two-Dimensional Lattice: Mn /Cu(111)". *Phys. Rev. Lett.* 86 (6 Feb. 2001), pp. 1106–1109. DOI: 10.1103/PhysRevLett.86.1106. URL: https://link.aps.org/doi/10.1103/PhysRevLett.86.1106.

[356] M. K. Ramazanov. "Phase transitions in the antiferromagnetic Heisenberg model on a layered triangular lattice with the next-nearest neighbor interactions". *JETP Letters* 94.4 (Oct. 2011), p. 311. ISSN: 1090-6487. DOI: 10.1134/S0021364011160156. URL: https://doi.org/10.1134/S0021364011160156.

[357] I. Brihuega, O. Custance, R. Pérez, and J. M. Gómez-Rodriguez. "Intrinsic Character of the (3×3) to $(\sqrt{3} \times \sqrt{3})$ Phase Transition in Pb/Si(111)". *Phys. Rev. Lett.* 94 (4 Feb. 2005), p. 046101. DOI: 10.1103/PhysRevLett.94.046101. URL: https://link.aps.org/doi/10.1103/PhysRevLett.94.046101.

[358] I. Brihuega, O. Custance, M. M. Ugeda, and J. M. Gómez-Rodriguez. "Defects in the $(\sqrt{3} \times \sqrt{3}) \Leftrightarrow (3 \times 3)$ phase transition in Pb/Si(111) system". *Phys. Rev. B* 75 (15 Apr. 2007), p. 155411. DOI: 10.1103/PhysRevB.75.155411. URL: https://link.aps.org/doi/10.1103/PhysRevB.75.155411.

[359] L. Floreano, D. Cvetko, G. Bavdek, M. Benes, and A. Morgante. "Order-disorder transition of the (3×3) Sn/Ge(111) phase". *Phys. Rev. B* 64 (7 July 2001), p. 075405. DOI: 10.1103/PhysRevB.64.075405. URL: https://link.aps.org/doi/10.1103/PhysRevB.64.075405.

[360] N. Manini, G. E. Santoro, A. Dal Corso, and E. Tosatti. "Sensitivity of the Mott transition to noncubic splitting of the orbital degeneracy: Application to $NH_3K_3C_{60}$". *Phys. Rev. B* 66 (11 Sept. 2002), p. 115107. DOI: 10.1103/PhysRevB.66.115107. URL: https://link.aps.org/doi/10.1103/PhysRevB.66.115107.

[361] M. Capone, M. Fabrizio, C. Castellani, and E. Tosatti. "Strongly Correlated Superconductivity". *Science* 296.5577 (2002), pp. 2364–2366. ISSN: 0036-8075. DOI: 10.1126/science.1071122. URL: http://science.sciencemag.org/content/296/5577/2364.

[362] M. Capone, M. Fabrizio, C. Castellani, and E. Tosatti. "Colloquium: Modeling the unconventional superconducting properties of expanded A_3C_{60} fullerides". *Rev. Mod. Phys.* 81 (2 June 2009), pp. 943–958. DOI: 10.1103/RevModPhys.81.943. URL: https://link.aps.org/doi/10.1103/RevModPhys.81.943.

[363] Y. Nomura, K. Nakamura, and R. Arita. "Ab initio derivation of electronic low-energy models for C_{60} and aromatic compounds". *Phys. Rev. B* 85 (15 Apr. 2012), p. 155452. DOI: 10.1103/PhysRevB.85.155452. URL: https://link.aps.org/doi/10.1103/PhysRevB.85.155452.

[364] S. Hoshino and P. Werner. "Spontaneous Orbital-Selective Mott Transitions and the Jahn-Teller Metal of A_3C_{60}". *Phys. Rev. Lett.* 118 (17 Apr. 2017), p. 177002. DOI: 10.1103/PhysRevLett.118.177002. URL: https://link.aps.org/doi/10.1103/PhysRevLett.118.177002.

[365] J. Duchene, M. Terraillon, P. Pailly, and G. Adam. "Filamentary Conduction in VO_2 Coplanar Thin-Film Devices". *Appl. Phys. Lett.* 19.4 (1971), pp. 115–117. DOI: 10.1063/1.1653835. URL: https://doi.org/10.1063/1.1653835.

[366] T. Driscoll, H.-T. Kim, B.-G. Chae, M. Di Ventra, and D. N. Basov. "Phase-transition driven memristive system". *Appl. Phys. Lett.* 95.4 (2009), p. 043503. DOI: 10.1063/1.3187531. URL: https://doi.org/10.1063/1.3187531.

[367] W. Bao, C. Broholm, G. Aeppli, P. Dai, J. M. Honig, and P. Metcalf. "Dramatic Switching of Magnetic Exchange in a Classic Transition Metal Oxide: Evidence for Orbital Ordering". *Phys. Rev. Lett.* 78 (3 Jan. 1997), pp. 507–510. DOI: 10.1103/PhysRevLett.78.507. URL: https://link.aps.org/doi/10.1103/PhysRevLett.78.507.

[368] F. Lechermann, S. Biermann, and A. Georges. "Interorbital Charge Transfers and Fermi-Surface Deformations in Strongly Correlated Metals: Models, $BaVS_3$ and Na_xCoO_2". *Prog. Theor. Phys. Supp.* 160 (June 2005), pp. 233–252. ISSN: 0375-9687. DOI: 10.1143/PTPS.160.233. URL: https://doi.org/10.1143/PTPS.160.233.

[369] A. I. Poteryaev, M. Ferrero, A. Georges, and O. Parcollet. "Effect of crystal-field splitting and interband hybridization on the metal-insulator transitions of strongly correlated systems". *Phys. Rev. B* 78 (4 July 2008), p. 045115. DOI: 10.1103/PhysRevB.78.045115. URL: https://link.aps.org/doi/10.1103/PhysRevB.78.045115.

[370] N. Parragh, G. Sangiovanni, P. Hansmann, S. Hummel, K. Held, and A. Toschi. "Effective crystal field and Fermi surface topology: A comparison of d- and dp-orbital models". *Phys. Rev. B* 88 (19 Nov. 2013), p. 195116. DOI: 10.1103/

PhysRevB.88.195116. URL: https://link.aps.org/doi/10.1103/PhysRevB.88.195116.

[371] V. I. Anisimov, I. A. Nekrasov, D. E. Kondakov, T. M. Rice, and M. Sigrist. "Orbital-selective Mott-insulator transition in $Ca_{2-x}Sr_xRuO_4$". *Eur. Phys. J. B* 25.2 (Jan. 1, 2002), pp. 191–201. ISSN: 1434-6036. DOI: 10.1140/epjb/e20020021. URL: https://doi.org/10.1140/epjb/e20020021.

[372] R. Arita and K. Held. "Orbital-selective Mott-Hubbard transition in the two-band Hubbard model". *Phys. Rev. B* 72 (20 Nov. 2005), p. 201102. DOI: 10.1103/PhysRevB.72.201102. URL: https://link.aps.org/doi/10.1103/PhysRevB.72.201102.

[373] L. de'Medici, S. R. Hassan, and M. Capone. "Genesis of coexisting itinerant and localized electrons in iron pnictides". *Journal of superconductivity and novel magnetism* 22.6 (2009), pp. 535–538.

[374] P. Werner and A. J. Millis. "High-Spin to Low-Spin and Orbital Polarization Transitions in Multiorbital Mott Systems". *Phys. Rev. Lett.* 99 (12 Sept. 2007), p. 126405. DOI: 10.1103/PhysRevLett.99.126405. URL: https://link.aps.org/doi/10.1103/PhysRevLett.99.126405.

[375] A. Hackl and M. Vojta. "Pressure-induced magnetic transition and volume collapse in FeAs superconductors: an orbital-selective Mott scenario". *New Journal of Physics* 11.5 (May 2009), p. 055064. DOI: 10.1088/1367-2630/11/5/055064. URL: https://doi.org/10.1088/1367-2630/11/5/055064.

[376] P. Werner, E. Gull, and A. J. Millis. "Metal-insulator phase diagram and orbital selectivity in three-orbital models with rotationally invariant Hund coupling". *Phys. Rev. B* 79 (11 Mar. 2009), p. 115119. DOI: 10.1103/PhysRevB.79.115119. URL: https://link.aps.org/doi/10.1103/PhysRevB.79.115119.

[377] L. de'Medici, S. R. Hassan, M. Capone, and X. Dai. "Orbital-Selective Mott Transition out of Band Degeneracy Lifting". *Phys. Rev. Lett.* 102 (12 Mar. 2009), p. 126401. DOI: 10.1103/PhysRevLett.102.126401. URL: https://link.aps.org/doi/10.1103/PhysRevLett.102.126401.

[378] T. Kita, T. Ohashi, and N. Kawakami. "Mott transition in three-orbital Hubbard model with orbital splitting". *Phys. Rev. B* 84 (19 Nov. 2011), p. 195130. DOI: 10.1103/PhysRevB.84.195130. URL: https://link.aps.org/doi/10.1103/PhysRevB.84.195130.

[379] L. Huang, L. Du, and X. Dai. "Complete phase diagram for three-band Hubbard model with orbital degeneracy lifted by crystal field splitting". *Phys. Rev. B* 86 (3 July 2012), p. 035150. DOI: 10.1103/PhysRevB.86.035150. URL: https://link.aps.org/doi/10.1103/PhysRevB.86.035150.

[380] Y. Wang, L. Huang, L. Du, and X. Dai. "Doping-driven orbital-selective Mott transition in multi-band Hubbard models with crystal field splitting". *Chinese Phys. B* 25.3 (Mar. 2016), p. 037103. DOI: 10.1088/1674-1056/25/3/037103. URL: https://doi.org/10.1088/1674-1056/25/3/037103.

[381] S. Hoshino and P. Werner. "Electronic orders in multiorbital Hubbard models with lifted orbital degeneracy". *Phys. Rev. B* 93 (15 Apr. 2016), p. 155161. DOI: 10.1103/PhysRevB.93.155161. URL: https://link.aps.org/doi/10.1103/PhysRevB.93.155161.

[382] K. Steiner, S. Hoshino, Y. Nomura, and P. Werner. "Long-range orders and spin/orbital freezing in the two-band Hubbard model". *Phys. Rev. B* 94 (7 Aug. 2016), p. 075107. DOI: 10.1103/PhysRevB.94.075107. URL: https://link.aps.org/doi/10.1103/PhysRevB.94.075107.

[383] F. B. Kugler, S.-S. B. Lee, A. Weichselbaum, G. Kotliar, and J. von Delft. "Orbital differentiation in Hund metals". *Phys. Rev. B* 100 (11 Sept. 2019), p. 115159. DOI: 10.1103/PhysRevB.100.115159. URL: https://link.aps.org/doi/10.1103/PhysRevB.100.115159.

[384] H. Park, K. Haule, and G. Kotliar. "Magnetic Excitation Spectra in $BaFe_2As_2$: A Two-Particle Approach within a Combination of the Density Functional Theory and the Dynamical Mean-Field Theory Method". *Phys. Rev. Lett.* 107 (13 Sept. 2011), p. 137007. DOI: 10.1103/PhysRevLett.107.137007. URL: https://link.aps.org/doi/10.1103/PhysRevLett.107.137007.

[385] S. Acharya, D. Pashov, C. Weber, H. Park, L. Sponza, and M. Van Schilfgaarde. "Evening out the spin and charge parity to increase T_c Sr_2RuO_4". *Commun. Phys.* 2.1 (2019), pp. 1–8. DOI: 10.1038/s42005-019-0254-1. URL: https://doi.org/10.1038/s42005-019-0254-1.

[386] Z. Zhong, M. Wallerberger, J. M. Tomczak, C. Taranto, N. Parragh, A. Toschi, G. Sangiovanni, and K. Held. "Electronics with Correlated Oxides: $SrVO_3$/$SrTiO_3$ as a Mott Transistor". *Phys. Rev. Lett.* 114 (24 June 2015), p. 246401. DOI: 10.1103/PhysRevLett.114.246401. URL: https://link.aps.org/doi/10.1103/PhysRevLett.114.246401.

[387] F. Nilsson, L. Boehnke, P. Werner, and F. Aryasetiawan. "Multitier self-consistent GW + EDMFT". *Phys. Rev. Materials* 1 (4 Sept. 2017), p. 043803. DOI: 10.1103/PhysRevMaterials.1.043803. URL: https://link.aps.org/doi/10.1103/PhysRevMaterials.1.043803.

[388] G. Rohringer, A. Toschi, H. Hafermann, K. Held, V. I. Anisimov, and A. A. Katanin. "One-particle irreducible functional approach: A route to diagrammatic extensions of the dynamical mean-field theory". *Phys. Rev. B* 88 (11 Sept. 2013), p. 115112. DOI: 10.1103/PhysRevB.88.115112. URL: https://link.aps.org/doi/10.1103/PhysRevB.88.115112.

[389] F. Krien, A. Kauch, and K. Held. "Tiling with triangles: parquet and $GW\gamma$ methods unified". *Phys. Rev. Research* 3 (1 Feb. 2021), p. 013149. DOI: 10.1103/PhysRevResearch.3.013149. URL: https://link.aps.org/doi/10.1103/PhysRevResearch.3.013149.

[390] E. A. Stepanov, V. Harkov, and A. I. Lichtenstein. *Supplemental material* (2019).

[391] L. de'Medici. "Hund's Induced Fermi-Liquid Instabilities and Enhanced Quasiparticle Interactions". *Phys. Rev. Lett.* 118 (16 Apr. 2017), p. 167003. DOI: 10.1103/PhysRevLett.118.167003. URL: https://link.aps.org/doi/10.1103/PhysRevLett.118.167003.

[392] M. Chatzieleftheriou, M. Berović, P. Villar Arribi, M. Capone, and L. de'Medici. "Enhancement of charge instabilities in Hund's metals by breaking of rotational symmetry". *Phys. Rev. B* 102 (20 Nov. 2020), p. 205127. DOI: 10.1103/PhysRevB.102.205127. URL: https://link.aps.org/doi/10.1103/PhysRevB.102.205127.

[393] A. Sherman. "Hubbard-Kanamori model: spectral functions, negative electron compressibility, and susceptibilities". *Physica Scripta* 95.9 (Aug. 2020), p. 095804. DOI: 10.1088/1402-4896/aba923. URL: https://doi.org/10.1088/1402-4896/aba923.

[394] M. Chatzieleftheriou. "Charge instabilities, Mott transition and transport in Hund metals". Theses. Université Paris sciences et lettres, July 2021. URL: https://pastel.archives-ouvertes.fr/tel-03391043.

[395] M. Chatzieleftheriou, A. Kowalski, M. Berović, A. Amaricci, M. Capone, L. De Leo, G. Sangiovanni, and L. de' Medici. *Mott Quantum Critical Points at finite doping*. Preprint arXiv:2203.02451. 2022. DOI: 10.48550/ARXIV.2203.02451. URL: https://arxiv.org/abs/2203.02451.

[396] J. Kanamori. "Electron correlation and ferromagnetism of transition metals". *Prog. Theor. Phys.* 30.3 (1963), pp. 275–289.

[397] J. Li, C. Aron, G. Kotliar, and J. E. Han. "Electric-Field-Driven Resistive Switching in the Dissipative Hubbard Model". *Phys. Rev. Lett.* 114 (22 June 2015), p. 226403. DOI: 10.1103/PhysRevLett.114.226403. URL: https://link.aps.org/doi/10.1103/PhysRevLett.114.226403.

[398] D. M. Newns, J. A. Misewich, C. C. Tsuei, A. Gupta, B. A. Scott, and A. Schrott. "Mott transition field effect transistor". *Appl. Phys. Lett.* 73.6 (1998), pp. 780–782. DOI: 10.1063/1.121999. URL: https://doi.org/10.1063/1.121999.

[399] J. Son, S. Rajan, S. Stemmer, and S. James Allen. "A heterojunction modulation-doped Mott transistor". *J. Appl. Phys.* 110.8 (2011), p. 084503. DOI: 10.1063/1.3651612. URL: https://doi.org/10.1063/1.3651612.

[400] A. Pustogow, R. Rösslhuber, Y. Tan, E. Uykur, A. Böhme, M. Wenzel, Y. Saito, A. Löhle, R. Hübner, A. Kawamoto, J. A. Schlueter, V. Dobrosavljević, and M. Dressel. "Low-temperature dielectric anomaly arising from electronic phase separation at the Mott insulator-metal transition". *npj Quantum Mater.* 6.1 (Jan. 27, 2021), p. 9. ISSN: 2397-4648. DOI: 10.1038/s41535-020-00307-0. URL: https://doi.org/10.1038/s41535-020-00307-0.

[401] M. Vandelli, A. Galler, A. Rubio, A. I. Lichtenstein, S. Biermann, and E. A. Stepanov. "The origin of the rich variety of phases in a system of Pb adatoms on Si(111) surface". *In preparation* (2022).

[402] E. A. Stepanov, S. V. Semin, C. R. Woods, M. Vandelli, A. V. Kimel, K. S. Novoselov, and M. I. Katsnelson. "Direct Observation of Incommensurate–Commensurate Transition in Graphene-hBN Heterostructures via Optical Second Harmonic Generation". *ACS Applied Materials & Interfaces* 12.24 (2020). PMID: 32442370, pp. 27758–27764. DOI: 10.1021/acsami.0c05965. URL: https://doi.org/10.1021/acsami.0c05965.

List of Publications

Refereed publications

1. M. Vandelli, V. Harkov, E. A. Stepanov, J. Gukelberger, E. Kozik, A. Rubio, and A. I. Lichtenstein. "Dual boson diagrammatic Monte Carlo approach applied to the extended Hubbard model". *Phys. Rev. B* 102 (19 Nov. 2020), p. 195109. DOI: 10.1103/PhysRevB.102.195109. URL: https://link.aps.org/doi/10.1103/PhysRevB.102.195109

2. V. Harkov, M. Vandelli, S. Brener, A. I. Lichtenstein, and E. A. Stepanov. "Impact of partially bosonized collective fluctuations on electronic degrees of freedom". *Phys. Rev. B* 103 (24 June 2021), p. 245123. DOI: 10.1103/PhysRevB.103.245123. URL: https://link.aps.org/doi/10.1103/PhysRevB.103.245123

3. M. Vandelli, J. Kaufmann, M. El-Nabulsi, V. Harkov, A. I. Lichtenstein, and E. A. Stepanov. "Multi-band D-TRILEX approach to materials with strong electronic correlations". *SciPost Phys.* 13 (2022), p. 036. DOI: 10.21468/SciPostPhys.13.2.036. URL: https://scipost.org/10.21468/SciPostPhys.13.2.036

Publications in preparation

1. M. Vandelli, J. Kaufmann, V. Harkov, A. I. Lichtenstein, K. Held, and E. A. Stepanov. "Extended regime of meta-stable metallic and insulating phases in a two-orbital electronic system". *arXiv e-prints*, arXiv:2204.02116 (2022), - under consideration in Phys. Rev. Lett.

2. M. Vandelli, A. Galler, A. Rubio, A. I. Lichtenstein, S. Biermann, and E. A. Stepanov. "The origin of the rich variety of phases in a system of Pb adatoms on Si(111) surface". *In preparation* (2022)

Unrelated refereed publications

1. E. A. Stepanov, S. V. Semin, C. R. Woods, M. Vandelli, A. V. Kimel, K. S. Novoselov, and M. I. Katsnelson. "Direct Observation of Incommensurate–Commensurate Transition in Graphene-hBN Heterostructures via Optical Second Harmonic Generation". *ACS Applied Materials & Interfaces* 12.24 (2020). PMID: 32442370, pp. 27758–27764. DOI: 10.1021/acsami.0c05965. URL: https://doi.org/10.1021/acsami.0c05965

Acknowledgments

I would like to express my gratitude to my supervisors, Prof. Dr. Angel Rubio and Prof. Dr. Alexander Lichtenstein, who believed in me and gave me the opportunity to pursue my doctoral studies on such a fascinating and challenging topic. Their support went far beyond their duties as supervisors, and I will always be grateful to them for that.

I am also grateful to Dr. Evgeny Stepanov, who not only guided me through everyday research work, but also constantly motivated me during difficult times. It is probably thank to his enthusiasm if I decided to pursue my doctoral studies in the first place. I am also thankful to Prof. Dr. Mikhail Katsnelson, who played an important role in sparking my interest towards condensed matter physics when I was a master student.

I would like to thank all my colleagues at the I. Institüt für Theoretische Physik for the stimulating scientific and informal discussions. In particular, I am grateful to Viktor Harkov, Andrej Lehmann, and Mohamed El-Nabulsi for not only developing an effective professional colaboration, but also for the friendship that connects us. Additionally, I cannot stress enough the support and valuable comments received by Dr. Viktor Valmispild, Yusuf Mohamed, Niklas Witt, Dr. Mikhail Danilov and the other professors, postdocs and doctoral fellows in the group.

I would like to thank all the members of the Theory group at the Max Plank Institute for the Structure and Dynamics of Matter (MPSD). In particular Dr. Enrico Ronca, for supporting me during the early stages of my PhD, Dr. Anna Galler, Dr. Michael Sentef and Dr. Hannes Hübener for the fruitful discussions. I cannot thank Dr. Neda Lotfiomran enough for her invaluable work in organizing the IMPRS: UFAST graduate school and helping me at every single step of the doctoral studies. I am honored to have had the chance to share part of my journey together with the other IMPRS fellows: Damian Hofmann, Lukas Windgaetter, Abhisek Kole, Kevin Lively, Mona Kalthoff, Ilke Albar and Christian Eckhart, just to name a few. I would like to thank Prof. Dr. Evgeny Kozik and his PhD student Connor Lenihan for hosting me in London and deepening my understanding of the methods that I developed during this work. I acknowledge valuable help from the PHYSNet Support Team of Universität Hamburg in all the matters concerning cluster setup and software installation. Navigating the German bureaucracy would have been a nightmare without support from Ute Ramseger, Jutta Voigtmann and the whole HR Teams of the MPSD and of the Cluster of Excellence: Advanced Imaging of Matter (CUI:AIM) of the Universität Hamburg.

This work would have been impossible without the continuous support of my family and friends. In particular, I want to thank my mum Milena for never doubting in me. I cannot express enough gratitude to Irene for always being there, even when we were separated by thousands of kilometers. I have to mention my grandmas Angela and Pina

for cooking delicious Italian food every time I went back home. I wish my father Fausto could be here today to witness my achievements. I am so grateful to him for sparking my interest in science when I was a child and for teaching me to do everything at my best.

Finally, I would like to thank my Italian friends in Hamburg, Matteo and Luca. Living two years during the Pandemics far away from home would have been unbearable without their company.

Matteo Vandelli   Hamburg, 2022

Eidesstattliche Versicherung / Declaration on oath

Hiermit versichere ich an Eides statt, die vorliegende Dissertationsschrift selbst verfasst und keine anderen als die angegebenen Hilfsmittel und Quellen benutzt zu haben.

Hamburg, 19.09.2022

_____

Unterschrift der Doktorandin / des Doktoranden

258

Ich versichere, dass dieses gebundene Exemplar der Dissertation und das in elektronischer Form eingereichte Dissertationsexemplar (über den Docata-Upload) und das bei der Fakultät (zuständiges Studienbüro bzw. Promotionsbüro Physik) zur Archivierung eingereichte gedruckte gebundene Exemplar der Dissertationsschrift identisch sind.

Hamburg, 19.09.2022

_____

Unterschrift der Doktorandin / des Doktoranden